Theoretical and numerical study of seismic tsunami dynamics

Marine Le Gal

▶ **To cite this version:**

Marine Le Gal. Theoretical and numerical study of seismic tsunami dynamics. Fluids mechanics [physics.class-ph]. Université Paris-Est, 2017. English. NNT : 2017PESC1008 . tel-01529253

HAL Id: tel-01529253
https://pastel.hal.science/tel-01529253

Submitted on 30 May 2017

HAL is a multi-disciplinary open access archive for the deposit and dissemination of scientific research documents, whether they are published or not. The documents may come from teaching and research institutions in France or abroad, or from public or private research centers.

L'archive ouverte pluridisciplinaire **HAL**, est destinée au dépôt et à la diffusion de documents scientifiques de niveau recherche, publiés ou non, émanant des établissements d'enseignement et de recherche français ou étrangers, des laboratoires publics ou privés.

UNIVERSITÉ PARIS-EST

École Doctorale SIE

Laboratoire d'Hydraulique Saint-Venant

Thèse

Présentée pour l'obtention du grade de DOCTEUR
DE L'UNIVERSITE PARIS-EST
par

Marine Le Gal

Influence des échelles de temps sur la dynamique des tsunamis d'origine sismique

---

Spécialité : Mécanique des fluides

Soutenue le 17 février 2017 devant un jury composé de :

Rapporteur	**Pr. Stephan Grilli**	(University of Rhode Island)
Rapporteur	**Dr. Denys Dutykh**	(Université Savoie Mont Blanc)
Examinateur	**Pr. Didier Clamond**	(Université de Nice-Sofia Antipolis)
Examinateur	**Dr. Mario Ricchiuto**	(Inria Bordeaux)
Examinateur	**Dr. Hélène Hébert**	(CEA)
Directeur de thèse	**Dr. Damien Violeau**	(EDF R&D)
Invité	**Dr. Riadh Ata**	(EDF R&D)

Thèse effectuée au sein du **Laboratoire d'Hydraulique Saint-Venant**

de l'Université Paris-Est

6, quai Watier

BP 49

78401 Chatou cedex

France

Tsunamis in the Atlantic and the English ChaNnel:
Definition of the Effects through numerical Modeling

Ce travail a été financé par le projet TANDEM, référence ANR-11-RSNR-0023-01 du programme français d'Investissement d'Avenir (PIA 2014-2018).

Résumé

Dû à leur impact destructeur et meurtrier, il est important de comprendre la dynamique des tsunamis afin d'améliorer les modèles de prévention et d'alerte. Le peu de données disponibles *in situ* rend la génération des tsunamis peu connue. Les modèles de générations, notamment la génération sismique qui est considérée ici, simplifient les phénomènes mis en jeu. De nombreux effets sont négligés, parmi eux la cinématique de déformation du fond. Deux paramètres temporels peuvent être définis pour décrire ce mouvement: la vitesse de propagation de rupture v_p qui est propre à l'évènement sismique, et le temps d'élévation t_r. Respectivement, ces paramètres caractérisent le mouvement horizontal et vertical. Une étude linéaire et théorique, puis non-linéaire et numérique, révèle un phénomène de résonance pour de courts t_r et des v_p de l'ordre de la célérité des ondes longues. Dans ces conditions, l'amplitude des vagues générées est amplifiée par rapport à celle de la déformation du fond marin, et des phénomènes dispersifs apparaissent. Pour illustrer ce phénomène, le cas du tsunami de 1947, qui frappa la Nouvelle Zélande, est simulé avec les modèles de Saint-Venant puis de Boussinesq du système Telemac2D. Rejoignant la théorie, l'influence de v_p est nettement observable tandis que les faibles valeurs de t_r ont un impact limité. Bien que des effets dispersifs soient attendus durant cet évènement, ils ne sont pas observés avec le modèle numérique. En parallèle de cette étude sur les échelles temporelles, cette thèse a permis de contribuer à la validation des modèles numériques du système Telemac dans le cadre du projet TANDEM. Ainsi, les modèles issus de Telemac2D et Telemac3D sont testés sur des cas tests représentant la génération, la propagation ou le run-up d'un tsunami. Il s'avère que dans la plupart des cas, les modèles numériques proposent de résultats très corrects. Cependant, on note une certaine dépendance aux paramètres numériques pour les cas délicats comme celui de la propagation d'une onde solitaire. En plus des cas idéalisés, le modèle de Saint-Venant de Telemac2D est utilisé pour modéliser l'évènement de Tohoku-Oki de 2011, pour lequel les résultats sont satisfaisants.

Mots-clés:

Modélisation des tsunamis, source sismiques, générations statiques et cinématiques.

Influence of timescales on the dynamics of seismically generated tsunamis

Abstract

The impact of tsunamis on mankind is well known. During recent years, several events showed us the disasters they can trigger which reiterate the importance of understanding their dynamics. Due to the lack of in-situ data, the generation is the least known aspect of tsunamis. As a result, simplified models of the source are used for numerical tsunami modeling, as for seismic generation for which the traditional approach neglects several phenomena, among which is the kinematic deformation of the sea floor. This motion can be characterized by two temporal parameters: the rupture velocity v_p and a hydraulic rise time t_r. The novelty here, is to investigate both parameters simultaneously and to extend the linear theoretical development to a non-linear numerical study. From these works, a resonance zone is identified for small t_r and v_p close to the long wave celerity. For these particular values, the waves are amplified beside the sea floor deformation and dispersive effects develop. To illustrate this theory, the 1947 New Zealand tsunami is simulated with the Non-Linear Shallow Water and Boussinesq models of Telemac2D. This seismic event corresponds to a tsunami earthquake with slow kinematics of deformation. Four generation models, with different values of v_p and t_r are compared. The impact of v_p on the generated wave amplitudes is strong whereas the influence due to t_r is significantly smaller. Additionally, it was found that the expected dispersive effects did not develop during the numerical modeling. Meanwhile, in the scope of the TANDEM project, the validation of the Telemac system is performed through test cases, covering: generation, propagation and run-up of tsunamis. Globally, the models from the Telemac system match the validation data, however we note a reliance on numerical parameters for sensitive cases as the propagation of a solitary wave. Finally, the Non-Linear Shallow Water model of Telemac2D is used to simulate the Tohoku-Oki tsunami that hit Japan in 2011. The numerical model succeeds in representing this real event incorporating all the stages of tsunami life, from generation to flooded areas. Some limitations in using the method were found, which one discussed in detail within the present manuscript.

Keywords:

Tsunami modeling, seismic source, static and kinematic generation.

Remerciements

La fin de ce paragraphe marquera sûrement le point final de ce travail de longue haleine, je profite donc de ces lignes pour remercier ceux qui ont été là pour m'épauler.

Je tiens tout d'abord à remercier Denys Dutykh et Stéphan Grilli pour avoir accepté d'être rapporteurs de ce travail, de leurs commentaires et encouragements. Je remercie aussi les examinateurs, Didier Clamond, Hélène Hébert et Mario Ricchiuto pour leur temps, leurs questions et conseils constructifs.

Cette thèse a été développée dans le cadre du projet TANDEM et n'aurait pu aboutir sans la collaboration et l'aide des différents partenaires. J'ai beaucoup appris au sein de ce projet et je les remercie tous pour leurs conseils.
J'ai une pensée particulière pour Anne Lemoine qui lors des différentes réunions s'est montrée très interressée à propos du travail des échelles temporelles, ce qui a permis l'élaboration du cas de la Nouvelle-Zélande.
Je voudrais également remercier l'équipe du CEA: Hélène Hébert, Audrey Gailler et Anne Loevenbruck pour nos nombreux échanges mais aussi pour leur confiance.
Je ne pourrai pas penser au projet sans faire part de mon amitié aux autres doctorants: Luca, Kevin, Andrea, puis la deuxième vague Manuel et Lucie, avec qui les réunions se prolongeaient régulièrement autour d'une bière à partager des données et bien plus.

Ces trois années se sont déroulées au sein du Laboratoire Hydraulique Saint-Venant sous la tutelle de Damien Violeau. Je le remercie et lui suis reconnaissante pour sa patience face à mes difficultés, doutes, paniques... mais aussi pour le temps qu'il a consacré à (essayer de) m'apprendre de nombreuses choses. Je n'oublierai pas la chance qu'il m'a offerte de voyager jusqu'au Japon.
J'en profite pour remercier aussi Marissa Yates et Jeffrey Harris d'avoir garder un oeil sur le déroulement de cette thèse durant ces trois années.
Le système de code TELEMAC peut parfois paraître complexe et donc je remercie chaleureusement Jean-Michel Hervouet ainsi que Riadh Ata pour son encadrement et ses coups de pouces qui m'ont plus d'une fois bien aiguillée. Pour cela aussi, je tiens à remercier Yoann pour son aide et soutien sans faille et surtout d'avoir continuer à répondre à mes appels même après trois ans ! Je le remercie aussi pour les virées piscine (véritable pause salvatrice dans la semaine.. quant on y allait), nos nombreuses discussions et les apéros.
En parlant d'apéro, je tiens à remercier la communauté du frisbee (et en particulier Ger-

main) de m'avoir accueilli dans leur cercle (discal) pour les réunions d'après 18h30...

Ces trois années au laboratoire n'ont pas été de tout repos et difficiles, mais heureusement j'ai pu croiser des personnes qui ont su me motiver et rendre mes journées plus ensoleillées, pour une marseillaise cela veut dire beaucoup. Merci à Virginie, Jérémie et Thibault pour les discussions de tout et (surtout) de rien, et des moments détentes au bureau. Merci aussi à Lamia et Jessie, ainsi que tous les autres doctorants pour les pauses au coin café et ailleurs. J'en profite pour leurs souhaiter bon courage pour la suite. Je ne me risquerai pas à citer la longue liste des personnes que j'ai agréablement croisé au laboratoire, mais merci à tous d'avoir partager ces bons moments, je vous souhaite plein de réussites et de nouveaux défis (sudoku ?) pour la suite. Je remercie quand même spécialement Cécile et Steve, qui ont été là pour les coups durs et les rires, les dessins, la gym, les glaces, l'escalade *etc*...
Je voudrais aussi remercier l'équipe du POMPHY, Franck, J.R., Nicolas, Clément, Kevin qui quelque soit le temps dehors avaient toujours un mot pour me faire sourire.

Enfin, je voudrais remercier ceux qui ont toujours été là même quand je ne l'étais pas, ceux qui ont essuyé mes plaintes mais qui m'ont rappelé qu'il n'y avait pas que la thèse: les Copains. Je remercie les Rennais et Enseirbiens, toujours là pour lever le coude, les Chimistes pour m'avoir accepter lors de nos voyages, les Breton(nes) pour les apéros parisiens et bien plus, et les Parisiens. Enfin, je me passerai de commentaires mais je voudrais adresser un merci tout particulier à Guillaume, Adeline, Rémi, Jess, Nina et Matis, sans qui je ne serais pas la personne que je suis aujourd'hui.

Je consacrerai ces dernières lignes à ma famille, mes parents et ma soeur à qui je dédie cette thèse, merci.

Marine

P.S.: Je remercie aussi l'Amaryllis et le Comptoir moderne de m'avoir (trop souvent) accueilli.
P.P.S.: Je me sens du coup obligé de remercier la RATP et la SNCF pour les (trop longues) heures sur leurs sièges (ou pas).

Contents

Introduction **1**

I Kinematic generation of seismic tsunamis **9**

1 State-of-the-art **11**

1.1 General overview 13

1.1.1 Generation 13

1.1.2 Propagation 23

1.1.3 Run-up 26

1.2 Seismic generation of tsunami 28

1.2.1 Seismic origin 29

1.2.2 Hydraulic models 31

2 Theoretical study **39**

2.1 Dimensional analysis 40

2.2 Linear theory 42

2.2.1 Methodology 42

2.2.2 Solution for a schematic uplift 43

2.2.3 Treatment of singularities 45

2.3 Free surface deformation analysis 45

2.3.1 At the end of the bottom deformation 46

2.3.2 Propagation stage 50

2.3.3 Comparison with numerical results 54

2.4 Discussion of the validity of the shallow water equations 55

2.5 Numerical simulation of non-linear propagation 59

2.6 Linear Shallow Water equations model 62
2.7 Conclusions 65

3 Application to 1947 New Zealand event 67
3.1 Case of resonance with Telemac2D 68
3.1.1 Non-linear Shallow Water model 68
3.1.2 Boussinesq model 70
3.2 The 1947 New Zealand event 71
3.2.1 Context and data 71
3.2.2 Resolution grid and mesh 74
3.2.3 Kinematic generations 75
3.2.4 Numerical results from Non-Linear Shallow Water models 76
3.2.5 Boussinesq model 82
3.2.6 Conclusions 86

II Evaluation of Telemac for modeling tsunamis 89

4 Test cases 91
4.1 Context 92
4.2 1D analytical sliding mass 92
4.3 Generation and propagation from a moving bed 94
4.4 Propagation of a solitary wave 99
4.5 Parabolic basin 101
4.6 Run up of a Gaussian wave on a uniform slope 104
4.7 Run-up of a solitary wave on a uniform beach 107
4.8 Conclusions 109

5 The 2011 Tohoku-Oki event 111
5.1 State of art 112
5.2 Construction of the mesh and bathymetry 114
5.3 Initial condition and seismic sources 115
5.3.1 Shao *et al.*'s Source 115
5.3.2 Satake *et al.*(2013) Source 118

5.4 Numerical results . . . 119
5.4.1 Propagation and comparisons with data . . . 119
5.4.2 Run-ups and inundations . . . 122
5.5 Dispersion . . . 126
5.5.1 Theoretical analysis . . . 127
5.5.2 Boussinesq model of the 2011 Tohoku-Oki event . . . 129
5.6 Conclusions about the Tohoku-Oki model . . . 131

Conclusions **133**
5.7 First concluding remarks . . . 135
5.8 Perspectives . . . 136
5.9 Main contributions . . . 137

A Fourier transform of the free surface **139**

B Treatment of the singularities **143**

C Description of the Telemac system **147**
C.1 Telemac2D . . . 147
C.2 Telemac3D . . . 149

Bibliography **162**

List of Figures

1 Introduction - Pictures from the NOAA website (`http://www.ngdc.noaa.gov/hazardimages/event/show/256`) of the Otsushi city in the wake of the March 2011 tsunami. 2

2 Introduction - Preliminary simulation of the propagation of the Cesium 137 flume with the Polyphemus codes 5, 10 and 25 days after the Fukushima accident (top to bottom respectively). The scale represents the concentration of Cesium 137 activity in Bq/m^3 (`http://cerea.enpc.fr/fukushima/index.html`). 3

3 Introduction - Nuclear power plants in France (*Picture's source: wikipedia*). 4

4 Introduction - First year annual meeting of the project TANDEM. 4

I State of the art **11**

1.1 Landslide generation – Pictures of the laboratory experiment of Enet and Grilli [2007]. The left picture shows the general view of the set up while the right picture shows the experimental landslide model moving only by gravity. 14

1.2 Landslide generation – First wave crest classification as function of the slide Froude number $F_r = v_s/\sqrt{gh}$ and the slide thickness $S = s/h$ with ◯ weakly nonlinear oscillatory wave, ◊ nonlinear transition wave, □ solitary-like wave, △ dissipative transient bore. Light-shaded square corresponds to the nonlinear transition region, the dark-shaded square to solitary-like region, and the black square to bore region. Result issued from the work of Fritz et al. [2004]. 15

1.3 Landslide generation – Comparison between linear theoretical solution (solid line) to numerical linear model (dashed line) and nonlinear numerical model (dotted line) for $\tan\beta/\mu = 0.87$ (left) and $\tan\beta/\mu = 3.5$. Result issued from the work of Liu et al. [2003]. 16

1.4 Landslide generation – Numerical result from a Navier-Stokes three-phase model considering a solid landslide (left) or a deformable landslide (right) at a) $t = 0.5s$, b) $t = 1s$, c) $t = 1.5s$ and d) $t = 2s$. These results are issued from the work of Abadie et al. [2010]. 17

1.5 Volcanic tsunami generation – Schematising of the tsunami generation by a discharge into water of a large volume of matter. Adapted from Levin and Nosov [2009]. 18

1.6 Volcanic tsunami – Free surface deformation η generated by an underwater eruption with a radius of $R_s/h = 1$ (up) and $R_s/h = 3$ (down) after $t = 100\sqrt{g/h}$. Figure adapted from Levin and Nosov [2009]. 19

1.7 Meteotsunami – Atmospheric pressures record on the 15 June 2006 at two ports in the Balearic Island: Mallorca and Mahon. The "PM" and "P" arrows indicate the suddenly change. Figure issued from the work of Monserrat et al. [2006]. 20

1.8 Meteotsunami – Pictures taken during the meteotsunami that occurred the 15 June 2006 at Ciutadella Harbour (Balearic Islands). Anonymous photographs on-line (`http://ichep.blogspot.fr/2006/06/rissaga-ciutadella.html`). 21

1.9 Cosmogenic tsunami – Comparison between the idealized impact cavity 1.4 (solid line) and numerical simulation of Ward and Asphaug [2003] at $t = 25s$ (dot line). The thin line is the sea ground. Graph adapted from Levin and Nosov [2009]. 22

1.10 Cosmogenic tsunami – Numerical propagation of the tsunami generated by the impact of the Eltanin asteroid $2.15Ma$ ago. The yellow dots show numerical tsunami heights. Work issued from Ward and Asphaug [2002]. . . 23

1.11 Propagation – Tsunami hitting the Koh Jum island during the event of 26 december 2004. Photo of Anders Grawin (`www.kohjumonline.com/anders.html`). 25

1.12 Run-up – Geometry and parameters of the model. 26

1.13 Run-up – Inundation studies performed by Borrero et al. [2004] along the Californian coast. Five sources (two landslides and three earthquakes) are identified as possible generation. The estimated run-ups are plotted in the upper graphs while the geographical context is represented in the second figure. The contours plots represent the initial free surface deformation of the hydraulic models, solid for uplift and dashed for subsidence. 29

1.14 Seismic source – World map of the main faults between the tectonic plates available on the website of the NOAA. The red, green and yellow faults correspond to the divergent, convergent and transform motion of the plates respectively. 30

1.15 Seismic source – Life cycle of a convergent fault with generation of tsunami. 30

1.16 Seismic tsunami source – Definition of the geometrical parameters of the fault for the Okada method. 32

1.17 Seismic tsunami source – Finite fault model proposed by Satake et al. [2013] to represent the generation of the Tohoku event, 2011 in Japan. The blue star is the epicenter and red dots are secondary earthquakes. 33

1.18 Kinematic generation – Geometry of the experiment of Hammack [1973], not at scale. The top frame is a top view and the bottom frame is a side view. The gray zone is the moving area of length b. The red crosses are locations of measurement gauges. 34

1.19 Kinematic generation – Free surface elevation comparison at $\frac{x}{h} = \frac{b}{h}$ between the exponential and the sinusoidal time history deformation for an impulsive motion (left) and a creeping motion (right). The geometrical parameters are: $b/h = 12.2$, $\zeta_0/h = 0.2$, $t_r\sqrt{gh}/b = 0.069$ for the impulsive motion and $t_r\sqrt{gh}/b = 106.14$ for the creeping motion. The figure is adapted from the work of Hammack [1973]. 34

1.20 Kinematic generation – Geometry of the domain considerated by Todorovska and Trifunac [2001] at a time smaller than the generation duration. The solid line is the instant deformation (propagation at velocity v_p) while the dashed line is the final deformation. The graph is a vertical cut of their 2D domain. 35

1.21 Kinematic generation – Numerical results obtained by Dutykh et al. [2013] (Figure adapted from their work). The free surface elevation is measured at different gauges and compared between static generation model (solid thick line, model WN static) and kinematic generation model (dashed and blurred line, models WN (active), linearized model and BBM–BBM). 37

1.22 Kinematic generation – Numerical domain defined by Grilli et al. [2013] for the subduction zone that is resolved by the FEM. The different part of the domain has their own material properties. Figure issued from the above-cited study. 38

I Theoretical study 39

2.1 Definition of the fluid domain and coordinate system (x, z), with h the initial depth, $\zeta(x,t)$ the deformation of the sea floor and $\eta(x,t)$ the deformation of the free surface. 40

2.2 Definition of the sea floor uplift $\zeta(x,t)$: 2.2a spatial profile of the sea floor and 2.2b, the black dashed lines represent the motion defined by Todorovska and Trifunac [2001], and the solid red lines are the motion used in this study. 40

2.3 An example of the free surface Fourier transform $\tilde{\eta}^*$ with critical k^* for $v_p^* = 10$ and $\tau^* = 0.5$ at $t^* = T^* = \frac{L^*}{v_p^*} + t_r^*$. The black line is the modulus of the Fourier transform $|\tilde{\eta}^*|$. The vertical blue, green and red lines represent the locations of the singularities k_1^*, k_2^*, k_3^*, respectively. 46

2.4 Free surface profiles at $t^* = T^*$ for $L^* = 50$ and different values of v_p^* and τ^* (v_p^* increases from top to bottom and τ^* increases from left to right). The red line is the linear solution 2.21-2.23, and the dashed black line is the numerical simulation results from the linear version of the Misthyc code (see section 2.3.3). The vertical scale of graph (d) for $v_{p*} = 1$ and $\tau^* = 0$ differs from the others for clarity. 47

2.5 Evolution of η_{max}^*/ζ_0^* as a function of τ^* for different values of v_p^* (2.5a, vertical axis in log scale) and as a function of v_p^* for different values of τ^* (2.5b, horizontal axis in log scale) for $L^* = 50$ at $t^* = T^*$. 48

2.6 The maximum free surface amplitude, η_{max}^*/ζ_0^* as function of v_p^* and τ^* for $L^* = 50$ at $t^* = T^*$ (colour in log scale). Figure 2.6a represents the original values while Figure 2.6b is an interpolation using a weighted average of the data. 49

2.7 Impact of the deformation length L^* for $v_p^* = 1$ and $\tau^* = 0$ at the end of the generation. 2.7a Spatial profiles of the free surface for different values of L^*. 2.7b Red crosses represent the η_{max}^*/ζ_0^* of the linear solution and the black line is the trend line $0.414(L^*)^{0.669}$. 50

2.8 Free surface profiles at $t^* = 100$ for $L^* = 50$ and different values of v_p^* and τ^*. Same legend as Figure 2.4. 51

2.9 Free surface profiles at $t^* = 500$ for $L^* = 50$ and different values of v_p^* and τ^*. Same legend as Figure 2.4. 52

2.10 Free surface profiles at $t^* = 1000$ for $L^* = 50$ and different values of v_p^* and τ^*. Same legend as Figure 2.4. 53

2.11 Evolution in space and time of the free surface deformation η^*/ζ_0^* for $v_p^* = 1$ and $\tau^* = 0$. The colour represents the wave amplitude. 54

2.12 Maximum free surface amplitude η_{max}^*/ζ_0^* as a function of v_p^* and τ^* for $L^* = 50$ at different times t^*. 54

2.13 Spatial relative error of the numerical free surface issued from Misthyc at $t^* = T^*$ for $L^* = 50$ and different values of v_p^* and τ^*. 56

2.14 Wave celerities (adimensionalised by $\sqrt{gh}$) from the general and the long wave theories, c_e^*, in black thick line, and c_{lw}^*, in dashed red line, respectively. The blue vertical line corresponds to $k^* = 0.2$ and the horizontal one to $c^* = 0.99$. The horizontal axis is in log scale. 57

2.15 The blue line represents the modulus of $\tilde{\eta}^*$ for $v_p^* = 50$ and $\tau^* = 0$ at $t^* = T^*$. The grey striped zone shows the domain of validity of the long wave approximation. Waves with wavenumbers outside of this zone are not taken into account properly in the SWE model. 57

2.16 Energy ratio $\varepsilon = \frac{E_l}{E_t}$, at $t^* = T^*$ as a function of v_p^* and τ^*. 58

2.17 Time profiles of the energy ratio $\varepsilon = \frac{E_l}{E_t}$ for different values of τ^* and v_p^*. The horizontal black line represents $\varepsilon = 0.5$. The vertical black line is at $t^* = (L/\sqrt{gh})^*$. 59

2.18 The maximum free surface amplitude (η_{max}^*/ζ_0^*) calculated with the non-linear numerical model as function of v_p^* and τ^* for $L^* = 50$ and $\zeta_0 = 0.001$ at $t^* = T^*$ (colour in log scale). 60

2.19 Free surface profiles from non-linear numerical results Misthyc, for $\zeta_0^* = 0.1$ for $v_p^* = 0.8, 0.9, 1, 1.1, 1.26$ at the end of the ground motion. 60

2.20 Deformation of the free surface at $t^* = T^*$ and for $v_p^* = 1$ and $\tau^* = 0$: comparison of the linear solution (black line) and non-linear numerical results. The coloured dashed lines represent the dimensionless non-linear numerical results for different increasing non-linearity levels: $\zeta_0^* = 0.001, 0.005, 0.01, 0.1$. 61

2.21 Temporal profiles of η_{max}^*/ζ_0^* for $v_p^* = 1$, $\tau^* = 0$ and $L^* = 50$. The solid black line is the theoretical linear solution. The coloured dashed lines are non-linear numerical results from Misthyc for $\zeta_0^* = 0.001, 0.005, 0.01$ and 0.1. 61

2.22 Comparison of the deformation of the free surface at $t^* = 100$ and 500 (2.22a and 2.22b respectively) for $v_p^* = 1$ and $\tau^* = 0$ of the linear solution and the non-linear numerical results. The thick black line is the theoretical linear solution and the coloured lines represent the non-linear numerical results of Misthyc for different initial deformations: $\zeta_0^* = 0.001, 0.005, 0.01, 0.1$. 63

2.23 Comparison between the shape of the generated wave with the non-linear numerical result Misthyc (black full curve) and the shape of the solitary wave from the algorithm of Dutykh and Clamond [2014] (dashed green curves) at $t^* = 993$. 64

2.24 Free surface profiles at $t^* = T^*$ for $L^* = 50$ and different values of v_p^* and $\tau^* = 0$. The black line is the linear Euler solution 2.21-2.23, and the dashed red line is the analytical LSWE solution 2.34-2.35. The scale of the Figure 2.24b is different from the others, the encapsulate figure is a zoom. 65

3 March 1947 New-Zealand event 67

3.1 Resonance phenomenon simulated with Telemac2D and NLSWE – Spatial profiles of the free surface deformation at the end of the ground motion ($t^* = T^*$ with an accuracy of dt^*) for different values of CFL and dx^*. The black line is the analytical free surface calculated from the LSWE theory. The coloured dashed curves represent numerical free surface profiles calculated with the different meshes. 69

3.2 Resonance phenomenon simulated with Telemac2D and NLSWE – Spatial profiles of the free surface deformation at the end of the ground motion ($t^* = T^*$) for $dx^* = 0.3$ and $dx^* = 0.5$ meshes. The black line is the analytical free surface calculated from the LSWE theory. The coloured dashed curves are the different values of the CFL. 69

3.3 Resonance phenomenon simulated with Telemac2D and Boussinesq model – Spatial profiles of the free surface deformation at the end of the ground motion ($t^* = T^*$ with an accuracy of dt^*) for different values of CFL and dx^*. The black line is the analytical free surface calculated from the linear theory. The coloured dashed curves represent numerical free surface profiles calculated with the different meshes. 70

3.4 Resonance phenomenon simulated with Telemac2D and Boussinesq model – Spatial profiles of the free surface deformation at the end of the ground motion ($t^* = T^*$) for $dx^* = 0.3$ and $dx^* = 0.5$ meshes. The black line is the analytical free surface calculated from the linear theory. The coloured dashed curves are the different values of the CFL. 71

3.5 1947 New Zealand event – Locations of the March and May 1947 Gisborne earthquakes, estimated tsunami run-ups, the main features of the plate boundary through New Zealand (inset), and the location of seismographs of the 1947 New Zealand seismograph network (inset). Bathymetry (contour interval 50 m) is from Lewis et al. (1997). Figure reprinted from the paper of Downes and Stirling [2001]. 72

3.6 1947 New Zealand event – Maximal amplitude of the free surface for $L^* = 35$ at $t^* = T^*$. Grey zone represents the ranges of values of the temporal parameters τ^* and v_p^* of the 1947 New Zealand event. (see Table 3.2). . . . 73

3.7 1947 New Zealand event – Numerical domain considered. Figure 3.7a represents the topography given by the NIWA, the black line is the coastline. Figure 3.7b is the mesh built for the case. Yellow box is the boundary of the zoom plotted in Figure 3.8. 74

3.8 1947 New Zealand event – Details of the mesh built for the event. The yellow boxes correspond to the boundary of the next zoom. The red line is the initial coast line. 75

3.9 1947 New Zealand event – Free surface deformation (in m) at the end of the ground motion for the four generation models calculated with the NLSWE model of Telemac2D. The indicated time corresponds to the time of end of ground motion varying between $t = 0s$ for the instantaneous deformation to $t = 310s$ for the generation with $v_p = 300m/s$ and $t_r = 120s$. 77

3.10 1947 New Zealand event – Free surface deformation (in m) for the four generation models calculated with the NLSWE model of Telemac2D at $t = 310s$. 78

3.11 1947 New Zealand event – Snapshots of the free surface (in m) every 5 min. during the numerical propagation of the wave generated by an instantaneous sea floor deformation (model ID) with the NLSWE model of Telemac2D. . 79

3.12 1947 New Zealand event – Snapshots of the temporal maximal free surface elevation (in m) calculated during one hour with the NLSWE model of Telemac2D for the different generation models. 80

3.13 1947 New Zealand – Maximal free surface elevations reached during the propagation along the transect $A - A'$ as defined in Figure 3.12. Only result for negative bathymetry is plotted. The colourful lines are numerical results from the different generation models. The orange and red lines are superimposed, models KD_60 and KD_120 respectively. 80

3.14 1947 New Zealand event – Definition of the different measures during a run-up. The data given by Downes and Stirling [2001] corresponds to run-up heights. The height measured in the numerical models is the inundation height at the shoreline. The blue line corresponds to the temporal maximal free surface elevation reached during the event. 81

3.15 1947 New Zealand event – Maximal water depth obtained at the coastline (black line in Figure 3.7a) during the event. The colourful lines represent the different generation models, and the black vertical bars the data of Downes and Stirling [2001]. The horizontal axis corresponds to the latitudes. 81

3.16 1947 New Zealand event – Energetic ratio ε for $L^* = 35$ at $t^* = T^*$. Grey zone represents the ranges of values of the temporal parameters τ^* and v_p^* for the New Zealand 1947 event (see Table 3.2). 82

3.17 1947 New Zealand event – Free surface deformation (in m) at the end of the sea floor motion, $t = 190s$, obtained with the NLSWE and the Boussinesq models of Telemac2D for $v_p = 300m/s$ and $t_r = 0s$. Same scale as Figure 3.9. 83

3.18 1947 New Zealand event – Snapshots of the temporal maximal free surface elevation (in m) calculated during one hour obtained with the NLSWE and the Boussinesq models of Telemac2D for $v_p = 300m/s$ and $t_r = 0s$. Same scale as Figure 3.12. 84

3.19 1947 New Zealand event – Maximal free surface elevations reached during the propagation along the transect $A - A'$ as defined in Figure 3.12. Only result in the ocean part is plotted. The black and blue lines are the numerical results from the NLSWE and the Boussinesq models of Telemac2D, respectively. The model generation corresponds to KD_0. The encapsulated figure is a zoom of the global curve near the coastline (distance$\in [15; 20]km$). 84

3.20 1947 New Zealand event – Snapshots of the free surface elevation (in m) at the end of the generation ($t = 380s$) with the NLSWE and the Boussinesq models of Telemac2D for $v_p = 150m/s$ and $t_r = 0s$. Same scale as Figure 3.9. 85

3.21 1947 New Zealand event – Snapshots of the free surface deformation (in m) during the propagation for NLSWE model (up) and Boussinesq model (down) of Telemac2D for $v_p = 150m/s$ and $t_r = 0s$. 86

3.22 1947 New Zealand event – Size element repartition in the sea zone up to $25km$ from the coastline. 87

3.23 1947 New Zealand event – Same nomenclature as Figure 3.18 for $v_p = 150m/s$ and $t_r = 0s$. (Free surface deformation in m.) 87

3.24 1947 New Zealand event – Maximal free surface elevations reached during the propagation along the transect $A - A'$ as defined in Figure 3.12. Only result for negative bathymetry is plotted. The black and blue line are the numerical results from the NLSWE and the Boussinesq models of Telemac2D, respectively. The model generation corresponds to $v_p = 150m/s$ and $t_r = 0s$. The encapsulated figure is a zoom of the global curve near the coastline (distance$\in [15; 23]km$). 88

3.25 1947 New Zealand event – Maximal water depth obtained at the coastline during the event. The black and blue lines represent numerical model issued of the generation with $v_p = 300m/s$ and $v_p = 150m/s$ respectively.The black vertical bars the data of Downes and Stirling [2001]. The horizontal axis corresponds to the latitude. 88

4 Citing references 91

4.1 1D analytical sliding mass – Geometry of the generation of a wave by a landslide. The coloured area represents the moving layer of the ground while the black line is the fixed bed. 93

4.2 1D analytical sliding mass – Comparisons of the spatial free surface profiles between the analytical solution (black line) and the numerical result from NLSWE Model of T2D (red line) at different times. 93

4.3 Generation and propagation from a moving bed – Geometry of the experiment of Hammack [1973], not at scale. The top frame is a top view and the bottom frame is a slice view. The gray zone is the moving area of length b. The red crosses are locations of measurement gauges. 94

4.4 Generation and propagation from a moving bed – Temporal free surface profiles during the generation at $x^* = 0$ (left) and $x^* = b^*$ (right) for an exponential motion. The blue lines are the numerical Boussinesq model of Telemac2D while Telemac3D is represented by the green dashed line. The numerical results issued from the code Misthyc are also plotted (black dashed line), Benoit et al. [2014]. The red points are measurements from Hammack [1973]. 96

4.5 Generation and propagation from a moving bed – Temporal free surface profiles during the generation at $x^* = 0$ (left) and $x^* = b^*$ (right) for a sinusoidal motion. Same nomenclature as Figure 4.4. 97

4.6 Generation and propagation from a moving bed – Temporal free surface deformation during the propagation of a wave initiated by an impulsive exponential motion ($b^* = 12$, $\zeta_0^* = 0.1$, $t_c^* = 0.148$) at four places along the flume. The time is modified to fit the same scale. Same nomenclature as Figure 4.4. 98

4.7 Propagation of a solitary wave – Spatial profiles of free surface deformation obtained with Telemac3D after $t^* = 500$ of propagation of a $\frac{H}{h} = 0.5$ high solitary wave for different values of $CFL = \frac{M_t}{M_x}$ with $M_x = 5$. The horizontal and vertical lines show the expected wave height and mean position, respectively. 99

4.8 Propagation of a solitary wave – Spatial profiles of free surface deformation obtained after $t^* = 500$ for the different grid resolutions at $CFL = 0.41$ and $\frac{H}{h} = 0.5$. The blue, green, orange and red lines are respectively NS Telemac3D results for $M_x = 5$, $M_x = 10$, $M_x = 20$ and $M_x = 40$ grids. The dashed black line is the numerical result from Misthyc with $M_x = 10$. The horizontal and vertical lines show the expected wave height and mean position, respectively. 100

4.9 Propagation of a solitary wave – Same nomenclature as Figure 4.8 for $\frac{H}{h} =$ 0.3 and 0.7 101

4.10 Parabolic basin – Geometry of the perfect paraboloid basin. 102

4.11 Parabolic basin – Initial paraboloid configuration. Spatial profiles on the slice $y = 0$ of the free surface deformation and of the horizontal velocity during one period. The dashed black line is the analytical NLSWE solution. The red line represents numerical results issued from the NLSWE model of T2D. 103

4.12 Parabolic basin – Temporal evolution of free surface elevation at the center of the basin. The thick black line is the analytical NLSWE solution. The red line represents numerical results issued of the NLSWE model of T2D. The L^2-error on h was calculated by the BRGM, partners of the TANDEM project, for the different codes. The error for the the NLSWE model of Telemac2D is less than 1%, see Violeau [2015]. 104

4.13 Parabolic basin – Initial flat configuration. Same nomenclature as Figure 4.11.105

4.14 Run up of a Gaussian wave on a uniform slope – Spatial profiles of the free surface displacement (left) and of velocity (right) at different times. The black thick line corresponds to the theoretical solution issued of the work of Carrier et al. [2003] while the red line is numerical result from the numerical NLSWE model of T2D. 106

4.15 Run up of a Gaussian wave on a uniform slope – Temporal evolution of the shoreline with it localisation (right) and it velocity (right). Same nomenclature as Figure 4.14 107

4.16 Run-up of a solitary wave on a uniform beach – Set up of the experiment of Synolakis [1987]. Not at scale. 107

4.17 Numerical domain for the test case of the solitary wave run up on a plane beach associated to the experiment of Synolakis [1987]. The variation of the bathymetry used is colourfully denoted. 108

4.18 Run-up of a solitary wave on a uniform beach – Temporal free surface deformation for the solitary wave run-up on a plane beach at different places on the slope. The blue line is the numerical result from the NLSWE Telemac2D model. The dashed green line is the numerical result from the Boussinesq Telemac2D model. The red symbols are the data from Synolakis [1987]. . . 108

4.19 Run-up of a solitary wave on a uniform beach – Spatial free surface deformation profiles at different instants. Same nomenclature as Figure 4.18. . . 110

5 Example of tables 111

5.1 2011 Tohoku-Oki event – Figure issued from the work of Koketsu et al. [2011]. Slip distribution pattern obtained from the single inversion of: A. teleseismic data, B. ground acceleration from seismometers, C. geodetic data, D. teleseismic + ground acceleration+ geodetic data, E. tsunamigram records. The yellow circles are aftershocks and the orange star is the epicenter of the main shock. 113

5.2 2011 Tohoku-Oki event – Limit of the four grids (black lines) used to create the mesh. The blue line represent the boundary of the Japan islands. 115

5.3 2011 Tohoku-Oki event – Bathymetry (left) and mesh (right) of the domain considered in the projection of Mercator. Figure 5.3a gives a glimpse of the total domain and a closest East part of Japan while figure 5.3b shows more precisely the bathymetry and the mesh of the Iwate bay, the thin black line is the isoline for a ground elevation $z = 0$, considered as the coastline. . . . 116

5.4 2011 Tohoku-Oki event – Graph issued from the work of Shao et al. [2011]. Snapshot of the slip distribution obtained from teleseismic data. The red star represents the epicenter location, red dots the aftershocks. The white line is the $5m$ slip contour. The white arrow shows the relative motion of tectonic plate. 117

5.5 2011 Tohoku-Oki event – Comparison of the initial free surface deformation (using the traditional way to generate tsunami) with the NLSWE model of Telemac2D (5.5a) and the seafloor deformation calculated by Chen et al. [2014] (5.5b). The scale is identical for both graphs. 117

5.6 2011 Tohoku-Oki event – Snapshot of the free surface deformation from NLSWE model of Telemac2D with source models of Shao et al. [2011]. The Figure 5.6a is the initial deformation for the static model. The Figure 5.6b is the free surface deformation at $t = 180s$ from the static initialisation (left) and the kinematic generation (right). The scale is the same for both models. 118

5.7 2011 Tohoku-Oki event – Evolution of the slip pattern during $5min$. The interval if each update is $30s$. The white star is the epicenter. Figure issued from the work of Satake et al. [2013]. 119

5.8 2011 Tohoku-Oki event – Seafloor deformations issued of the model source of Satake et al. [2013] at $30s$ time intervals. 120

5.9 2011 Tohoku-Oki event – Snapshots of the free surface deformation calculated from the source model of Satake et al. [2013] with Telemac2D at the end of the ground motion (5.9a) and at $t = 4min$ (5.9b) in comparison with the free surface deformation obtained by Satake et al. at the same time (5.9c). 121

5.10 2011 Tohoku-Oki event – Snapshots of the free surface elevation calculated with the NLSWE model of Telemac2D simulation and using the generation issued of Satake et al. [2013]. The snapshots are taken every $5min$ for the first $35min$ of the propagation. 121

5.11 2011 Tohoku-Oki event – Localisations of the GPS buoys along the East Japanese coast. 122

5.12 2011 Tohoku-Oki event – Comparisons between measurements from GPS gauges and numerical results of the free surface deformation. The black thick line is the data. The blue line is Telemac2D result from Satake et al. [2013] source. The orange and the green lines are respectively the Telemac2D results from the kinematic and static Shao et al. [2011] sources. 123

5.13 2011 Tohoku-Oki event – Location of the DART buoys. Their measurement are available at `https://www.ngdc.noaa.gov/hazard/dart/2011honshu_dart.html`. 124

5.14 2011 Tohoku-Oki event – Comparisons between measurements from DART buoys and numerical results of the free surface deformation. The black thick line is the data. The blue line is Telemac2D result from Satake et al. [2013] source. The orange and the green lines are respectively the Telemac2D results from the kinematic and static Shao et al. [2011] source. 125

5.15 2011 Tohoku-Oki event – Comparison between the inundation heights obtained by the numerical models and the survey measurements at the Iwate Bay. The black dots are data from the 2011 Tohoku Earthquake Tsunami Joint Survey Group, release 20120330, `http://www.coastal.jp/ttjt/`, the blue dots are numerical result from Telemac2D with the generation from Satake et al. [2013] and the green dots numerical results with the generation from Shao et al. [2011]. 126

5.16 2011 Tohoku-Oki event – Snapshots of the flooded area obtained by the numerical models in the North area of the bay of Iwate. Results in Figures 5.16a and 5.16c are obtained respectively from the model of Satake et al. [2013] and Shao et al. [2011]. Figure 5.16b is adapted of the work of Chen et al. [2014]. 126

5.17 2011 Tohoku-Oki event – Zoom on the Hei River. The grey zone is the land and the blue elements correspond to the flooded area with a minimum water depth of $0.5m$. The elements of the mesh are in black, they are of the order of $100m$. The white line is the initial coastline. 127

5.18 2011 Tohoku-Oki event – Snapshots of the flooded area obtained by the numerical models in the South area of the bay of Iwate. Results in Figures 5.18a and 5.18c are obtained respectively from the model of Satake et al. [2013] and Shao et al. [2011]. Figure 5.18b is adapted of the work of Chen et al. [2014]. 127

5.19 2011 Tohoku-Oki event – Snapshots of the flooded area obtained in the North and South areas of the Iwate bay by the NLSWE model of Telemac2D without and with friction bottom, Figures 5.19a, 5.19c and Figures 5.19b, 5.19d, respectively. The friction law is the Strickler law with a coefficient of $30m^{1/3}/s$. The white line is the initial coastline. 128

5.20 2011 Tohoku-Oki event – Potential energy ratio ε at $t^* = T^*$ for $L^* = 267$. The striped grey zone shows the possible parameter values for the Tohoku, 2011 event. 129

5.21 2011 Tohoku-Oki event – Comparisons between measurements and numerical results of the free surface deformation. The black thick line is the data. The red and blue lines are the result from the NLSWE and Boussinesq models of Telemac2D, respectively. The source is the one from the model of Shao et al. [2011]. 130

A Appendix A **139**

B Appendix B **143**

C Appendix C **147**

List of Tables

I State of the art **11**

I Theoretical study **39**

2.1 Variables and units of the problem. 41

3 March 1947 New-Zealand event **67**

3.1 1947 New Zealand event – Temporal parameters v_p^* and τ^* estimated for few tsunami earthquakes. The "X" indicates unknown values. 72

3.2 1947 New Zealand event – Estimation of the characteristic parameters of the 25 March 1947 event, which occurred in the Offshore Poverty Bay (NZ). These values were given in personal communication. 73

3.3 1947 New Zealand event – Generation models considered for this event. The dimensionless parameters are estimated for a water depth varying between 100 and 3000 m. 75

4 Citing references **91**

4.1 Generation and propagation from a moving bed – Parameter values for the different cases. 95

5 Example of tables **111**

5.1 2011 Tohoku-Oki event – Data set used for the different source models. . . 112

5.2 2011 Tohoku event – non-dimensional temporal and geometric parameters of the Tohoku event. The values are issued of Ito et al. [2011], Satake et al. [2013] and Koketsu et al. [2011]. 129

A Appendix A **139**

B Appendix B **143**

C Appendix C **147**

Nomenclature

Abbreviations

DART	Deep-ocean Assessment and Reporting of Tsunamis
DTM	Digital Terrain Model
FEM	Finite Element Modeling
FNPP	Fukushima Dai-ici Nuclear Power Plant
KdV	Korteweg-de Vries
LSWE, NLSWE	Linear, Non-Linear Shallow Water Equations
NS	Navier-Stokes
TANDEM	Tsunami en Atlantique et Manche: Définition des Effets par Modélisation

Parameters

ϵ	Linearity factor
η_0	Initial free surface elevation
η_{max}	Maximal amplitude of the free surface at $t^* = T^*$
λ	Wavelength
$\mu,\ \mu^2$	Dispersive factor
ω	Frequency
ε	Energetic ratio
ζ_0	Maximal amplitude of the sea floor deformation
a	Wave amplitude
$b,\ L$	Length of the sea floor deformation, of the fault

$c_0 = \sqrt{gh}$	Long wave celerity
CFL	Courant, Friedrichs and Lewy number
dt	Numerical time step
dx	Numerical element size of the mesh
F_r	Froude number
g	Gravity acceleration
k	Wave number
O_i	Amplitude of the sea floor deformation calculated with the Okada [1992] method for the fault i
R	Run-up height
$T,\ T^*$	Time at the end of the ground motion
t_f	Seismic rise time
$t_r,\ \tau^* = \frac{t_r}{L}\sqrt{gh}$	Hydraulic rise time
U	Depth average velocity
$v_p,\ v_p^* = \frac{v_p}{\sqrt{gh}}$	Rupture velocity

Subscripts

a^*	Dimensionless a
a_t	Derivative of a with respect to t
a_x	Derivative of a with respect to x

Variables

η	Free surface elevation
ϕ	Velocity potential
ζ	Vertical sea floor deformation
h	Water depth
t	Time
u, v, w	Velocity components

x, y, z	Spatial coordinates

Mathematical Symbols

$\mathscr{F}(f),\ \hat{f}(k)$	Fourier transform of f
$\mathscr{FL}(f),\ \bar{f}$	Fourier–Laplace transform of f
$\mathscr{L}(f),\ \mathbf{f}(s)$	Laplace transform of f
H	Heaviside function
$J_0,\ J_1$	Bessel functions of the first kind

Introduction

Le 11 Mars 2011, un tsunami d'une rare ampleur frappa la côte est du Japon, provoquant la destruction de nombreuses villes ainsi qu'un accident nucléaire. Cette catastrophe eut une répercussion internationale. Cet évènement et ses conséquences rappellent l'enjeu important qu'est la compréhension de la dynamique des tsunamis ainsi que leurs prédictions. Suite à l'accident, le projet Tsunami en Atlantique et MaNche: Définition des Effets par Modélisation (TANDEM) a été lancé en 2014 afin de mesurer les risques de tsunamis sur les côtes françaises métropolitaines, sur lesquelles cinq centrales nucléaires sont en activité. Cette thèse s'inscrit dans le cadre de ce projet. Il regroupe dix partenaires, comprenant des entreprises industrielles, des instituts nationaux et des universités. Quatre objectifs ont ainsi été définis. Le premier a pour but de construire une banque de cas tests qui permettent de tester les codes numériques à disposition chez les partenaires du projet et de mesurer leur capacité à reproduire un tsunami. Le deuxième quantifie les incertitudes et les influences des paramètres lors de la simulation d'un tel évènement. Le troisième se consacre à la reproduction du tsunami Tohoku-Oki de Mars 2011. Enfin, le dernier objectif consiste à appliquer toutes ces connaissances acquises à l'évaluation des risques sur les côtes françaises et donc de quantifier ces risques. Cette thèse participe à la réalisation du premier et troisième objectifs avec le système de codes numériques Telemac, ainsi que le deuxième objectif avec l'étude de l'influence de paramètres temporels lors d'une génération sismique d'un tsunami. Ainsi, ce manuscrit est divisé en deux parties: la première se consacre à l'étude théorique des échelles temporelles et la deuxième porte sur la validation des codes issus du système Telemac avec leur application aux cas tests du projet et au cas réel du tsunami Tohoku-Oki de 2011.

Context of the thesis

On the 11^{th} of March 2011, an earthquake of magnitude M_w 9.1 generated a huge tsunami that hit the Japan East coast. This tsunami reached extremely high elevation, with $30m$ run-ups at some locations in the Tohoku Bay (Mori et al. [2011]). The impact on the coast was particularly devastating, and some cities were destroyed as it was the case for Otsushi (Figure 1).

Figure 1: Introduction - Pictures from the NOAA website (http://www.ngdc.noaa.gov/hazardimages/event/show/256) of the Otsushi city in the wake of the March 2011 tsunami.

Witnesses of the tsunami were recorded all over the Pacific up to California. Besides the catastrophic impact along the coast, the accident of the Fukushima Dai-ichi Nuclear Power Plant (FNPP) provoked a worldwide concern. As illustrated in Figure 2, a preliminary simulation of the propagation of the Cesium 137 plume released in the atmosphere was performed during one month. This result has to be analysed with caution, however one can see the flume leaving the Japanese coast after 5 days, then covering half of the Pacific ocean after 10 days, and after 25 days the flume reached a major part of North America. This simulation was performed with the polyphemus code of the CEREA laboratory, and the complete results of the simulation are available at http://cerea.enpc.fr/fukushima/index.html.

Following this event, the French project TANDEM (Tsunami in the Atlantic and the English Channel: Definition of the Effects through numerical Modeling) was launched in February 2014. The final aim of this project is to evaluate the tsunami risk along the French coast, focusing on the Atlantic and Channel coastlines. As shown in Figure 3, five active French nuclear power plants are based in or around this area. The geophysical nature of the French coast is not similar to that of Japan: there is no subduction zone able to produce such an event as the 2011 Japanese case. However, the lack of information of the possible triggering sources shows a crucial need to increase our knowledge in this field.

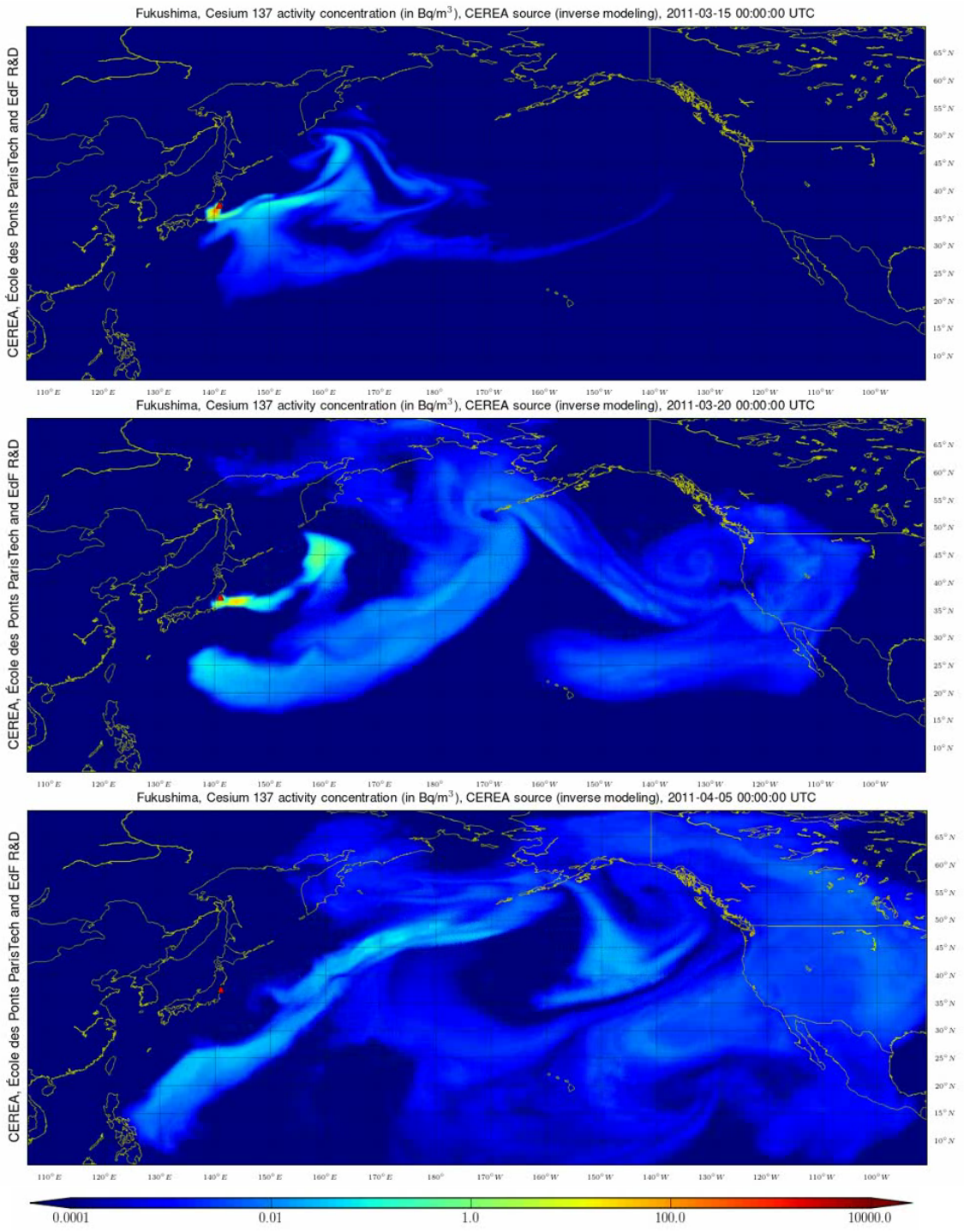

Figure 2: Introduction - Preliminary simulation of the propagation of the Cesium 137 flume with the Polyphemus codes 5, 10 and 25 days after the Fukushima accident (top to bottom respectively). The scale represents the concentration of Cesium 137 activity in Bq/m^3 (http://cerea.enpc.fr/fukushima/index.html).

Figure 3: Introduction - Nuclear power plants in France (*Picture's source: wikipedia*).

In light of the 2011 event in Japan, a country which has always dealt with tsunamis, it is important either for the nuclear plants or the civil coasts to define the tsunami hazard. This ANR project gathers ten French partners (Figure 4) with industrial companies (EDF, Principia), universities (University of Pau, ENPC), scientific institutes (BRGM, CEA, Ifremer, Inria, IRSN, SHOM) and one Japanese correspondent (MRI, Meteorological Research Institute). My contribution in this project is done with my affiliation to ENPC through the Saint-Venant Hydraulics Laboratory. This collaboration aims to use lessons learned from the Japanese event, to improve the currently available numerical skills and to apply them to France.

Figure 4: Introduction - First year annual meeting of the project TANDEM.

The project is structured in four work-packages, so called WP1, WP2, WP3 and WP4. Similarly to the one of the NOAA (Synolakis [1987]), the aim of WP1 is to build a numerical benchmark where each partner's code is validated and compared with a set of test cases. This work-package permits to adapt and improve the existent numerical models and also to identify any weaknesses. Through this benchmark, the numerical resolutions of idealized and simplified generations, propagations and impacts on the coast of tsunamis are addressed, see Violeau et al. [2016]. This work-package is a first important step in the evolution of the project because it permits to validate the use of the different codes prior to modeling real cases.
The WP2 treats the influence of the model parameters and uncertainties focusing on seismic and landslide generations. The sensitivity to the source characteristics of the generated waves and flooded area are tested. These parameters concern the geometrical aspects of the source (size, direction, density) but also the generation parameters as its motion velocities. The influence of the bathymetric and topographic data, values of the tides and seasonal fluctuations has also been tested (Antoshchenkova et al. [2016]).
The third work-package, WP3, concerns the study of the 2011 Tohoku-oki tsunami. This real case permits to test the numerical models and compare them to real scale tsunami data. Four steps are defined for this work: the construction of Digital Elevation and bathymetric Maps (DEM) thanks to the Japanese partner (MRI), the identification of co-seismic source models from the literature, the modeling of the propagation with the different codes and its comparison with data, the modeling of the impact of the waves on the coast and protection structures.
The last work-package, WP4, is the application to the French coasts from creating an inventory of the possible tsunamigenic sources in order to estimate water height approaching the French coasts and finally to study the response of local sites and specific coast configurations.

Objectives and contents of the thesis

This thesis takes part in the WP1, WP2 and WP3 workpackages of the above mentioned project.
One aim of this work is to validate the Telemac system to model tsunamis. The Telemac system is an open source system initially developed by the *Laboratoire National d'Hydraulique*, a department of *Electricité de France*'s Research and Development Division. It gives tools to simulate free surface flows, either for a purely hydrodynamics point or for sediment transport and water quality. In the particular case of tsunami modeling only two branches are used: Telemac2D and Telemac3D. A brief description of the equations and numerical methods is given in Appendix C, and a complete description is available by Hervouet [2007] and on the system website `http://www.opentelemac.org`. Thus, during these

three years of work, I performed some test cases taking part of the benchmark defined by the TANDEM project in WP1. I was also responsible of one of these cases: the generation of waves by a moving vertical step, built on the works of Hammack [1973]. The aim is to reproduce the different experiments and to compare the result from the numerical models to the experimental data. At the end, only three codes participate to the realisation of this test case: Telemac2D, Telemac3D and Misthyc (Yates and Benoit [2015]). The ultimate validation is the application to a real case: the Tohoku-oki tsunami that hit on March 11^{th} of 2011 the East coast of Japan, which is my participation to the WP3.
To the best of my knowledge, only preliminary and limited studies about tsunamis have been performed with Telemac and in the Saint-Venant Hydraulics Laboratory, respectively. Thus, there was a need to review what was done by the scientific community from the basis processes. A first state-of-the-art review gave me a global landscape of the phenomena. This work led to identifying the generation process as the least well-known due to its diversity and complexity. Ultimately, the impact of kinematic seismic source on the wave generation became the subject of interest of this thesis. Thus, inspired by the literature where only one temporal parameter is studied, the horizontal or the vertical scale, a study using both temporal parameters is carried out here. An analytical solution is then developed and compared to numerical solutions. Furthermore, to test its applicability in general cases, and to assess its influence in numerical simultation, a real event is simulated with the Telemac system. The results show a real impact of the temporal parameters, thus validating our approach.

Structure of the thesis

Related to the duality of the work, between the study on the influence of timescales and the applications for the TANDEM project, this manuscript has two distinct parts.
The first part focuses on the influence of the timescales on the generation of the waves. This part is structured in three chapters. First, Chapter 1 presents the state-of-the-art. In this review, a global approach of the tsunami processes is presented from the different generations to the run-up (impact on the coast). Particular attention is given to the seismic generation and the kinematic processes that can be important but usually neglected. Chapter 2 details the development of the linear analytical solution of the generation of waves by an idealised sea floor motion taking into consideration both vertical and horizontal motions simultaneously. In this chapter, the analytical solution is compared to linear and nonlinear numerical models, permitting a more in-depth study of the impact of the temporal parameters. During this study, a resonance phenomena is enhanced for slow ground motions. Thus, Chapter 3 presents an application case of a tsunami earthquake (with slow deformation) performed with Telemac2D: the event of March 1947 that occurred in New-Zealand for which unexpected wave heights were observed.

The second part gathers the different applications performed for the project TANDEM in order to validate the Telemac System for modeling tsunamis. In Chapter 4, my different contributions to the benchmark are presented with the different models within the Telemac system. There are test cases about the generation: a sliding mass and a moving step, one case about the propagation of a solitary wave, and three cases about the run-up: oscillations in a close basin, run-ups of Gaussian and solitary waves. Finally, Chapter 5 concerns the study of the Tohoku-Oki event of the 11^{th} March 2011 that hit Japan. This incorporates all the aspect of the simulation developed, from the construction of meshes to the conclusions about the capacity of the Telemac codes to model such an event.

Part I

Kinematic generation of tsunamis

Chapter 1

State-of-the-art

Ce chapitre est un bref récapitulatif de notre connaissance sur la dynamique des tsunamis, en particulier ceux générés par les tremblements de terre. Le phénomène de tsunami est étudié depuis bien longtemps, étant donné leur direct impact sur les Hommes. Il peut vite se révéler catastrophique comme en témoignent les récents évènements de 2004 en Indonésie et 2011 au Japon. La compréhension de ces évènements ainsi que leur prévention et alerte sont des défis importants à relever. La vie d'un tsunami peut être découpée en trois phases: la génération, la propagation et l'arrivée/impact sur les côtes que l'on appellera le run-up. La génération est sûrement la partie la plus ardue à aborder en vue de sa complexité, ses approches multidisciplinaires et le nombre d'inconnues. Un tsunami peut être engendré par de nombreuses sources: glissements de terrain, éruptions volcaniques, chutes d'astéroïdes, variations atmosphériques et séismes. Cette dernière source est la plus probable. Cependant, dans les modèles numériques et théoriques de nombreux phénomènes physiques sont négligés: il est supposé que la déformation du fond se fait instantanément et est transmise directement à la surface libre avec un champ de vitesse nul. En utilisant cette méthode, la cinématique du fond est négligée, point qui sera développé dans cette thèse. Contrairement à la source, la propagation est la phase la plus connue car elle se traduit par la propagation d'onde plus ou moins longue. Ainsi, généralement les équations de Saint-Venant sont utilisées pour modéliser cette étape. Néanmoins, des phénomènes de dispersion fréquentielle ne sont pas négligeables pour certains évènements, posant la question de l'usage de modèles plus précis. Enfin, la dernière étape est l'inondation, conséquence direct du tsunami sur les Hommes. Beaucoup d'études théoriques

ont été développées mais limitées par la difficulté du phénomène: la non-linéarité se développe fortement lors de cette phase. Ainsi, de nombreuses études numériques et expérimentales ont été construites pour compléter la connaissance sur le sujet. Les études théoriques et expérimentales font généralement des concessions et se focalisent sur des phénomènes simplifiés. En plus de l'apport de connaissance, ces modèles idéalisés permettent la validation des modèles numériques, ce qui permet de légitimer leur utilisation pour les alertes et préventions en conditions réelles.

1.1 General overview

In the recent past, catastrophic events reminded us how important it is to understand tsunamis, and in particular their generation mechanisms and propagation dynamics. These natural disasters can cause dramatic human losses and huge material damages as we experienced with the Indonesian tsunami of December 2004, and more recently with the Japanese event of March 2011. The aim of the present chapter is to present a global state-of-the-art of the tsunami researches performed until now. It does not claim to present in depth studies of each point but has the intention to give an overview on most of the phenomena that occur during the life of a tsunami. I want to highlight the work of Levin and Nosov [2009] that was intensively used to prepare this Chapter, and strongly recommend this work for more details. A recent historical review was also performed by Kânoğlu et al. [2015]. In their work, the authors traced the history of the major events and the responses and advances of the scientific community. Kânoğlu et al. constructed their work around the historical background while in the present chapter, the review is built around the physical processes. First, this Chapter chronologically describes the different steps of a tsunami from its generation in Section 1.1.1, to its propagation in Section 1.1.2 before finishing with its impact on the coasts and wave run-up, in Section 1.1.3. Then, the second part of this chapter is focused on the subject of interest for this thesis, that is the seismic generation of tsunami and the necessity to consider kinematic model for the source, Section 1.2.

1.1.1 Generation

The generation of tsunamis may be the most complex part of its life. One of the difficulties is that we rarely have in situ measurement data. Moreover, the generation processes can be very complex and multidisciplinary. In the present section, the main features of some tsunami generations are described.

1.1.1.1 Landslide tsunami

After seismic generation that will be investigated in Section 1.2, the generation of tsunami by landslide is the most probable. The landslide process consists of an accumulation of sedimentary material until an event triggers the destabilisation of the sediment layer. Among them, one can find the erosion on a steep underwater slope, coastal construction projects, prolonged rain leading to a saturation of coastal land, volcanic activities and often earthquakes. Indeed, some seismic events are accompanied by tsunamigenic landslides as suggested by Tappin et al. [2014] for the Japan 2011 event or the catastrophic event of the Papua New Guinea July, 1998 (Gelfenbaum and Jaffe [2003], Synolakis et al.

[2002], Imamura and Hashi [2003], Tappin et al. [2008]). The latter was such destructive that it awakes the awareness of this hazardous type of generation, that was until there less investigated than seismic generation, Bardet et al. [2003].
Landslide tsunamis are considerated as more local events than seismic events, with large run-ups close to the source, Harbitz et al. [2006]. A famous example is the Lituya bay, 1958 event in Alaska where a $524m$ run-up was measured on the other side of the bay, Miller [1960], Mader and Gittings [2002]. This event corresponded to a sub-aerial landslide, starting from air to water. Some tsunamis are triggered by only submarine landslide, that makes them difficult to identify. Moreover, the nature of the landslide can be diverse: a rock fall, a motion of a solid bloc or a fluid flow. In all these cases, the characterising parameters that influence the amplitude of the generated wave, are the landslide volume, velocity, initial acceleration, length and thickness. Its parameters influencing the wavelength are its length and its run-out distance. However, the best indicator of tsunamigenic potential seems to be the ratio between the volume and the initial acceleration of the sliding material (Masson et al. [2006]). It can also be noted that an abrupt deceleration of the landslide can contribute to large water surface elevation (Harbitz et al. [2006]).
Bardet et al. [2003] recalled us how important the study of landslide tsunami generation is. Many studies have been devoted to this aim. Describing precisely all the possibilities will be out of the scope of the present work. However, I noted that this problem was addressed either theoretically than experimentally or numerically. Experimentally, lots of works have been performed for solid landslides, as done by Grilli and Watts [2005] and Enet and Grilli [2007]. The latest considered a sliding mass moving under the action of gravity. Figure 1.1 shows pictures of their set up experiment.

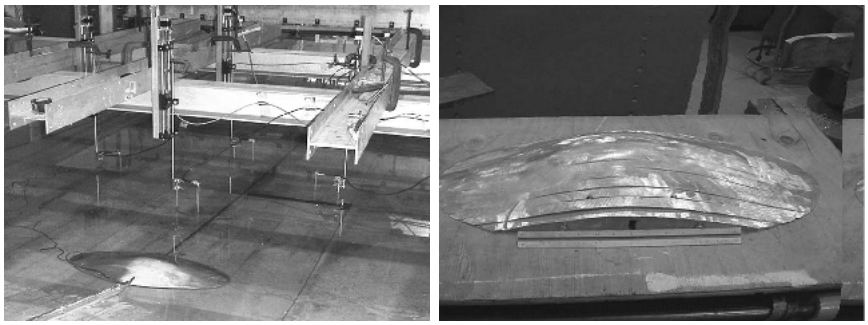

Figure 1.1: Landslide generation – Pictures of the laboratory experiment of Enet and Grilli [2007]. The left picture shows the general view of the set up while the right picture shows the experimental landslide model moving only by gravity.

Besides of providing an accurate benchmark for numerical models, this experiment permitted to highlight the influence of the initial acceleration on the generated waves and to confirm an analytical kinematic motion of the landslide: the 1D displacement of the mass

center $s(t)$ is evaluated such as:

$$s(t) = s_0 \ln \cosh \frac{t}{t_0},$$

with $s_0 = \frac{u_t^2}{a_0}$, $t_0 = \frac{u_t}{a_0}$, a_0 and u_t the landslide initial acceleration and terminal velocity, respectively. The latter are calculated from the characteristics of the landslide. Another possibility is to consider the landslide as being deformable, corresponding more to the reality (Levin and Nosov [2009]). Thus, some studies were performed with granular slide as done by Fritz et al. [2004]. In their work, a slide Froude number, $F_r = \frac{v_s}{\sqrt{gh}}$ with v_s the slide impact velocity, is defined as the predominant parameter characterizing the generated waves. They identified weakly nonlinear oscillatory wave, nonlinear transition wave, solitary-like wave and dissipative transient bore for small to important Froude numbers. The diverse water surface response as function of F_r and S is illustrated in Figure 1.2 where here S is the slide thickness.

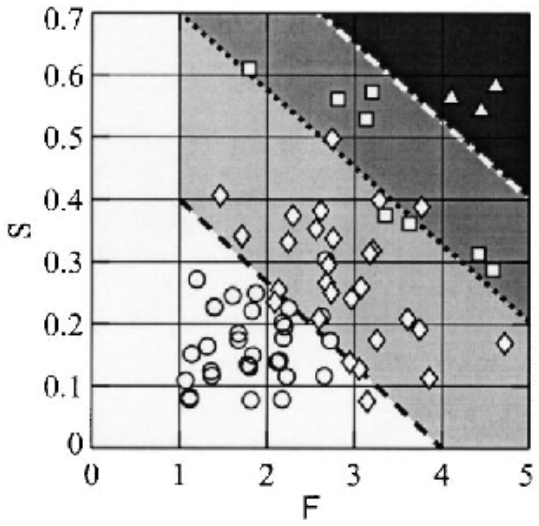

Figure 1.2: Landslide generation – First wave crest classification as function of the slide Froude number $F_r = v_s/\sqrt{gh}$ and the slide thickness $S = s/h$ with ◯ weakly nonlinear oscillatory wave, ◊ nonlinear transition wave, □ solitary-like wave, △ dissipative transient bore. Light-shaded square corresponds to the nonlinear transition region, the dark-shaded square to solitary-like region, and the black square to bore region. Result issued from the work of Fritz et al. [2004].

Among the theoretical works, we can mention the work of Jiang and LeBlond [1992], Jiang and Leblond [1994] for which the landslide is considered as an incompressible viscous fluid. Under specific assumptions (important difference between the water and landslide densities, thickness of the landslide much smaller than water depth, laminar and quasistationary landslide flow, neglected mixing effects mainly), the velocity of the landslide flow can be

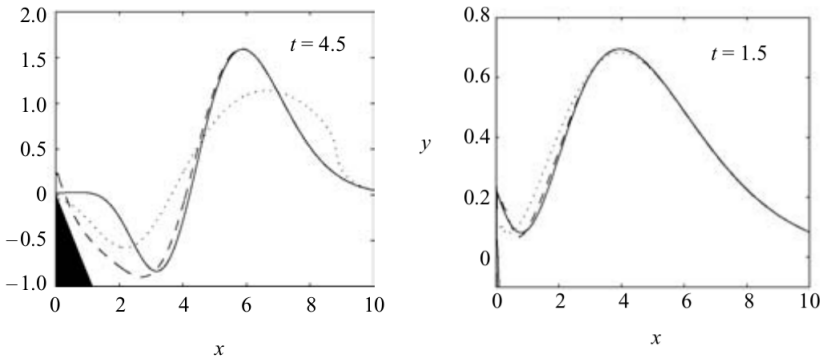

Figure 1.3: Landslide generation – Comparison between linear theoretical solution (solid line) to numerical linear model (dashed line) and nonlinear numerical model (dotted line) for $\tan\beta/\mu = 0.87$ (left) and $\tan\beta/\mu = 3.5$. Result issued from the work of Liu et al. [2003].

estimated with a parabolic profile. Using this property, Jiang and LeBlond coupled the hydrodynamics equations in landslide with Nonlinear Shallow Water Equations. However, Bardet et al. [2003] and Murty [2003] suggested caution about applying hydrodynamic simulation codes to the landslide because Murty found important differences between numerical simulations and observations. Liu et al. [2003] proposed a 1D analytical solution for the forced Linear Shallow Water Equations (fLSWE) for which the author imposed the landslide on a uniform beach as a motion of the ground. The 1D dimensionless sea floor deformation h_0 is considered as: $h_0(x,t) = \exp i\omega(2\sqrt{\frac{\mu x}{\tan\beta}} - t)$, with ω the frequency, $\tan\beta$ the beach slope and $\mu = \frac{\text{vertical thickness of the slide}}{\text{horizontal length of the slide}}$. Thus, the dimensionless fLSWE is:

$$\eta_{tt} - \frac{\tan\beta}{\mu}(x\eta_x)_x = h_{0tt},$$

η being the free surface deformation. This equation is solved by applying an Hankel transformation. Then, the authors confronted the linear analytical solution to numerical nonlinear and linear shallow water models for different values of $\tan\beta/\mu$. Figure 1.3 shows a comparison between the linear analytical solution and numerical results. Unlike the theoretical solution, the numerical linear model uses an algorithm to track the real shoreline, see Liu et al. [2003].

These comparisons permit the authors to conclude that the theoretical solution gives a good approximation of the generated waves for thin slides ($\tan\beta/\mu$ large) while for thick slides ($\tan\beta/\mu$ small), the nonlinear propagation aspects are not correctly represented. Beyond this limitation, this landslide stays a idealized special case. As suggested by the authors, this analytical study is still a good benchmark because analytical solution is helping for validate computational techniques, and this case is performed in the frame of the project TANDEM (see Chapter 4). Up to now, theoretical studies and experiment have

the technical bias to impose the nature of the landslide and adapted the model from it. Abadie et al. [2010] remove this limitation of numerical models by using a three-phase model that solves the Navier-Stokes equations for the air, the water and the landslide. Thus the landslide is considered as a fluid but its density and viscosity can be modified to consider the landslide as a solid. In Figure 1.4, one can see numerical result for a solid case ($\mu = 10^{10} Pa.s$) and a deformable slide ($\mu = 10^{2} Pa.s$).

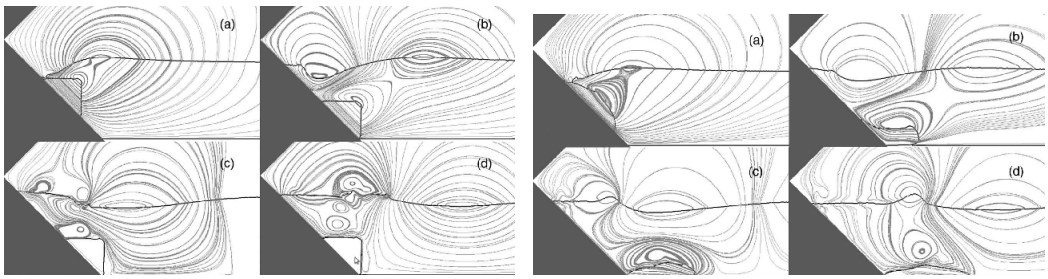

Figure 1.4: Landslide generation – Numerical result from a Navier-Stokes three-phase model considering a solid landslide (left) or a deformable landslide (right) at a) $t = 0.5s$, b) $t = 1s$, c) $t = 1.5s$ and d) $t = 2s$. These results are issued from the work of Abadie et al. [2010].

1.1.1.2 Volcanic tsunami

The Earth is covered with volcanoes. They can be land based, close or not to the coast, underwater, and thus they can generate their own tsunamis. Humankind has been marked by some of these events; as example the explosion and tsunami of the volcanic Thera that occurred 3500 years ago and eradicated the local population, the Minoans on Crete; or the Krakatau volcano event that occurred in three steps between the 26^{th} and 27^{th} of August 1883 (Mader and Gittings [2006], Choi et al. [2003]). The mechanisms of tsunami generation by volcano are complex, they can be caused by:

- discharge matter into water,
- collapse of a caldera,
- landslide, pyroclastic flow,
- volcano earthquake.

The last mechanism is assimilated to seismic generation and thus will not be developed here as this part will be detailed in the following. Volcano landslides and pyroclastic flows have similar dynamics than landslides, see Tinti et al. [2003], and create dispersive waves. Pyroclastic flows are particular as they are first lighter than water, then become colder

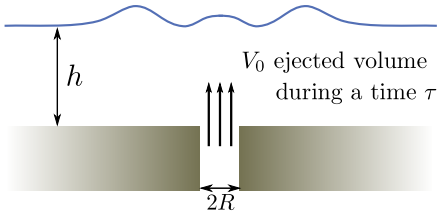

Figure 1.5: Volcanic tsunami generation – Schematising of the tsunami generation by a discharge into water of a large volume of matter. Adapted from Levin and Nosov [2009].

and heavier. Thus, the disturbance of the water level is created by an overpressure on the free surface. Tinti et al. [2003] idealized this condition assuming the pressure as an impulse function. However, the dynamics of pyroclastic flow is complex, mixing multiphase elements and deserves its own model. This was done by Todesco et al. [2002] for a possible Vesuvius eruption.

A collapse of a caldera corresponds to a lowering of the ocean bottom, that is similar to a negative displacement of the seafloor during an earthquake. The generated wave, depending of the width of the caldera, is assumed to be a long wave.

The last possible generation, a discharge of matter into water, is proper to the tsunami generation by volcanoes. This generation can be idealized as shown in Figure 1.5. h is the water depth, R the radius of the pipe, V_0 the volume of matter released during the time τ of the eruption.

A first approximation permits to estimate the amplitude of the initial water level elevation η_0 (Levin and Nosov [2009]):

$$\eta_0 = \frac{V_0}{\pi\tau^2 gh}. \tag{1.1}$$

If a potential model is considered with ϕ the velocity potential and H the heaviside function, the dynamic boundary condition can be fixed in the cylindrical coordinate as (see Levin and Nosov):

$$\phi_z(r) = \frac{V_0}{\tau\pi R^2}(1 - H(r - R))(H(t) - H(t - \tau)) \quad z = -h. \tag{1.2}$$

This condition is valid only if the process is slow. Unfortunately, it can be explosive, and in this case, the dynamics of the discharge are much more complex to represent within particular high temperature gases. The works of Le Méhauté and Wang [1996] and Kurkin and Pelinovsky [2004] (see Levin and Nosov [2009]) approach the real phenomena with the following estimation of the initial free surface deformation:

$$\eta_0(r) = H_s\left(2\left(\frac{r}{R_s}\right)^2 - 1\right)(1 - H(r - R_s)), \tag{1.3}$$

where R_s is the source radius and H_s the amplitude of the water level displacement at the source calculated from the delivered energy. In both cases (slow and explosive), the generation and the propagation of waves can be calculated with a linear model. It appears that, depending on the radius of the initial perturbation, the waves are strongly dispersive. Levin and Nosov [2009] illustrated this conclusion by computed the free surface elevation for two cases with different radius of the initial perturbation (Equation 1.3). In Figure 1.6, we can see the profile of the waves excited by an underwater eruption for a radius $R_s/h = 1$ and $R_s/h = 3$, h the uniform water depth.

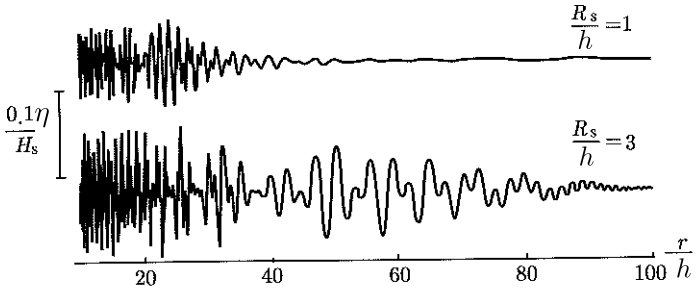

Figure 1.6: Volcanic tsunami – Free surface deformation η generated by an underwater eruption with a radius of $R_s/h = 1$ (up) and $R_s/h = 3$ (down) after $t = 100\sqrt{g/h}$. Figure adapted from Levin and Nosov [2009].

For the larger radius, the wave signal is more complex and dispersive as can be seen by the extended wave trains.

1.1.1.3 Meteotsunami

Some complete studies about meteotsunami are available in the literature as in the reviews of Levin and Nosov [2009], Monserrat et al. [2006] or the compilation from Vilibić et al. [2014].
It seems that meteotsunami are often confused with seismic tsunami due to their similarities (Monserrat et al. [2006]), but they are rarer. Meteotsunami are also long waves; nevertheless they are less energetic than seismic tsunami and thus, they are considered local tsunami. The term of "meteotsunami" was first given by Nomitsu [1935]. They find their origin in the variation of atmospheric processes upon the water layer[1]. It can be a suddenly variation of the atmospheric pressure of few hPa, the example of atmospheric pressure record of the event of the 15 June 2006 that occurred in the Balearic island is shown in Figure 1.7.

However, these variations of the atmosphere are not strong enough to generate significant

[1]Meteostunami and storm surge are in the same scope, however they have different time and spatial scales as mentionned by Monserrat et al. [2006] and Levin and Nosov [2009].

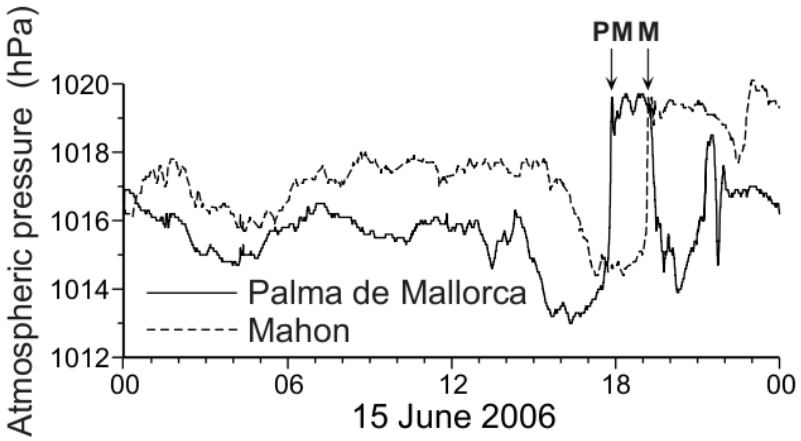

Figure 1.7: Meteotsunami – Atmospheric pressures record on the 15 June 2006 at two ports in the Balearic Island: Mallorca and Mahon. The "PM" and "P" arrows indicate the suddenly change. Figure issued from the work of Monserrat et al. [2006].

sea level response as tsunami wave. In fact, the disturbance of atmospheric pressure or wind friction tension need a resonance effect (Levin and Nosov [2009]) to be efficient. In these cases:

- the velocity of the atmospheric perturbation is close to the long wave celerity,
- the period of the atmospheric perturbation matches the period of oscillation of the basin.

Considering these characteristics, meteotsunami are favoured by semi-closed coastal basins, in particular places well-known to be subject to seiche oscillation. Among these places, one can find the Nagasaki Bay (Japan) and the Balearic Island (Spain). The first one was victim of an extreme seiche oscillation (*abiki*) on 31 March 1979 for which wave heights reached $4.8m$, Hibiya and Kajiura [1982]. The second place was touched more recently, on 15 June 2006, by a locally called *rissaga*: a $4m$ negative wave reached the bay emptying the Ciutadella Harbour (Jansa et al. [2007]) as illustrated in the pictures Figure 1.8.

1.1.1.4 Cosmogenic tsunami

As for meteotsunamis, this paragraph on the cosmogenic tsunami is a first approach for this phenomenon; complete work could be found in the studies of Crawford and Mader [1998], Levin and Nosov [2009], Ward and Asphaug [2000], Ward and Asphaug [2002], Ward and Asphaug [2003], Massel [2012].
As suggested by its name, a cosmogenic tsunami is created by the impact of a meteorite

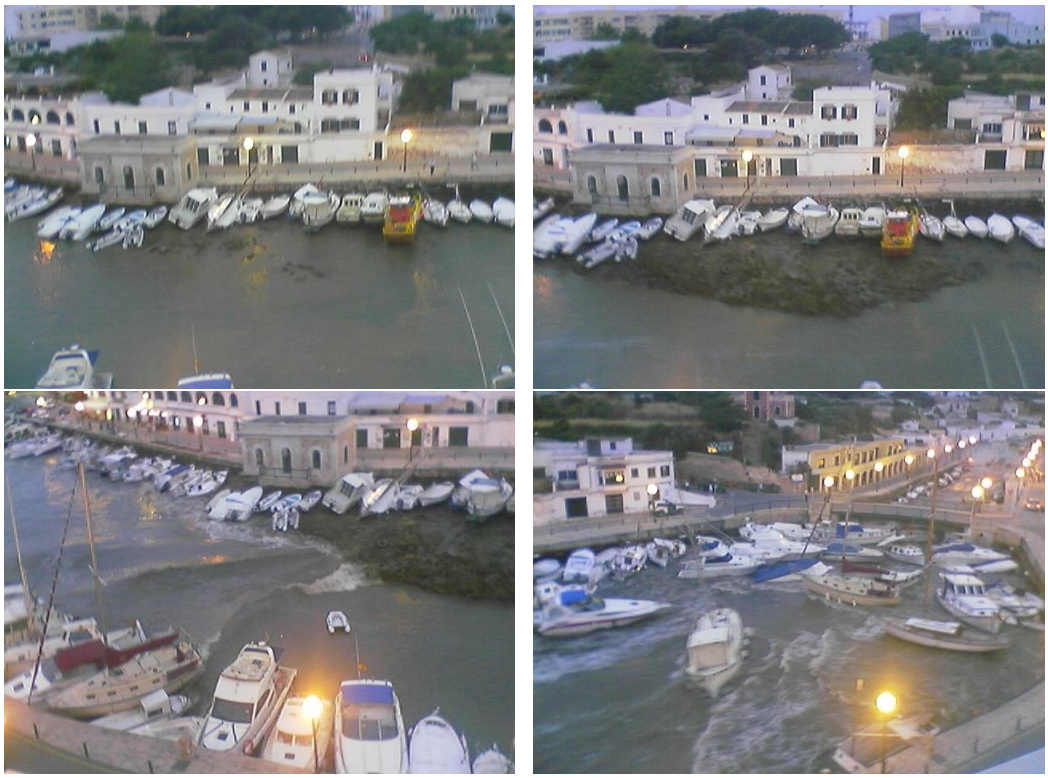

Figure 1.8: Meteotsunami – Pictures taken during the meteotsunami that occurred the 15 June 2006 at Ciutadella Harbour (Balearic Islands). Anonymous photographs on-line (http://ichep.blogspot.fr/2006/06/rissaga-ciutadella.html).

in the ocean. No human being has been witness of this kind of events (Levin and Nosov [2009]). Nevertheless, the risk exists: every year objects penetrate in our atmosphere. The probabilities of impact per year are (Massel [2012]):

- 0.001% for an object of $500m$ radius,
- 0.2% for a $50m$ radius object,
- 50% for a $5m$ radius object,
- 100% for a $1m$ radius object.

The impact cavity of the object is usually modeled in cylindrical coordinates by:

$$\eta_0(r) = d\left(\frac{r^2}{RC^2} - 1\right)\left(1 - H(r - \sqrt{2}RC)\right), \tag{1.4}$$

where η_0 is the initial free surface deformation, d the cavity depth, RC is the internal radius of the cavity and $\sqrt{2}RC$ the external radius of the cavity. RC and d are parameters that are calculated from the radius of the meteorite and its physical properties and also from water properties. This idealized initial state is compared in Figure 1.9 to a numerical

simulation of Crawford and Mader [1998] for an asteroid of $500m$ diameter, with a density of $3.32g/cm^3$ in a $5km$ depth ocean and a fall velocity of $20km/s$. Using the previous relationships between the initial state and the meteorite properties, the part of energy transmitted from the meteorite to the water is estimated at 16% of the meteorite energy.

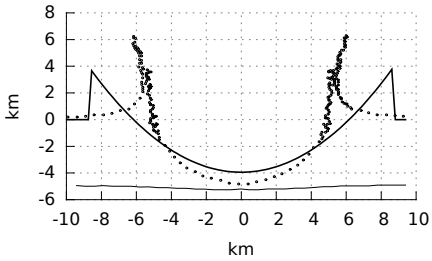

Figure 1.9: Cosmogenic tsunami – Comparison between the idealized impact cavity 1.4 (solid line) and numerical simulation of Ward and Asphaug [2003] at $t = 25s$ (dot line). The thin line is the sea ground. Graph adapted from Levin and Nosov [2009].

To describe the propagation from the initial state, linear theory is commonly used even if it is not really appropriate to the heights of the generated waves which are of the order of the ocean depth, but it permits a first approach. In this case, the dispersion is important, the wavelengths are smaller than the one of a seismic tsunami and the wave train is slower (see Levin and Nosov [2009]). Long wave theory is not adapted here. Also, the maximal wave height decreases rapidly. This attenuation depends on, for instance, the size of the meteorite and the ocean depth.
A famous example is the $4km$ diameter Eltanin asteroid that impacted the South Pacific Ocean $2.15Myr$ ago (Ward and Asphaug [2002]). Using the linear tsunami theory and initiating the cavity with the approximation 1.4, the authors numerically estimated the propagation of the generated wave as can be seen on the illustration of Figure 1.10.

Ward and Asphaug [2002] estimated a $200 - 300m$ height wave reaching the Antartic Peninsula and the tip of South America ($1200 - 1500km$ from the point of impact) while waves of $60m$ amplitude hit New-Zealand, $6000km$ away. Another possible future example is the 1950 DA asteroid ($\sim 1km$ of diameter), see Ward and Asphaug [2003]. This asteroid, discovered in 1950, has between 0 and 0.3% chance to impact the Earth in 2880. Ward and Asphaug built a numerical model supposing that such an asteroid will fall close to the east coast of United States. The predicted waves are at least $60m$ high at the United States coast while they will decrease to $15m$ at the European coasts.

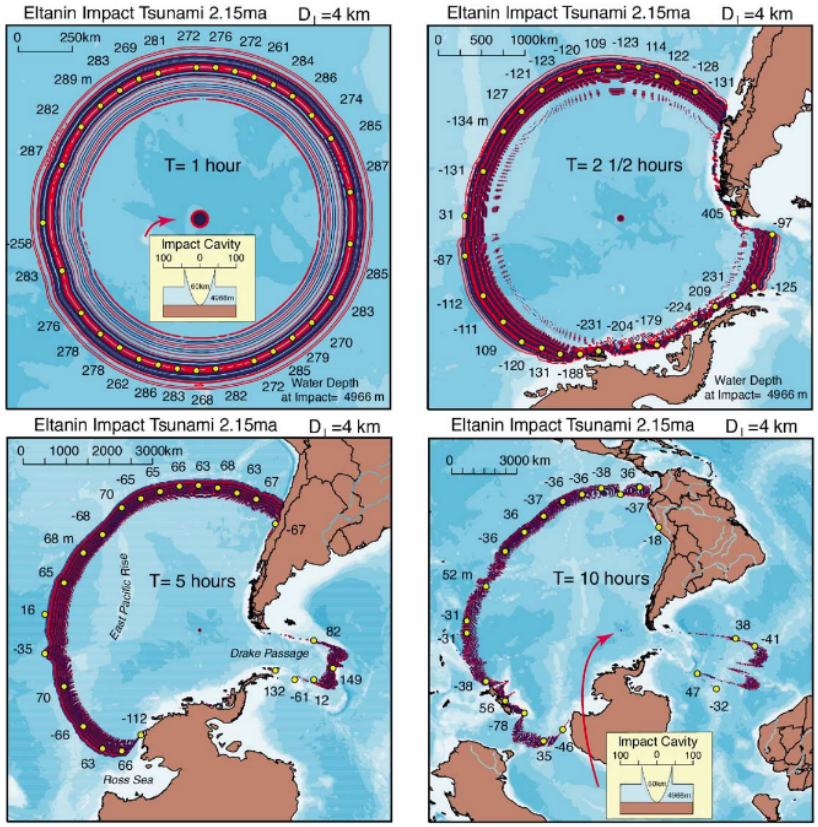

Figure 1.10: Cosmogenic tsunami – Numerical propagation of the tsunami generated by the impact of the Eltanin asteroid $2.15Ma$ ago. The yellow dots show numerical tsunami heights. Work issued from Ward and Asphaug [2002].

1.1.2 Propagation

After its generation, the second part of a tsunami life is its propagation. Similarly to the review of Dutykh [2007], the following section recalls the general models used for it.
The propagation of tsunamis is supposed to be the most well known part of the tsunami life, considering here that a tsunami is a wave propagating along large distances. We use the following designation:

- the free surface deformation : $\eta(x, y, t)$,
- the vertical displacement of the sea floor : $\zeta(x, y, t)$,
- the initial water depth : h, (assumed constant)
- the sea floor depth : $z = -h + \zeta(x, y, t)$,
- the wavelength : λ,
- the wave amplitude : a,

- the velocity : $\boldsymbol{u} = (u, v, w)$.

Coriolis effects associated with the rotation of the Earth are not considered here for simplicity, however, in reality according to the source parameters, they should (Kirby et al. [2013]). The wave length of a tsunami is much larger than the capillary length scale, thus surface tension effects are not taken into account. Moreover, fluid is assumed to be incompressible and inviscid. Thus, the flow is assumed irrotational, and there exists a velocity potential $\phi(x, z, t)$, $\boldsymbol{u} = \nabla\phi$, that satisfies the Laplace equation and the boundary conditions as follows:

$$\bigtriangledown^2\phi = 0, \tag{1.5a}$$
$$\phi_z = \eta_t + \phi_x\eta_x \qquad z = \eta(x,t), \tag{1.5b}$$
$$\phi_t + \tfrac{1}{2}|\bigtriangledown\phi|^2 + g\eta = 0 \qquad z = \eta(x,t), \tag{1.5c}$$
$$\phi_z = \zeta_t + \phi_x\zeta_x \qquad z = -h + \zeta(x,t), \tag{1.5d}$$

where subscripts t, x indicate partial derivatives. This system describes the general case issued from the Euler equation for an irrotational flow. To simplify the resolution, approximations can be done on the dispersion and/or the linearity of the system. The latest is addressed in Chapter 2. The factor evaluating the dispersion effects is μ^2, $\mu = \frac{h}{\lambda}$ and the linearity factor is $\epsilon = \frac{a}{h}$. To scale the mathematical model, Equations 1.5a-1.5d are non-dimensionalised using:

$$\begin{aligned} x^* &= \tfrac{x}{\lambda}, \quad y^* = \tfrac{y}{\lambda}, \quad z^* = \tfrac{z}{h}, \quad t^* = \tfrac{c_0 t}{\lambda} \\ \eta^* &= \tfrac{\eta}{a}, \quad \zeta^* = \tfrac{\zeta}{a}, \quad \phi^* = \tfrac{c_0}{ag\lambda}\phi, \quad \epsilon = \tfrac{a}{h} \end{aligned} \tag{1.6}$$

where $c_0 = \sqrt{gh}$. The previous system becomes:

$$\phi^*_{zz} + \mu^2\left(\phi^*_{xx} + \phi^*_{yy}\right) = 0 \tag{1.7a}$$
$$\phi^*_z = \mu^2\eta^*_t + \epsilon\mu^2\left(\phi^*_x\eta^*_x + \phi^*_y\eta^*_y\right) \qquad z^* = \epsilon\eta^* \tag{1.7b}$$
$$\phi^*_z = \mu^2\zeta^*_t + \epsilon\mu^2\left(\phi^*_x\zeta^*_x + \phi^*_y\zeta^*_y\right) \qquad z^* = -1 + \epsilon\zeta^* \tag{1.7c}$$
$$\mu^2\phi^*_t + \tfrac{1}{2}\epsilon\left(\mu^2\phi^{*2}_x + \mu^2\phi^{*2}_y + \phi^{*2}_z\right) + \mu^2\eta^* = 0 \qquad z^* = \epsilon\eta^* \tag{1.7d}$$

The mathematical simplification of the dispersion is performed by conserving only certain order of μ^2 as illustrated below for Boussinesq and Nonlinear Shallow Water Equations. The non-dimensionalised potential velocity ϕ^* is decomposed on a Taylor expansion in μ^2:

$$\phi^* = \phi^*_0 + \mu^2\phi^*_1 + \mu^4\phi^*_2 + ...$$

This expansion is introduced in Equations 1.7a-1.7d. Then, the Boussinesq equations are found by keeping the terms of order $\epsilon\mu^2$ and μ^4:

$$(\eta-\zeta)_t + [(1+\epsilon(\eta-\zeta))u]_x + [(1+\epsilon(\eta-\zeta))v]_y = \mu^2(\tfrac{1}{6}(\triangle u_x + \triangle v_y)), \tag{1.8a}$$

$$u_t + \epsilon(uu_x + vv_x) + \eta_x - \tfrac{1}{2}\mu^2(u_{txx} + v_{txx}) = 0, \tag{1.8b}$$

$$v_t + \epsilon(uu_y + vv_y) + \eta_y - \tfrac{1}{2}\mu^2(u_{txy} + v_{txy}) = 0. \tag{1.8c}$$

While the Non Linear Shallow Water equations are recovered by keeping the terms of order $\epsilon\mu^2$ and μ^2:

$$(\eta-\zeta)_t + [(1+\epsilon(\eta-\zeta))u]_x + [(1+\epsilon(\eta-\zeta))v]_y = 0, \tag{1.9a}$$

$$u_t + \epsilon(uu_x + vv_x) + \eta_x = 0, \tag{1.9b}$$

$$v_t + \epsilon(uu_y + vv_y) + \eta_y = 0. \tag{1.9c}$$

Usually, the numerical models used to simulate tsunami are based on the NonLinear Shallow Water equations (NLSWE). However, the impact of dispersive effects on the propagation of tsunami is still an open question. Indeed, some events showed dispersive wave packets, as for the case of the 24 December 2004 tsnami that occurred in Thailand. Its wave trains hitting the Koh Jum islande are illustrated in Figure 1.11.

Figure 1.11: Propagation – Tsunami hitting the Koh Jum island during the event of 26 december 2004. Photo of Anders Grawin (www.kohjumonline.com/anders.html).

This problem was addressed in studies by Glimsdal et al. [2013] or Kirby et al. [2013]. The dispersive effects can be linked to the source parameters as seen in Sections 1.1.1 or 2.4, but as it is a cumulative effect, a characteristic distance L_d, at which the dispersive effects become important, can be defined. Beginning with the dispersion relation obtained in the

general Euler–potential case, $\omega^2 = gk \tanh kh$, the group velocity is defined as

$$C_g = \omega_k = \frac{g(\frac{kh}{\cosh^2 kh} + \tanh kh)}{2\sqrt{gk \tanh kh}}.$$

Where ω_k means $\partial\omega/\partial k$. Then, the distance L_d corresponds to long waves velocity multiplied by the time t_d for which the wave packet is dispersed over the length λ (Levin and Nosov [2009]):

$$L_d = \sqrt{gh}t_d = \frac{\lambda}{1 - \frac{C_g}{\sqrt{gh}}}. \tag{1.10}$$

Thus, after propagated along a distance L_d, the dispersive effects should affect the considered wave train.

Another possibility, that was first explored in the literature then later criticized, is to consider a balance between the dispersive and nonlinear effects and thus to assimilate tsunamis to solitary waves. This assumption was done either during experiments (Liu et al. [1995], Lin et al. [1999], Gedik et al. [2005]) or in theory (Synolakis [1987], Kânoğlu [2004], Madsen and Schaeffer [2010]). Solitary waves are solutions of the Korteweg–de Vries (KdV) equations that are obtained from the Euler equations by considering that nonlinear and dispersive effects balance themselves, in other words: $\epsilon = O(\mu^2)$, see Johnson [1997]. A solitary wave propagates with constant velocity and amplitude. This assimilation for tsunamis came from some observations, among them Russell [1844] and Hammack [1972]. Nowadays, this assumption is contested due to non-conformed geophysical scales between tsunamis and solitons, Madsen et al. [2008], Madsen and Schaeffer [2010].

1.1.3 Run-up

The run-up may be the most important part of tsunamis due to its direct impact on humans. In a wider context, Pelinovsky [1996] defined three types of wave run-ups: spilling when only the crest breaks, plunging when the wave curls and surging when a wave flood arrives on the coast without breaking. These types of wave run-up can be parametrized by the Iribarren number (Battjes [1988]): $I_r = \frac{\tan\beta}{\sqrt{a/\lambda}}$, where λ and a are the wavelength and the wave amplitude far from the coast, and β the slope of the beach, see Figure 1.12.

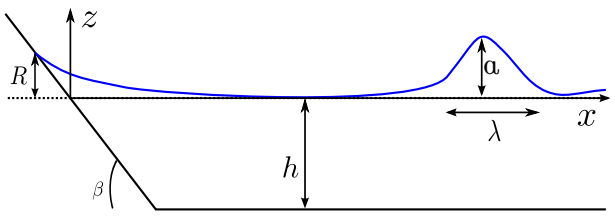

Figure 1.12: Run-up – Geometry and parameters of the model.

The difficulties here come from the strong nonlinearity and the moving boundary (the shoreline). The important contribution of Pelinovsky [1996] lies in the analytical approaches of the run-up problem. In a case of a run-up on a vertical wall ($\beta = 90°$), the run-up R can be estimated by:

$$R = 4h(1 + \frac{a}{h} - \sqrt{1 + \frac{a}{h}}). \tag{1.11}$$

From Equation 1.11, one can see the strong influence of the nonlinear effects $\frac{\eta_0}{h}$ on the run-up. Thus, usually, the Nonlinear Shallow Water Equations are used to model this phenomenon. However Carrier and Greenspan [1958] succeeded to reduce this problem to a linear wave equation, with the so-called Carrier-Greenspan transformation as described below. The domain considered is the same as presented in Figure 1.12, t is the time, u is the vertical averaged horizontal velocity and ℓ a reference length that can be different to λ. The dimensionless variables are:

$$\begin{aligned} x^* &= \tfrac{x}{\ell} \quad h^* = \tfrac{h}{\ell tan\beta} \quad \eta^* = \tfrac{\eta}{\ell tan\beta} \\ u^* &= \tfrac{u}{\sqrt{g\ell tan\beta}} \quad t^* = t\sqrt{g\tfrac{tan\beta}{\ell}} \end{aligned} \tag{1.12}$$

Thus, dropping the * for sake of clarity, the non-dimensional Nonlinear Shallow Water Equations are:

$$u_t + uu_x + \eta_x = 0 \tag{1.13a}$$

$$(u(h+\eta))_x + \eta_t = 0 \tag{1.13b}$$

The Equations 1.13 correspond to the Equations 1.9 by considering a $1D$ domain and that there is not sea floor deformation, $\zeta = 0$. The Carrier-Greenspan transformation is an hodograph transformation in a new domain (σ, γ) with a potential ϕ. The transformation is:

$$\begin{aligned} u &= \tfrac{\partial_\sigma \phi}{\sigma} \\ \eta &= \tfrac{1}{4}\partial_\gamma \phi - \tfrac{1}{2}u^2 \\ x &= \tfrac{1}{16}\sigma^2 - \tfrac{1}{4}\partial_\gamma \phi + \tfrac{1}{2}u^2 \\ t &= u - \tfrac{1}{2}\gamma \end{aligned} \tag{1.14}$$

Applying 1.14 to 1.13, the following linear equation is obtained:

$$\sigma \partial^2_{\gamma\gamma}\phi - \partial_\sigma(\sigma \partial_\sigma \phi) = 0.$$

Its solution is:

$$\phi(\sigma,\gamma) = -\int_0^\infty \int_0^\infty \frac{1}{\omega}\xi^2\Phi(\xi)J_0(\omega\sigma)J_1(\omega\xi)sin(\omega\gamma)d\omega d\xi,$$

with $\Phi(\sigma) = \partial_\gamma u(\sigma,0) = 4\frac{\partial_\sigma \eta(\sigma,0)}{\sigma}$ the initial data, and J_0 and J_1 Bessel functions of the first kind. Thus, the free surface deformation is given by :

$$\begin{aligned}\eta(\sigma,\gamma) &= \frac{1}{4}\partial_\gamma\phi - \frac{1}{2}u^2 \\ &= -\frac{1}{4}\left\{\int_0^\infty \xi^2\Phi(\xi)\int_0^\infty J_0(\omega\sigma)J_1(\omega\xi)cos(\omega\gamma)d\omega d\xi\right\} \\ &- \frac{1}{2}\left\{\int_0^\infty \xi^2\Phi(\xi)\int_0^\infty \frac{J_1(\omega\sigma)}{\sigma}J_1(\omega\xi)sin(\omega\gamma)d\omega d\xi\right\}^2\end{aligned}$$

From here, two major difficulties arise. First, the expression of the initial condition in the (σ,γ) space for which Kânoğlu [2004] proposed a linearisation of the transformation $x \simeq \frac{1}{16}\sigma^2$. And the second difficulty is to obtain the solution for a given time and location. This problem was treated by Synolakis [1987] and then Madsen and Schaeffer [2010]. The latter provided analytical solutions for single wave and $N-waves$ on a plane beach.
Beyond the analytical studies, numerous numerical and experimental works were also performed. The experimental studies cover run-up from a simple wave on plane beach (Synolakis [1987], Li and Raichlen [1998], Li and Raichlen [2003], Jensen et al. [2003]), to more complex bathymetry (Liu et al. [1995], Lynett et al. [2011]), and to more realistic cases as run-up and flood in a city (Liu et al. [2008], Park et al. [2013]). The previous works are often used to validate numerical codes. As detailed by Kânoğlu et al. [2015], the validation process of numerical codes, combining generation, propagation and run-up, is important to justify the use of the latter for real time forecast and alert systems, as well as the elaboration of tsunami scenarios with inundation maps for civil preparedness. Examples of the latter are the work of Borrero et al. [2001] and Borrero et al. [2004]. The authors identified possible seismic and landslide sources and tested them along the Californian coast. Figure 1.13 sums up their results.

1.2 Seismic generation of tsunami

The description of research devoted to tsunamis generated by seismic sources is addressed in this section. Particular attention is given to this kind of event because they are the only source considered in this thesis. First, the seismic process is described in Para-

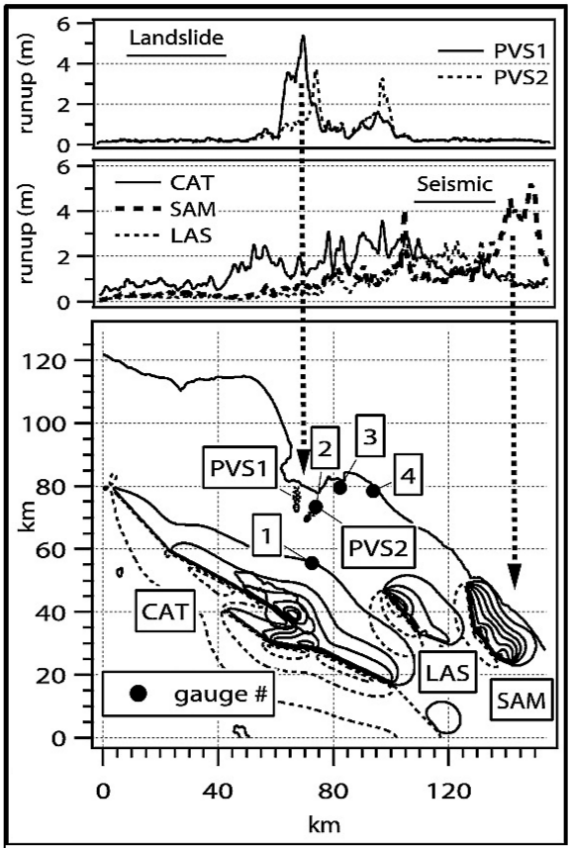

Figure 1.13: Run-up – Inundation studies performed by Borrero et al. [2004] along the Californian coast. Five sources (two landslides and three earthquakes) are identified as possible generation. The estimated run-ups are plotted in the upper graphs while the geographical context is represented in the second figure. The contours plots represent the initial free surface deformation of the hydraulic models, solid for uplift and dashed for subsidence.

graph 1.2.1, before detailing the traditional hydraulic mothod for these kind of events in Paragraph 1.2.2.1. Finally, alternative kinematic models are outlined in Paragraph 1.2.2.2. This last paragraph summerizes the background of Chapters 2 and 3 that focus on the impact of timescale during the generation.

1.2.1 Seismic origin

Among all the tsunamigenic generation mechanisms, the seismic source is far more frequent than the others. Earthquakes take part in the fault life cycle. A fault is a fracture in the Earth crust. The largest faults join the tectonic plates, they are represented on the map in Figure 1.14.

Thus, they behave in function of the tectonic plate motion. The life cycle of a convergent fault, that is the main source of tsunamigenic earthquakes, is represented in Figure 1.15.

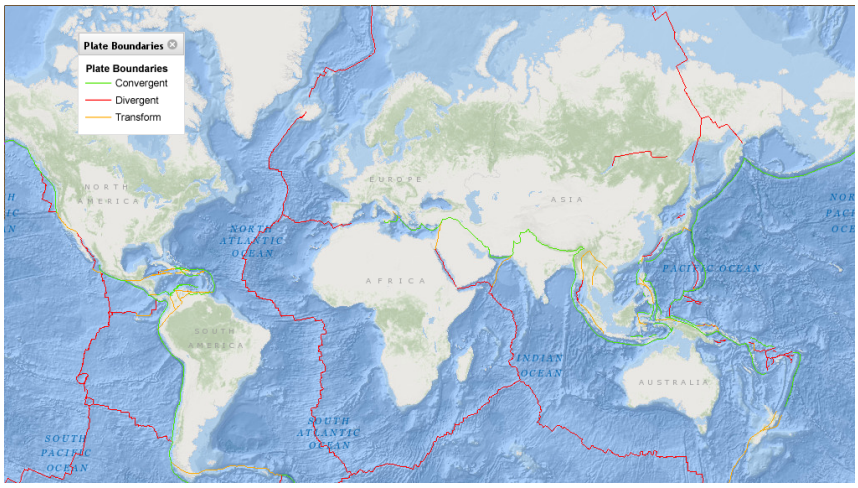

Figure 1.14: Seismic source – World map of the main faults between the tectonic plates available on the website of the NOAA. The red, green and yellow faults correspond to the divergent, convergent and transform motion of the plates respectively.

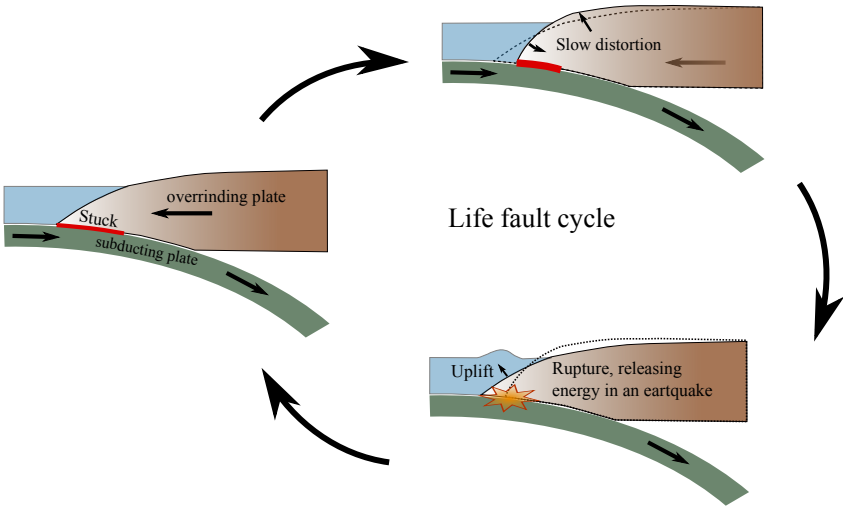

Figure 1.15: Seismic source – Life cycle of a convergent fault with generation of tsunami.

Even if the forces responsible for the plate motions are exerted continuously, initially the fault stays at rest until the stress is too large for the material to handle and causing the latter to rip up. This is the rupture. During this stage, all the conserved energy is suddenly released. Then the fault comes back to a static state and the cycle begins again. Among the parameters defining the rupture, there are the propagation rupture velocity on the fault plane v_p and the rise time t_f. Special attention is paid to this rise time, that is the duration of the rupture at one point of the fault plane. It is a seismic rise time and is different from the hydraulic rise time defined later. The rupture velocity v_p permits to identify different types of earthquakes. For ordinary earthquake $v_p \in [1, 10] km/s$, but slower events exist:

slow earthquake or tsunami earthquake (Kanamori [1972]) with $v_p \in [0.1, 1]km/s$ and silent earthquake with $v_p \in [0.01, 0.1]km/s$ have already been observed. A tsunami event of a slow earthquake will be studied in Chapter 3.
Not all the earthquakes generate a tsunami. Indeed the water perturbation is created by the ground motion, that depends on the energy released and on the fault depth. Usually, an earthquake of magnitude 6 is at least necessary to cause a deformation of the sea floor.

1.2.2 Hydraulic models

Nosov [2014] gave a complete review of the physical processes that interact during a seismic tsunami event, but also of forecasting and recording systems. In the present section, the traditional way to model this kind of events will be first approached before focusing on the generation kinematics.

1.2.2.1 Traditional way to model seismic tsunami

For a seismic generation, the tsunami is triggered by the spatiotemporal deformation of the sea floor. This generation has been the subject of numerous studies and several models have been developed as explained below. Usually, to model the generation of a tsunami, a data inversion is first performed. This inversion permits from seismic (mostly) or hydraulic information, measured by gauges or satellites, to recover some characteristics of the source. The magnitude, epicenter, slip amplitude and main geometrical parameters of the fault are usually determined by inversion directly, see Ji et al. [2002], Shao et al. [2011], Yagi and Fukahata [2011a].
The second step is to calculate, from the source parameters, the vertical deformation of the sea floor. It is important to represent precisely these deformations because they directly trigger the wave. A famous model is the one of Okada [1992] that calculates the deformation in the ground from the seismic data using the elasticity theory in a idealised homogeneous half-space (corresponding to the crust). In Figure 1.16, a sketch of the domain with the main parameters is represented.

The fault is considered as a finite rectangle of length L, width W and situated at a depth d in the ground. The axis O_x is parallel to the fault. The block motion is represented by the Burger vector $D = (U_1, U_2, U_3)$, U_i being the elementary motion. Four angles are defined: the strike angle φ, the dip angle δ, the rake or slip angle θ, and γ the angle between D and the fault plane. From these parameters, the calculations performed by Okada permit to find the vertical displacement of the sea floor surface, see Okada [1992] or Levin and Nosov [2009] for detail and the final solution.
However, seismic events are not made of a unique fault that is moreover considered as a rectangle. To better represent the complexity of the ground dynamics, a finite fault model

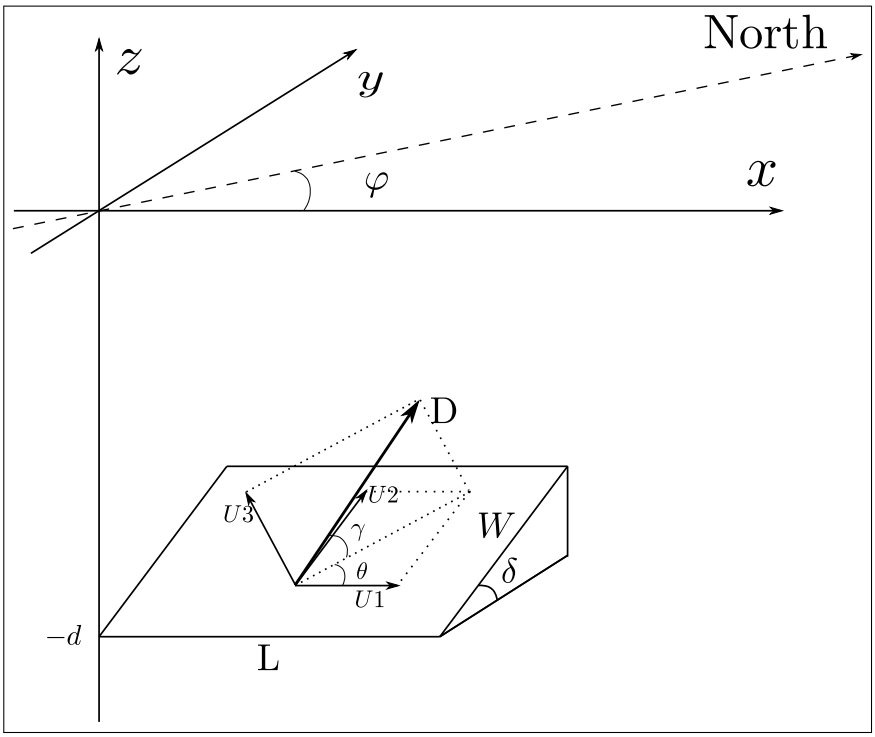

Figure 1.16: Seismic tsunami source – Definition of the geometrical parameters of the fault for the Okada method.

is prefered as described and suggested by Ji et al. [2002], Yagi [2004] or Dutykh et al. [2013]. The aim is to create not a single fault but a patch of small faults (subfaults) with their own characteristics. An example, issued from the work of Satake et al. [2013], is illustrated in Figure 1.17. It represents the finite fault model proposed for the event of Tohoku, 2011 in Japan.

Once the vertical deformation of the sea floor is calculated, the last part of the seismic generation modeling process is to assume that the initial perturbation of the free surface is equal to the final vertical perturbation sea floor. Thus the initial condition is given by this free surface deformation with a null velocity field, which then propagates in the considered spatial domain. This traditional approach neglects a certain number of effects as horizontal displacements, compressibility of water, nonlinear effects, rotation of the Earth and dynamics of the bottom deformation, see Nosov [2014]. The present work only concerns the impact of some timescale parameters as described in the next paragraph and Chapter 2.

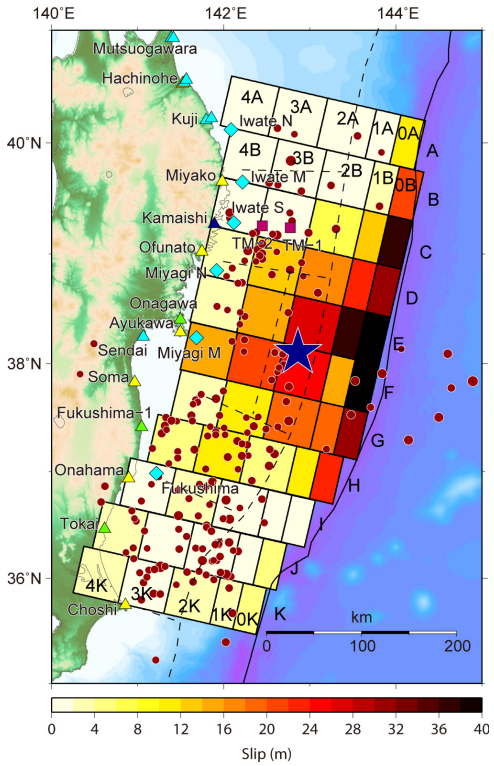

Figure 1.17: Seismic tsunami source – Finite fault model proposed by Satake et al. [2013] to represent the generation of the Tohoku event, 2011 in Japan. The blue star is the epicenter and red dots are secondary earthquakes.

1.2.2.2 Kinematics seismic generation of tsunami

The influence of the temporal history of the bottom on the waves has been studied several times. However, the authors usually took into account only one temporal parameter, the rise time t_r or the rupture velocity v_p. The rise time concerns the time of the vertical elevation of the bottom deformation; it is the hydraulic rise time. The rupture velocity is the speed of the evolution of the deformation on the horizontal direction (in our case along the fault).
One of the major contributions about the influence of the rise time t_r is the work from Hammack [1973]. The author confronted an experimental study and an analytical solution from a linearised theory about the wave generation by a moving up or down a 1D step at different velocities and temporal displacement histories. In Figure 1.18, the geometry of the domain and the experimental set up are represented. This experiment was chosen as a test case for the TANDEM project benchmark, thus a more complete description of the case will be presented in Section 4.3.

One of the main conclusions of the approach of Hammack is the definition of three dimensionless parameters: $\frac{\zeta_0}{h}$, $\frac{b}{h}$ and $\frac{t_r\sqrt{gh}}{b}$, where h is the uniform depth, b is the width of the

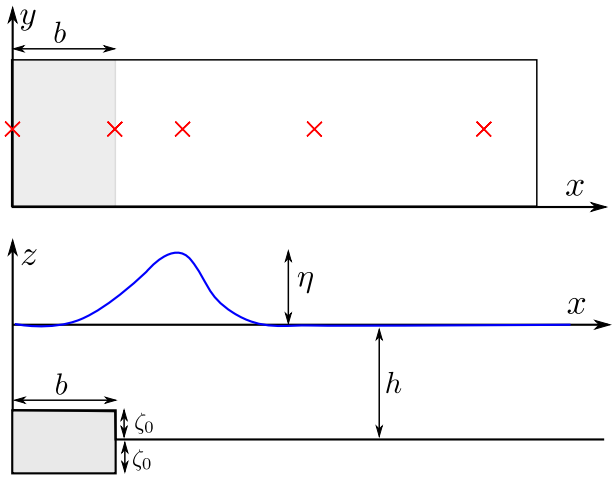

Figure 1.18: Kinematic generation – Geometry of the experiment of Hammack [1973], not at scale. The top frame is a top view and the bottom frame is a side view. The gray zone is the moving area of length b. The red crosses are locations of measurement gauges.

step, see Figure 1.18. He also characterised the velocity of the motion: when $\frac{t_r\sqrt{gh}}{b} \ll 1$, the motion is so-called impulsive while when $\frac{t_r\sqrt{gh}}{b} \gg 1$, the motion is creeping. From these parameters, Hammack estimated thresholds for which the linear theory accurately represents the wave generation. Besides, the study was done for two kinds of motions. It appears that for impulsive motions, the wave structure is equivalent to the shape deformation and does not depend on the time displacement history, contrary to the creeping motion, see Figure 1.19. This conclusion will be used in Chapter 3: the displacement history chosen to represent the ground motion of the event should not impact the result.

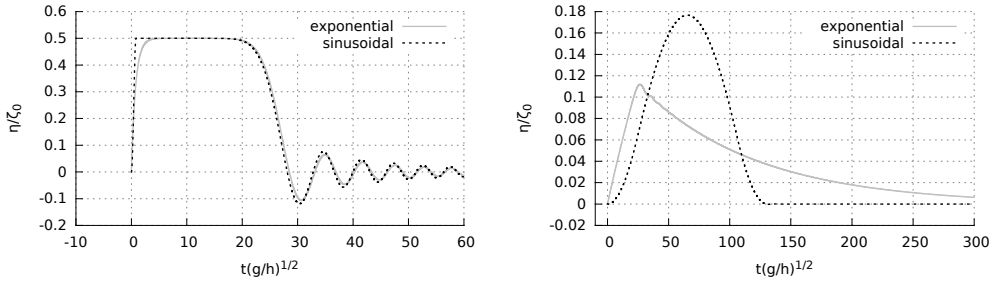

Figure 1.19: Kinematic generation – Free surface elevation comparison at $\frac{x}{h} = \frac{b}{h}$ between the exponential and the sinusoidal time history deformation for an impulsive motion (left) and a creeping motion (right). The geometrical parameters are: $b/h = 12.2$, $\zeta_0/h = 0.2$, $t_r\sqrt{gh}/b = 0.069$ for the impulsive motion and $t_r\sqrt{gh}/b = 106.14$ for the creeping motion. The figure is adapted from the work of Hammack [1973].

Hammack [1973] also remarked that the maximal elevation reached by the wave at the edge of the generation and propagation zones remains constant for impulsive motion while

for creeping motion, this maximum decreases proportionally to $\frac{t_r\sqrt{gh}}{b}$. Hammack only considered the so-called "piston" motions, meaning with residual displacement. Later, Dotsenko and Soloviev [1995] and Levin and Nosov [2009] developed also theory about "membrane" motions, meaning that the sea floor comes back to its initial position at the end of the deformation. Both works showed differences between the two types of motion. By comparing the energies, they concluded that for oceanic conditions, "piston" motions are more energetic while for small generation area or large depth, the "membrane" motions are stronger. However, important tsunamis are usually initiated by "piston" motion. More recently, Stefanakis et al. [2015] and Jamin et al. [2015] gave more details on the impact on generated waves of a cylindrical piston. The first, using a theoretical approach, showed a wave trapping phenomenon that can also be associated to seamount. The authors of the second work built up an experimental study and highlighted that the motion of the sea floor is transferred to the sea surface through temporal high-pass and spatial low-pass filters properties.

Another parameter that deserved investigation is the rupture velocity v_p. In this thesis, the work of reference is the one from Todorovska and Trifunac [2001]. As done by Hammack [1973] with the parameter t_r, the authors developed a 2D solution for a linearised system taking into account this parameter v_p. The domain they considered is represented in Figure 1.20.

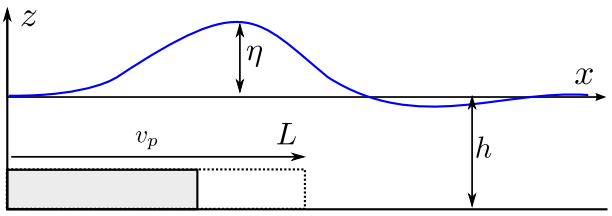

Figure 1.20: Kinematic generation – Geometry of the domain considerated by Todorovska and Trifunac [2001] at a time smaller than the generation duration. The solid line is the instant deformation (propagation at velocity v_p) while the dashed line is the final deformation. The graph is a vertical cut of their 2D domain.

As emphasized also by Lee et al. [1989] and Levin and Nosov [2009], a Froude number $v_p^* = v_p/\sqrt{gh}$ can be identified. When v_p^* tends to 1, the authors noted a wave focusing phenomenon that provided a wave larger than the ground deformation. Besides the dependency on the rupture velocity, this amplification and the amplitude wave maximum vary with the size of the deformation: larger the size, larger the amplification is. This study corresponds to a particular case of the problem addressed in the Chapter 2, thus more details will be given there.

For now, only simplified deformations have been presented, however the long term aim of these studies is to improve the numerical tsunami model for real cases, taking into

account the different aspects of a kinematic generation. In their study, Dutykh et al. [2013] proposed the use of the finite fault model to introduce the temporal deformation. Instead of simply superposing the contribution of each subfaults, the latter are triggered as a function of the rupture velocity v_p and for each subfault, the deformation $\zeta(\boldsymbol{x}, t)$ is then controlled by the rise time t_r:

$$\zeta(\boldsymbol{x}, t) = \sum_{i=1}^{N} H(t - t_i) T(t - t_i) O_i(\boldsymbol{x}) \tag{1.15}$$

Where N is the number of subfaults, $O_i(\boldsymbol{x})$ is the amplitude of the deformation calculated with Okada method for subfault i. The activation time t_i corresponds to the rupture starting time of the subfault deduced from the rupture velocity v_p. H is the Heaviside step function. $T(t)$ corresponds to the temporal history of the deformation:

$$T(t) = H(t - t_r) + \frac{1}{2} H(t) H(t_r - t)(1 - \cos(\pi t / t_r)).$$

Dutykh et al. applied this method to the Java 2006 tsunami event and compared the numerical result of the static and kinematic method at some gauges as presented in Figure 1.21. From this study, it clearly appears that taking into account the kinematic deformation influences the results.

An alternative to improve the generation model is to use a Finite Element Model (FEM) of the subduction zone considered. This method was first proposed by Masterlark and Hughes [2008] for the 2004 Sumatra-Anderman earthquake and then also used by Romano et al. [2014] and Grilli et al. [2013] for the 2011 Tohoku event. The principle of this method is to couple the hydraulic model to a 3D FEM that simulates the deformation in the crust. For the model used by Masterlark and Hughes [2008] and Grilli et al. [2013], the developed FEM permits the authors, besides to impose a time sequence, to construct different regions with different material properties, taking into account the forearc of the trench and the inhomogeneities of the subduction zone as illustrated in Figure 1.22.

In their work, Grilli et al. [2013] compared the numerical free surface elevations issued from the coupled model to the only hydraulic model (with the generation model of Shao et al. [2011]) with a traditional generation at GPS buoys near the Japan and far field DART buoys. The authors concluded by finding a better agreement between the coupled model and the data than the traditional model. More recently, Ide and Aochi [2014] proposed to use a fractal circular patch models to better describe the rupture propagation. However, these latter works are complex and more expensive to calculate. They need the development of a new coupled model while the proposition of Dutykh et al. [2013] with the kinematic finite fault method is easier to apply.

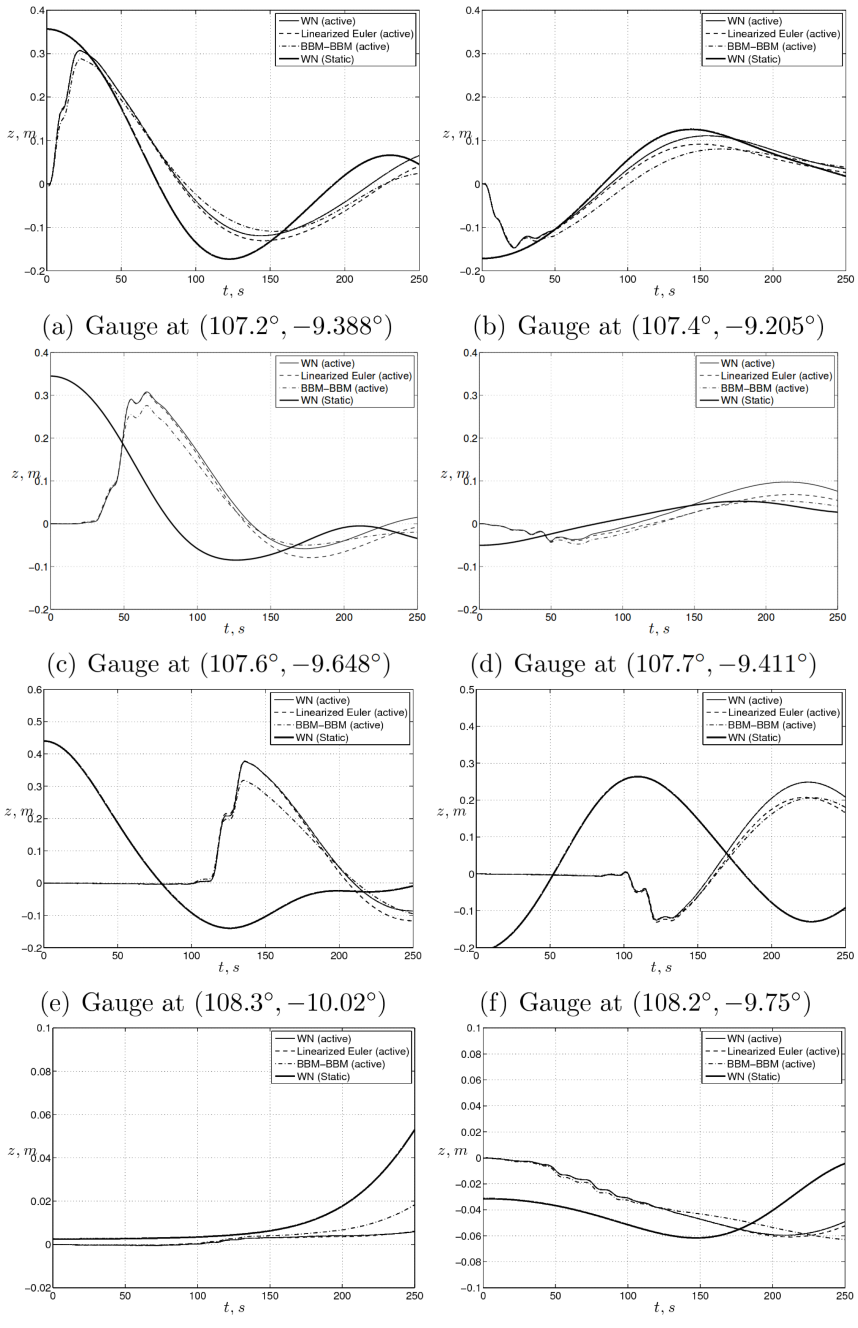

(a) Gauge at $(107.2°, -9.388°)$ (b) Gauge at $(107.4°, -9.205°)$

(c) Gauge at $(107.6°, -9.648°)$ (d) Gauge at $(107.7°, -9.411°)$

(e) Gauge at $(108.3°, -10.02°)$ (f) Gauge at $(108.2°, -9.75°)$

(g) Gauge at $(108°, -10.5°)$ (h) Gauge at $(108°, -9°)$

Figure 1.21: Kinematic generation – Numerical results obtained by Dutykh et al. [2013] (Figure adapted from their work). The free surface elevation is measured at different gauges and compared between static generation model (solid thick line, model WN static) and kinematic generation model (dashed and blurred line, models WN (active), linearized model and BBM–BBM).

In the next chapter, Chapter 2, the works of Hammack [1973] and Todorovska and Trifunac [2001] are combined and extended. A new analytical version of an 1D idealised

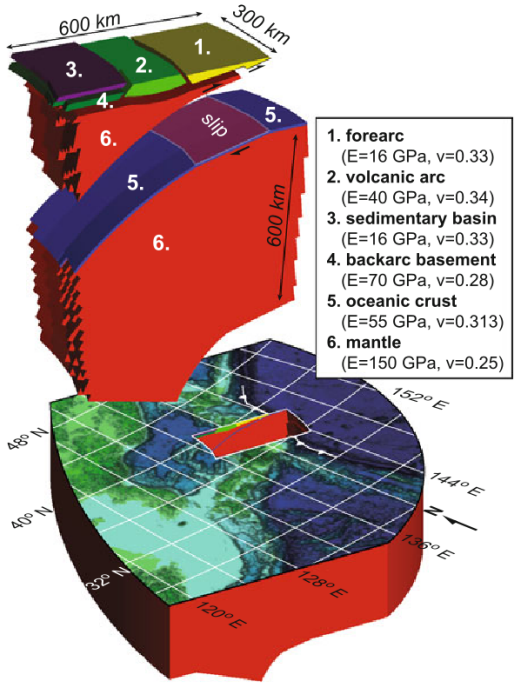

Figure 1.22: Kinematic generation – Numerical domain defined by Grilli et al. [2013] for the subduction zone that is resolved by the FEM. The different part of the domain has their own material properties. Figure issued from the above-cited study.

deformation of the sea floor is defined depending on the rise time t_r and the rupture velocity v_p. Thus, the cases studied by Hammack [1973] and Todorovska and Trifunac [2001] are particular cases of the new deformation. Similar to their works, a theoretical linear solution is developed to measure the impact of simultaneously both parameters and the influence that has one on the other. To go further, this study is also performed by a theoretical Linear Shallow Water model and an accurate numerical nonlinear model. To illustrate this study, a real event is simulated in Chapter 3. In this case the kinematic finite fault model suggested by Dutykh et al. [2013] will be chosen, due to its simplicity.

Chapter 2

Theoretical study

Dans le cadre de la théorie potentielle et linéaire d'un écoulement, une solution semi-analytique est développée pour la génération de vagues de type tsunamis, par une déformation cinématique du fond. Cette déformation est idéalisée et représente une déformation simplifiée généralement engendrée par certains séismes. Cette étude tend à étendre le travail déjà fourni par Hammack [1973] et Todorovska and Trifunac [2001] en prenant en compte simultanément deux paramètres temporels de la déformation, respectivement, le temps d'élévation t_r et la vitesse de propagation de rupture v_p. Le premier paramètre t_r correspond au mouvement vertical, tandis que v_p caractérise le mouvement horizontal du fond. L'influence de ces deux paramètres est mesurée en calculant la solution linéaire théorique pour un large panel de valeurs. Deux aspects de la génération sont étudiés par la définition de deux ratios : le premier est le rapport entre l'amplitude maximale de la déformation de la surface libre et l'amplitude de la déformation du fond, et le deuxième est un ratio énergétique évaluant la quantité d'énergie potentielle mal estimée par les approximations de la théorie des ondes longues. Ainsi, une zone de résonance a pu être identifiée en fonction de v_p et t_r pour laquelle l'amplitude de la vague générée peut être beaucoup plus importante que celle de la déformation, tandis que des phénomènes dispersifs apparaissent remettant en question l'utilisation des équations de Saint-Venant pour ces valeurs particulières de paramètres temporels. La résonance de l'amplitude avait déjà été identifiée mais seulement en fonction de v_p par Todorovska and Trifunac [2001]. De plus, une relation empirique est proposée en fonction de la longueur de déformation. Une étude numérique a permis de généraliser ce phénomène de résonance en étendant ce résultat à des modèles dispersifs et non-linéaires. Pour illustrer cette étude et ce comportement, on simule l'évènement qui a eu lieu en 1947 en Nouvelle Zélande, dont les échelles temporelles correspondent à la zone de résonance, afin de voir l'impact que peut avoir cette résonance souvent négligée par les modèles de tsunamis.

2.1 Dimensional analysis

In order to identify the dominant parameters of schematic seismic tsunami generation, a dimensional analysis is first applied. The considered fluid domain is presented in Figure 2.1. The analysis is limited to one horizontal direction, with an unbounded domain in the wave propagation direction x. The same assumptions considered in Section 1.1.2 are applied here, *i.e.* no-viscous and incompressible fluid, irrotational flow, no-tension surface and no Coriolis effects. The fluid is bounded above by the free surface at $z = \eta(x,t)$, and below by the sea bottom at $z = -h + \zeta(x,t)$, where h is the initial water depth and ζ the deformation of the sea bottom. Initially, the fluid is at rest, with a flat free surface and bottom: $\eta(x, t = 0) = 0$ and $\zeta(x, t = 0) = 0$.

To simplify the problem, the ground motion can be reduced to an uplift of a rectangular

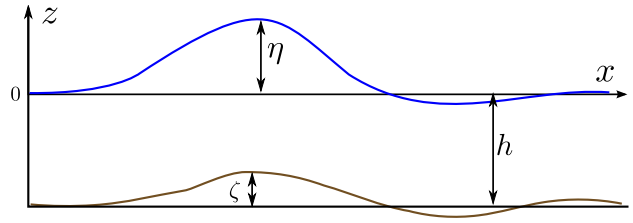

Figure 2.1: Definition of the fluid domain and coordinate system (x, z), with h the initial depth, $\zeta(x,t)$ the deformation of the sea floor and $\eta(x,t)$ the deformation of the free surface.

block that propagates with a given velocity v_p along the x axis for $x \in [0; L]$. The vertical deformation reaches the maximum amplitude ζ_0 in a finite time, the rising time t_r, along the z axis. Figure 2.2 gives a schematic representation of this movement. In Section 2.2.2, we will analyse the case of a sinusoidal rise motion.

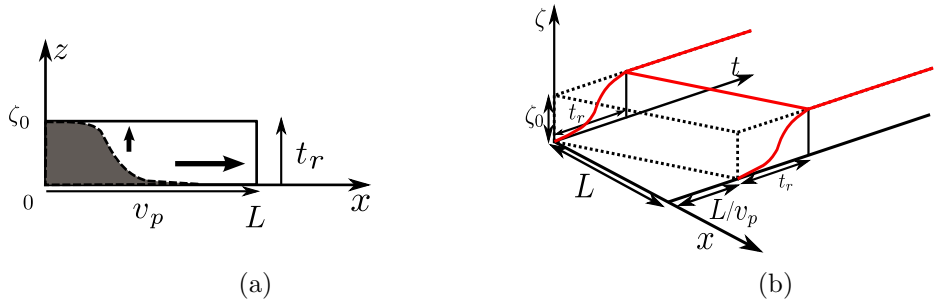

(a) (b)

Figure 2.2: Definition of the sea floor uplift $\zeta(x,t)$: 2.2a spatial profile of the sea floor and 2.2b, the black dashed lines represent the motion defined by Todorovska and Trifunac [2001], and the solid red lines are the motion used in this study.

The movement of the sea bottom is defined by the parameters: ζ_0, t_r, L and v_p. The variables of the problem in the gravity field g are these four parameters with the free surface

Variables	η	h	g	ζ_0	t_r	L	v_p
units	$[m]$	$[m]$	$[m.s^{-2}]$	$[m]$	$[s]$	$[m]$	$[m.s^{-1}]$

Table 2.1: Variables and units of the problem.

elevation η and the water depth h. The Vaschy-Buckingham, or Π theorem [see Buckingham, 1914; Vaschy, 1892] is used to identify the non-dimensional parameters. There are two independent units (time $[s]$, and space $[m]$) and seven variables summarised in Table 2.1. Thus five non-dimensional variables can be defined:

$$\begin{aligned} \eta^* &= \tfrac{\eta}{h}, & \zeta_0^* &= \tfrac{\zeta_0}{h} \\ t_r^* &= t_r\sqrt{\tfrac{g}{h}}, & L^* &= \tfrac{L}{h} \\ v_p^* &= \tfrac{v_p}{\sqrt{gh}}. \end{aligned} \tag{2.1}$$

To be consistent with previous studies, the non-dimensional temporal parameters are $\tau^* = \frac{t_r^*}{L^*} = \frac{t_r}{L}\sqrt{gh}$, as chosen by Hammack [1973] and v_p^*, as in Todorovska and Trifunac [2001]. τ^* represents the ratio between the vertical timescale t_r and the time that the wave takes to propagate over the distance of deformation L, and v_p^* is the ratio between the horizontal timescale v_p and the long wave celerity $c = \sqrt{gh}$. The free surface elevation depends on x and t, thus non-dimensional space and time: $x^* = \frac{x}{h}$ and $t^* = t\sqrt{\frac{g}{h}}$ should be included in the parameters of the system. We will thus seek to express the free surface elevation as:

$$\eta^* = \Phi\left(\zeta^*, L^*, \tau^*, v_p^*, t^*, x^*\right). \tag{2.2}$$

In this study, the effects of both τ^* and v_p^* are investigated. Hammack [1973] worked only on the effects of τ^*, and Todorovska and Trifunac [2001] only on the effects of v_p^*. In this study, the effects of both τ^* and v_p^* are simultaneously investigated. Note that Dutykh [2007] also studied the impact of the Ursell number, defined by $S = \eta^* L^{*2}$ with our notations.

Usually, the horizontal dimension of the seismic source exceeds the water depth: $L^* \gg 1$. Based on the analysis of past events, L^* can vary between 16 as for the 1946 Aleutian event [Johnson and Satake, 1997] and 300 as for the 2004 Sumatra-Andaman event [Fujii and Satake, 2007]. If the wavelength of the generated wave is considered equivalent to L as suggested by Levin and Nosov [2009] and Wu [1981], L^* varies between 10 and 5000 in deep ocean [Wu, 1981]. Then, a long wave theory could be used to study long waves in the spectrum of the tsunami, as done by Wu [1981] among others, but we will not restrict ourselves to this assumption in this work. Moreover, the drawback of such an approach will be discussed in section 2.4 with the analysis of consequences implied by the Shallow Water approximation. The present study will not consider any restriction on the wave lengths and periods. The particular case of long waves is investigated in Section 2.6.

2.2 Linear theory

2.2.1 Methodology

We review here the method presented by Hammack [1973] and also described by Todorovska and Trifunac [2001] and Dutykh [2007], among others. We consider the motion of the fluid domain defined in the previous section. Since the fluid is assumed to be incompressible and the flow irrotational, there exists a velocity potential $\phi(x, z, t)$ that satisfies the Laplace equation and the boundary conditions as follows:

$$\bigtriangledown^2\phi = 0, \tag{2.3a}$$

$$\phi_z = \eta_t + \phi_x\eta_x \qquad z = \eta(x,t), \tag{2.3b}$$

$$\phi_t + \tfrac{1}{2}|\bigtriangledown\phi|^2 + g\eta = 0 \qquad z = \eta(x,t), \tag{2.3c}$$

$$\phi_z = \zeta_t + \phi_x\zeta_x \qquad z = -h + \zeta(x,t), \tag{2.3d}$$

where subscripts t, x indicate partial derivatives. Equations 2.3b and 2.3c are the kinematic and dynamic free surface boundary conditions, respectively, and equation 2.3d is the kinematic bottom boundary condition. By assuming small perturbations of the free surface and the bottom, the boundary conditions are linearised and the previous system of equations becomes:

$$\bigtriangledown^2\phi = 0, \tag{2.4a}$$

$$\phi_z = \eta_t \qquad z = 0, \tag{2.4b}$$

$$\phi_t + g\eta = 0 \qquad z = 0, \tag{2.4c}$$

$$\phi_z = \zeta_t \qquad z = -h. \tag{2.4d}$$

Note that the three linearised boundary conditions now apply at the undisturbed horizontal surfaces, *i.e.* at $z = 0$ for 2.4b and 2.4c and $z = -h$ for 2.4d. Combining 2.4b and 2.4c, the following free surface boundary condition is obtained:

$$\phi_{tt} + g\phi_z = 0 \quad \text{at} \quad z = 0. \tag{2.5}$$

The 1D space Fourier transform of a function $f(x)$ is defined as:

$$\mathscr{F}(f) = \hat{f}(k) = \int_{\mathbb{R}} f(x)e^{-ikx}dx, \tag{2.6}$$

$$\mathscr{F}^{-1}(\hat{f}) = f(x) = \frac{1}{2\pi}\int_{\mathbb{R}} \hat{f}(k)e^{ikx}dk, \tag{2.7}$$

and the Laplace transform of $f(t)$ for $t > 0$ is:

$$\mathscr{L}(f) = \mathbf{f}(s) = \int_0^{+\infty} f(t)e^{-st}dt, \tag{2.8}$$

$$\mathscr{L}^{-1}(\mathbf{f}) = f(t) = \frac{1}{i2\pi}\int_{\gamma-i\infty}^{\gamma+i\infty} \mathbf{f}(s)e^{st}ds, \tag{2.9}$$

where γ is a real constant that insures the existence of the integral. Following Hammack [1973], the Laplace-Fourier transform is built for a function $f(x,t)$ combining these two transforms:

$$\mathscr{F}\mathscr{L}(f) = \bar{f}(k,s) = \int_{\mathbb{R}} e^{-ikx}dx \int_0^{+\infty} f(x,t)e^{-st}dt, \tag{2.10}$$

$$\mathscr{F}\mathscr{L}^{-1}(\bar{f}) = f(x,t) = \frac{1}{2\pi}\int_{\mathbb{R}} e^{ikx}\frac{1}{i2\pi}\int_{\gamma-i\infty}^{\gamma+i\infty} \bar{f}(k,s)e^{st}dkds. \tag{2.11}$$

This transform is applied to the system 2.4a, 2.4d, 2.5, giving:

$$\bar{\phi}_{zz} - k^2\bar{\phi} = 0, \tag{2.12a}$$

$$\bar{\phi}_z = -\tfrac{s^2}{g}\bar{\phi} \qquad z = 0, \tag{2.12b}$$

$$\bar{\phi}_z = s\bar{\zeta} \qquad z = -h, \tag{2.12c}$$

$$s\bar{\phi} = -g\bar{\eta} \qquad z = 0. \tag{2.12d}$$

This system can be solved analytically in (k,s) space to obtain:

$$\bar{\phi}(k,z,s) = \frac{-sg\bar{\zeta}(k,s)}{\cosh kh[s^2 + gk\tanh kh]}\left[\cosh kz - \frac{s^2}{gk}\sinh kz\right], \tag{2.13}$$

thus,

$$\bar{\eta}(k,s) = \frac{s^2\bar{\zeta}(k,s)}{(s^2+\omega^2)\cosh kh}, \tag{2.14}$$

where

$$\omega = \sqrt{gk\tanh kh}$$

is the linear dispersion relation.
The final formula for the free surface deformation as a function of the bottom deformation is obtained in the physical space by taking the inverse Fourier–Laplace transform of 2.14:

$$\eta(x,t) = \frac{1}{2\pi}\int_{\mathbb{R}} \frac{e^{ikx}}{\cosh kh}\frac{1}{i2\pi}\int_{\gamma-i\infty}^{\gamma+i\infty} \frac{s^2\bar{\zeta}(k,s)e^{st}}{(s^2+\omega^2)}dsdk. \tag{2.15}$$

2.2.2 Solution for a schematic uplift

To go further we need to choose a schematic bed deformation $\zeta(x,t)$. Of special interest in the present study is the impact of t_r and v_p, as described in section 2. The area of

deformation is a segment of length L, horizontally deformed at the velocity v_p and taking a time t_r of uplift. This leads to:

$$\begin{aligned}\zeta(x,t) &= \zeta_0 H(L-x)H(x)\mathscr{T}(x,t) && (2.16)\\ \mathscr{T}(x,t) &= H(t-\frac{x}{v_p})H(\frac{x}{v_p}+t_r-t)\frac{1}{2}(1-\cos\omega_r(t-\frac{x}{v_p})) && (2.17)\\ &\quad +H(t-\frac{x}{v_p}-t_r), && (2.18)\end{aligned}$$

where $\omega_r = \frac{\pi}{t_r}$. Unlike Hammack [1973] or Todorovska and Trifunac [2001], both parameters are included in the present definition of $\mathscr{T}(x,t)$. This definition coincides with that of Hammack [1973] when $v_p \to \infty$ (*i.e.* the horizontal movement of the bottom deformation is assumed to occur instantaneously). On the other hand, if t_r vanishes (*i.e.* instantaneous vertical displacement), this definition corresponds to the 1D solution of Todorovska and Trifunac [2001].

The Laplace-Fourier transform 2.10 is applied to ζ, and we find:

$$\bar{\zeta}(k,s) = \frac{\zeta_0}{2}(1+e^{-st_r})\frac{\omega_r^2}{s(s^2+\omega_r^2)}\frac{1-e^{-L(ik+\frac{s}{v_p})}}{ik+\frac{s}{v_p}}, \tag{2.19}$$

Substituting $\bar{\zeta}$ into 2.14, we obtain:

$$\bar{\eta}(k,s) = \frac{\zeta_0}{2}\frac{s}{(s^2+\omega^2)\cosh kh}(1+e^{-st_r})\frac{\omega_r^2}{s^2+\omega_r^2}\frac{1-e^{-L(ik+\frac{s}{v_p})}}{ik+\frac{s}{v_p}}. \tag{2.20}$$

From here, only the Fourier transform of η, $\tilde{\eta}$, can be found analytically. The analytical solution of the integration over k can only be performed in particular cases or by invoking some approximations, see Mei et al. [2005]. This limitation is due to the complexity of the expression associated to the dispersion relation. To determine $\tilde{\eta}$, we used the inverse Laplace transform and its properties (details of the calculations can be found in A). The non-dimensional variables are noted with *. We define: $k^* = kh$ in addition to the definitions 2.1, leading to:

$$\tilde{\eta}^*(k^*,t^*) = \frac{\zeta_0^*}{2}\frac{v_p^*}{\cosh k^*}\frac{\omega_r^{*2}}{\omega_r^{*2}-\omega^{*2}}\begin{pmatrix} f^*(k^*,t^*) \\ +H(t^*-t_r^*)f^*(k^*,t^*-t_r^*) \\ -H(t^*-\frac{L^*}{v_p^*})e^{-ik^*L^*}f^*(k^*,t^*-\frac{L^*}{v_p^*}) \\ -H(t^*-t_r^*-\frac{L^*}{v_p^*})e^{-ik^*L^*}f^*(k^*,t^*-t_r^*-\frac{L^*}{v_p^*}) \end{pmatrix}, \tag{2.21}$$

where:

$$f^*(k^*,t^*) = \begin{array}{l} \frac{1}{\omega^{*2}-k^{*2}v_p^{*2}}\left(ik^*v_p^*\cos\omega^*t^* + \omega^*\sin\omega^*t^* - ik^*v_p^*e^{-ik^*v_p^*t^*}\right) \\ -\frac{1}{\omega_r^{*2}-k^{*2}v_p^{*2}}\left(ik^*v_p^*\cos\omega_r^*t^* + \omega_r^*\sin\omega_r^*t^* - ik^*v_p^*e^{-ik^*v_p^*t^*}\right). \end{array} \tag{2.22}$$

And the non-dimensional free surface is:

$$\eta^*(x^*,t^*) = \frac{1}{2\pi}\int_R e^{ik^*x^*}\tilde{\eta}^*dk^*. \tag{2.23}$$

Again, one can verify that if t_r tends to 0, this solution tends to the 1D solution of Todorovska and Trifunac [2001], and if v_p tends to infinity, the solution of Hammack [1973] is recovered. As previously stated, this integral is difficult to perform or cannot be performed in a closed form, thus a numerical inverse Fourier transform is used to obtain the resulting free surface $\eta(x,t)$. In particular in this study, the integral is calculated numerically using Simpson's method.

2.2.3 Treatment of singularities

We note that the previous solution (2.21-2.23) of the Fourier transform of the free surface has some singularities that should be addressed. For this purpose, we take the limit of $\tilde{\eta}^*$ at the critical values of k^*, defined by:

1. $k_1^* = \pm\sqrt{\frac{\omega_r^*}{v_p^*}}$,
2. $k_{2a}^* = 0$,
3. if $|v_p^*| < 1$, $k_{2b}^* = p^{-1}(\frac{1}{v_p^{*2}})$,
4. $k_3^* = q^{-1}(\omega_r^*)$,

where $p(x) = \frac{x}{\tanh x}$ and $q(x) = gx\tanh x$. The limits are computed in Appendix B. Figure 2.3 shows an example of these critical wavenumbers in the spectrum. One can see that $|\tilde{\eta}^*|$ remains continuous everywhere.

2.3 Free surface deformation analysis

The linear solution derived in the previous section is now used to study the wave trains generated by a dynamical bottom deformation of the form 2.16. First (Section 2.3.1), the impact of the temporal parameters is investigated by looking the free surface deformation at the end of the ground motion, then particularly by looking the maximum amplitude in

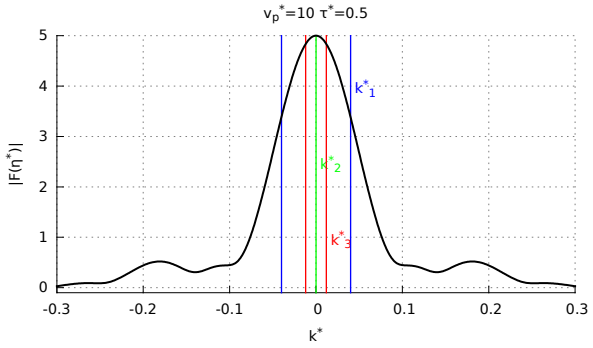

Figure 2.3: An example of the free surface Fourier transform $\tilde{\eta}^*$ with critical k^* for $v_p^* = 10$ and $\tau^* = 0.5$ at $t^* = T^* = \frac{L^*}{v_p^*} + t_r^*$. The black line is the modulus of the Fourier transform $|\tilde{\eta}^*|$. The vertical blue, green and red lines represent the locations of the singularities k_1^*, k_2^*, k_3^*, respectively.

x. In a second step (Section 2.3.2), the propagation of the wave is studied in order to see if the impact of v_p^* and τ^* remains during this stage. Section 4.3. addresses the comparisons of the previous developed solution and numerical results from the code Misthyc. At this point of the study, these comparisons permit to validate the solution obtained with the calculations from the theory.

2.3.1 At the end of the bottom deformation

By convention, we define the end of the generation period (and thus the beginning of the propagation period) as the time when the sea floor stops moving, or $t^* = T^* = \frac{L^*}{v_p^*} + t_r^*$. In the following analysis, the geometric parameter representing the horizontal extent of the bottom deformation is chosen as $L^* = 50$. Since the model is linear, the value of ζ_0^* is not important (provided it is small), and therefore all subsequent results will show the ratio η^*/ζ_0^*. The horizontal velocity v_p^* is varied between 0.5 and 50, and the rising time τ^* is varied between 0 and 5. As an example, if the dimensions of the 1992 Nicaragua event are considered [Satake, 1994], $L = 250$ km in an ocean of depth $h = 5$ km, the dimensionless numbers correspond to rupture velocities $v_p \in [110; 11000]$ m.s^{-1} and rise times $t_r \in [0; 5644]$ s.

Figure 2.4 shows the free surface profiles for: $v_p^* = 0.5$, 1, 2, 10 and 50, and $\tau^* = 0$, 1 and 2. The maximum free surface elevation η_{max}^*/ζ_0^* varies with v_p^* and τ^*. If $v_p^* = 50$ (*i.e.* very large) and $\tau^* = 0$, the free surface deformation is almost identical to the sea floor deformation (*i.e.* $\eta_{max}^*/\zeta_0 \simeq 1$) since the deformation is nearly instantaneous in both horizontal and vertical directions. When τ^* increases, the wave begins to propagate before the end of the ground motion as noted by Jamin et al. [2015], the wave amplitude is smaller, and

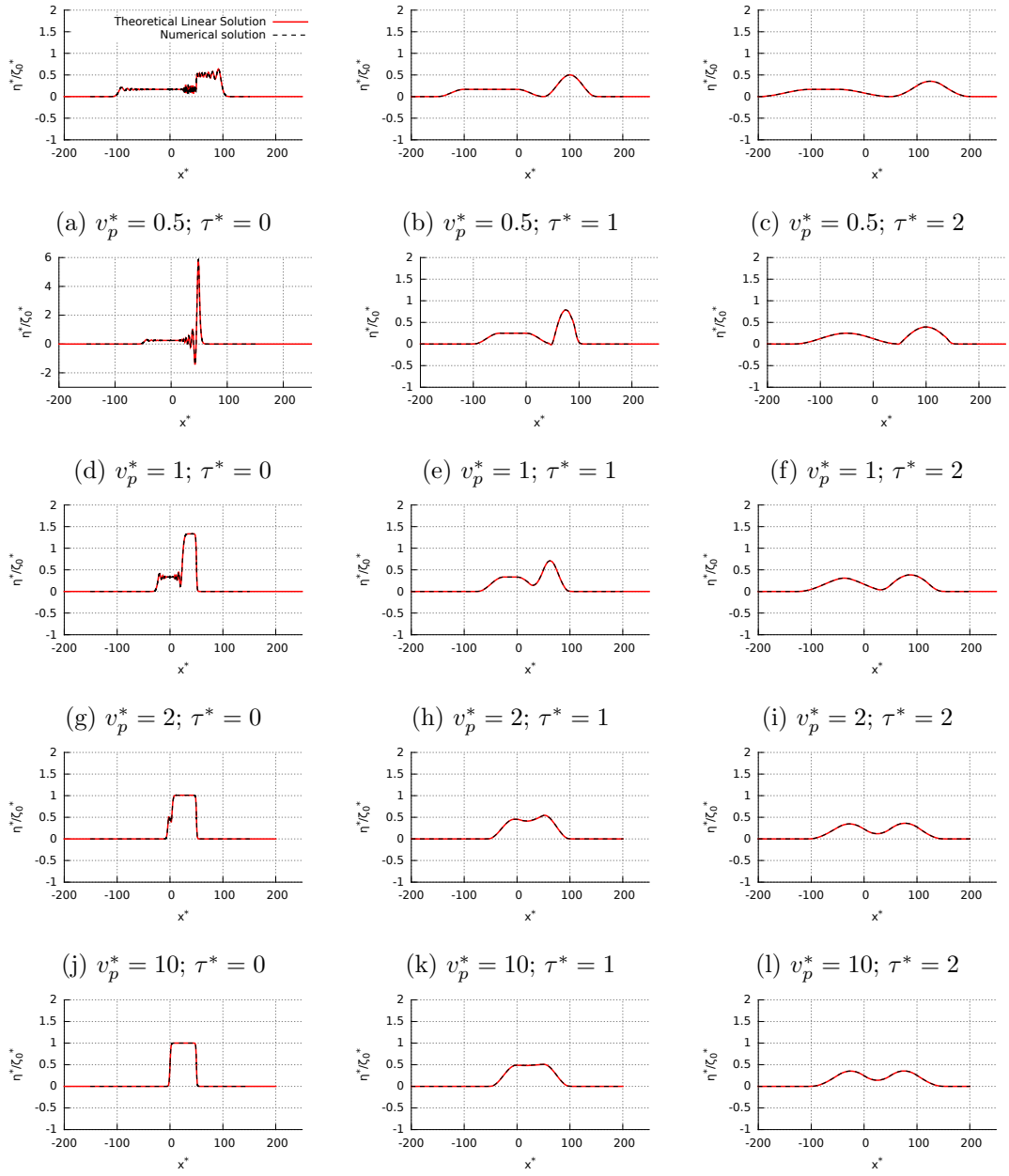

(a) $v_p^* = 0.5$; $\tau^* = 0$ (b) $v_p^* = 0.5$; $\tau^* = 1$ (c) $v_p^* = 0.5$; $\tau^* = 2$

(d) $v_p^* = 1$; $\tau^* = 0$ (e) $v_p^* = 1$; $\tau^* = 1$ (f) $v_p^* = 1$; $\tau^* = 2$

(g) $v_p^* = 2$; $\tau^* = 0$ (h) $v_p^* = 2$; $\tau^* = 1$ (i) $v_p^* = 2$; $\tau^* = 2$

(j) $v_p^* = 10$; $\tau^* = 0$ (k) $v_p^* = 10$; $\tau^* = 1$ (l) $v_p^* = 10$; $\tau^* = 2$

(m) $v_p^* = 50$; $\tau^* = 0$ (n) $v_p^* = 50$; $\tau^* = 1$ (o) $v_p^* = 50$; $\tau^* = 2$

Figure 2.4: Free surface profiles at $t^* = T^*$ for $L^* = 50$ and different values of v_p^* and τ^* (v_p^* increases from top to bottom and τ^* increases from left to right). The red line is the linear solution 2.21-2.23, and the dashed black line is the numerical simulation results from the linear version of the Misthyc code (see section 2.3.3). The vertical scale of graph (d) for $v_p* = 1$ and $\tau^* = 0$ differs from the others for clarity.

the wave propagates in both directions ($\pm x$). When v_p^* decreases, an asymmetry appears: the wave propagating in the same direction as the ground deformation ($+x$) is larger. In this direction the wave and the deformation propagate in parallel. Moreover when the

deformation moves at the same velocity of the wave, $v_p^* = 1$, then the energy created is directly injected in the initial wave, that amplified the lattest. A resonance is observed.

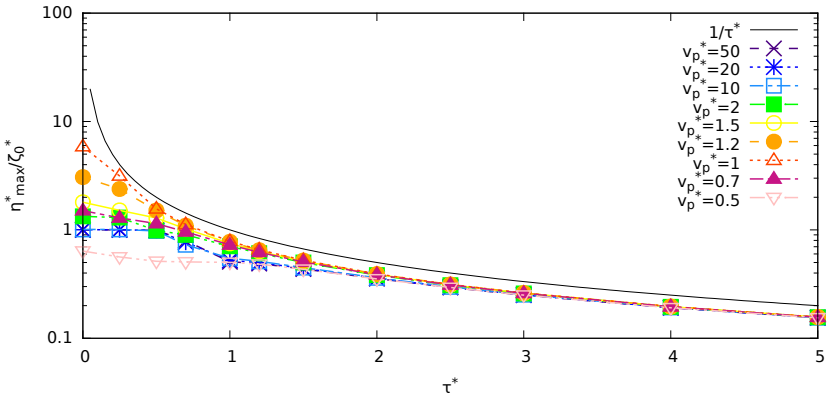

(a)

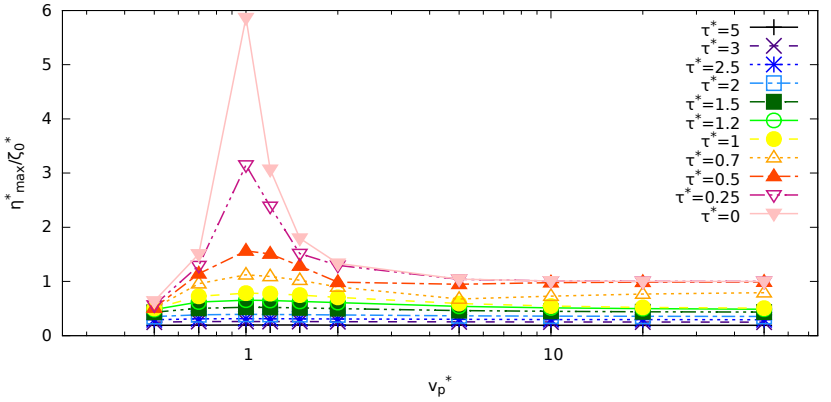

(b)

Figure 2.5: Evolution of η^*_{max}/ζ^*_0 as a function of τ^* for different values of v_p^* (2.5a, vertical axis in log scale) and as a function of v_p^* for different values of τ^* (2.5b, horizontal axis in log scale) for $L^* = 50$ at $t^* = T^*$.

Profiles of η^*_{max}/ζ^*_0 as a function of τ^*, for several rupture velocities are plotted in Figure 2.5a. When τ^* increases, η^*_{max}/ζ^*_0 decreases. Similarly to observed by Hammack [1973], for slow motions with $\tau^* \gg 1$, the maximum is inversely proportional to τ^*. However, where Hammack [1973] had a constant maximum for impulsive motion, the maximum here is strongly impacted by the rupture velocity v_p. If $\tau^* > 2$, the influence of v_p^* is negligible. For $v_p^* = 10, 20, 50$, the free surface profiles are almost identical, except when $\tau^* \sim 1$. Thus for $v_p^* > 10$, the motion in the x direction can be considered as nearly instantaneous. In Figure 2.5b, η^*_{max}/ζ^*_0 is plotted as a function of v_p^* for several values of rise time τ^*. In a similar way as Figure 2.5a, one can conclude that: for $v_p^* > 10$, the curves reach a constant asymptote; around $v_p^* = 1$ and $\tau^* < 0.7$, the resonance is observed; for $\tau^* > 2$,

the curves are very flat, thus the influence of v_p^* seems negligible for these values of τ^*.

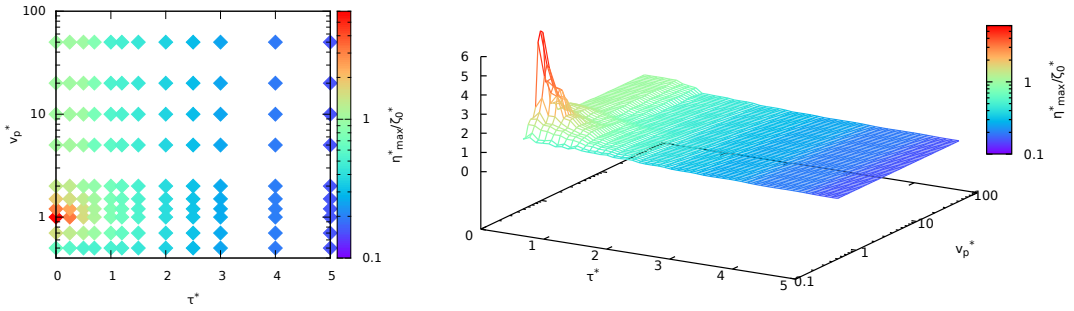

(a) (b)

Figure 2.6: The maximum free surface amplitude, η_{max}^*/ζ_0^* as function of v_p^* and τ^* for $L^* = 50$ at $t^* = T^*$ (colour in log scale). Figure 2.6a represents the original values while Figure 2.6b is an interpolation using a weighted average of the data.

Figure 2.6 shows the dependency of η_{max}^*/ζ_0^* on the temporal parameters in $v_p^* - \tau^*$ space. For small τ^*, the parameter v_p^* has a strong influence on the maximum amplitude as previously shown. As in the particular case studied by Todorovska and Trifunac [2001], a resonance appears for v_p^* in the range 0.7 to 2 (*i.e.* close to $v_p^* = 1$) generating a wave that reaches an amplitude η_{max}^*/ζ_0^* larger than 1. The maximum free surface amplitude can reach six times the bottom deformation amplitude at $v_p^* = 1$ as shown in Figure 2.5. Thus, when the rupture velocity is close to the wave velocity, the amplitude of the generated wave is much larger than the amplitude of the sea floor deformation at the beginning of the propagation phase. This resonance only exists for small values of τ^*.
The deformation length is then varied, and η^*/ζ_0^* and η_{max}^*/ζ_0^* are compared to the case $L^* = 50$ for $v_p^* = 1$ and $\tau^* = 0$. In Figure 2.7a, wave profiles are plotted for different L^*: while the wave in the negative direction keeps a constant amplitude, the wave in the positive direction increases with L^*. This is consistent with the fact that a larger volume of water is displaced. The maximum amplitude of the deformation is also sensitive to L^* (Figure 2.7b). The maxima can be reasonably well fit with a power law of the form:

$$\eta_{max}^*/\zeta_0^* = 0.414(L^*)^{0.669} \quad \text{for} \quad L^* \in [0; 5000]. \tag{2.24}$$

According to the fitting law (2.24), η_{max}^*/ζ_0^* increases with L^*, as said earlier. However, by looking at the expression of the free surface Fourier transform (2.21), $\tilde{\eta}$ is modulated by the low pass filter factor $1/\cosh k^*$, giving this property (low pass filter) to the water

layer [Jamin et al., 2015]. If this property is not taken into account, the generation and propagation of short waves can be expected. In a favourable case, as L^* is small enough, a spatial frequency dispersion could appear and reduce η^*_{max}/ζ^*_0.

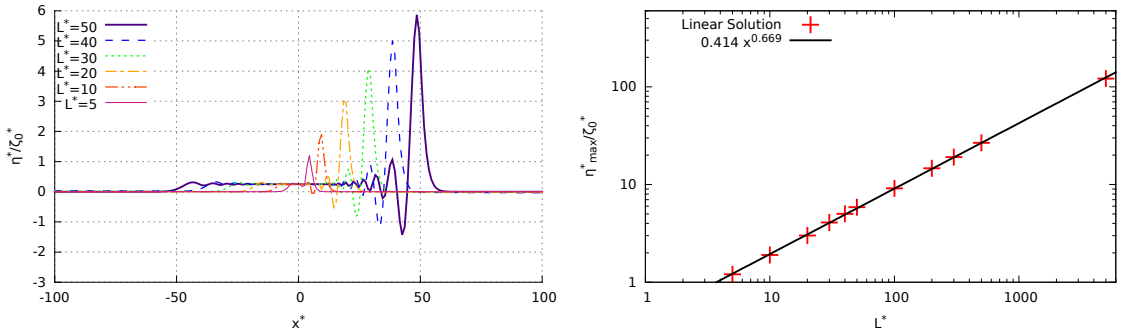

(a) (b)

Figure 2.7: Impact of the deformation length L^* for $v_p^* = 1$ and $\tau^* = 0$ at the end of the generation. 2.7a Spatial profiles of the free surface for different values of L^*. 2.7b Red crosses represent the η^*_{max}/ζ^*_0 of the linear solution and the black line is the trend line $0.414(L^*)^{0.669}$.

2.3.2 Propagation stage

The propagation of the generated wave is analysed as a function of v_p^* and τ^*, with fixed $L^* = 50$. The spatial profiles of the free surface at $t^* = 100, 500$ and 1000 are shown in Figures 2.8, 2.9, 2.10, respectively, for $v_p^* = 0.5, 1, 2, 10, 50$ and $\tau^* = 0, 1, 2$. Note that t^* may be interpreted as the ratio of the propagation distance to the initial water depth.

At $t^* = 100$ (Figure 2.8), two waves propagate in both directions for all parameters values. For $v_p^* = 50$, the two waves are almost symmetrical. When τ^* decreases, the amplitude decreases. For $v_p^* = 1$ and 2, the asymmetry of the propagation appears clearly. The wave propagating in the positive direction is larger. By superimposing the curves of $v_p^* = 10$ and $v_p^* = 50$ (not shown here), the results from $v_p^* = 10$ appear weakly non symmetrical, which confirms that the free surface deformation is asymmetrical when v_p^* decreases. These conclusions are also valid for $t^* = 500$ (Figure 2.9) and $t^* = 1000$ (Figure 2.10). Moreover, for $\tau^* = 0$, the free surface deformations show the development of frequency dispersion increasing in time as shown by Hammack [1973] and Stefanakis et al. [2015]. Except for $\tau^* = 1$ and $v_p^* = 1$ at $t^* = 1000$, this dispersion does not exist for larger τ^*. In the general case, each wave has the shape of a single hump of water, and the maximum amplitude

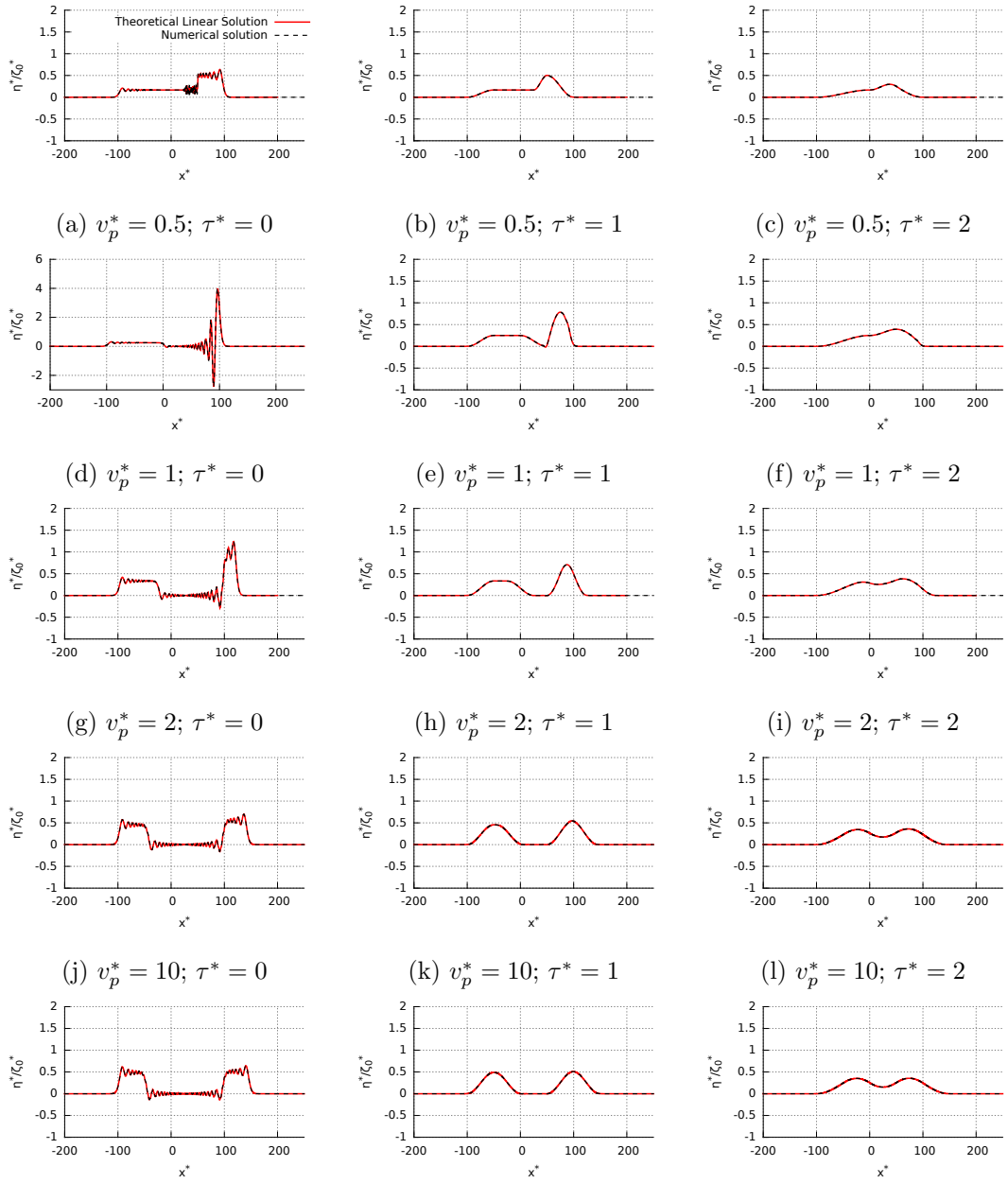

(a) $v_p^* = 0.5$; $\tau^* = 0$ (b) $v_p^* = 0.5$; $\tau^* = 1$ (c) $v_p^* = 0.5$; $\tau^* = 2$

(d) $v_p^* = 1$; $\tau^* = 0$ (e) $v_p^* = 1$; $\tau^* = 1$ (f) $v_p^* = 1$; $\tau^* = 2$

(g) $v_p^* = 2$; $\tau^* = 0$ (h) $v_p^* = 2$; $\tau^* = 1$ (i) $v_p^* = 2$; $\tau^* = 2$

(j) $v_p^* = 10$; $\tau^* = 0$ (k) $v_p^* = 10$; $\tau^* = 1$ (l) $v_p^* = 10$; $\tau^* = 2$

(m) $v_p^* = 50$; $\tau^* = 0$ (n) $v_p^* = 50$; $\tau^* = 1$ (o) $v_p^* = 50$; $\tau^* = 2$

Figure 2.8: Free surface profiles at $t^* = 100$ for $L^* = 50$ and different values of v_p^* and τ^*. Same legend as Figure 2.4.

does not change with time. For $v_p^* = 1$ and $\tau^* = 0$ (resonance condition), the maximum amplitude decreases in time, but even at $t^* = 1000$, this maximum is still greater than 1: the impact of the resonance at the generation is still present.

Figure 2.11 shows the evolution of the free surface deformation η^*/ζ_0^* as a function of x^* and t^* for $v_p^* = 1$ and $\tau^* = 0$. In this graph, the frequency dispersion and wave asymmetry

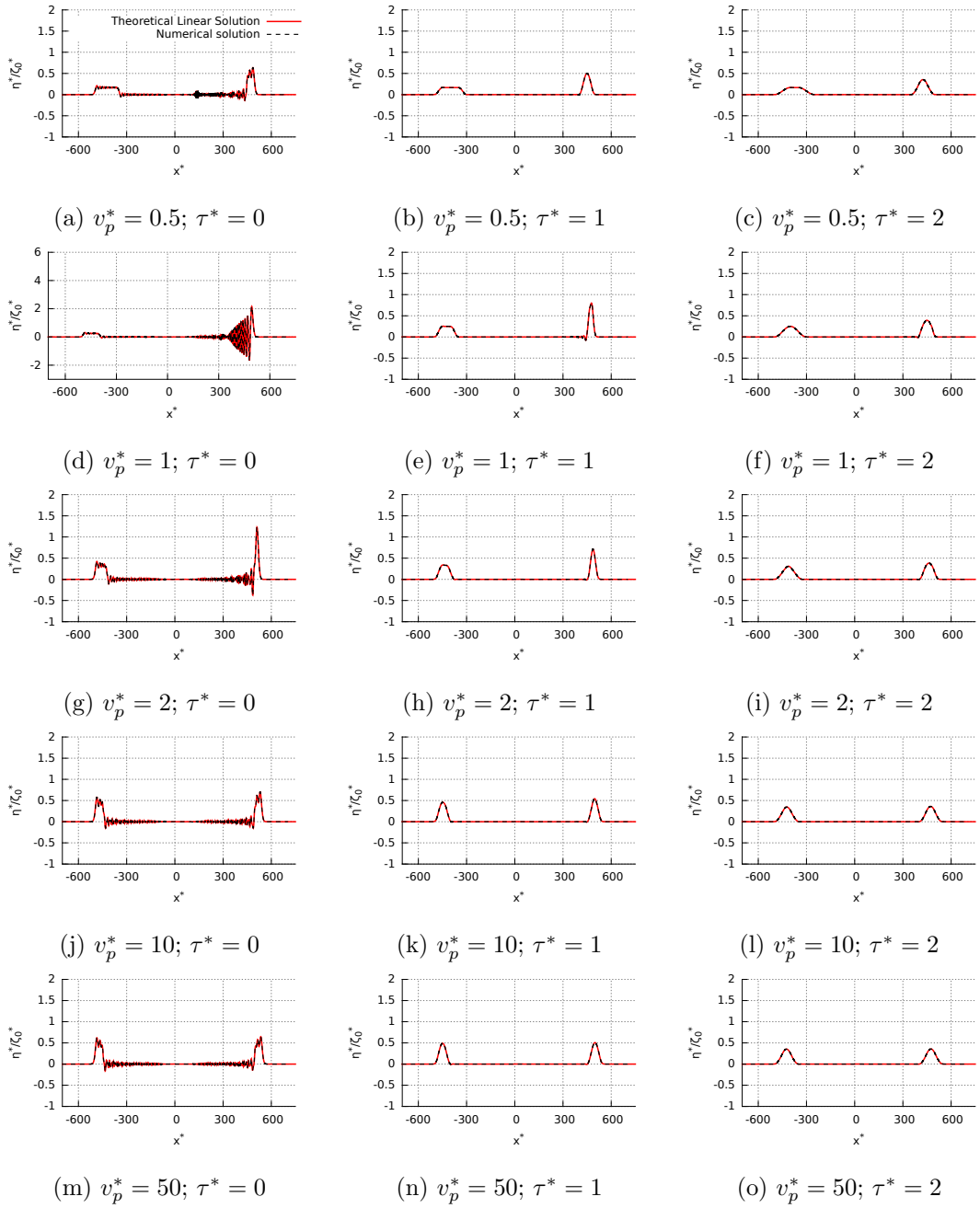

(a) $v_p^* = 0.5$; $\tau^* = 0$ (b) $v_p^* = 0.5$; $\tau^* = 1$ (c) $v_p^* = 0.5$; $\tau^* = 2$

(d) $v_p^* = 1$; $\tau^* = 0$ (e) $v_p^* = 1$; $\tau^* = 1$ (f) $v_p^* = 1$; $\tau^* = 2$

(g) $v_p^* = 2$; $\tau^* = 0$ (h) $v_p^* = 2$; $\tau^* = 1$ (i) $v_p^* = 2$; $\tau^* = 2$

(j) $v_p^* = 10$; $\tau^* = 0$ (k) $v_p^* = 10$; $\tau^* = 1$ (l) $v_p^* = 10$; $\tau^* = 2$

(m) $v_p^* = 50$; $\tau^* = 0$ (n) $v_p^* = 50$; $\tau^* = 1$ (o) $v_p^* = 50$; $\tau^* = 2$

Figure 2.9: Free surface profiles at $t^* = 500$ for $L^* = 50$ and different values of v_p^* and τ^*. Same legend as Figure 2.4.

appear clearly. In the $-x$ direction, a smaller but wider wave propagates almost with a constant amplitude. In the $+x$ direction, the amplified wave propagates with strong dispersion, and its maximum amplitude decreases during propagation.

Figure 2.12 shows the variations of the maximum amplitude η^*_{max}/ζ^*_0 as a function of v_p^* and τ^* for $t^* = 100, 500$ and 1000. The shape of the dependence does not change with

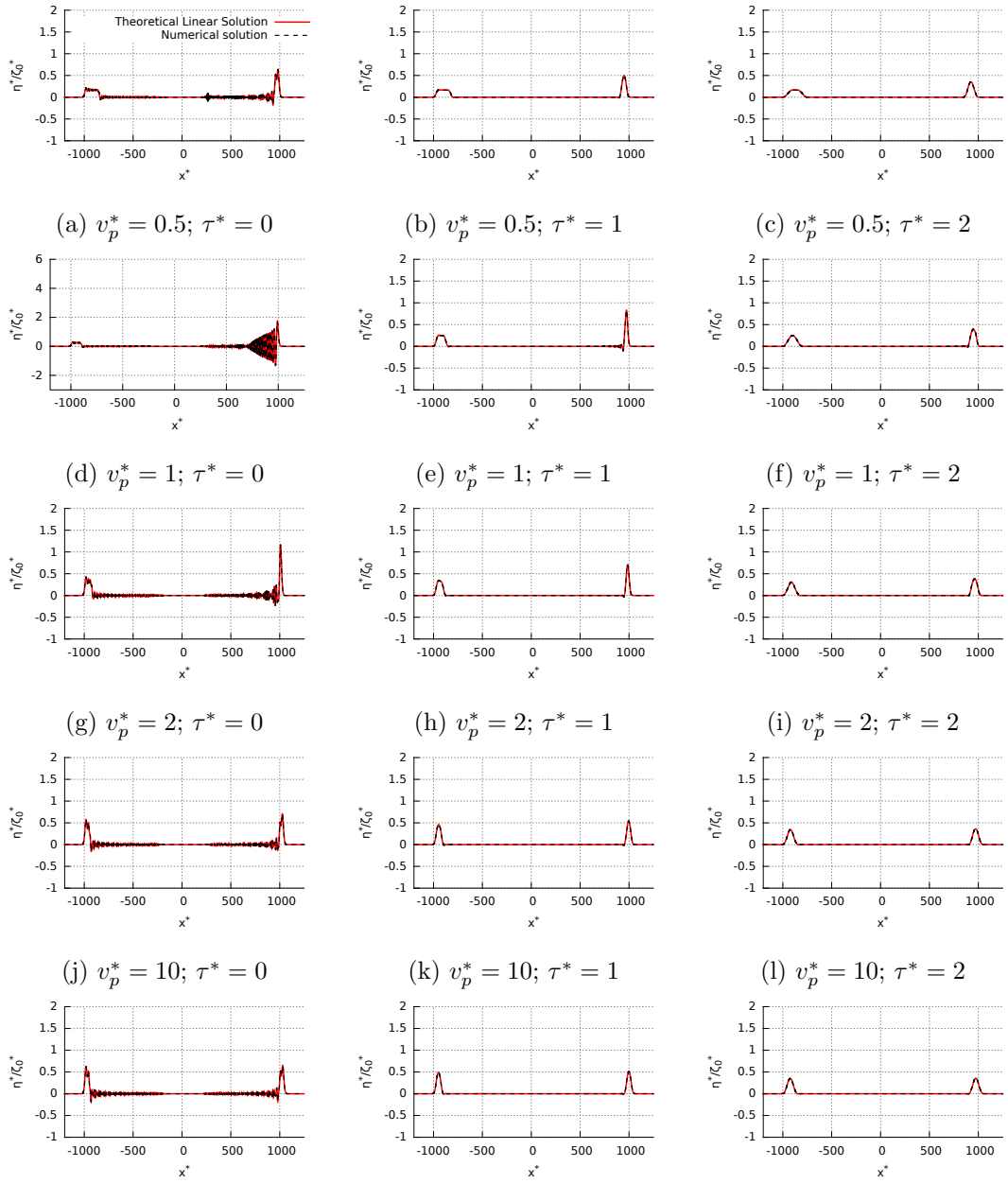

(a) $v_p^* = 0.5$; $\tau^* = 0$ (b) $v_p^* = 0.5$; $\tau^* = 1$ (c) $v_p^* = 0.5$; $\tau^* = 2$

(d) $v_p^* = 1$; $\tau^* = 0$ (e) $v_p^* = 1$; $\tau^* = 1$ (f) $v_p^* = 1$; $\tau^* = 2$

(g) $v_p^* = 2$; $\tau^* = 0$ (h) $v_p^* = 2$; $\tau^* = 1$ (i) $v_p^* = 2$; $\tau^* = 2$

(j) $v_p^* = 10$; $\tau^* = 0$ (k) $v_p^* = 10$; $\tau^* = 1$ (l) $v_p^* = 10$; $\tau^* = 2$

(m) $v_p^* = 50$; $\tau^* = 0$ (n) $v_p^* = 50$; $\tau^* = 1$ (o) $v_p^* = 50$; $\tau^* = 2$

Figure 2.10: Free surface profiles at $t^* = 1000$ for $L^* = 50$ and different values of v_p^* and τ^*. Same legend as Figure 2.4.

time, except for small v_p^* and large τ^* because their T^* is over 100, or around $v_p^* = 1$ and small τ^*, where the amplitudes are greater than 1 (see the spatial profiles in Figures 2.8, 2.9, 2.10). The resonance is preserved but these maxima decrease in time, which confirms the previous conclusion.

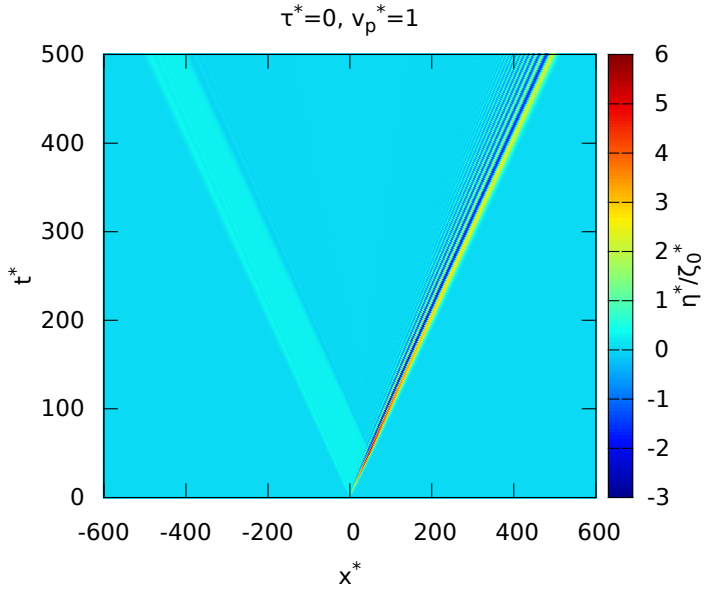

Figure 2.11: Evolution in space and time of the free surface deformation η^*/ζ_0^* for $v_p^* = 1$ and $\tau^* = 0$. The colour represents the wave amplitude.

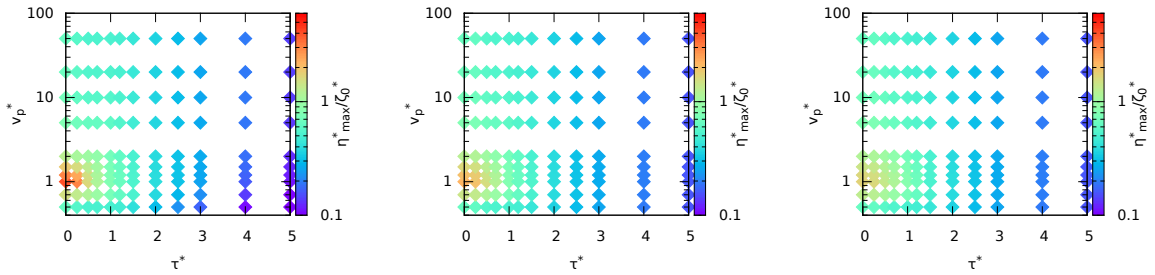

(a) $t^* = 100$ (b) $t^* = 500$ (c) $t^* = 1000$

Figure 2.12: Maximum free surface amplitude η_{max}^*/ζ_0^* as a function of v_p^* and τ^* for $L^* = 50$ at different times t^*.

2.3.3 Comparison with numerical results

In order to verify the proposed analytical solution, a cross validation is used: these results are compared to simulation results from a numerical model called Misthyc [Yates and Benoit, 2015], which solves the Euler–Zakharov equations [Zakharov, 1968] for a homogeneous incompressible and inviscid fluid in an irrotational flow:

$$\begin{aligned}\eta_t &= -\bigtriangledown\tilde{\phi}.\bigtriangledown\eta + \tilde{w}(1+(\bigtriangledown\eta)^2),\\ \tilde{\phi}_t &= -g\eta - \tfrac{1}{2}(\bigtriangledown\tilde{\phi})^2 + \tfrac{1}{2}\tilde{w}^2(1+(\bigtriangledown\eta)^2),\end{aligned}$$

where $\tilde{\phi}$ is the potential at the free surface and $\tilde{w}$ is the vertical velocity at the free surface. These equations correspond to 2.3a-2.3d, rewriting the system using free surface variables. These equations are solved by using a 4th order Runge-Kutta (RK4) scheme in time, a spectral approach in the vertical direction, and high-order finite difference schemes (4^{th} order) in the x direction. The spectral approach uses a base of Chebyshev polynomials of the first kind, and for the present simulations, the maximum polynomial order is 7. The choice of this model is justified by its capacity to represent correctly the propagation of non-linear and dispersive waves, see Raoult et al. [2016]. However, first, in the following paragraph, the linear version of the code is used.
Figures 2.4, 2.8, 2.9 and 2.10 show comparisons between the present linear solution and the results from the linear version of Misthyc. On the overall, the curves globally match very well indicating a very good agreement between the theoretical solution and the results of the numerical simulations. At $t^* = T^*$, the relative errors $e_r(x^*, t^*)$ (see Figure 2.13) are found to be less than 1% for every v_p^* as soon as $\tau^* > 0$.

The cases with $\tau^* = 0$ correspond to an instantaneous vertical uplift speed, which can be represented only approximately in the numerical model. In practice a small but finite value of τ^* was used in Misthyc ($\tau^* = 0.001$), leading to slightly larger errors in these cases. The results are thus consistent, which provides an independent validation of the solution developed in the previous section.

2.4 Discussion of the validity of the shallow water equations

The next point of discussion is the validity of using the Shallow Water Equations (SWE) to model dynamic tsunami generation and propagation. Indeed, it is commonly proposed that the wavelength of a seismic tsunami is equivalent to the horizontal dimension of the source (see section 2 and Wu [1981]), thus the wavelength is much larger than the water depth. However, the question about dispersion effects during the tsunami process is fully relevant and has already been asked and explored. Glimsdal et al. [2013] proposed a "dispersion time" depending mainly on the initial water depth, the source width and the distance from the source region to the shore. This "dispersion time" gives a glimpse of the magnitude of the dispersive effects. With a similar aim, in this study, a parameter ε is defined as function of v_p^* and τ^* using the potential energy, as explained below, to measure the part of the energy lying in the dispersive range of k^* poorly represented with

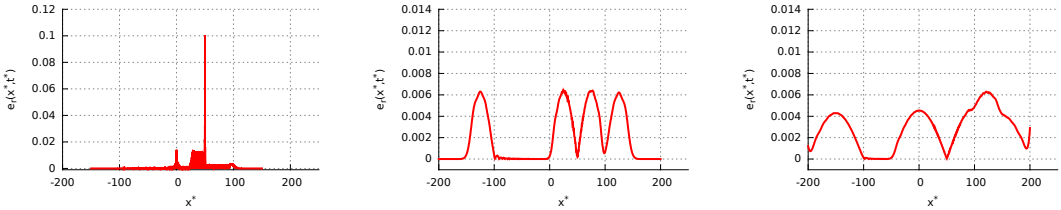

(a) $v_p^* = 0.5$; $\tau^* = 0$ (b) $v_p^* = 0.5$; $\tau^* = 1$ (c) $v_p^* = 0.5$; $\tau^* = 2$

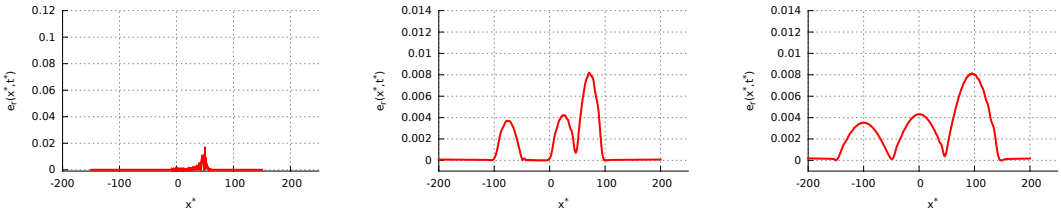

(d) $v_p^* = 1$; $\tau^* = 0$ (e) $v_p^* = 1$; $\tau^* = 1$ (f) $v_p^* = 1$; $\tau^* = 2$

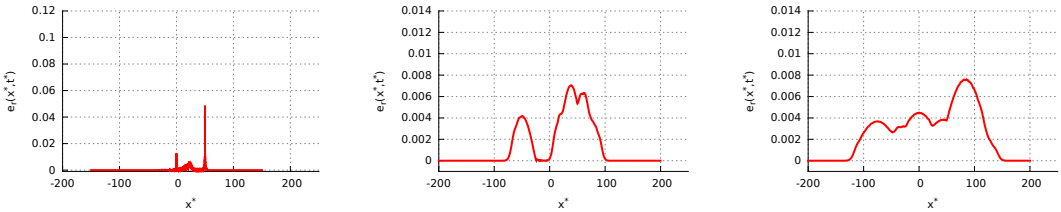

(g) $v_p^* = 2$; $\tau^* = 0$ (h) $v_p^* = 2$; $\tau^* = 1$ (i) $v_p^* = 2$; $\tau^* = 2$

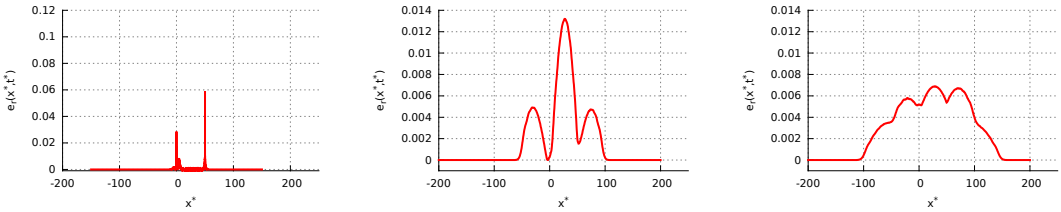

(j) $v_p^* = 10$; $\tau^* = 0$ (k) $v_p^* = 10$; $\tau^* = 1$ (l) $v_p^* = 10$; $\tau^* = 2$

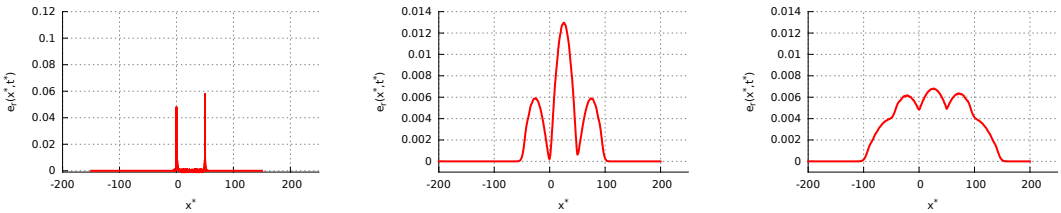

(m) $v_p^* = 50$; $\tau^* = 0$ (n) $v_p^* = 50$; $\tau^* = 1$ (o) $v_p^* = 50$; $\tau^* = 2$

Figure 2.13: Spatial relative error of the numerical free surface issued from Misthyc at $t^* = T^*$ for $L^* = 50$ and different values of v_p^* and τ^*.

the SWE.

Generally within the linear theory, the dispersion relation is

$$\omega = \sqrt{gk \tanh kh} \tag{2.25}$$

, leading to the wave celerity $c_e = \frac{\omega}{k} = \sqrt{\frac{g \tanh kh}{k}}$. For the long wave approximation, it is assumed that as the wavelength $\lambda \gg h$, the dispersion relation becomes $\omega = k\sqrt{gh}$ and thus $c_{lw} = \sqrt{gh}$. To figure out what is the limit of acceptable long wave approximations, the velocities are non-dimensionalised by $\sqrt{gh}$ and plotted in Figure 2.14.

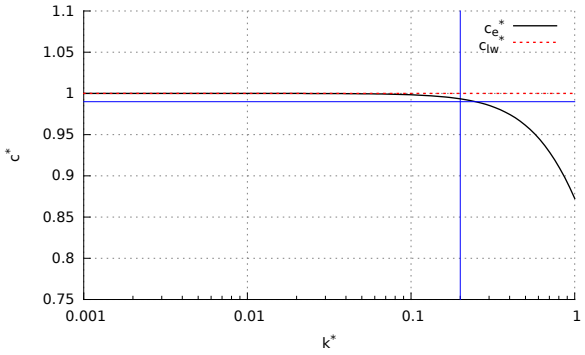

Figure 2.14: Wave celerities (adimensionalised by $\sqrt{gh}$) from the general and the long wave theories, c_e^*, in black thick line, and c_{lw}^*, in dashed red line, respectively. The blue vertical line corresponds to $k^* = 0.2$ and the horizontal one to $c^* = 0.99$. The horizontal axis is in log scale.

Until $kh \sim 0.2$, the relative error between the long wave celerity and the exact celerity is less than 1%. Thus, we assume here that the long wave theory, and consequently the SWE assumptions are acceptable for $k^* \leq 0.2$. This threshold corresponds to wave lengths greater than approximately $30h$. Figure 2.15 illustrates the validity of this approximation for $v_p^* = 50$ and $\tau^* = 0$ at $t^* = T^*$ on the modulus of the free surface Fourier transform $\tilde{\eta}^*$ of the linear solution. Outside of the grey striped zones, the long wave approximation is no longer valid, and the energy is not properly modelled by the SWE.

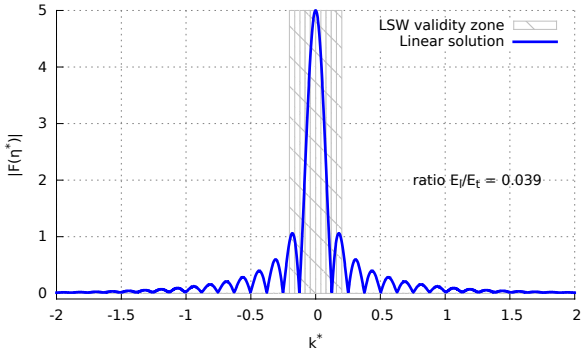

Figure 2.15: The blue line represents the modulus of $\tilde{\eta}^*$ for $v_p^* = 50$ and $\tau^* = 0$ at $t^* = T^*$. The grey striped zone shows the domain of validity of the long wave approximation. Waves with wavenumbers outside of this zone are not taken into account properly in the SWE model.

To estimate the impact of the SWE approximations on the present tsunami waves, we study the total potential energy. The amount of energy that lies outside the range of validity of the SWE is simply called "residual" energy hereafter. The ratio ε between the residual energy E_l and the total energy E_t is estimated. The total potential energy is calculated numerically by integrating $\tilde{\eta}^{*2}(k^*)$ over $]-\infty;\infty[$, and the "residual" energy is calculated by integrating $\tilde{\eta}^{*2}(k^*)$ over $]-\infty;-0.2]\cup[0.2;\infty[$ (*i.e.* the part of the spectrum not properly handled by the SWE):

$$\varepsilon(t^*) = \frac{E_l(t^*)}{E_t(t^*)} = \frac{\int_{|k^*|\geq 0.2}(\tilde{\eta}^*)^2 dk^*}{\int_{-\infty}^{+\infty}(\tilde{\eta}^*)^2 dk^*}. \tag{2.26}$$

In the present study, only the potential energy is considered. We can suppose that the nonlinear part of the total energy (kinematic energy) can be added by integrating u^{*2}. However this possibility is not developped here.

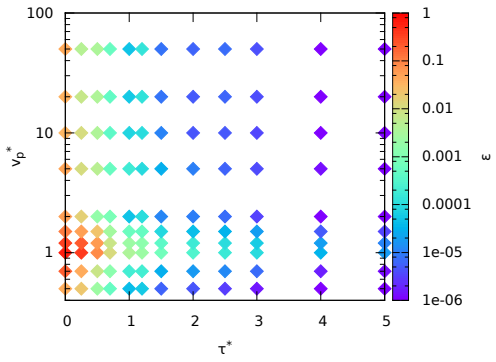

Figure 2.16: Energy ratio $\varepsilon = \frac{E_l}{E_t}$, at $t^* = T^*$ as a function of v_p^* and τ^*.

In Figure 2.16, the ratio $\varepsilon(t^*)$ is presented as a function of v_p^* and τ^* at $t^* = T^*$. Here again, the resonance around $v_p^* = 1$ and small τ^* is visible. The energy ratio ε for $v_p^* = 1$ and $\tau^* = 0$ reaches 0.61, which means that more than half of the potential energy is not properly accounted for at the end of the deformation if a shallow water model is used for the spatial parameters taken here. For larger τ^* and v_p^*, the ratio is typically less than 0.1, indicating that shallow water models are more appropriate. Globally, the energy ratio ε decreases when τ^* increases.

Profiles of ε as function of time for $v_p^* = 0.5, 1, 2, 10$ and 50 and $\tau^* = 0, 1, 2$ are shown in Figure 2.17. For sake of clarity, profiles for different τ^* are plotted on different graphs, and each colour line represents a rupture velocity v_p^*.

In all cases, three phases can be identified in the evolution of ε: an initial steady phase is followed by a decrease and then by a second steady state. The first phase, with $t^* < L^*$, is

nearly independent of τ^* and slightly sensitive to v_p^*: for $v_p^* = 0.5, 1, 2$, the initial value of ε is above 0.5, and decreases when v_p^* increases. During this phase, ε remains high (> 0.1) thus SWE models are not recommended for this range of parameters.
The transition phase, around $t^* = (L/\sqrt{gh})^*$, shows a rapid decrease of ε. Its value oscillates before it reaches an asymptotic value in the third phase ($t^* > L^*$). Except for $v_p^* = 1$, this limit value is the same for all v_p^* but varies with τ^*. When τ^* increases, this limit decreases: for $\tau^* = 0$, ε is close to 0.05, for $\tau^* = 1$, ε is around 10^{-4}; and for $\tau^* = 2$, ε reaches 5 10^{-5}. During this phase, and for these values of v_p^*, SWE models are appropriate. For $v_p^* = 1$ and $\tau^* = 1, 2$, ε follows the same pattern but with a higher asymptotic value in the third phase than for the other rupture velocities. The evolution of ε is different when $\tau^* = 0$. In this case, ε remains above 0.5 and seems to increase slightly. The resonance is still observed. Thus, when $v_p^* = 1$ and τ^* is very small, SWE models should not be used.

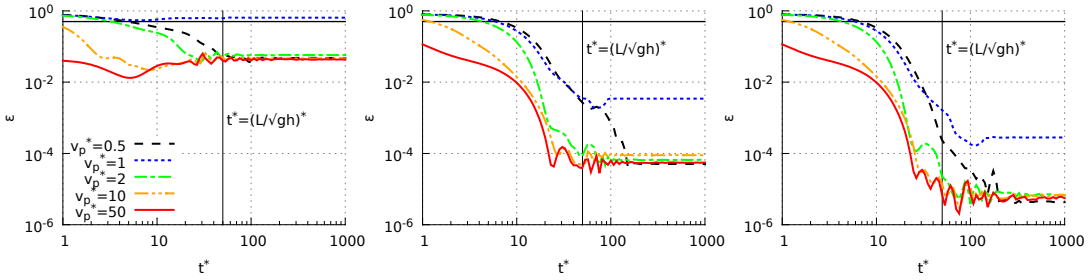

(a) $\tau^* = 0$ (b) $\tau^* = 1$ (c) $\tau^* = 2$

Figure 2.17: Time profiles of the energy ratio $\varepsilon = \frac{E_l}{E_t}$ for different values of τ^* and v_p^*. The horizontal black line represents $\varepsilon = 0.5$. The vertical black line is at $t^* = (L/\sqrt{gh})^*$.

2.5 Numerical simulation of non-linear propagation

In this section, we investigate how the resonance observed in the linear model behaves when non-linear effects are taken into account. The previous problem is now solved with the non-linear version of Misthyc (see Paragraph 2.3.3).

Initially the deformation is nearly linear with $\zeta_0^* = 0.001$ (small deformation of the sea floor compared to the water depth). Figure 2.18 shows the resulting distribution of η_{max}^*/ζ_0^* for the same range of parameters (v_p^* and τ^*) considered in section 2.3.
The panel obtained for the numerical non-linear model is similar to linear theory (Figure 2.6), thus as for the linear theory, the resonance phenomena is still presence here.
Then non-linear effects are introduced by increasing ζ_0^* from 0.001 to 0.1. Indeed, if ζ_0 increases, η_{max} increases too because the volume of displaced water is larger. Thus the non-linearity, that increases with η_{max}^*, also increases with ζ_0^*. With non-linearity, it can be expected that the resonance is shifted towards higher values of v_p^*. Indeed, the linear

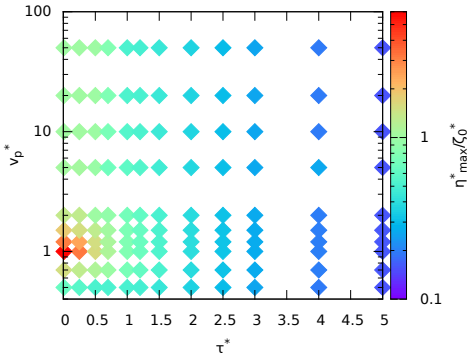

Figure 2.18: The maximum free surface amplitude (η^*_{max}/ζ^*_0) calculated with the non-linear numerical model as function of v^*_p and τ^* for $L^* = 50$ and $\zeta_0 = 0.001$ at $t^* = T^*$ (colour in log scale).

theory showed that the resonance occurs when v_p is equal to the long wave celerity. In weakly non-linear conditions, the latter can be approximated by $c = \sqrt{gh(1 + \eta_{max}/h)}$. The peak of resonance should occur for $v^*_p = \sqrt{1 + \eta^*_{max}}$. As the value of η_{max} is initially unknown, tests are performed for $\zeta^*_0 = 0.1$ and $v^*_p \in [0.8; 1.26]$ at the end of the ground motion. The free surface profiles are plotted in Figure 2.19.

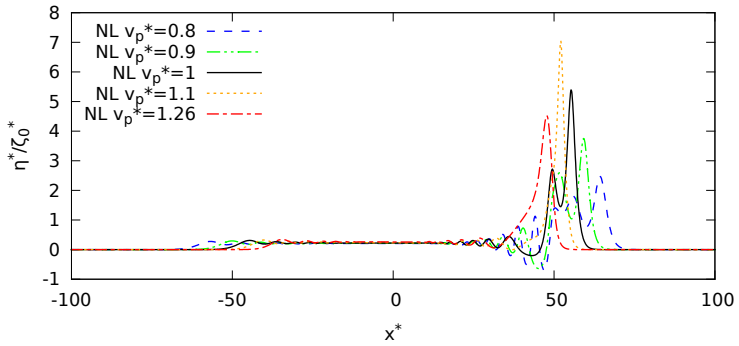

Figure 2.19: Free surface profiles from non-linear numerical results Misthyc, for $\zeta^*_0 = 0.1$ for $v^*_p = 0.8, 0.9, 1, 1.1, 1.26$ at the end of the ground motion.

As expected, the amplitude of the motion with $v^*_p = 1.1$ is larger than the one with $v^*_p = 1$. However, for sake of simplicity, we keep $v^*_p = 1$ thereafter.
Figure 2.20 shows the deformation of the free surface for different values of ζ^*_0 at $t^* = T^*$.

We can see that η^*_{max} varies from 5.10^{-3} to 6.10^{-1}, increasing non-linear effects. The numerical results for $\zeta^*_0 = 0.001, 0.005, 0.01$ are close to the linear solution. The general wave form is preserved, and the maximum amplitude increases slightly with ζ^*_0. For $\zeta^*_0 = 0.05$

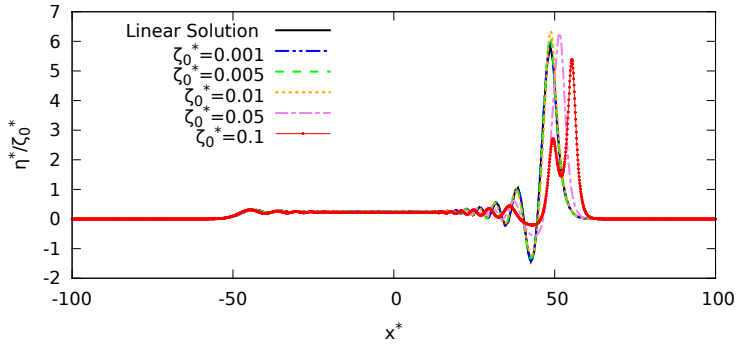

Figure 2.20: Deformation of the free surface at $t^* = T^*$ and for $v_p^* = 1$ and $\tau^* = 0$: comparison of the linear solution (black line) and non-linear numerical results. The coloured dashed lines represent the dimensionless non-linear numerical results for different increasing non-linearity levels: $\zeta_0^* = 0.001, 0.005, 0.01, 0.1$.

and 0.1, the propagation is faster. The frequency dispersion is more pronounced, and the first generated wave seems to have split already in two for $\zeta_0^* = 0.1$, leading to a lower maximum amplitude than observed in the other cases. In reality, this kind of deformation ($\zeta_0^* = 0.05$ and 0.1) is not representative of seismic tsunami generation: the sea floor deformation is usually on the order of 10 m for a water depth of 4000 m, leading to ζ_0^* on the order of 10^{-3}.

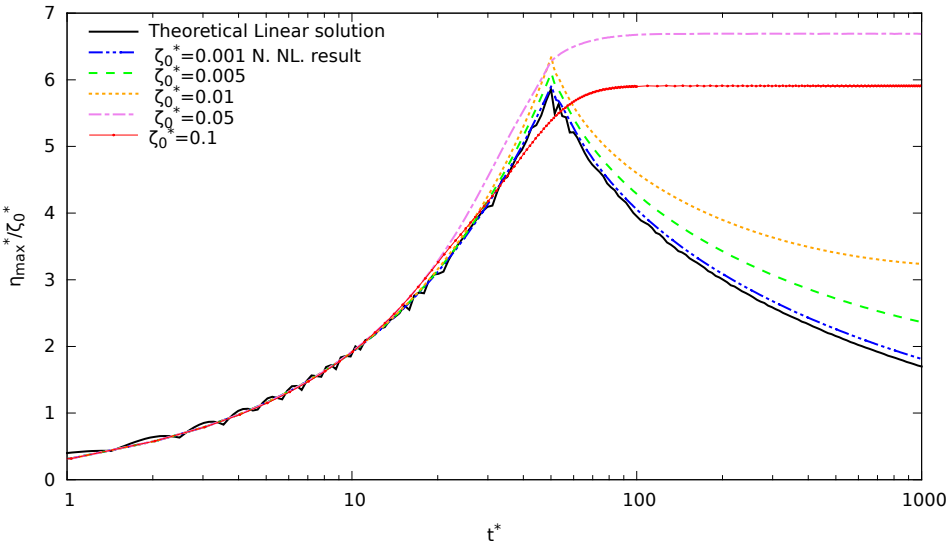

Figure 2.21: Temporal profiles of η_{max}^*/ζ_0^* for $v_p^* = 1$, $\tau^* = 0$ and $L^* = 50$. The solid black line is the theoretical linear solution. The coloured dashed lines are non-linear numerical results from Misthyc for $\zeta_0^* = 0.001, 0.005, 0.01$ and 0.1.

Temporal profiles of the maximum free surface amplitude are drawn in Figure 2.21 for a range of ζ_0^* (from 0.001 to 0.1). Until the end of the ground deformation ($t^* = T^* = 50$ here), η_{max}^*/ζ_0^* increases similarly, reaching an almost identical maximum for all the ground deformation amplitudes ζ_0^* ($\eta_{max}^* \sim 6\zeta_0^*$). Thus, the resonance remains when non-linear effects are included. However, the decrease of η_{max}^* is different. The slope is smaller for larger ζ_0^*. In addition, for $\zeta_0^* > 0.05$, η_{max}^* remains nearly constant in time.

The free surface deformation after the end of the ground deformation: $t^* = 100$ and $t^* = 500$, is shown in Figure 2.22. For small ζ_0^*, the shape of the waves generated by the non-linear numerical model is similar to the linear solution, even though the propagation velocity is slightly higher for $\zeta_0^* = 0.005$ and 0.01. However, for $\zeta_0^* = 0.05$ and 0.1, a different pattern is observed. Solitary waves appear, which explains the constant value of η_{max}^* in time after some duration (Figure 2.21) as solitary wave solutions amplitude does not vary during their propagation. A more in-depth analysis of the transition between the two regimes illustrated in Figures 2.21 and 2.22. A first comparison is done with numerical results from the algorithm of Dutykh and Clamond [2014]. The shapes of solitary wave created for a same η_{max}^* are superimposed in Figure 2.23 on the free surface profile of the generated wave with a deformation of $\zeta_0^* = 0.05, 0.1$ at $t^* = 993$. Qualitatively, the shapes match very well, which confirms that these leading waves are of solitary type. The generation of solitary waves by moving disturbance has already been studied by Wu [1987] and Lee et al. [1989] for a continuous running deformation. The latter compared numerical Boussinesq and KdV models with experiments. They defined the Froude number as the disturbance velocity and $\sqrt{gh}$ ratio and showed its importance on the wave signal generated: solitons appear only for trans-critical speeds. However, as the linear theory does not permit the creation of soliton, they only used a width disturbance ζ_0 of 0.15 and 0.2.

2.6 Linear Shallow Water equations model

As Section 2.2, a solution for the Linear Shallow Water Equations (LSWE) is developed in this section. Indeed, one of the codes of reference is Telemac 2D that solves the Non-Linear Shallow Water Equations. To estimated the relevance of its use, it is compared in Chapter 3 to the theoretical solution developped here that should also represent the resonance. Thus, the aim in this paragaph is to observe the evolution of the resonance on the maximal amplitude of the wave. The non-linear shallow water equations are:

$$\eta_t - \zeta_t + ((\eta - \zeta)U)_x + hU_x = 0, \tag{2.27}$$

$$U_t + U.U_x = -g\eta_x, \tag{2.28}$$

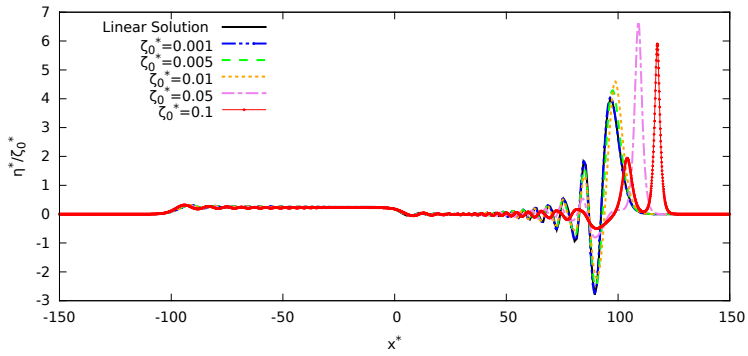

(a) $t^* = 100$

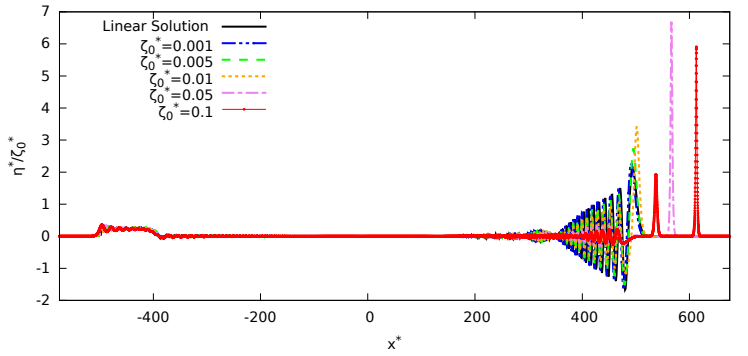

(b) $t^* = 500$

Figure 2.22: Comparison of the deformation of the free surface at $t^* = 100$ and 500 (2.22a and 2.22b respectively) for $v_p^* = 1$ and $\tau^* = 0$ of the linear solution and the non-linear numerical results. The thick black line is the theoretical linear solution and the coloured lines represent the non-linear numerical results of Misthyc for different initial deformations: $\zeta_0^* = 0.001, 0.005, 0.01, 0.1$.

If the equations (2.27) and (2.28) are linearised, the previous system becomes:

$$\eta_t - \zeta_t + hU_x = 0 \tag{2.29}$$

$$U_t = -g\eta_x \tag{2.30}$$

Differentiating equation (2.29)with respect to t and equation (2.30) with respect to x and combining both expressions, the following expression is obtained:

$$\eta_{tt} - \zeta_{tt} - hg\eta_{xx} = 0. \tag{2.31}$$

The Fourier–Laplace transform (2.10) is applied to (2.31), giving the solution $\bar{\eta}$ in the Fourier–Laplace space:

$$\bar{\eta}(k,s) = \frac{s^2\bar{\zeta}(k,s)}{s^2+\omega^2}, \tag{2.32}$$

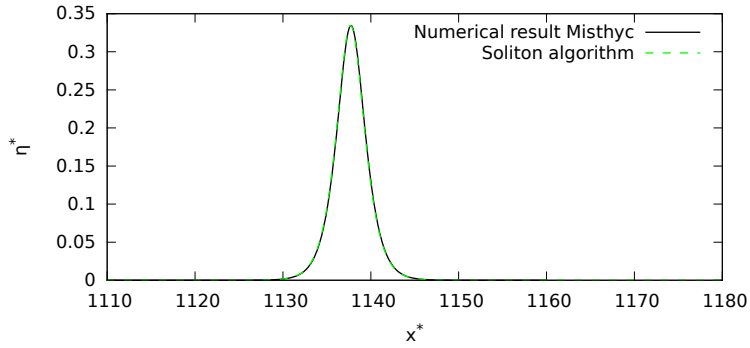

(a) $\zeta_0^* = 0.05$

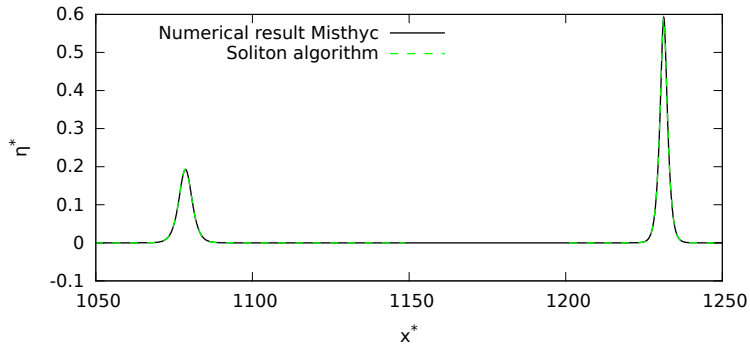

(b) $\zeta_0^* = 0.1$

Figure 2.23: Comparison between the shape of the generated wave with the non-linear numerical result Misthyc (black full curve) and the shape of the solitary wave from the algorithm of Dutykh and Clamond [2014] (dashed green curves) at $t^* = 993$.

where, here, $\omega = \sqrt{ghk}$ is the linear long wave dispersion relation. The only difference between the solution (2.32) and the solution of the linearised Euler system (2.14) is the lost of the division by $\cosh kh$. Keeping the definition of ζ (2.2.2), the same calculations as for the linearised Eulerian solution give:

$$\bar{\eta}(k,s) = \frac{\zeta_0}{2}\frac{s}{(s^2+\omega^2)}(1+e^{-st_r})\frac{\omega_r^2}{s^2+\omega_r^2}\frac{1-e^{-L(ik+\frac{s}{v_p})}}{ik+\frac{s}{v_p}}. \tag{2.33}$$

Thus,

$$\tilde{\eta}(k,t) = \frac{\zeta_0}{2}v_p\frac{\omega_r^2}{\omega_r^2-\omega^2}\begin{pmatrix} f(k,t) \\ +H(t-t_r)f(k,t-t_r) \\ -H(t-\frac{L}{v_p})e^{-ikL}f(k,t-\frac{L}{v_p}) \\ -H(t-t_r-\frac{L}{v_p})e^{-ikL}f(k,t-t_r-\frac{L}{v_p}) \end{pmatrix}, \tag{2.34}$$

where:

$$f(k,t) = \begin{array}{l} \frac{1}{\omega^2 - k^2 v_p^2}\left(ikv_p\cos(\omega t) + \omega\sin(\omega t) - ikv_p e^{-ikv_p t}\right) \\ -\frac{1}{\omega_r^2 - k^2 v_p^2}\left(ikv_p\cos(\omega_r t) + \omega_r\sin(\omega_r t) - ikv_p e^{-ikv_p t}\right). \end{array} \tag{2.35}$$

As for the linearised Eulerian solution, this expression presents some singularities. Except for $v_p^* = 1$ and $\tau^* > 0$, a limit can analytically be found. Spatial free surface deformation profiles for both theoretical solutions are plotted in Figure 2.24 for $\tau^* = 0$ and $v_p^* = 0.5, 1, 2, 10$ and 50. For $\tau^* \neq 0$ (not shown), no important differences appear between the solutions, while for $\tau^* = 0$, the form and amplitude of the wave more or less differ. When a strong frequency dispersion appears for the linearised Eulerian solution, *i.e.* $v_p^* = 1$ and $\tau^* = 0$, as expected the LSWE solution does not reproduce it and the amplitude of the wave is higher.

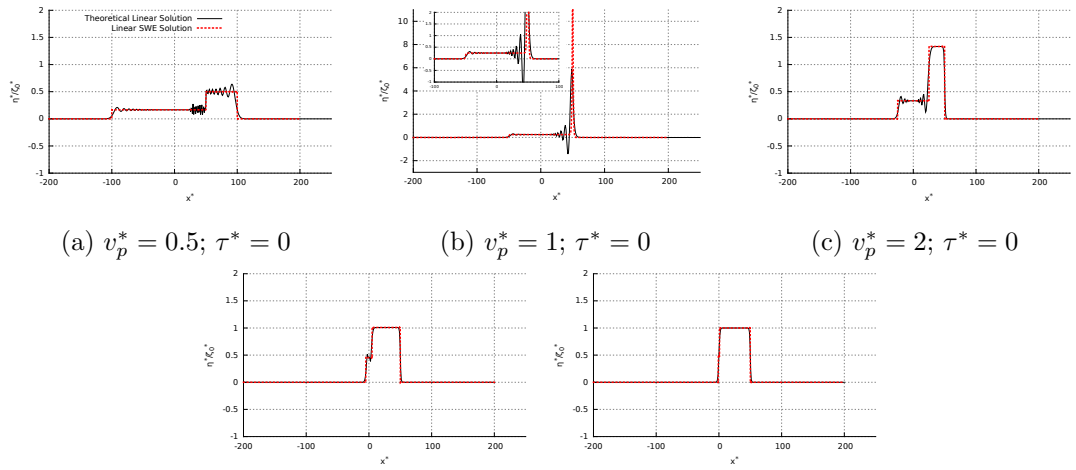

(a) $v_p^* = 0.5$; $\tau^* = 0$ (b) $v_p^* = 1$; $\tau^* = 0$ (c) $v_p^* = 2$; $\tau^* = 0$

(d) $v_p^* = 10$; $\tau^* = 0$ (e) $v_p^* = 50$; $\tau^* = 0$

Figure 2.24: Free surface profiles at $t^* = T^*$ for $L^* = 50$ and different values of v_p^* and $\tau^* = 0$. The black line is the linear Euler solution 2.21-2.23, and the dashed red line is the analytical LSWE solution 2.34-2.35. The scale of the Figure 2.24b is different from the others, the encapsulate figure is a zoom.

2.7 Conclusions

A semi-analytical expression of the free surface elevation induced by a simple seismic-like motion of the sea ground has been established in a linear theory framework as a function of τ^* (rise time in the vertical direction) and v_p^* (rupture velocity along the horizontal direction), which are the dimensionless temporal parameters of a schematic fault revealed by the dimensional analysis. The derived solution permits to study and conclude about

two aspects: the maximal amplitude η^*_{max} reached by the first wave (as a function of the amplitude of bottom upthrust ζ^*_0) and the validity of the long-wave assumption of the shallow water equations (SWE).

Regarding the maximal amplitude η^*_{max}/ζ^*_0, it was observed that:

1. when τ^* is large (*i.e.* slow vertical motion), v^*_p does not impact the maximal amplitude. On the contrary, when τ^* is small (*i.e.* rapid vertical motion), v^*_p influences it a lot.

2. Around the particular values $v^*_p = 1$ and $\tau^* = 0$, there is a resonance phenomenon. The free surface amplitude is amplified compared to the deformation of the ground, by a factor depending of the deformation's length within the considered range of conditions. The maximal amplitude could be approximated by a power function of L^* (see equation 2.24).

3. The resonance remains during the propagation phase even if it is slightly reduced.

It has been verified that this resonance phenomenon remains when non-linear effects are included by using a fully non-linear and dispersive numerical model. Furthermore, if ζ^*_0 is large enough, solitary waves appear after a certain time/distance and remain stable in time.

To evaluate the impact of timescales on the validity of the shallow water equations, an energy ratio ε was defined evaluating the fraction of potential energy which is not properly handled by the SWE (as this energy is associated with wave lengths shorter that the non-dispersive limit $L \approx 30h$) over the total potential energy. It comes that:

1. There is also a resonance around $v^*_p = 1$ and $\tau^* = 0$. With these exact values and $L^* = 50$, the energy outside the shallow-water range is more than half of the total energy.

2. During the propagation, ε reaches an asymptotic state which depends of τ^*: the larger τ^*, the smaller ε, except for $v^*_p = 1$ and $\tau^* = 0$ where ε remains important. This analysis has thus permitted to better identify in which cases models based on the SWE can be employed, or conversely should not be used.

Finally, a solution for the Linear Shallow Water Equations was developed. Compared to the linearised Eulerian solution, the differences are important when the frequency dispersion effects are more important *i.e.* $\tau^* = 0$ and $v^*_p = 1$. For the latter, the amplitude of the generated wave is higher.

Chapter 3

Application to the March 1947 New Zealand event

Le but de l'analyse théorique, développée dans le Chapitre 2, est de pouvoir l'appliquer à des évènements réels, et de rapidement estimer si une génération cinématique permet d'améliorer les modèles numériques. Ainsi en premier, on teste si les codes issus de Telemac2D sont bien capables de représenter le phénomène de résonance dans le cas théorique avant de l'appliquer à un cas réel: celui du tsunami de mars 1947 qui frappa la Nouvelle Zélande. Ce tsunami fut généré par une source sismique particulièrement lente. En effet, cet événement est associé à un "tsunami earthquake" avec une vitesse de rupture de l'ordre de $300m/s$*. En idéalisant cette source, les paramètres temporels adimensionnels* v_p^* *et* t_r^* *rentrent dans la zone de résonance définie au Chapitre 2. Cet événement est modélisé avec le modèle Saint-Venant de Telemac2D afin d'illustrer le possible impact de ces paramètres. Plusieurs types de déformation du fond marin sont testés: un modèle instantané et trois modèles cinématiques avec* $v_p = 300m/s$ *et différentes valeurs de* t_r*. Au final, il s'avère que la vitesse de rupture a une grande influence sur les hauteurs de vagues générées corroborant les résultats de l'analyse théorique. Les vagues sont amplifiées.* t_r *n'influence que peu les résultats. Pour aller plus loin, le cas avec* $v_p = 300m/s$ *et* $t_r = 0s$ *est simulé avec le modèle de Boussinesq de Telemac2D. En se basant sur la théorie, des effets dispersifs sont attendus dès la génération. Cependant peu de différences apparaissent entre les modèles numériques de Boussinesq et de Saint-Venant, même en diminuant la vitesse de rupture à* $v_p = 150m/s$*. Trois suppositions peuvent être suggérées pour ce résultat: la théorie a surestimé les effets dispersifs, la distance de propagation n'est pas suffisante pour les laisser se développer, ou encore le maillage utilisé n'est pas adapté pour modéliser ce type de phénomène.*

3.1 Case of resonance with Telemac2D

To justify the use of Telemac models to simulate events close to the resonance zone as defined in Chapter 2, the analytical case of a generation of waves by an idealised sea floor deformation with $v_p^* = 1$ and $\tau^* = 0$ is reproduced with Telemac2D.
First the numerical results from the Non-Linear Shallow Water Equations (NLSWE) model of Telemac2D, are compared to the theoretical free surface obtained with the Linear Shallow Water theory (see section 2.6) in a linear situation. The same case is treated with the Boussinesq model of Telemac2D, and compared to the theoretical potential Euler model (see section 2.2).

3.1.1 Non-linear Shallow Water model

We start with the NLSWE model of Telemac2D. For this case, five regular meshes are built with $dx^* = \frac{dx}{h} = 0.01; 0.1; 0.3; 0.5; 1$, where dx is the mesh element size and h the uniform water depth. The non-dimensionalisation used here is the same as in the previous Chapter 2. We supposed than the amplitude of the ground deformation is small enough ($\zeta_0^* = 0.001$) to neglect the non-linearity and we define the CFL number (Courant, Friedrichs and Lewy) as: $CFL = \sqrt{gh}\frac{dt}{dx}$, dt the numerical time step. The latter is adapted in order to get $CFL = 1; 0.8; 0.5; 0.1$. To evaluate the numerical model, the numerical free surface deformation obtained at the end of the ground deformation ($t^* = T^*$) is compared to the theoretical one. For each value of the CFL, a study of convergence is performed. The values of dx^* is decreased adapting dt^* to keep a constant value of CFL. Figure 3.1 shows the different numerical free surfaces modeled for the different values of CFL and meshes.

For every value of the CFL, the convergence is not reached before the appearance of a non-physical deformation of the free surface at $dx^* = 0.01$. The time step has an important impact on the result. Indeed, if we focus only on the meshes of $dx^* = 0.3$ and $dx^* = 0.5$, Figure 3.2, the amplitude strongly varies with the CFL.

Following the work of Burwell et al. [2007], a precise analytical study of the numerical model of Telemac would permit to explain this behaviour, that is similar to the case of the propagation of a solitary wave (presented later in section 4.4). Even if the case here does not really treat the propagation of a wave (it is more like a generation) and the numerical scheme is different, the results tend toward the same behaviour of the propagation of short waves in the study of Burwell et al.. For $CFL < 0.7$, the numerical diffusion seems to decrease with the CFL while the numerical dispersion increases. In the study of Burwell et al., they considered that waves are not very well resolved for $k.dx > 0.2$. In our case, two wavelengths (L_i) can be drawn: one for the global deformation of the free surface,

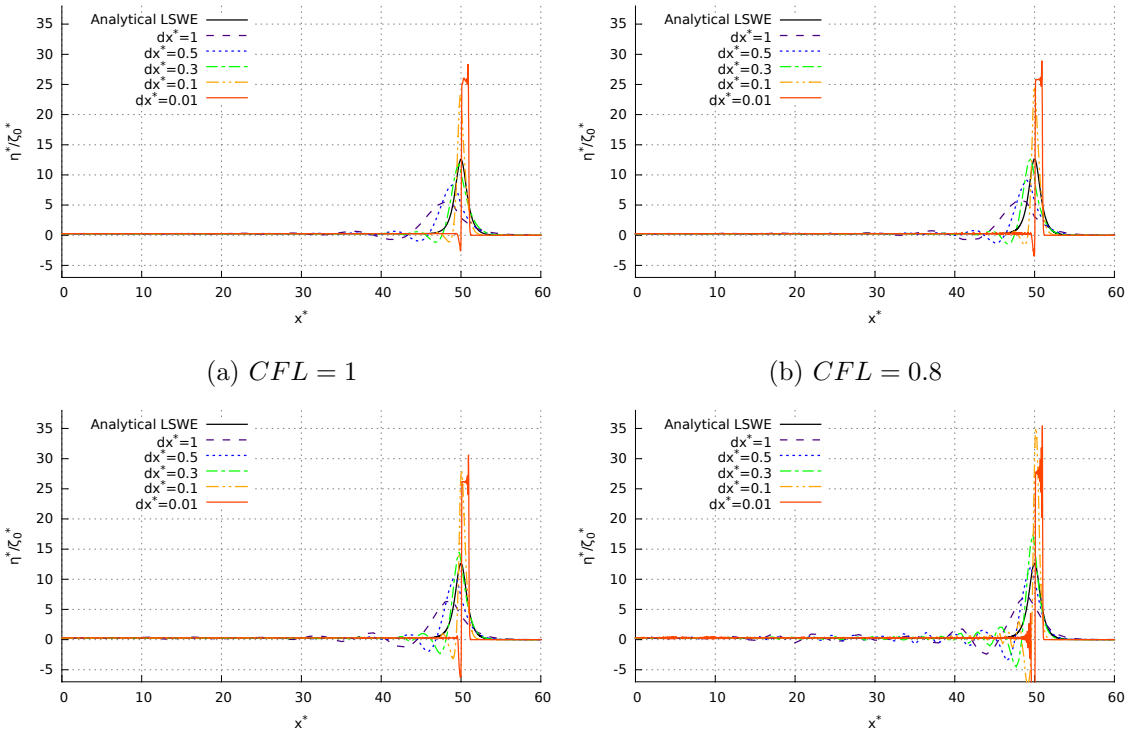

(a) $CFL = 1$ (b) $CFL = 0.8$

(c) $CFL = 0.5$ (d) $CFL = 0.1$

Figure 3.1: Resonance phenomenon simulated with Telemac2D and NLSWE – Spatial profiles of the free surface deformation at the end of the ground motion ($t^* = T^*$ with an accuracy of dt^*) for different values of CFL and dx^*. The black line is the analytical free surface calculated from the LSWE theory. The coloured dashed curves represent numerical free surface profiles calculated with the different meshes.

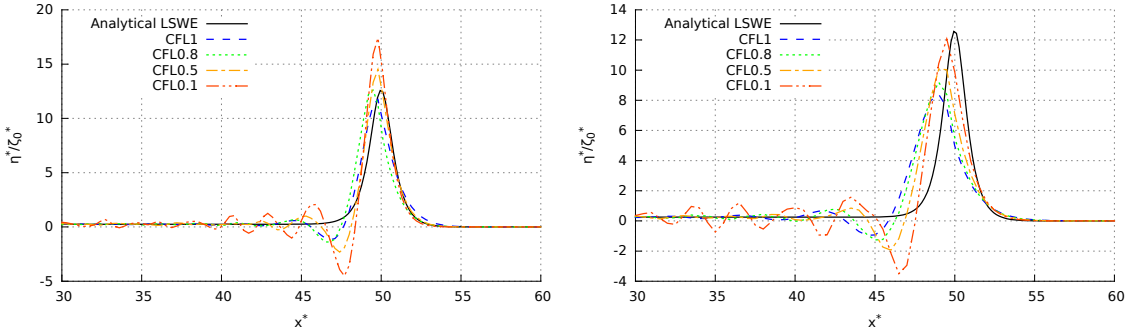

(a) $dx^* = 0.3$ (b) $dx^* = 0.5$

Figure 3.2: Resonance phenomenon simulated with Telemac2D and NLSWE – Spatial profiles of the free surface deformation at the end of the ground motion ($t^* = T^*$) for $dx^* = 0.3$ and $dx^* = 0.5$ meshes. The black line is the analytical free surface calculated from the LSWE theory. The coloured dashed curves are the different values of the CFL.

around $\frac{L_1}{h} \simeq 106$ (not perceptible on graphs) and one for the bigger front wave, around $\frac{L_2}{h} \simeq 13$. The corresponding wave number $k_1.dx$ is included between 0.0007 and 0.07 and $k_2.dx$ between 0.005 and 0.5. Only the first wave should be badly represented with $dx^* = 0.5$ and $dx^* = 1$. The case where $CFL = 0.8$ and $dx^* = 0.3$ is identified as the best result. However, it can be noticed that the amplification of the first wave is reproduced for every case, thus, the NLSWE model of Telemac is capable to model events close to the resonance zone. However, a study of numerical convergence should be done in the future.

3.1.2 Boussinesq model

This theoretical case is performed again with the Boussinesq model of Telemac2D. This time only four meshes are tested with $dx^* = 1, 0.5, 0.3, 0.1$ and the four previous values of CFL. As for the NLSWE, numerical free surfaces are compared to the analytical free surface from the linear theory (section 2.2) at the end of the ground motion, see Figure 3.3.

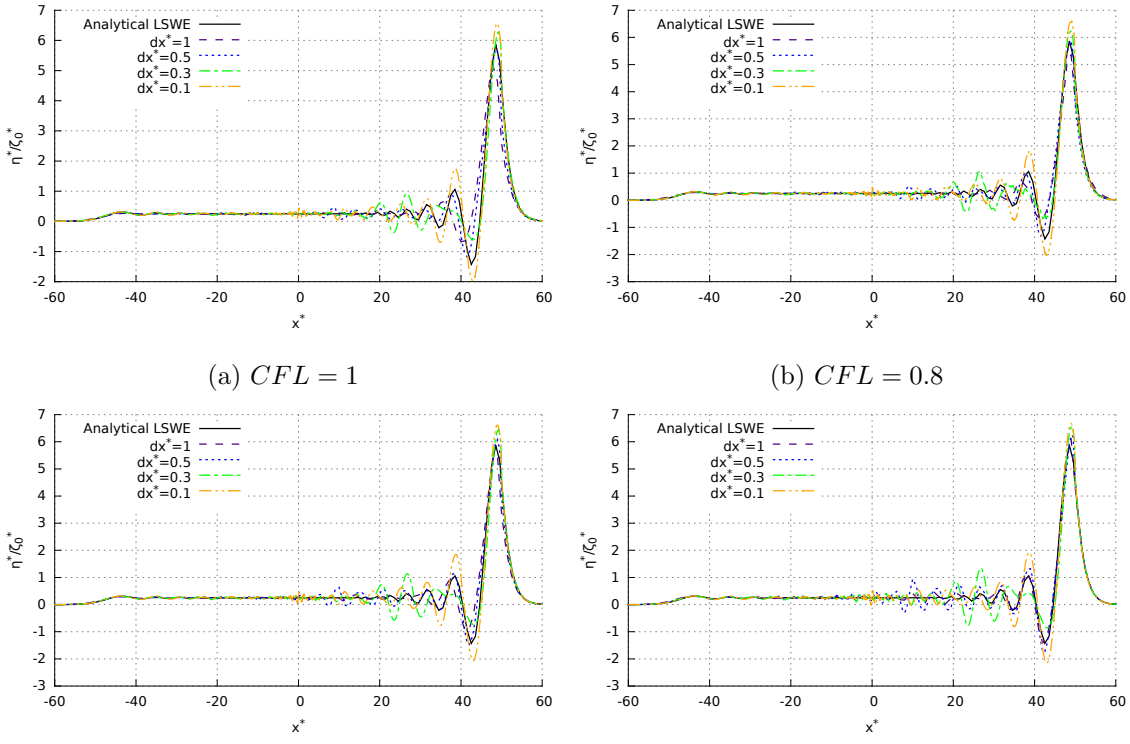

(a) $CFL = 1$ (b) $CFL = 0.8$

(c) $CFL = 0.5$ (d) $CFL = 0.1$

Figure 3.3: Resonance phenomenon simulated with Telemac2D and Boussinesq model – Spatial profiles of the free surface deformation at the end of the ground motion ($t^* = T^*$ with an accuracy of dt^*) for different values of CFL and dx^*. The black line is the analytical free surface calculated from the linear theory. The coloured dashed curves represent numerical free surface profiles calculated with the different meshes.

Unlike the NLSWE model, the numerical results match well the theoretical result. The amplitude of the front wave seems to converge while the amplitude of the shorter dispersive waves increases with smaller time step for every CFL. Spatial free surface profiles for meshes $dx^* = 0.3$ and $dx^* = 0.5$ are plotted in Figure 3.4 for different values of CFL. The curves slightly differ, the CFL does not impact. In this case, the mesh with $dx^* = 0.5$ better represents the dispersive tail than the mesh with $dx^* = 0.3$, that poorly represents it. It appears clearly that the Boussinesq model of Telemac2D reproduces well the resonance.

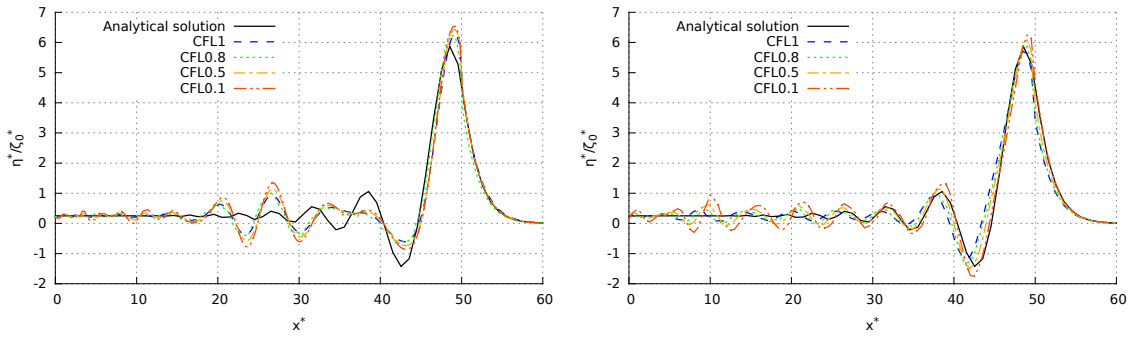

(a) $dx^* = 0.3$ (b) $dx^* = 0.5$

Figure 3.4: Resonance phenomenon simulated with Telemac2D and Boussinesq model – Spatial profiles of the free surface deformation at the end of the ground motion ($t^* = T^*$) for $dx^* = 0.3$ and $dx^* = 0.5$ meshes. The black line is the analytical free surface calculated from the linear theory. The coloured dashed curves are the different values of the CFL.

3.2 The 1947 New Zealand event

3.2.1 Context and data

"Tsunami earthquake" is a category of events proposed by Kanamori [1972], which generates larger tsunamis than suggested by the seismic magnitude. Generally, they invoke slow rupture velocities, $1km/s$ or less. A few of these events are presented in Table 3.1, for which the temporal parameters v_p^* and τ^* are estimated. When the data is available, the rise time is estimated here with: t_r = event's duration − fault's length/v_p.

In light of our special interest, we illustrate the present study with the 25^{th} March 1947 event that occurred near New Zealand (seismic magnitude $M_w = 7.1$) [see Bell et al., 2014; Downes and Stirling, 2001]. Figure 3.5 shows the domain of application and the location of the event.

Event	τ^*	v_p^*	Reference
Sanriku, 1896	X	~ 8.65	Kanamori [1972]
Nicaragua, 1992	$0.002 - 0.0123$	$5 - 33.86$	Kikuchi and Kanamori [1995]
Mentawai, 2010	$0.02 - 0.048$	$5 - 15$	Lay et al. [2011]
Aleutian, 1946	X	$6.52 - 11.3$	López and Okal [2006]
Java, 2006	$0.025 - 0.033$	$5 - 15$	Ammon et al. [2006]
New Zeland, 1947	$0.034 - 0.36$	$0.89 - 10$	Bell et al. [2014]

Table 3.1: 1947 New Zealand event – Temporal parameters v_p^* and τ^* estimated for few tsunami earthquakes. The "X" indicates unknown values.

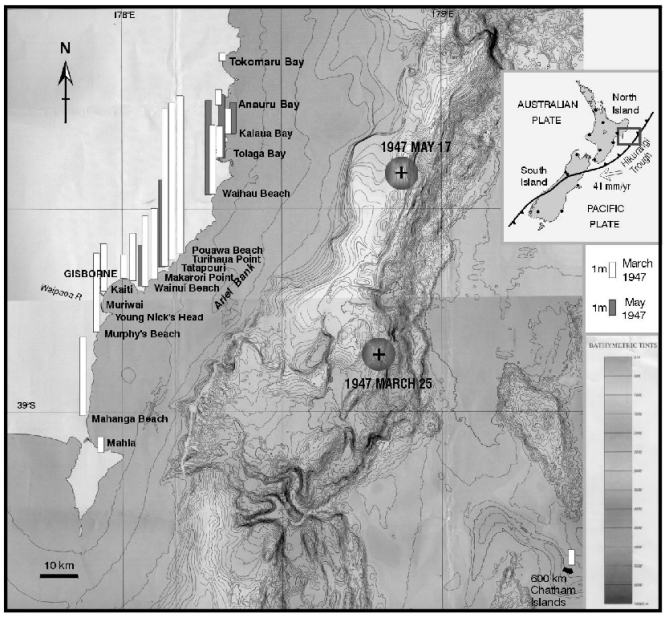

Figure 3.5: 1947 New Zealand event – Locations of the March and May 1947 Gisborne earthquakes, estimated tsunami run-ups, the main features of the plate boundary through New Zealand (inset), and the location of seismographs of the 1947 New Zealand seismograph network (inset). Bathymetry (contour interval 50 m) is from Lewis et al. (1997). Figure reprinted from the paper of Downes and Stirling [2001].

The fault rupture is close to the Hikurangi subduction margin and the tsunami was observed along the coast from Tokomaru Bay to Mahia Peninsula. The fault characteristics and information are summed up in Table 3.2. With a water depth near the source around $1500m$ and a sea floor deformation ζ_0 around $1m$, the ratio $\frac{\zeta_0}{h} \sim 6\ 10^{-4}$ is much smaller than 1, thus this generation can be considered as linear.

The water depth h is considered varying between 100 and $3000m$ at the fault area. If we assume that $v_p \in [150; 300] m/s$ with a mean value of $175m/s$, then $v_p^* \in [0.87; 9.57]$ with a mean value of $v_p^* = 1.44$. The smallest v_p^* is reached for $v_p = 150m/s$ and a depth of $3000m$. The largest v_p^* is reached for $v_p = 300m/s$ and $h = 100m$.

Date	03/25/1947
Epicentre Location	38.92SS, 178.24E
Fault Characteristics	
Length	$55km$
Width	$50km$
Depth of the fault	$5 - 12km$
Dip angle	$8°$
Rise time (fault's rupture)	$10 - 20s$
Water depth near the source	$\sim 1500m$ (between 100 and $3000m$)
Rise time t_r	$\sim 90s$ (between 60 and $120s$)
Rupture velocity v_p	$\sim 175m/s$ (between 150 and $300m/s$)
Deformation of the ground ζ_0	$\sim 1m$

Table 3.2: 1947 New Zealand event – Estimation of the characteristic parameters of the 25 March 1947 event, which occurred in the Offshore Poverty Bay (NZ). These values were given in personal communication.

Likewise, if $t_r \in [60; 120]s$ with a mean value of $t_r = 90s$, we have $\tau^* \in [0.034; 0.36]$ with a mean value of $\tau^* = 0.2$. The smallest τ^* is reached for $t_r = 60s$ and a depth of $100m$. The largest τ^* is reached for $t_r = 120s$ and $h = 3000m$. These numerical values were provided by Dr. William Power of the Institute of Geological and Nuclear Sciences (GNS Sciences, personal communication).
Following the study developed in Chapter 2, the amplification of the generated wave η_{max}/ζ_0 of the $1D$ theoretical solution is calculated for an idealized step deformation with the spatial parameters of this event.

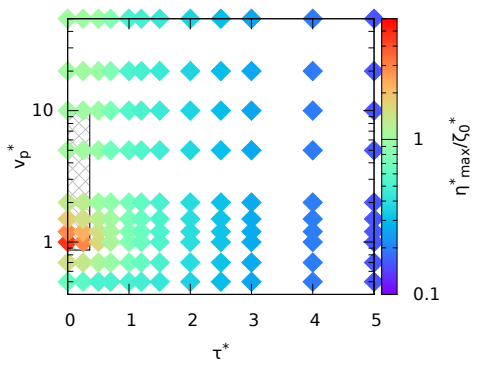

Figure 3.6: 1947 New Zealand event – Maximal amplitude of the free surface for $L^* = 35$ at $t^* = T^*$. Grey zone represents the ranges of values of the temporal parameters τ^* and v_p^* of the 1947 New Zealand event. (see Table 3.2).

The corresponding panel is plotted in Figure 3.6 as function of v_p^* and τ^*. Considering

the range of temporal parameters described earlier, this event could enter in the resonance zone as previously defined in Chapter 2. Hence, we can suspect that generated water waves should be larger than the numerical ones generated by an instantaneous model of generation, as suggested by Bell et al. [2014]. This hypothesis may also explain the high water waves observed for this event. To confirm this conclusion, this event is simulated with numerical models, varying the temporal parameters of the source (v_p and t_r) and using the NLSWE then Boussinesq models of Telemac2D.

3.2.2 Resolution grid and mesh

The bathymetry grid is provided by the National Institute of Water and Atmospheric Research (NIWA), Mitchell et al. [2016]. It delivered a $250m$ ($\sim 300m$ in the Mercator projection) grid resolution of New Zealand and its region. The numerical domain is bounded between the latitudes $-39.5°$ and $-37°$ and the longitudes $177.5°$ and $180°$, focusing on the Gisborne coast. Figure 3.7a shows the bathymetry of the concerned zone in the Mercator projection.

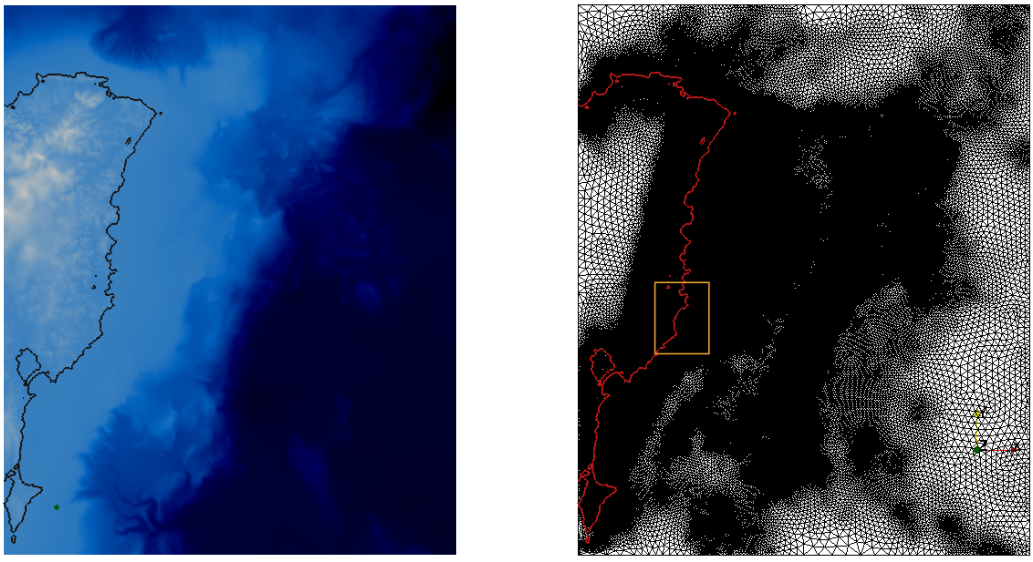

(a) width $\sim 240km$ (b) width $\sim 240km$

Figure 3.7: 1947 New Zealand event – Numerical domain considered. Figure 3.7a represents the topography given by the NIWA, the black line is the coastline. Figure 3.7b is the mesh built for the case. Yellow box is the boundary of the zoom plotted in Figure 3.8.

The mesh is built such as the element size is adapted to the bathymetric gradient: more important the gradient, smaller the elements are. Using this method, the shoreline and

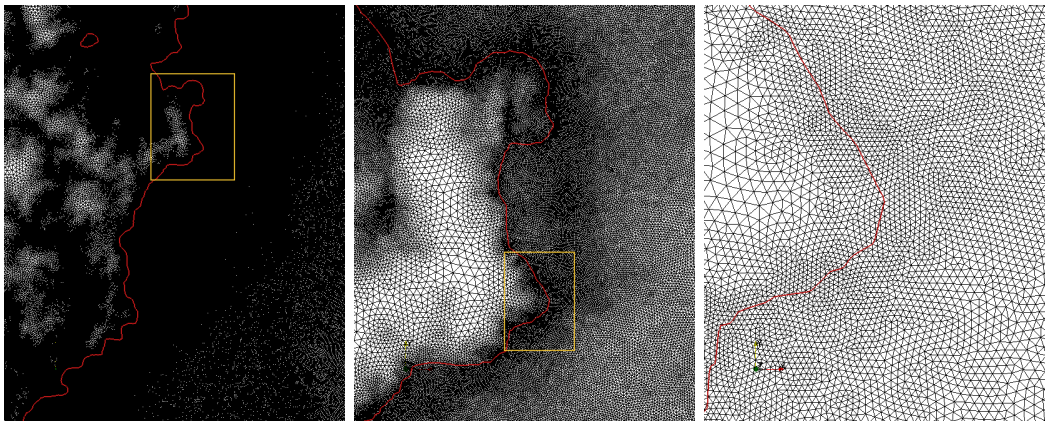

(a) width $\sim 30km$ (b) width $\sim 7.5km$ (c) width $\sim 2km$

Figure 3.8: 1947 New Zealand event – Details of the mesh built for the event. The yellow boxes correspond to the boundary of the next zoom. The red line is the initial coast line.

the fault areas are refined as we can see in Figures 3.7b and 3.8. The smaller elements are around $15m$ while the largest reach $9km$, finally giving a 1.7 millions nodes mesh. As the data corresponds to flooded measurements, the inland of the island is included in the numerical domain. This mesh is the final result of a convergence study on the numerical water depth results at the coastline (black line in Figure 3.7a).

3.2.3 Kinematic generations

The co-seismic source parameters were given by Bell et al. [2014]. Four configurations of generation are tested. The four models are finite fault models: the global fault is divided into 191 subfaults with their own characteristics. Then, as suggested by Dutykh et al. [2013], kinematic finite fault models are used: each subfault is activated according to the rupture velocity v_p and the motion of the seafloor is regulated by the rise time t_r. Only the $v_p = 300m/s$ value of rupture velocity is used because it is the most plausible from seismic data. The different source models and their designation are presented in Table 3.3.

Theoretically, $\tau^* < 1$, thus, the time history function of the ground motion should not

Type of deformation	v_p [m/s]	v_p^*	t_r [s]	τ^*	Generation duration [s]	Model designation
Instantaneous	$\to \infty$	$\to \infty$	0	0	0	ID
Kinematic	300	$[2.47; 9.57]$	0	0	190	KD_0
			60	$[0.034; 0.18]$	250	KD_60
			120	$[0.068; 0.36]$	310	KD_120

Table 3.3: 1947 New Zealand event – Generation models considered for this event. The dimensionless parameters are estimated for a water depth varying between 100 and 3000 m.

impact the generated wave, see Hammack [1973]. In Telemac, the motion of the seafloor is initiated by uplifting the bathymetry:

- if $t_r \neq 0$ then $z_f(i,t) = z_f(i,0) + \sum_k O_k(i)\frac{1}{2}(1 - \cos(\pi\frac{t-t_k}{t_r}))$,
- if $t_r = 0$ then $z_f(i,t) = z_f(i,0) + \sum_k O_k(i)H(t-t_k)$,
- if the deformation is instantaneous then $z_f(i,t) = z_f(i,0) + \sum_k O_k(i)$.

Where z_f is the sea floor elevation, $O_k(i)$ is the amplitude of the sea floor deformation generated by the subfault k at the point i, estimated with the calculation of Okada [1992]. The activation time t_k corresponds to the rupture start time of the subfault taking into account the value of the rupture velocity v_p. H is the Heaviside step function. Applying this method, the four free surface deformations are obtained at the end of the ground motion, see Figure 3.9.

For the kinematic models (models KD_0, KD_60, KD_120), as the generation duration is longer, the wave already begins to propagate creating a principal wave in the direction of the coast. To compare the same thing, the spatial free surface deformation is observed for the same time, $t = 310s$, when the ground motion has stopped for all models, see Figure 3.10.

At this time, differences between models appear not due to propagation time but due to the generation model nature. The free surface deformation obtained for the model ID is smaller and more diffused than the one from kinematic models. The signal is concentrated towards the coast and diametrically opposed while for the kinematic generations, the signal is focused towards the coast and the North. Moreover, the depression in front of the main wave is smaller for the instantaneous model than the others. The impact of the rupture velocity v_p is significant while the rise time t_r does not seem to have an important role: qualitatively, there is no difference between the models KD_60 and KD_120. Between the models KD_0 and KD_60, the second wave towards offshore is more diffused for the second model: two waves are distinct for KD_0 while only one wider appear for KD_60.

3.2.4 Numerical results from Non-Linear Shallow Water models

The numerical simulations include the generation part and one hour of propagation. As there are no measurements during this event, the quality of the propagation of the numerical wave can not be evaluated. However, in Figure 3.11, snapshots of the propagation of the free surface deformation are presented for the model ID.

We can see that one hour of propagation is enough to visualise the run-up of the leading

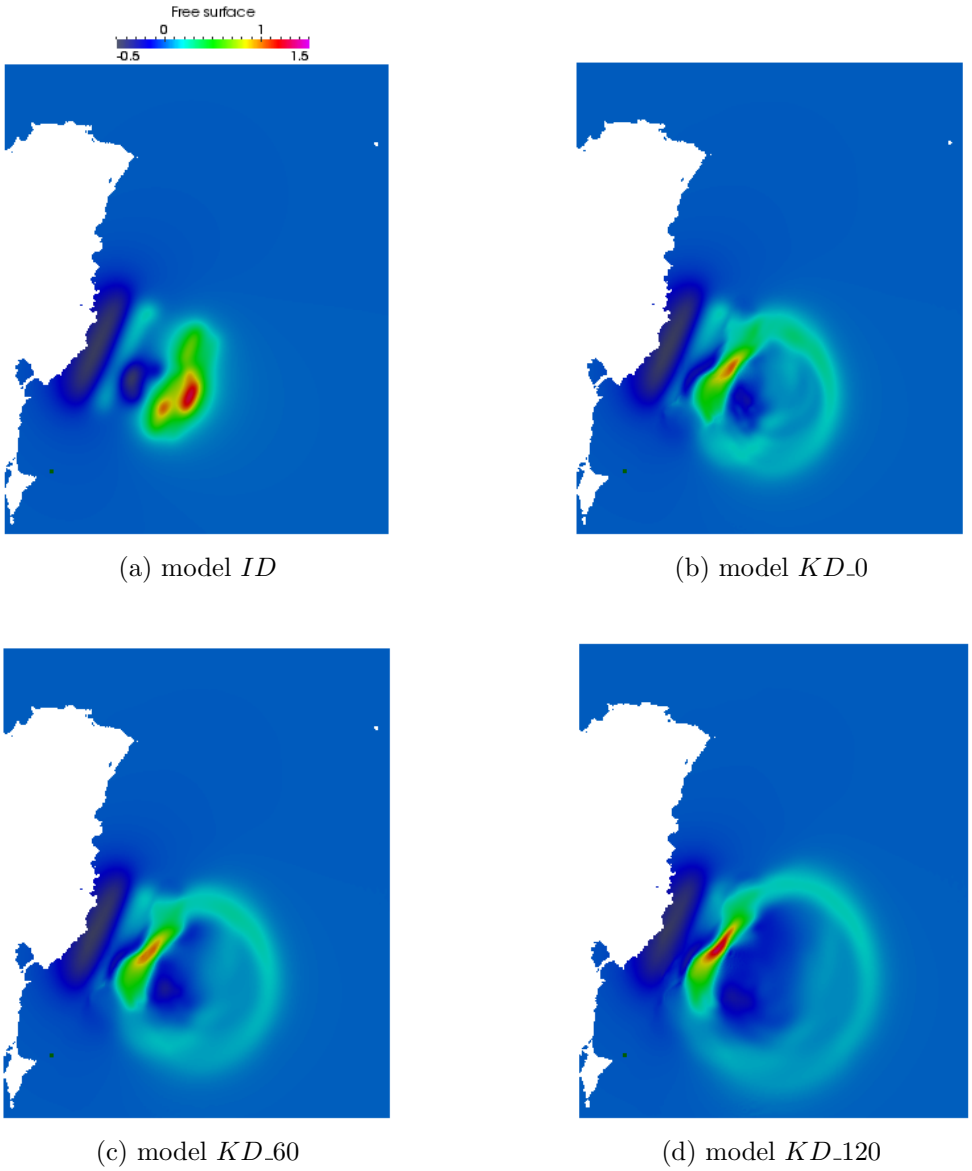

(a) model ID

(b) model KD_0

(c) model KD_60

(d) model KD_120

Figure 3.9: 1947 New Zealand event – Free surface deformation (in m) at the end of the ground motion for the four generation models calculated with the NLSWE model of Telemac2D. The indicated time corresponds to the time of end of ground motion varying between $t = 0s$ for the instantaneous deformation to $t = 310s$ for the generation with $v_p = 300m/s$ and $t_r = 120s$.

wave on the coast.

To compare the different generation models, the temporal maximal free surface deformation is calculated during the entire event and plotted in Figure 3.12.

The transect $A - A'$ is defined as shown in Figure 3.12. To permit quantitative comparison between models, the maximal free surface elevations reached during the propagation are plotted along this transect in Figure 3.13, only for negative bathymetry.

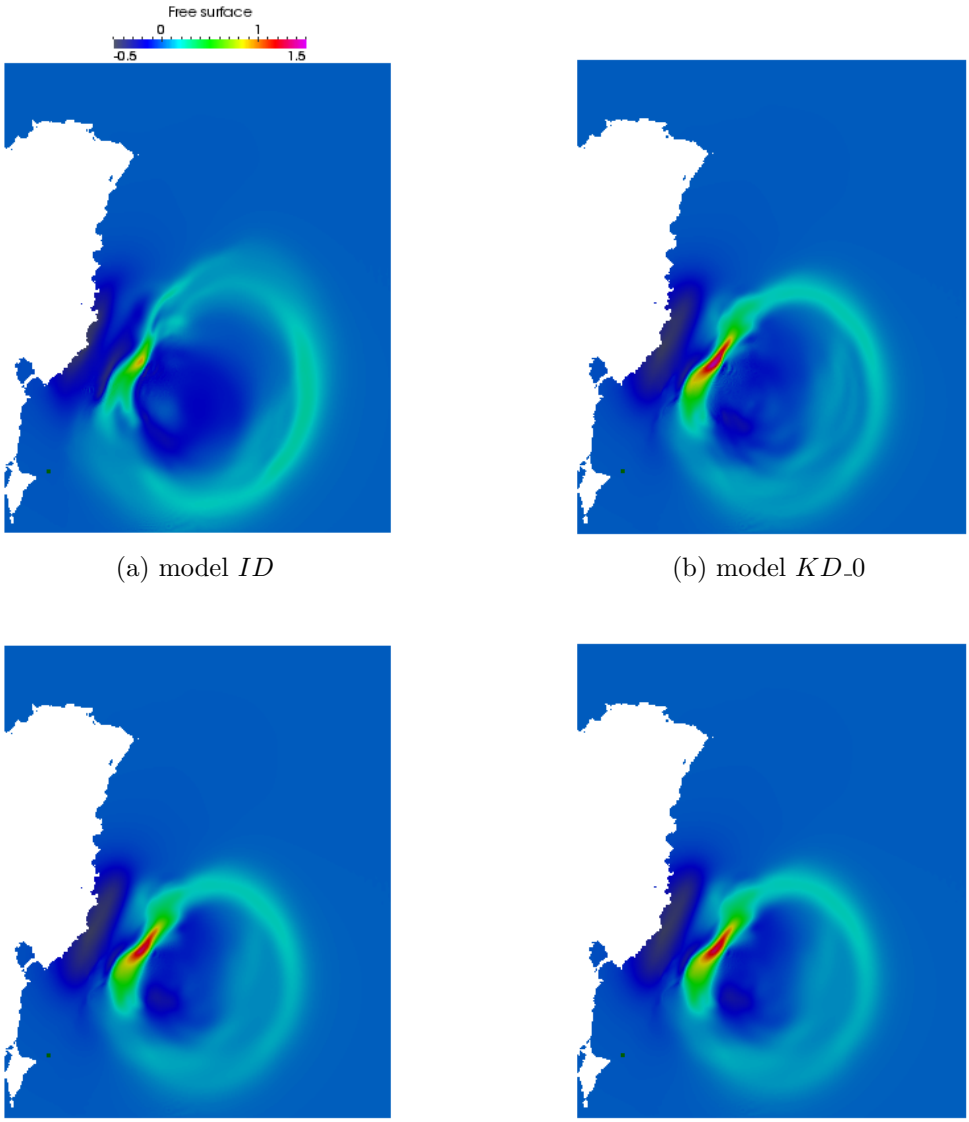

(a) model ID

(b) model KD_0

(c) model KD_60

(d) model KD_120

Figure 3.10: 1947 New Zealand event – Free surface deformation (in m) for the four generation models calculated with the NLSWE model of Telemac2D at $t = 310s$.

Excepted at the fault area, the model ID produces smaller maximal amplitudes than kinematic models. The maximum are focused on the area of generation and the Waihou Bay (see map in Figure 3.5). While for the kinematic generations, the maxima are bigger, closer to the coast and cover a larger area. There are no significant differences between the maximal results obtained by kinematic models, excepted at the initial generation zone where the maximum are slightly higher for KD_0 than for KD_60 and KD_120 models. Moreover, the curves issued of KD_60 and KD_120 are superimposed, confirming the similitude between both models. As previously observed for the initial free surface ele-

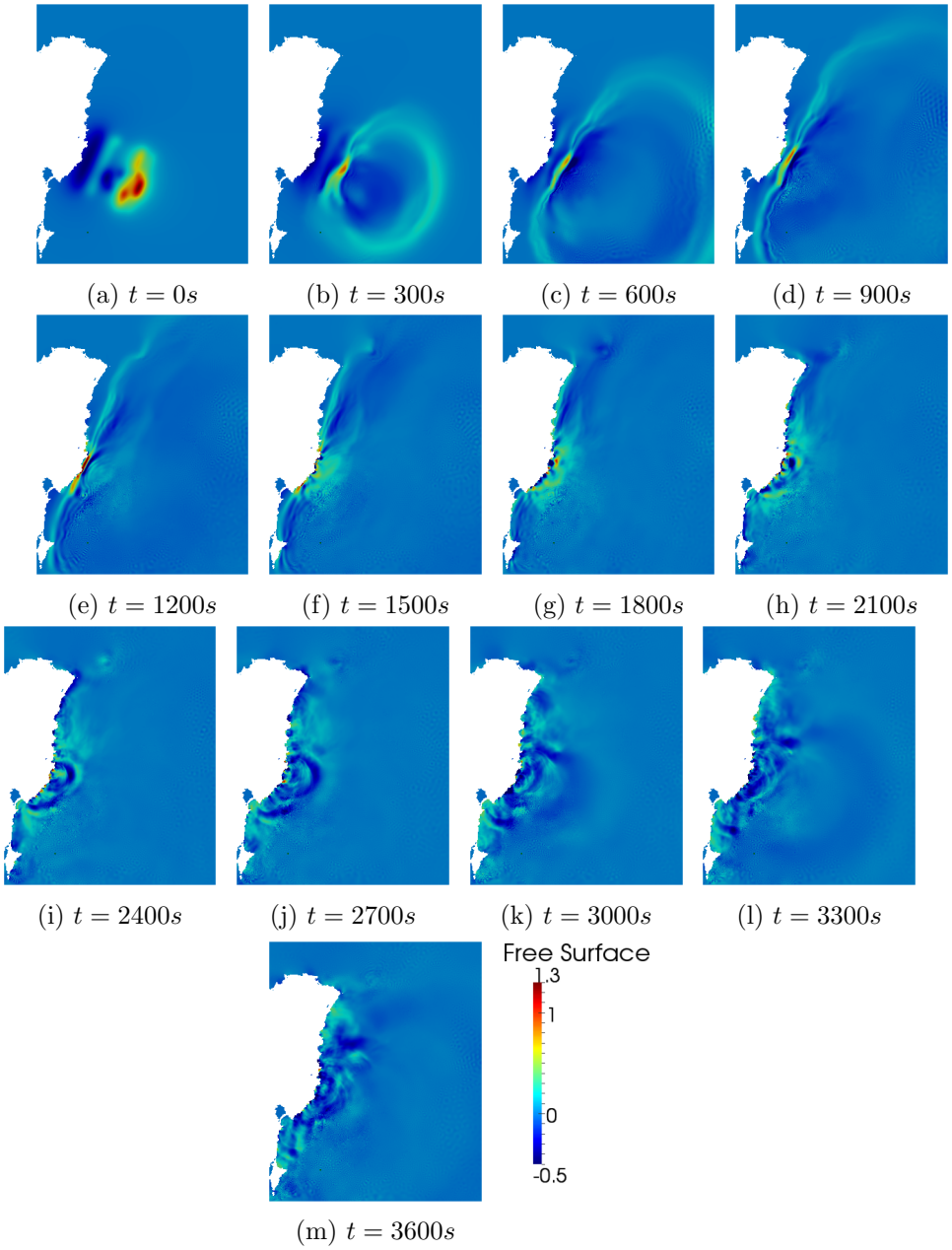

Figure 3.11: 1947 New Zealand event – Snapshots of the free surface (in m) every 5 min. during the numerical propagation of the wave generated by an instantaneous sea floor deformation (model ID) with the NLSWE model of Telemac2D.

vation, the impact of the rupture velocity v_p clearly appears and the rise time t_r slightly influences the wave generated. For each value of t_r, the associated τ^* stays small, less than 1 (see Table 3.2), which explains its minor role.

Finally, the impact on the coast can be quantified by comparing numerical results to observed data from Downes and Stirling [2001]. However, there is a vagueness about the nature of the data: Downes and Stirling [2001] considered them as estimated run-ups

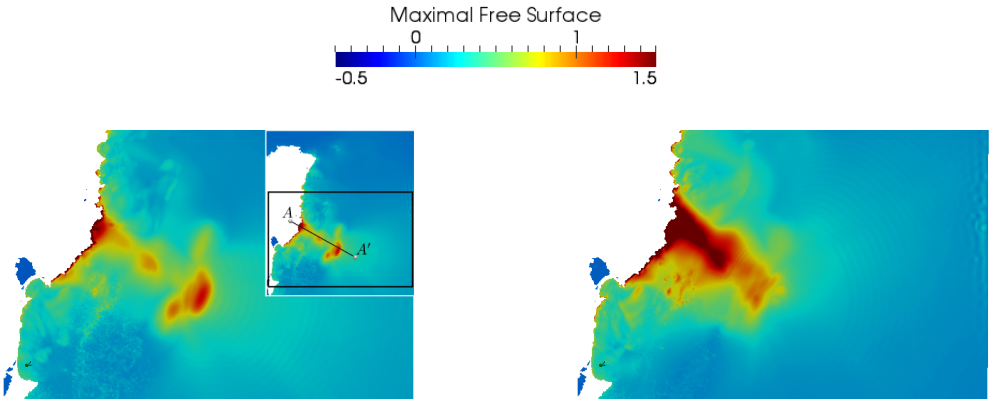

(a) model ID (b) model KD_0

(c) model KD_60 (d) model KD_120

Figure 3.12: 1947 New Zealand event – Snapshots of the temporal maximal free surface elevation (in m) calculated during one hour with the NLSWE model of Telemac2D for the different generation models.

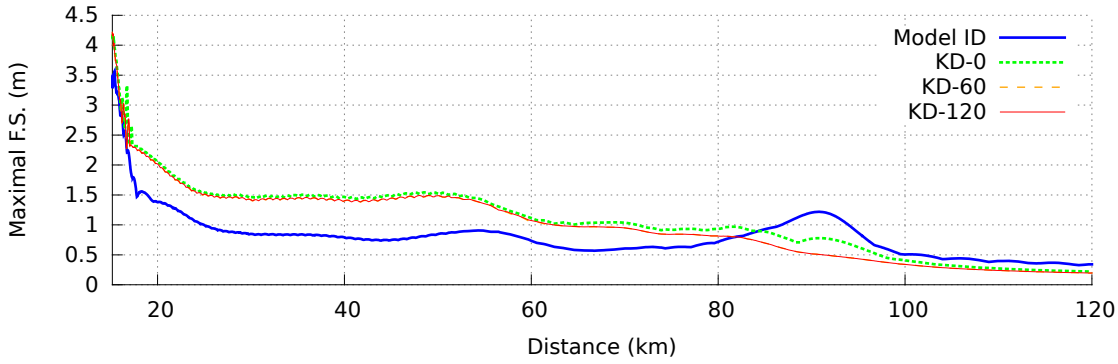

Figure 3.13: 1947 New Zealand – Maximal free surface elevations reached during the propagation along the transect $A - A'$ as defined in Figure 3.12. Only result for negative bathymetry is plotted. The colourful lines are numerical results from the different generation models. The orange and red lines are superimposed, models KD_60 and KD_120 respectively.

while they are tsunami wave heights observed at the coast for Bell et al. [2014]. In the present numerical model, the bathymetric resolution (~ 300 in Mercator projection) and then the element size ($\sim 50m$) at the coast does not permit to work on the run-up heights

as defined in Figure 3.14.

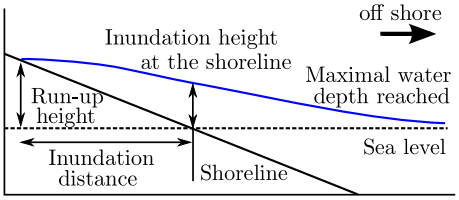

Figure 3.14: 1947 New Zealand event – Definition of the different measures during a run-up. The data given by Downes and Stirling [2001] corresponds to run-up heights. The height measured in the numerical models is the inundation height at the shoreline. The blue line corresponds to the temporal maximal free surface elevation reached during the event.

However, the inundation heights at the initial shoreline, corresponding to the temporal maximal water depth reached during the simulation, can be measured. Thus, the inundation heights issued from the different generation models are compared to the data in Figure 3.15. This comparison can be inappropriate thus it has to be considered with caution.

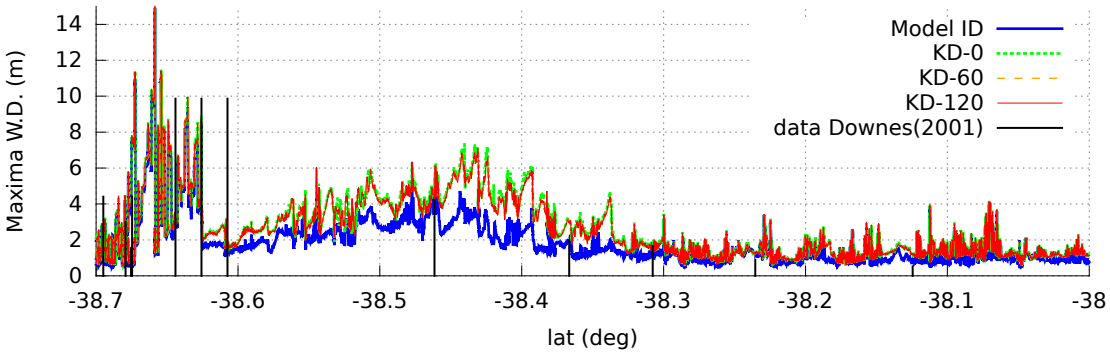

Figure 3.15: 1947 New Zealand event – Maximal water depth obtained at the coastline (black line in Figure 3.7a) during the event. The colourful lines represent the different generation models, and the black vertical bars the data of Downes and Stirling [2001]. The horizontal axis corresponds to the latitudes.

Between the latitudes $-38.6°$ and $-38.3°$, the inundation height differs between the models. This height is more important for the kinematic models and slightly smaller when t_r differs from $0s$. These results are coherent with the one found by Bell et al. [2014] and the observations done in Chapter 2. This zone corresponds to the area around the Waihou Bay. These results are also consistent with the comparison of the maximal free surface amplitude in Figure 3.12. In Figure 3.11, we can see that the wave first hits this part of the coast. Outside this zone, the models give similar results. The numerical models globally follow well the tsunami wave height data with some differences sometimes that

can be issued from an error of the observation location.

3.2.5 Boussinesq model

From the theory described in Section 2.4, an energetic ratio ε has been defined between the potential energy poorly represented by LSWE and the total potential energy as a function of v_p^* and τ^* (Equation 2.26). This ratio ε is calculated at the end of the sea floor motion for this event with the parameters in Table 3.2. The panel of ε values is represented in Figure 3.16.

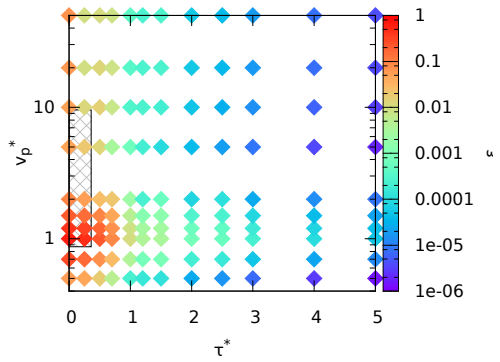

Figure 3.16: 1947 New Zealand event – Energetic ratio ε for $L^* = 35$ at $t^* = T^*$. Grey zone represents the ranges of values of the temporal parameters τ^* and v_p^* for the New Zealand 1947 event (see Table 3.2).

The temporal range that interests us is the grey zone for which ε varies between 1% to 60% approximately. For the KD_0 model of generation, the ratio varies between 4 and 9%. The Boussinesq model of Telemac2D is used to simulate this event with $v_p = 300m/s$ and $t_r = 0s$. At the end of the sea floor motion, differences appear between the Boussinesq and the NLSWE models, as shown in Figure 3.17.

Even if the global form of the generated waves are similar with a depression near the coast and a principal wave oriented North-West, the Boussinesq model gives a more complex pattern. The amplitude of the main wave is smaller with the Boussinesq model than the NLSWE model but wider. During this simulation, a strong increase of the free surface amplitude appears at the South part of the coast. This increase does not seem physical but numerical, as the Boussinesq model of Telemac2D can be more sensitive to the numerical parameters (Hervouet [2007]). Thus to calculate the maximum free surface, only 30 min. of propagation is used (this time well covers the propagation until the coast), and to compare the same thing, in this section this restriction is also applied to the NLSWE

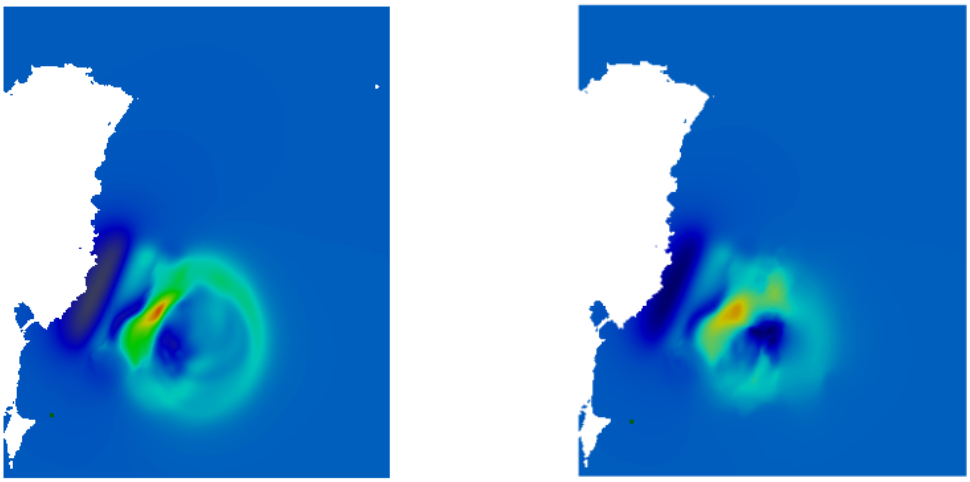

(a) NLSWE model of Telemac2D (b) Boussinesq model of Telemac2D

Figure 3.17: 1947 New Zealand event – Free surface deformation (in m) at the end of the sea floor motion, $t = 190s$, obtained with the NLSWE and the Boussinesq models of Telemac2D for $v_p = 300m/s$ and $t_r = 0s$. Same scale as Figure 3.9.

model.
The amplitude of waves during the propagation seems similar as we can see with the qualitative comparison between the spatial maximal amplitude reached in Figure 3.18 and more precisely along the transect $A - A$ in Figure 3.19. We can note that for the Boussinesq model, even if the duration of propagation has been decreased, the beginning of the numerical error is visible in the Gisborne Bay. Exempting this numerical error, small differences appear at the source area, where the Boussinesq model gives smaller waves. Moreover, there is not a distinct wave toward the North unlike for the NLSWE model. However, as shown by the spatial profile along $A - A'$, globally, the models behaves similarly even if the Boussinesq model gives slightly smaller maximal amplitude.

In front of this conclusion, we can suppose that $\varepsilon \sim 4 - 9\%$ is not big enough to say that the contribution of the dispersive effects is visible.
Thus, even if this kind of generation is seismically less probable, the generation with $v_p = 150m/s$ is tested with the NLSWE model and the Boussinesq model in order to possibly note some improvement with the latter. In Figure 3.20, we can see the initial free surface deformation, and in Figure 3.21 the propagation of the waves.

Contrary to what was expected, no wave packets develop during the propagation.

Few hypothesis can be given to justify this behaviour: as the dispersive effect is a cumula-

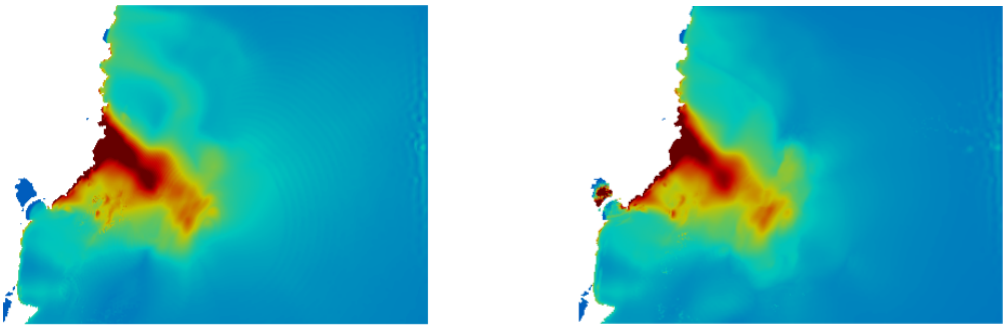

(a) NLSWE model of Telemac2D (b) Boussinesq model of Telemac2D

Figure 3.18: 1947 New Zealand event – Snapshots of the temporal maximal free surface elevation (in m) calculated during one hour obtained with the NLSWE and the Boussinesq models of Telemac2D for $v_p = 300m/s$ and $t_r = 0s$. Same scale as Figure 3.12.

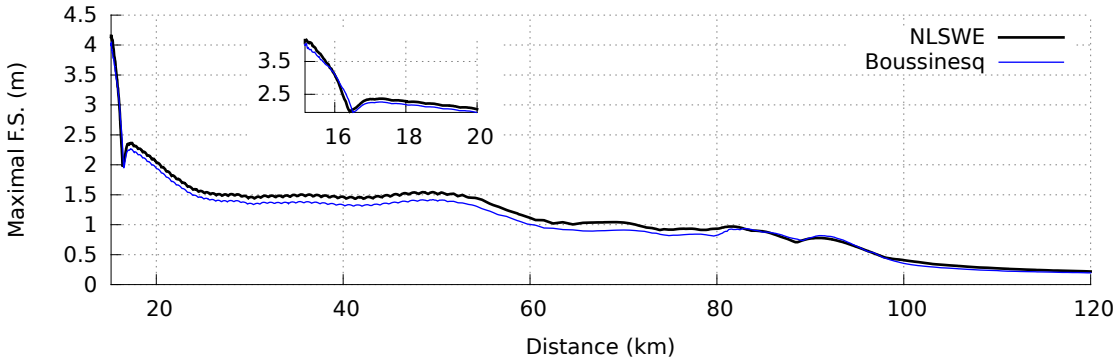

Figure 3.19: 1947 New Zealand event – Maximal free surface elevations reached during the propagation along the transect $A - A'$ as defined in Figure 3.12. Only result in the ocean part is plotted. The black and blue lines are the numerical results from the NLSWE and the Boussinesq models of Telemac2D, respectively. The model generation corresponds to KD_0. The encapsulated figure is a zoom of the global curve near the coastline (distance$\in [15; 20]km$).

tive phenomenon, the distance of propagation may not be large enough, or the estimated ε over-predicts the importance of the dispersion. Another hypothesis about the mesh can be suggested: the element sizes are too large to represent the deconstruction of the wave. Up to $25km$ of the coasts, the sizes of elements are included between $15m$ and $400m$, with a majority of $30 - 40m$ (see Figure 3.22) that can be too rough to represent a dispersive wave packet.

The maximal free surface amplitude reached during the propagation is plotted in Figure 3.23 for both models, and the result along the transect $A - A'$ are shown in Figure 3.24 (again due to numerical difficulties, only 30 min. of propagation are considered for the Boussinesq model, and thus the NLSWE model). Qualitatively, the differences between the models are more noticeable than for $v_p = 300m/s$: the maximal amplitude deforma-

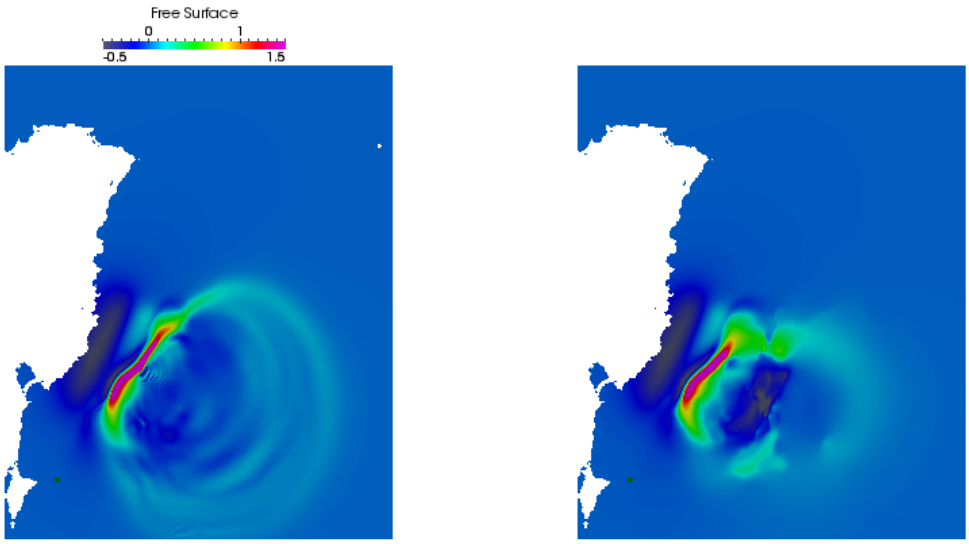

(a) NLSWE model of Telemac2D (b) Boussinesq model of Telemac2D

Figure 3.20: 1947 New Zealand event – Snapshots of the free surface elevation (in m) at the end of the generation ($t = 380s$) with the NLSWE and the Boussinesq models of Telemac2D for $v_p = 150m/s$ and $t_r = 0s$. Same scale as Figure 3.9.

tion towards the North is bigger for the NLSWE model than for the Boussinesq model, for which the over-wall distribution is more narrow. Also, along the transect $A - A'$, the numerical results from the Boussinesq model are slightly smaller than the ones from the NLSWE model. Small discrepancies are observable close to the coast but globally the trend of the curves are similar.

The maxima area is much larger for $v_p = 150m/s$ than for $v_p = 300m/s$ (Figure 3.18). The tsunami heights modeled at the coastline with the $v_p = 150m/s$ and $t_r = 0s$ generation model are compared to the one from the $v_p = 300m/s$ and $t_r = 0s$ generation model (KD_0 model) in Figure 3.25.

The rupture velocity $v_p = 150m/s$ gives a v_p^* closer to 1 than $v_p = 300m/s$, thus, as supposed, the tsunami heights are bigger in the impacted zone concerned by the wave amplification (between the latitudes -38.6 and -38.2). However, they are in a poor agreement with data in this zone and over-predicts the tsunami heights, that consolidates the idea that $v_p = 300m/s$ is more probable than $v_p = 150m/s$.

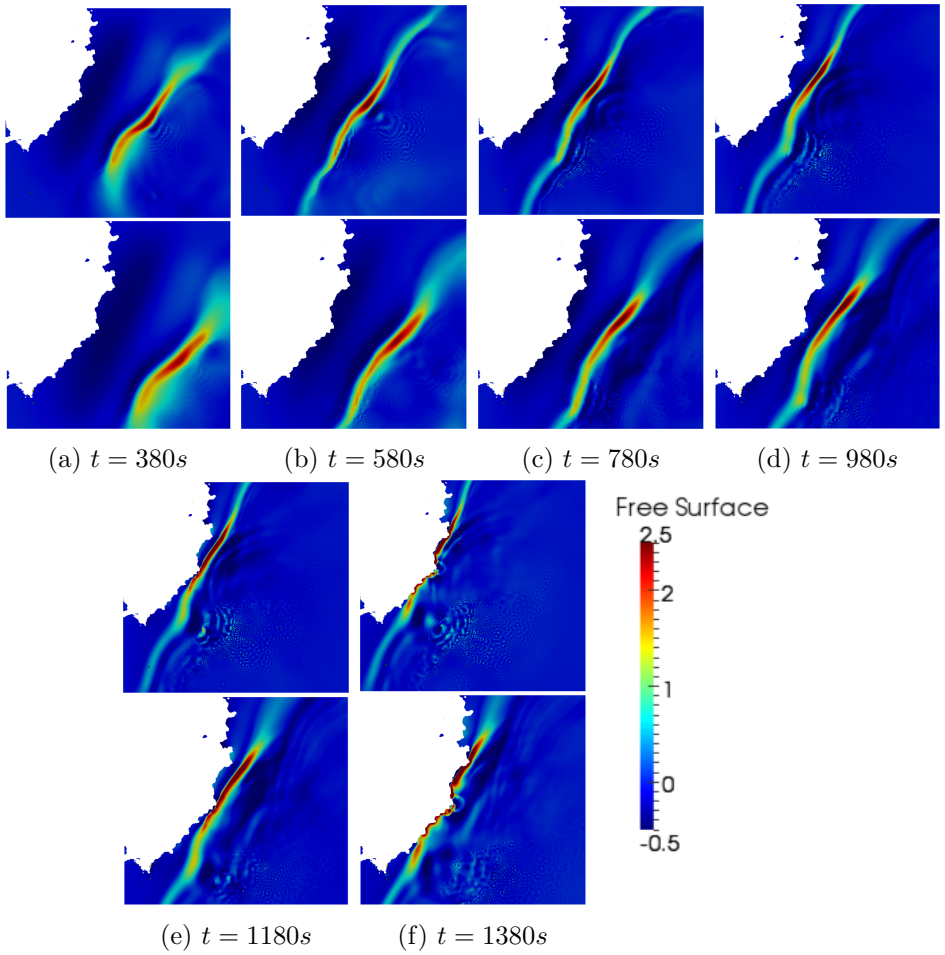

(a) $t = 380s$ (b) $t = 580s$ (c) $t = 780s$ (d) $t = 980s$

(e) $t = 1180s$ (f) $t = 1380s$

Figure 3.21: 1947 New Zealand event – Snapshots of the free surface deformation (in m) during the propagation for NLSWE model (up) and Boussinesq model (down) of Telemac2D for $v_p = 150m/s$ and $t_r = 0s$.

3.2.6 Conclusions

In Chapter 2, it has been shown that for an idealised deformation, the temporal parameters can have an important impact on generated waves if they respected some particular conditions: the rise time should be short and the propagation rupture velocity close to the long wave velocity. We defined a theoretical resonance zone depending of both of these parameters. To illustrate this phenomenon, we choose to simulate the tsunami that occurred in March 1947 in New Zealand. The temporal parameters of this event are close to the values of interest: its v_p^* varies between 2.47 and 9.57 if the initial rupture velocity is set to $300m/s$; and the rise time associated is supposed to be short, $\tau^* < 1$. Thus, four generation models, that differ with the values of v_p and t_r, are tested to measure the impact of the timescale with the NLSWE model of Telemac2D. It appeared that the rupture velocity v_p has an important impact on the tsunami heights along a localised coast

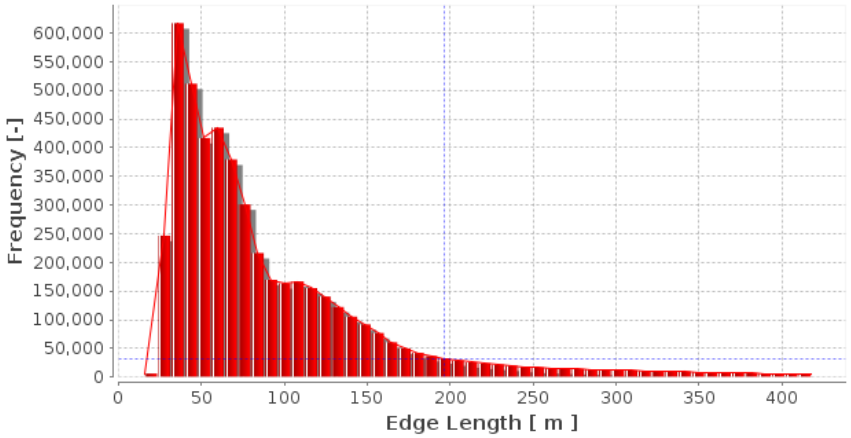

Figure 3.22: 1947 New Zealand event – Size element repartition in the sea zone up to $25km$ from the coastline.

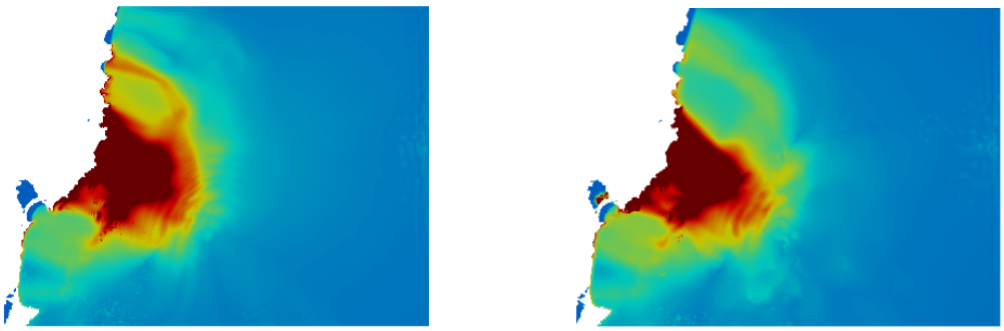

(a) NLSWE model of Telemac2D (b) Boussinesq model of Telemac2D

Figure 3.23: 1947 New Zealand event – Same nomenclature as Figure 3.18 for $v_p = 150m/s$ and $t_r = 0s$. (Free surface deformation in m.)

(latitudes between $-38.6°$ and $-38.2°$): when $v_p = 300m/s$ the estimated tsunami heights are larger than for $v_p = \infty$ (instantaneous deformation). Also, when t_r is non null, the heights slightly decrease but its influence is limited.

After the impact on the wave amplitude, we wanted to quantify the dispersive effects by building a Boussinesq model. For this model, only the case with $v_p = 300m/s$ and $t_r = 0s$ is considered. The aim is to compare the numerical results issued from the Boussinesq model to the previous one of the NLSWE model of Telemac2D. Following the theoretical study, the energy ratio ε is defined to evaluating the quantity of potential energy poorly represented by the LSWE. ε is estimated at $4 - 9\%$ for this idealised event. This value is small and indeed the models give similar numerical results. Thus, to force the appearance of dispersive effects and to observe the front wave decomposites into smaller waves, the value of the rupture velocity is decreased to $v_p = 150m/s$ for which ε is estimated at 40%. However, again, the dispersive effect does not manifest and three conclusions can be drawn: ε overpredicts the dispersive effect, the propagation length considered is too small

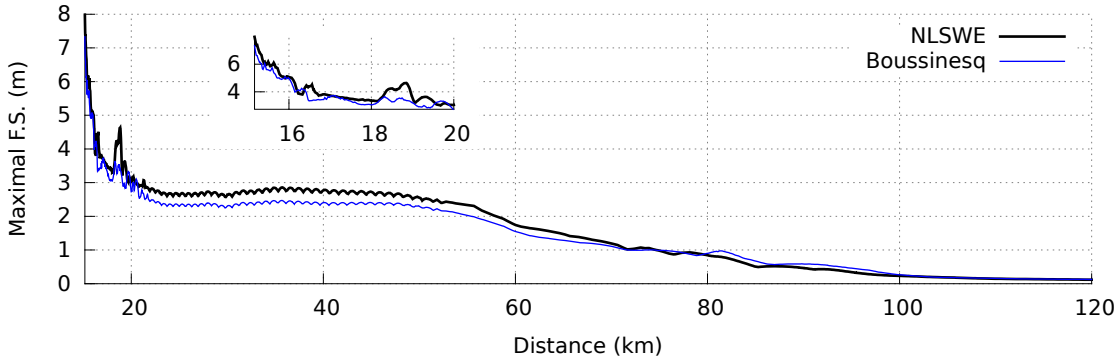

Figure 3.24: 1947 New Zealand event – Maximal free surface elevations reached during the propagation along the transect $A - A'$ as defined in Figure 3.12. Only result for negative bathymetry is plotted. The black and blue line are the numerical results from the NLSWE and the Boussinesq models of Telemac2D, respectively. The model generation corresponds to $v_p = 150m/s$ and $t_r = 0s$. The encapsulated figure is a zoom of the global curve near the coastline (distance$\in [15; 23]km$).

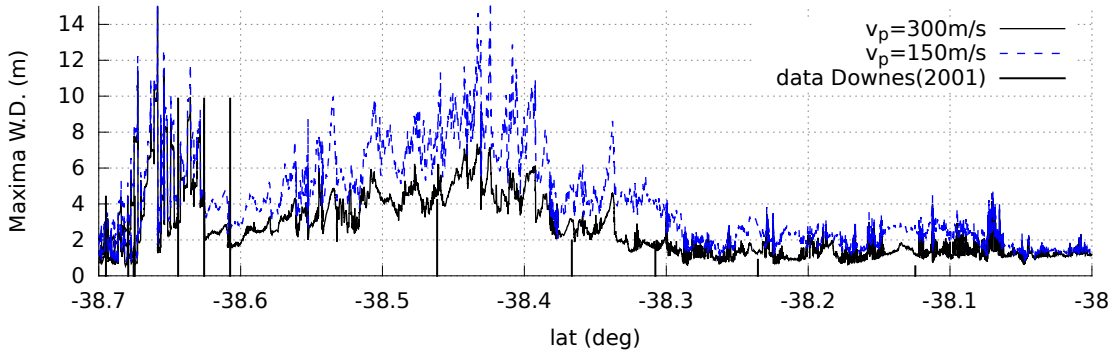

Figure 3.25: 1947 New Zealand event – Maximal water depth obtained at the coastline during the event. The black and blue lines represent numerical model issued of the generation with $v_p = 300m/s$ and $v_p = 150m/s$ respectively.The black vertical bars the data of Downes and Stirling [2001]. The horizontal axis corresponds to the latitude.

to permit its development, or the mesh with element size of order $50m$ is not adapted to model this kind of phenomena.

Part II

Evaluation of Telemac for modeling tsunamis

Chapter 4

Test cases

Ce chapitre présente ma contribution aux cas de validation définis dans le cadre du projet TANDEM. Ces cas ont pour but de tester les modèles numériques afin de légitimer leur utilisation pour des cas réels. Les modèles testés ici sont issus du système Telemac. Les trois modèles sont Telemac2D avec les équations de Saint-Venant, Telemac2D avec les équations de Boussinesq et Telemac3D avec les équations de Navier-Stokes (descriptions disponibles en Annexe C). Le modèle numérique est choisi en fonction du phénomène regardé et des données de validation. Ainsi, deux cas de génération sont modélisés. Pour commencer, on traite un cas 1D de génération par glissement de terrain sur pente. Dans ce cas les vagues sont générées par un mouvement imposé du fond représentant le glissement, et la validation s'effectue avec une solution théorique des équations de Saint-Venant. Le deuxième cas est une génération par mouvement vertical d'une marche sur un fond plat pour lequel les résultats numériques sont confrontés à des mesures expérimentales. Un seul cas de propagation a été défini: celui de la propagation d'une onde solidaire sur une grande distance. La validation de ce cas se base sur des connaissances théoriques: l'amplitude et la forme de la vague ne doivent pas se déformer, la vitesse est comparée à celle calculée par un algorithme précis. Enfin, trois cas de run-up sont considérés. Un cas d'oscillations dans un bassin où les modèles numériques sont comparés à des solutions théoriques, et deux impacts d'une vague sur une pente uniforme. Pour le premier cas, il s'agit d'une vague de type gaussienne pour laquelle une solution théorique des équations non-linéaires de Saint-Venant est connue. Pour le deuxième cas, la vague est une onde solitaire, et la comparaison se fait sur des mesures d'expérience. Généralement, les modèles numériques issus du système Telemac représentent bien les phénomènes considérés et les comparaisons aux données sont satisfaisantes. On note tout de même un bémol pour le cas de la propagation d'une onde solitaire, pour lequel une forte influence des paramètres numériques s'est fait ressentir.

4.1 Context

Following the work of Synolakis et al. [2007], one objective of the TANDEM project is to build a benchmark evaluating different codes for modeling tsunamis. The entire benchmark is available in Violeau [2015] and Violeau et al. [2016]. This chapter gathers my own contribution with the evaluation of the models of the Telemac system.
Tsunami life can be split into three phases: the generation of the wave, its propagation in deep ocean and its run up on the ocean shore. In the TANDEM project, the test cases are chosen to fit in these different steps, and permit to study one of these processes. The test cases presented here consist of two generation studies: *1D analytical sliding mass*, *Generation from a moving bed*; one propagation study: *Propagation of a solitary wave* and three run-up cases: *Oscillations in a parabolic basin*, *Run-up of a Gaussian wave on a uniform slope* and *Run-up of a solitary wave on plane beach* (not included in the TANDEM project).
The choice of the model is done according to the theoretical solution or data proposed for the comparisons. Three models of Telemac are considered here: two with a 2D resolution, the Nonlinear Shallow Water Equation model of Telemac 2D (NLSWE T2D), the Boussinesq model of Telemac 2D (Boussinesq T2D) and one 3D resolution of the Navier–Stokes equations (NS T3D). Descriptions of these models are available in Appendix C. Numerical results from Telemac are compared to either measurements or analytical solution, and sometimes with numerical result from the code Misthyc, [Yates and Benoit, 2015]. Comparisons with the other codes involved in the project TANDEM are available in Violeau [2015]. The present chapter will study whether the Telemac system is capable of modeling tsunamis, in view of the real-world applications proposed in Chapters 3 and 5.

4.2 1D analytical sliding mass

Liu et al. [2003] proposed a 1D analytic solution for tsunami wave generated by landslide using the Linear Shallow Water Equation (LSWE). Figure 4.1 shows the considered domain, where h is the initial water depth, d the thickness of the moving layer, representing the landslide, $\beta = 5.7°$ the angle of the steady ground and η the deformation of the free surface.
The thickness of the landslide is defined as:

$$d(x,t) = \delta \exp\left[-\left(2\sqrt{\frac{x\mu^2}{\delta \tan\beta}} - \sqrt{\frac{g}{\delta}\mu t}\right)^2\right], \tag{4.1}$$

with $\delta = 1m$ the maximum thickness of the slide and $\mu = \frac{\delta}{L}$ the ratio between δ and the length L of the slide, g the gravitational acceleration and μ a parameter defined later. In

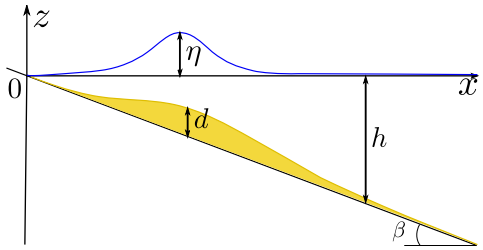

Figure 4.1: 1D analytical sliding mass – Geometry of the generation of a wave by a landslide. The coloured area represents the moving layer of the ground while the black line is the fixed bed.

the code Telemac 2D, the motion of the ground is generated by redefining the bathymetry at each time step following the previous definition. The free surface η is normalised by δ and x by L, giving respectively η^* and x^*. The dimensionless time is defined as $t^* = \sqrt{\frac{g}{\delta}}\frac{t}{\mu}$. μ is fixed at 0.01, such that $\frac{\tan\beta}{\mu} = 10$. Due to the small value of μ, the motion can be considered as linear, as required by the analytical solution. The simulation is performed with the NLSWE model of T2D. An irregular mesh is built for this case with element size around $1m$. Spatial free surface profiles are visible in Figure 4.2 and compared with the linear solution of Liu et al. [2003] at $t^* = 0.5; 1; 1.5$.

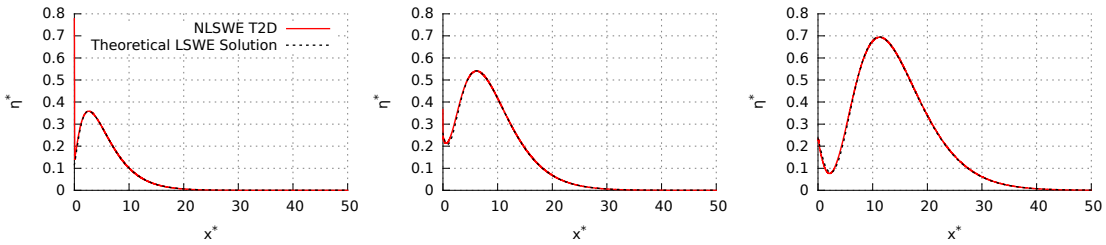

(a) $t^* = 0.5$ (b) $t^* = 1.0$ (c) $t^* = 1.5$

Figure 4.2: 1D analytical sliding mass – Comparisons of the spatial free surface profiles between the analytical solution (black line) and the numerical result from NLSWE Model of T2D (red line) at different times.

Numerical results are in very good agreement with the analytical solution: the curves seem superposed. Thus with these conditions and parameters, NLSWE model of Telemac2D is capable of simulating the generation of a wave by a schematic landslide.
In the frame of the project TANDEM, a second case was proposed with $\mu = 0.1$, $\frac{\tan\beta}{\mu} = 1$. With this value, the numerical results were strongly different to the analytical solution. The explanation was found directly in the work of Liu et al. [2003]: indeed the authors remarked that the omission of the nonlinearity, and the approximation on the water depth are acceptable only for $\frac{\tan\beta}{\mu} > 10$, thus small μ. They concluded also that for $\frac{\tan\beta}{\mu} < 1$ nonlinear effects should deeply impact the evolution of the wave. This behaviour was also observed with other numerical codes used within TANDEM, Violeau [2015].

4.3 Generation and propagation from a moving bed

The aim of this test case is to reproduce the experiment of Hammack [1973]. As described in Chapter 2, this experiment consists of a long flume with constant uniform bed and a small segment moving up vertically at different velocities. A wave is generated and propagates along the flume. Hammack [1973] proposed an analytical linear solution. However, in this benchmark, only the measures are taken as reference. Indeed while during the generation the linear solution remains close to the measurements, it develops differently during the propagation for which the nonlinear effects grow, see Hammack [1973]. Figure 4.3 shows a sketch of the experimental set up.

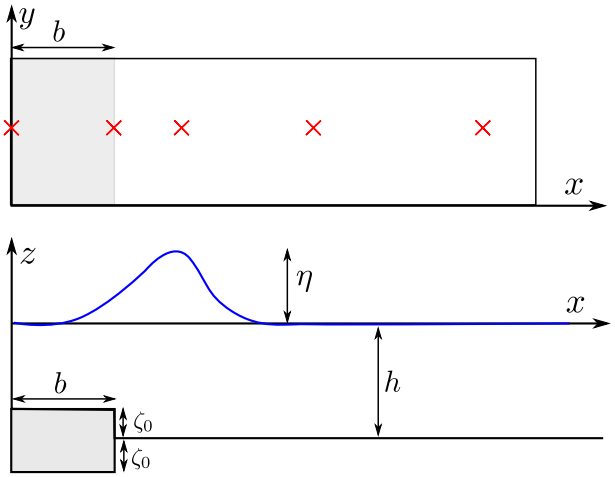

Figure 4.3: Generation and propagation from a moving bed – Geometry of the experiment of Hammack [1973], not at scale. The top frame is a top view and the bottom frame is a slice view. The gray zone is the moving area of length b. The red crosses are locations of measurement gauges.

Two temporal functions are considered to model the motion of the moving section:

- exponential motion, $\alpha = \frac{\ln 3}{t_r}$:

$$\zeta_e(x,t) = \zeta_0(1 - e^{-\alpha t})H(b^2 - x^2)$$

- sinusoidal motion:

$$\zeta_s(x,t) = \zeta_0 \left[\frac{1}{2}\left(1 - \cos\frac{\pi t}{t_r}\right) H(t_r - t) + H(t - t_r)\right] H(b^2 - x^2).$$

Where H is the Heaviside step function and $\zeta_{i,(i=e,s)}$ the amplitude of the deformation of the motion. The dimensionless variables are defined as $x^* = \frac{x}{h}$, $b^* = \frac{b}{h}$, $\zeta_0^* = \frac{\zeta_0}{h}$, $\eta^* = \frac{\eta}{h}$, $t^* = t\sqrt{\frac{g}{h}}$, $t_r^* = t_r\frac{\sqrt{gh}}{b}$.
Hammack [1973] defined three velocities, an impulsive motion with $t_r^* \ll 1$, a creeping

	Exponential motion			Sinusoidal motion		
Velocities	b^*	ζ_0^*	t_r^*	b^*	ζ_0^*	t_r^*
Impulsive		0.2	0.069	6.10		0.13
Transitional	12.2	0.1	0.39	1.22	0.1	0.90
Creeping		0.3	8.70	0.61		31.4

Table 4.1: Generation and propagation from a moving bed – Parameter values for the different cases.

motion with $t_r^* \gg 1$ and a transitional motion between the latter two. First, these three motions are studied here during the generation stage for both time history functions (parameter values are in Table 4.1). Then the propagation of a wave generated by an impulsive exponential motion is studied.

For this case, the Boussinesq model of Telemac2D and the NS model Telemac3D are tested with a Strickler friction law (coefficient set at 100 $m^{1/3}s^{-1}$ in order to minimize the bottom friction) and without viscosity. Numerical results from the code Misthyc are added to the comparison, see Benoit et al. [2014]. The mesh and time step used satisfy $\sqrt{gh}\frac{dt}{dx} < 1$. Figure 4.4 shows comparisons between the numerical simulations and measures during the generation for an exponential motion.

At $x^* = 0$, all the numerical models give a correct estimation of the free surface deformation. At $x^* = b$, the motion velocity impacts the Boussinesq numerical result. While the other numerical models still give correct deformation, the Boussinesq model creates numerical dispersion with apparition of spurious oscillations for the transitional and impulsive motion. The amplitudes of these oscillations are small for the first motion but become important for the second one. Similar results are obtained for the sinusoidal motion, Figure 4.5.

With the sinusoidal time function, the numerical models of Telemac have more difficulties to represent the generation of the wave. For the creeping motion at $x^* = 0$, the models represent well the deformation of the free surface while the numerical code Misthyc gives a too strong decrease. At $x^* = b$, only the result from Telemac3D well matches the measures, Misthyc and Boussinesq model of Telemac2D giving an earlier or delayed decrease. However all the numerical results are globally correct. That is not the case for the transitional motion, where the Boussinesq model does not capture the right deformation of the free surface by creating too much numerical dispersion, especially at $x^* = b$. The NS model of Telemac3D seems better even if the amplitude of the second wave is over-predicted while the result of Misthyc is consistent with the data. For the impulsive motion at $x^* = 0$, the height of the wave is under-predicted by all the numerical models. Its dispersive tail is well represented by Misthyc and Telemac3D (the amplitude slightly over-predicted for the latter) but the one from Boussinesq model does not fit the data, affecting the results at $x^* = b$ where Telemac3D and Misthyc match the data while the

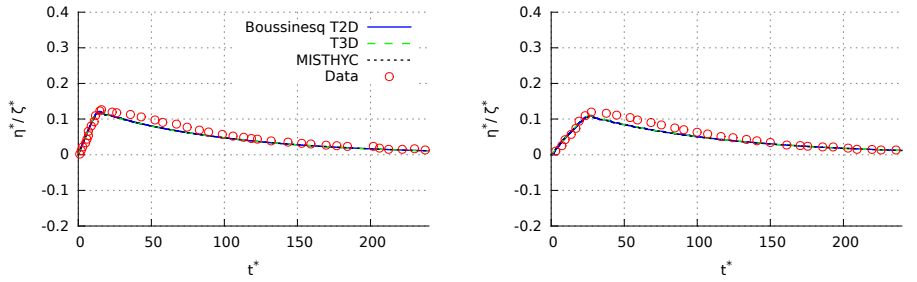

(a) Creeping motion

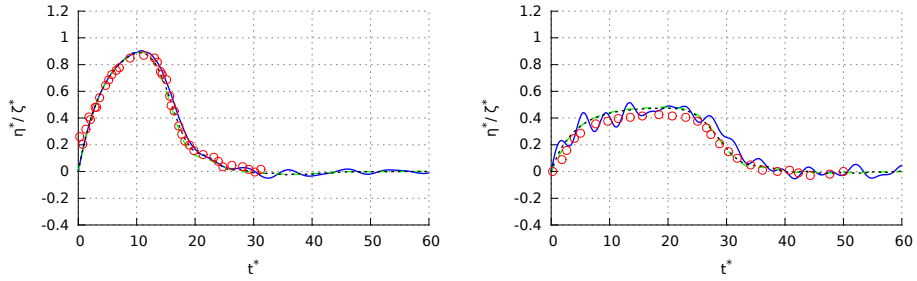

(b) Transitional motion

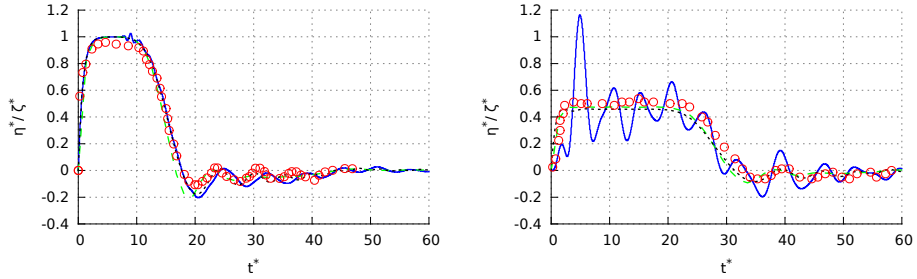

(c) Impulsive motion

Figure 4.4: Generation and propagation from a moving bed – Temporal free surface profiles during the generation at $x^* = 0$ (left) and $x^* = b^*$ (right) for an exponential motion. The blue lines are the numerical Boussinesq model of Telemac2D while Telemac3D is represented by the green dashed line. The numerical results issued from the code Misthyc are also plotted (black dashed line), Benoit et al. [2014]. The red points are measurements from Hammack [1973].

Boussinesq model is delayed and has numerical dispersion. However the amplitude and global form of the generated wave is in agreement with the data.

The last part of this test case is the propagation of a wave along the flume. An impulsive exponential motion is generated with $b^* = 12$, $\zeta_0^* = 0.1$ and $t_c^* = 0.148$. The temporal free surface elevation profiles at $x^* = b^*, b^* + 20, b^* + 180, b^* + 400$ are plotted in Figure 4.6 and compared to the measurements.

The differences between the numerical models grow during the propagation. At $x^* = b$, even if the Boussinesq model slightly diverges with numerical dispersion and small spu-

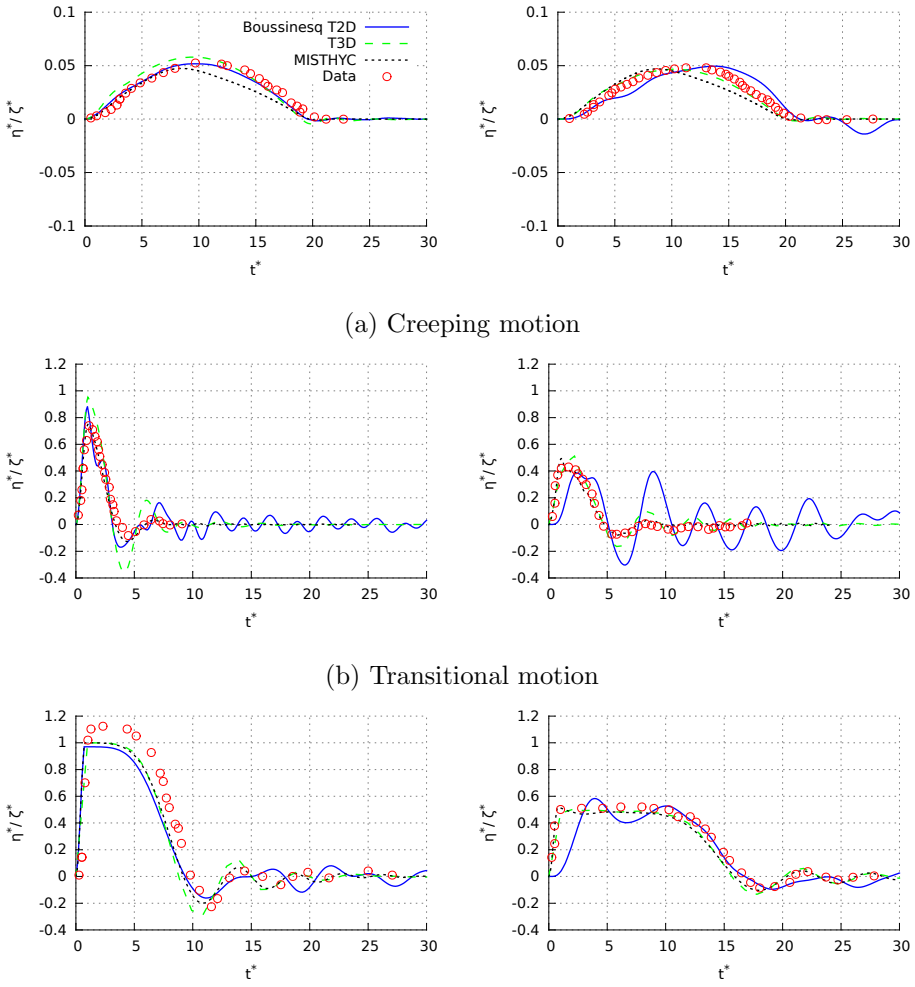

(a) Creeping motion

(b) Transitional motion

(c) Impulsive motion

Figure 4.5: Generation and propagation from a moving bed – Temporal free surface profiles during the generation at $x^* = 0$ (left) and $x^* = b^*$ (right) for a sinusoidal motion. Same nomenclature as Figure 4.4.

rious oscillations, the wave generated by all the numerical models is similar and close to the data. At $x^* = 20$, the previous comments are still valid and moreover the numerical dispersion for Boussinesq model seems to decrease. The models differ from $x^* = 180$. At this point, the NS model of Telemac3D is the closest to the data with a tiny lead while the velocity and amplitude of the wave from Misthyc are over-predicted, but this model does not include bottom friction nor viscous forces in the fluid mass (inviscid potential model). A more in depth study of this case with this model is depicted in Raoult [2016]. It is shown that the results from Misthyc are close to Furhman and Madsen's numerical predictions (Fuhrman and Madsen [2009]), using a nonlinear Korteweg–de Vries model and a nonlinear Boussinesq model. None of these models include dissipation, which is suspected to explain the difference with the data. Here, the wave resulting from the Boussinesq

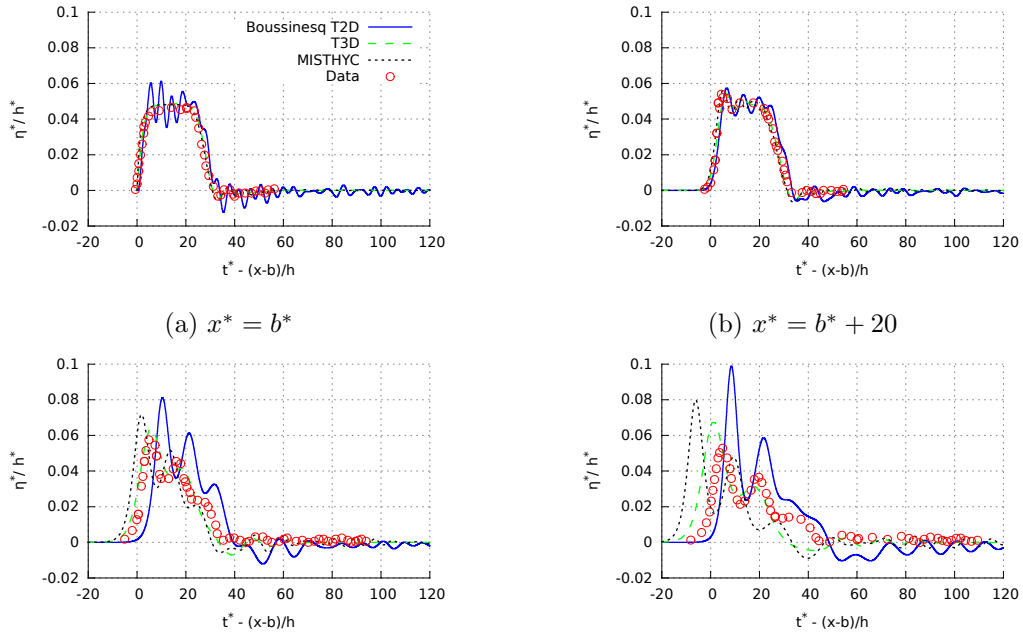

(a) $x^* = b^*$ (b) $x^* = b^* + 20$

(c) $x^* = b^* + 180$ (d) $x^* = b^* + 400$

Figure 4.6: Generation and propagation from a moving bed – Temporal free surface deformation during the propagation of a wave initiated by an impulsive exponential motion ($b^* = 12$, $\zeta_0^* = 0.1$, $t_c^* = 0.148$) at four places along the flume. The time is modified to fit the same scale. Same nomenclature as Figure 4.4.

model is higher than expected and late. However the global form of the wave is respected for all the numerical models. At $x^* = 400$, all models over-predict the amplitude of the wave. The gap widened between them: the result from Telemac3D is still the closest to the measures but represents less the frequency dispersion than Misthyc for which every small oscillation is well estimated. The wave velocity from the Boussinesq model seems to be more correct than the others but the amplitude is over-predicted (almost twice) and except the second peak, the numerical wave does not match in detail the measured one. Globally, this case is well handled by the numerical models. In detail, Misthyc gives a good approximation of the generated wave regardless of the time behaviour imposed to the ground motion. The models of Telemac are more sensitive to this temporal motion, especially the Boussinesq model of Telemac2D that tends to create too much numerical dispersion, as one can see for the transitional sinusoidal generation of the wave and during the propagation stage. The NS model of Telemac3D gives a good estimation of the free surface deformation for the different generations, however it slightly under-predicts the frequency dispersion after a long propagation time.

4.4 Propagation of a solitary wave

The aim of this case is to propagate a solitary wave of height H, along a great distance on a uniform depth h. During its propagation, the wave keeps its shape and move with constant velocity. The solitary wave is a solution of selected mathematical models (Boussinesq, Serre, Korteweg–de Vries equations, *etc.*., see Malfliet [1992]). Here the Euler model is chosen even not a closed-form solution is known. However, it can be efficiently approached by numerical model as the one from Dutykh and Clamond [2014] that is taken as reference. This test is simulated with the NS model Telemac3D and compared with the initial amplitude and its expected position, and numerical result issued of Misthyc which agrees very well with the reference (see Benoit et al. [2014]).
Different resolution grids are tested: the dimensionless element size is defined as $\frac{dx}{h} = \frac{1}{M_x}$ and dimensionless time step $dt\sqrt{\frac{g}{h}} = \frac{1}{M_t}$, thus the $CFL = \sqrt{gh}\frac{dt}{dx}$ can defined as $CFL = \frac{M_x}{M_t}$. The simulations were performed with $M_x = 5, 10, 20, 40$ and a constant CFL. Preliminary tests are performed with $M_x = 5$ and $\frac{H}{h} = 0.5$ in order to test the sensitivity of the model to the time step. Then, the others grids are used. For each grid, a convergence study is performed on the vertical resolution, giving the maximal element size on the vertical (dz) to have the converged numerical result. It was observed that the converged result is reached faster for the finer horizontal grids . Thus, the relative vertical resolutions are: $\frac{dz}{dx} = \frac{1}{2}$ for $M_x = 5$ and 10, $\frac{dz}{dx} = 1$ for $M_x = 20$ and $\frac{dz}{dx} = 2$ for $M_x = 40$. The numerical parameters are kept for $\frac{H}{h} = 0.3; 0.7$. The wave is generated by giving an initial free surface deformation, vertical and horizontal velocity profiles. The propagation of the wave is modeled until $t^* \approx 159.64s$ ($t\sqrt{\frac{g}{h}} = 500$) giving the approximated traveled distance $\frac{d}{h} \approx 608$ (this distance is calculated with an accurate velocity and provided by the algorithm of Dutykh and Clamond [2014]). Preliminary tests for different values of CFL are plotted in Figure 4.7.

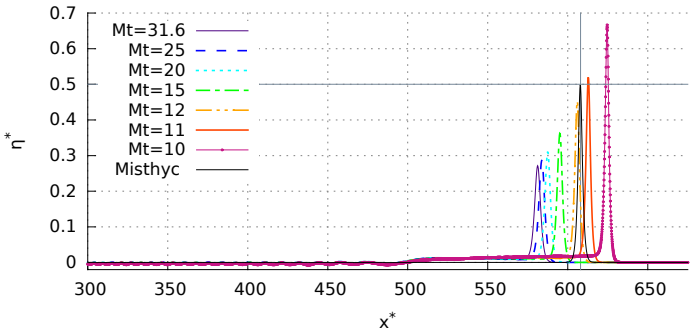

Figure 4.7: Propagation of a solitary wave – Spatial profiles of free surface deformation obtained with Telemac3D after $t^* = 500$ of propagation of a $\frac{H}{h} = 0.5$ high solitary wave for different values of $CFL = \frac{M_t}{M_x}$ with $M_x = 5$. The horizontal and vertical lines show the expected wave height and mean position, respectively.

One can see that this case is difficult for the NS model T3D. When M_t increases, the time step and the CFL decrease. For lower CFL, convergence seems to appear but far away from expected result. It can be concluded that the time step influences significantly the numerical results, and that for the lower time steps, *i.e.* the bigger M_t, the wave amplitude is much smaller than expected. This may be due to numerical diffusion, and a theoretical study of the numerical scheme, as done by Burwell et al. [2007] for another model, should be done to understand this behaviour. Also, a small non-physical plateau is created on the tail of the wave, with lengths increasing with the time step. For now on, we observe that an optimal result is obtained for $M_t = 12$, thus $CFL = 0.41$. We will keep this value in the following. We understand this approach may be criticized, but it is the best available one in the current state of the Telemac3D code. Numerical results for $M_x = 10, 20$ and 40 are plotted in Figure 4.8.

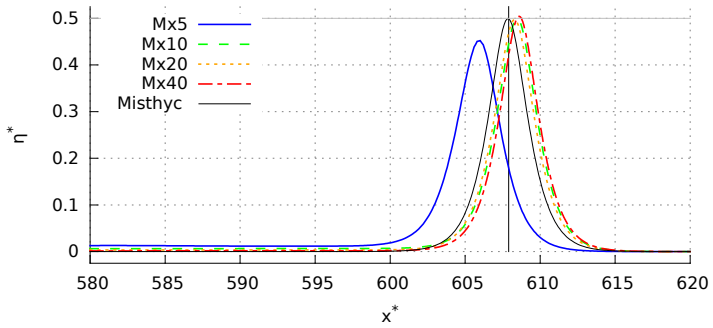

Figure 4.8: Propagation of a solitary wave – Spatial profiles of free surface deformation obtained after $t^* = 500$ for the different grid resolutions at $CFL = 0.41$ and $\frac{H}{h} = 0.5$. The blue, green, orange and red lines are respectively NS Telemac3D results for $M_x = 5$, $M_x = 10$, $M_x = 20$ and $M_x = 40$ grids. The dashed black line is the numerical result from Misthyc with $M_x = 10$. The horizontal and vertical lines show the expected wave height and mean position, respectively.

The numerical free surface deformations obtained for the finer grids are similar and give a better approximation of the wave than for $M_x = 5$, the NS Telemac3D model converges with the CFL as soon as $M_x = 10$. Also, the non-physical plateau created for $M_x = 5$ decreases in amplitude and finally disappears with the finest meshes. However, the wave moves slightly faster than predicted by the algorithm of Dutykh and Clamond [2014]. It also clearly appears that the code Misthyc gives better result even with $M_x = 5$ resolution ($M_x = 10$ in Figure 4.8).
Free surface deformation for $\frac{H}{h} = 0.3, 0.7$ are visible in Figure 4.9.
The position of the peak of the wave is unknown for $\frac{H}{h} = 0.3, 0.7$, thus the comparisons are only based on the amplitude of the wave. The numerical result for $\frac{H}{h} = 0.3$ converges faster than for $\frac{H}{h} = 0.5, 0.7$. Indeed, smaller is $\frac{H}{h}$, smaller are the nonlinear effects. Moreover, for $\frac{H}{h} = 0.7$, regardless of the grid, the wave is smaller than expected. Performing a

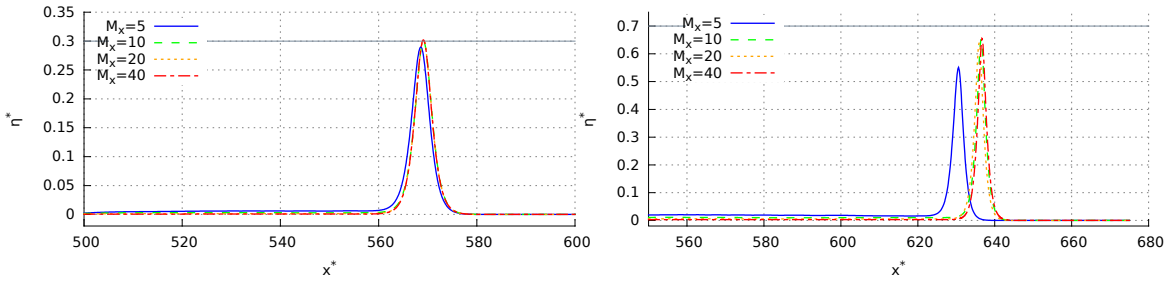

(a) $\frac{H}{h} = 0.3$ (b) $\frac{H}{h} = 0.7$

Figure 4.9: Propagation of a solitary wave – Same nomenclature as Figure 4.8 for $\frac{H}{h} = 0.3$ and 0.7

similar sensitivity analysis as explained above would allow choosing a better CFL in this case.

To conclude, this case is a conundrum for Telemac. It seems that the numerical parameters of NS model of Telemac3D has to be adapted to each case and that the user should be very careful of the spatial and temporal parameters, especially when the nonlinearity is important. The NS model of Telemac3D tends to decrease the wave amplitude and thus the propagation velocity, probably because of numerical diffusion. However, an *ad hoc* CFL choice (though questionable) allows us to approach a correct solution as seen Figure 4.7.

4.5 Parabolic basin

This theoretical case concerns water oscillations in a perfect parabolic basin. The aim is to conserve the motion without loss of amplitude nor time delay, and to address the ability of a numerical model to predict wave run-up (dry/wet area). The solution of this motion is given by Thacker [1981] for the NLSWE. The topography basin is defined by a function d, as shown in Figure 4.10, $d(r) = -h_0(1 - \frac{r^2}{a^2})$ where r is the radius of the basin, $r = \sqrt{x^2 + y^2}$. The parameters h_0 and a are fixed respectively to $4m$ and $2000m$, and $[x; y] \in [-3000m; 3000m]^2$. The mesh is imposed to be regular with a $10m$ grid resolution and the time step is chosen such as $CFL \leqslant 0.5$.

Two initial conditions are proposed. First a paraboloid configuration is tested: the initial free surface deformation, $\eta_0(r)$, is fixed as (see Figure 4.11a):

$$\eta_0(r) = h_0 \left[\frac{\sqrt{1 - A^2}}{1 - A} - 1 - \frac{r^2}{a^2} \left(\frac{1 - A^2}{(1 - A)^2} - 1 \right) \right] \tag{4.2}$$

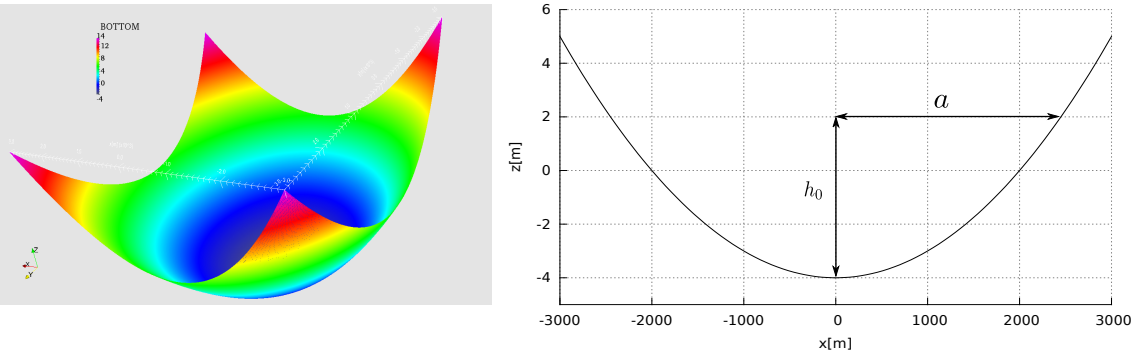

Figure 4.10: Parabolic basin – Geometry of the perfect paraboloid basin.

with $A = \frac{(h_0+\eta_1)^2-h_0^2}{(h_0+\eta_1)^2+h_0^2}$ and $\eta_1 = 1m$. Vertical and horizontal initial velocities are null. The solution given by Thacker [1981] is:

$$\begin{cases} \eta(r,t) = h_0 \left[\dfrac{\sqrt{1-A^2}}{1-A\cos(\omega_1 t)} - 1 - \dfrac{r^2}{a^2}\left(\dfrac{1-A^2}{(1-A\cos(\omega_1 t))^2} - 1 \right) \right], \\ u(r) = \dfrac{1}{1-A\cos(\omega_1 t)} \dfrac{1}{2} \omega_1 x A \sin(\omega_1 t), \\ v(r) = \dfrac{1}{1-A\cos(\omega_1 t)} \dfrac{1}{2} \omega_1 y A \sin(\omega_1 t) \end{cases}$$

with $\omega_1 = \sqrt{\frac{8gh_0}{a^2}}$.

The numerical results on the slice $y = 0$ of the free surface deformation and horizontal velocity obtained with the NLSWE model of Telemac2D are plotted in Figure 4.11.

The numerical results are in good agreement with the analytical solution. The transition between the wet and dry zones is well represented except for the last times where a small instability appears in the velocity field. The amplitude of the oscillation is then observed at the center of the basin, see Figure 4.12. After five oscillations, the amplitude of the motion does not decrease, the free surface deformation still corresponds to the analytical solution. Moreover, no delay is detected.

The second configuration corresponds to an initially flat free surface with:

$$\begin{cases} \eta(x,y) = \dfrac{\eta_2 h_0}{a^2}(2x - \eta_2), \\ u(x,y) = 0, \\ v(x,y) = \eta_2 \omega_2 \end{cases} \tag{4.3}$$

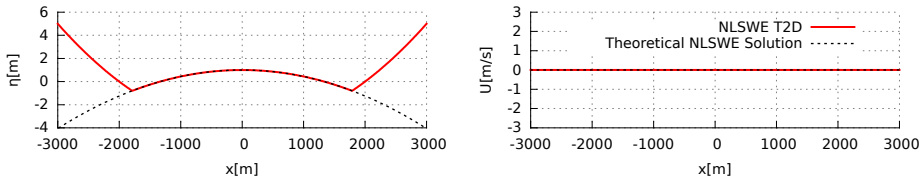

(a) $t = 0s$

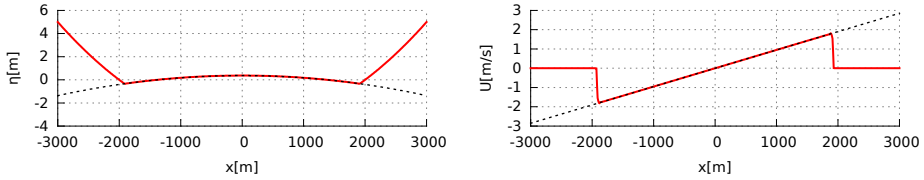

(b) $t = 120s$

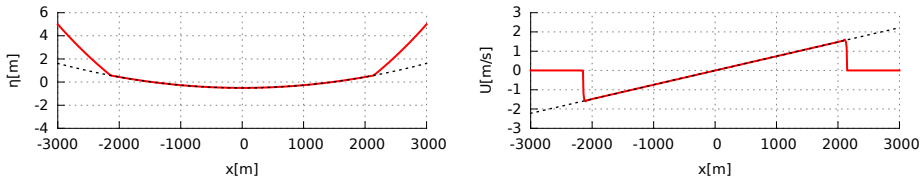

(c) $t = 240s$

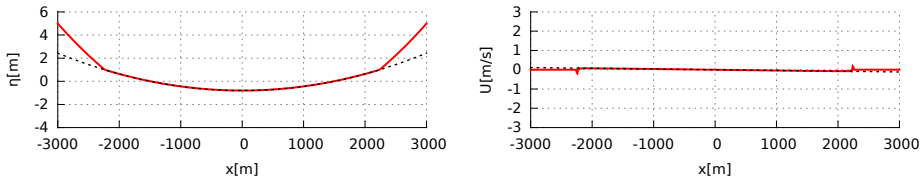

(d) $t = 360s$

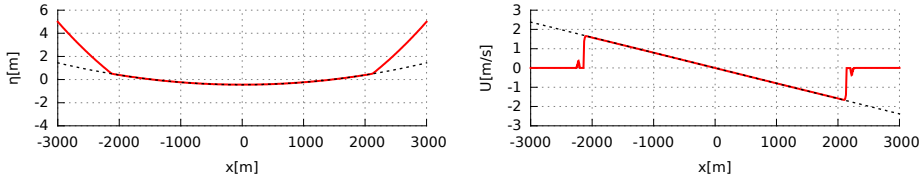

(e) $t = 480s$

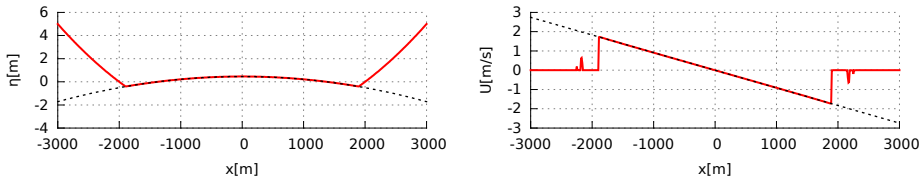

(f) $t = 600s$

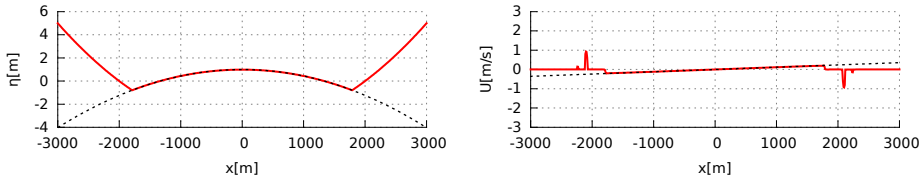

(g) $t = 720s$

Figure 4.11: Parabolic basin – Initial paraboloid configuration. Spatial profiles on the slice $y = 0$ of the free surface deformation and of the horizontal velocity during one period. The dashed black line is the analytical NLSWE solution. The red line represents numerical results issued from the NLSWE model of T2D.

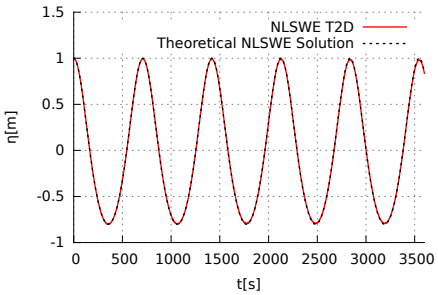

Figure 4.12: Parabolic basin – Temporal evolution of free surface elevation at the center of the basin. The thick black line is the analytical NLSWE solution. The red line represents numerical results issued of the NLSWE model of T2D. The L^2-error on h was calculated by the BRGM, partners of the TANDEM project, for the different codes. The error for the the NLSWE model of Telemac2D is less than 1%, see Violeau [2015].

and $\omega_2 = \frac{\sqrt{2gh_0}}{a}$, $\eta_2 = 250m$. The analytical solution given by Thacker [1981] is:

$$\begin{cases} \eta(x,y,t) = \dfrac{\eta_1 h_0}{a^2}(2x\cos(\omega_2 t) + 2y\sin(\omega_2 t) - \eta_2), \\ U(x,y) = -\eta_2\omega_2\sin(\omega_2 t), \\ V(x,y) = \eta_2\omega_2\cos(\omega_2 t) \end{cases}$$

Figure 4.13 shows free surface deformation and horizontal velocity profiles for a half period.

With this configuration, the numerical results are almost superimposed to the analytical solution. There is no more instability for the velocity field. It appears clearly that the NLSWE model of Telemac2D represents almost perfectly the analytical solution.
It can be concluded, for both configurations, than the NLSWE model of Telemac2D well represents this kind of wet-dry transitions and oscillations. A graph representing the L_2 error for each codes used in the TANDEM project is available in Violeau [2015], in which one can see that for this case, Telemac2D gives one of the lower errors for both configurations.

4.6 Run up of a Gaussian wave on a uniform slope

The aim of this benchmark is to model a real dimension tsunami run-up case on a beach proposed by Carrier et al. [2003]. Numerical results issued of the NLSWE model of Telemac2D are compared to a theoretical solution. The domain is considered 1D with a plane beach of uniform slope of angle $\beta = 0.1$. The origin of the domain is fixed at the initial shoreline. The mesh used in this case is progressively refined from offshore (element length $\sim 40m$) to the shoreline (element length $\sim 0.5m$). The dimensionless

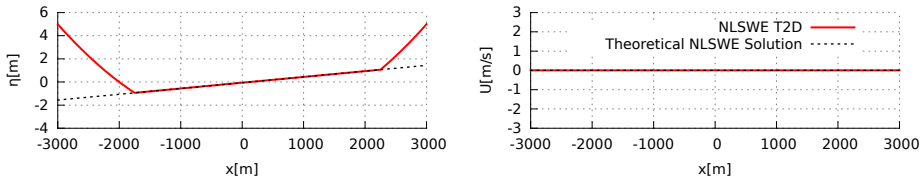

(a) $t = 0s$

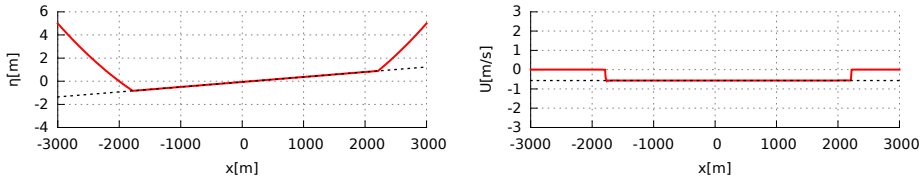

(b) $t = 120s$

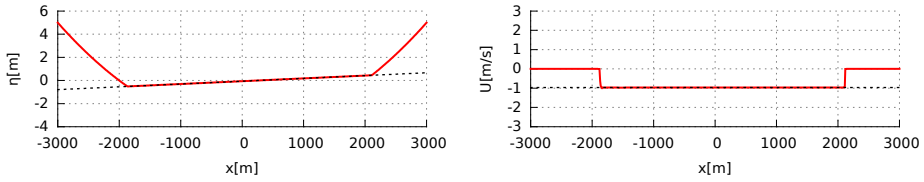

(c) $t = 240s$

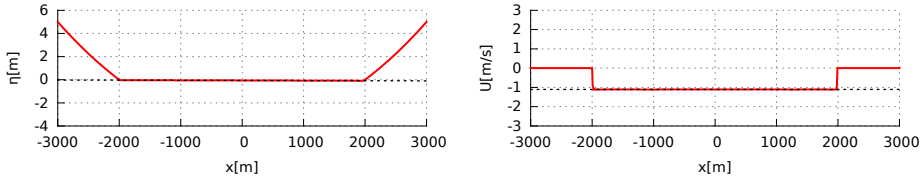

(d) $t = 360s$

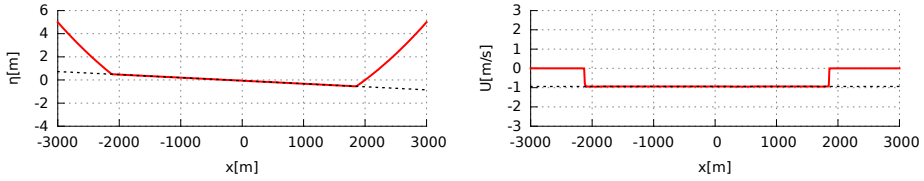

(e) $t = 480s$

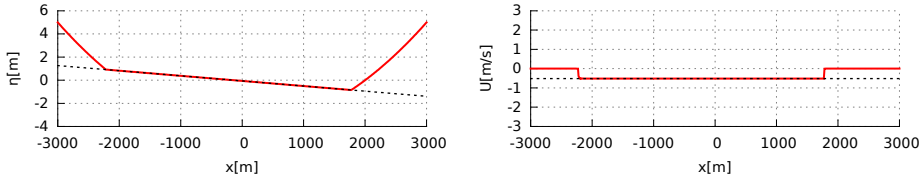

(f) $t = 600s$

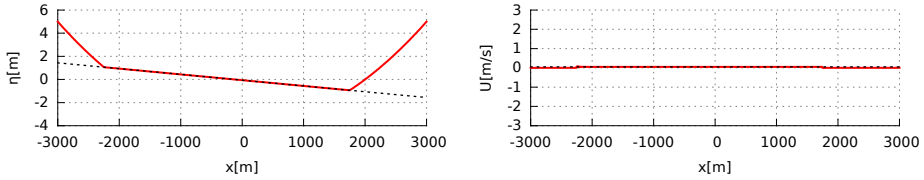

(g) $t = 720s$

Figure 4.13: Parabolic basin – Initial flat configuration. Same nomenclature as Figure 4.11.

variables are defined as following: $u^* = \frac{u}{\sqrt{g\beta L}}$, $t^* = t\sqrt{\frac{\beta g}{L}}$, $x^* = \frac{x}{L}$ and $\eta^* = \frac{\eta}{\beta L}$, where L is the horizontal length scale. The free surface elevation is initiated by a N-wave shape deformation, typical from submarine landslide generation:

$$\eta^*(x^*, 0) = a_1 \exp\left[-k_1(x^* - x_1)^2\right] - a_2 \exp\left[-k_2(x^* - x_2)^2\right], \tag{4.4}$$

with $a_1 = 0.006$, $a_2 = 0.018$, $k_1 = 0.4444$, $k_2 = 4.0$, $x_1 = 4.1209$ and $x_2 = 1.6384$. These parameters correspond to a wave with an approximated $9m$ depression generated by a landslide $L = 5km$ offshore.

First, comparisons are performed on spatial free surface deformation and velocity profiles, Figure 4.14, at $t^* = 2.24, 2.45, 3.08$.

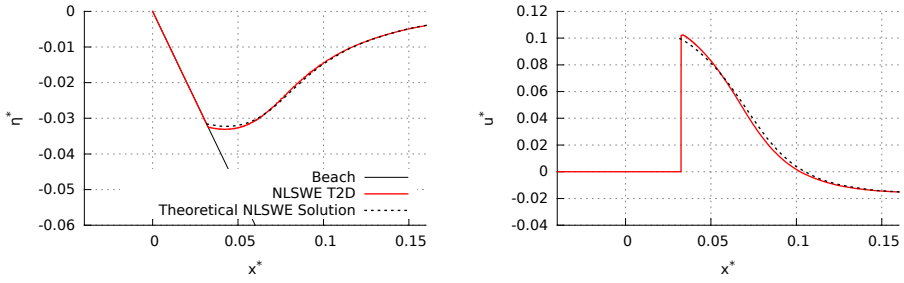

(a) $t^* = 2.24$

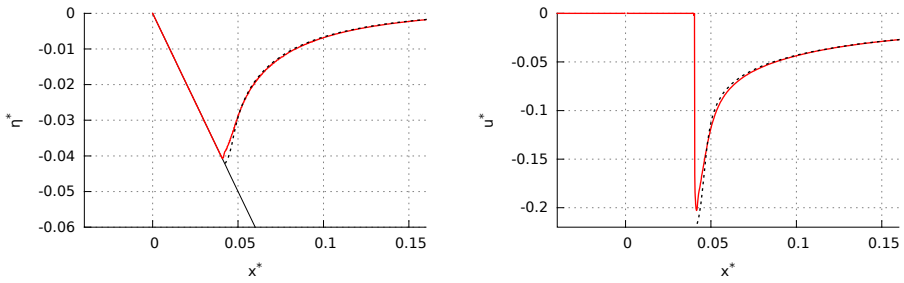

(b) $t^* = 2.45$

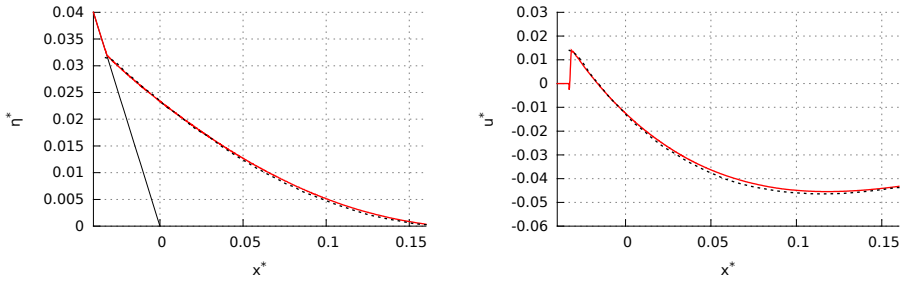

(c) $t^* = 3.08$

Figure 4.14: Run up of a Gaussian wave on a uniform slope – Spatial profiles of the free surface displacement (left) and of velocity (right) at different times. The black thick line corresponds to the theoretical solution issued of the work of Carrier et al. [2003] while the red line is numerical result from the numerical NLSWE model of T2D.

The numerical results obtained are similar to the theoretical solution of Carrier et al. [2003]. Globally, the curves are almost superimposed. in Figure 4.15, the evolution of the shoreline is displayed. Both temporal position and velocity are represented. Excepted during the draw down where the velocity is negative, the NLSWE model of Telemac2D well represents the evolution of the shoreline.

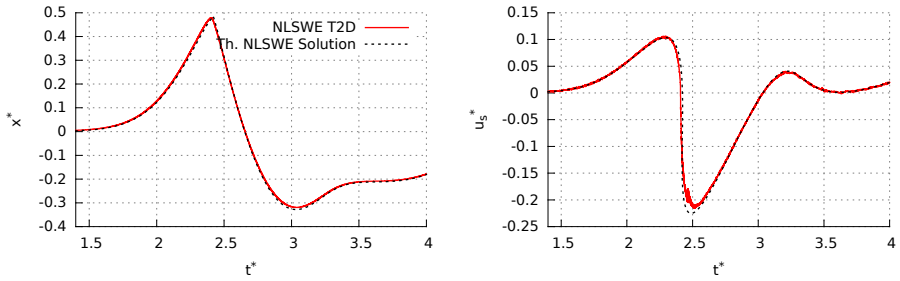

Figure 4.15: Run up of a Gaussian wave on a uniform slope – Temporal evolution of the shoreline with it localisation (right) and it velocity (right). Same nomenclature as Figure 4.14

In view of the correct numerical results of the NLSWE model of T2D, it can be concluded that it can well model the run-up of a real dimension tsunami on a plane beach.

4.7 Run-up of a solitary wave on a uniform beach

The aim of this test case is to reproduce the experiment of Synolakis [1987] of a 1D run-up of a solitary wave on a plane sloping beach of angle β. The set up of the experiment is shown in Figure 4.16.

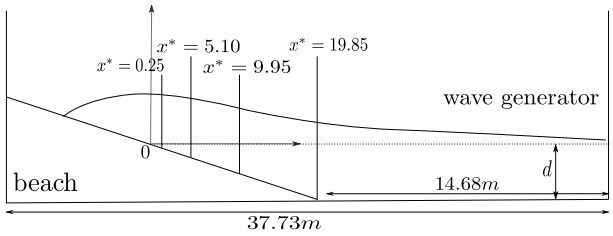

Figure 4.16: Run-up of a solitary wave on a uniform beach – Set up of the experiment of Synolakis [1987]. Not at scale.

The size of the canal is $37.76m \times 0.61m \times 0.39m$ and the wave generator is at one end of it. The sloping beach begins after $14.68m$ of flat bottom, and $\tan\beta = 1 : 19.85$. With a NLSWE model, the solitary wave would become distorted during the propagation, thus this part of the canal is not included in the numerical domain, the latter taking into account only the beach, shown in Figure 4.17. The element sizes of the mesh are between $dx = 0.1m$ and $dx = 0.025m$ from the beginning of the beach to the shoreline, respectively.

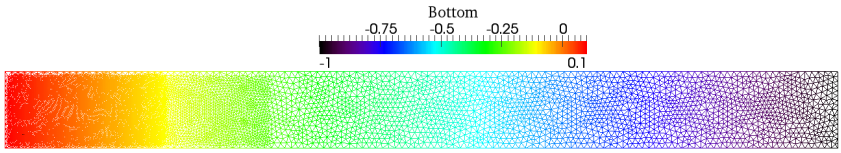

Figure 4.17: Numerical domain for the test case of the solitary wave run up on a plane beach associated to the experiment of Synolakis [1987]. The variation of the bathymetry used is colourfully denoted.

The incoming wave has the following free surface profile:

$$\eta(x,0) = H\,\mathrm{sech}^2\,\gamma(x - x_1) \tag{4.5}$$

with $\gamma = \sqrt{\frac{3H}{4}}$, H the amplitude of the wave: $H = 0.0185d\ m$ where d is the initial water depth at the flat bottom, and x_1 is the initial position of the wave.
A friction law at the bottom is applied during the simulation, the law of Strickler with a coefficient of $100m^{1/3}s^{-1}$. Both NLSWE and Boussinesq models are tested. Temporal profiles of the numerical free surface deformation at $x^* = \frac{x}{d} = 0.25; 5.10; 9.95; 19.85$ are compared to measurements in Figure 4.18 (see location of the gauges in Figure 4.16). The dimensionless time is defined as $t^* = t\sqrt{\frac{g}{d}}$.

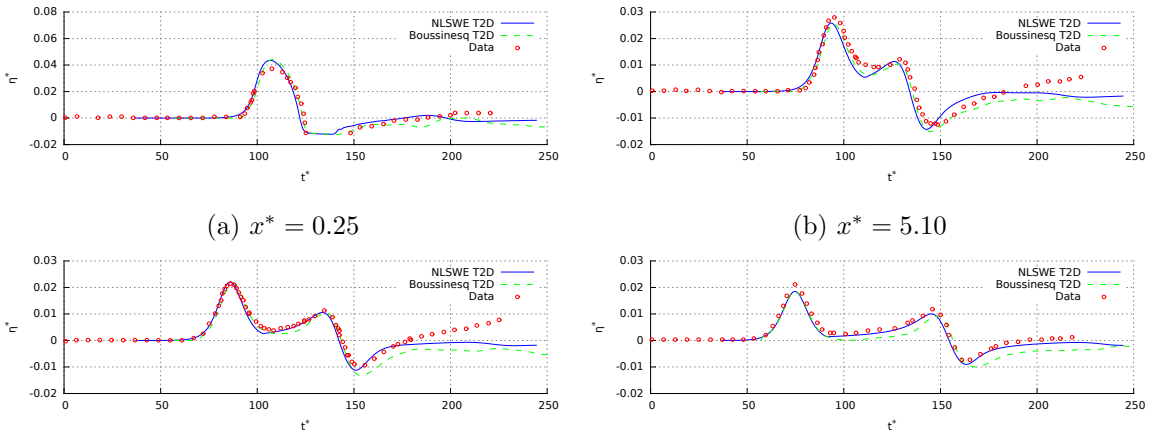

(a) $x^* = 0.25$ (b) $x^* = 5.10$

(c) $x^* = 9.95$ (d) $x^* = 19.85$

Figure 4.18: Run-up of a solitary wave on a uniform beach – Temporal free surface deformation for the solitary wave run-up on a plane beach at different places on the slope. The blue line is the numerical result from the NLSWE Telemac2D model. The dashed green line is the numerical result from the Boussinesq Telemac2D model. The red symbols are the data from Synolakis [1987].

The incoming wave and its reflection are globally well reproduced. At the entrance of the slope, $x^* = 19.85$, the data gives a slightly higher wave than the one numerically

implemented and globally the numerical reflected wave is smaller than the data. The wave of the NLSWE model of Telemac2D is barely faster than the one from the Boussinesq model: at $x^* = 19.85$ incoming waves are superimposed while a small decay increases during the propagation and then is amplified for the reflected waves. The amplitude of the wave from the Boussinesq model is closer to the data than the one from the NLSWE model but the following decrease is too important. However, it can be concluded that both models give satisfactory temporal profiles.
The spatial free surface deformation profiles are plotted in Figure 4.19 at different instants.

For all times, the numerical results are in good agreement with data. The modeled run-up is close to the one measured: $Run - up_{T2D}/d = 0.077$ while $Run - up_{measured}/d = 0.078$ (see Synolakis [1987]). For the NLSWE model the wave is faster than the data and the draw-down is over-predicted. Indeed, the NLSWE model assumes hydrostatic pressure, thus the error on the free surface is bigger for arched waves. Expectedly, the Boussinesq model gives closer result to the data, the draw-down is slightly over-predicted and the free surface displacement matches the measurements. For this part of the simulation the Boussinesq model gives better result than NLSWE.
To conclude, both numerical models well represent the run-up of a solitary wave on a plane beach with a correct estimation of the run-up. However the Boussinesq model give better spatial results while the NLSWE over-predicts the draw-down.

4.8 Conclusions

Through these different test cases, an evaluation of the models of the Telemac system can be drawn. Two kinds of wave generation are tested: one by landslide for which the NLSWE model of Telemac2D well represents the generated wave and matches the theoretical solution. The second is a generation by vertical ground motion. This case is more delicate, the numerical models of Telemac, especially the Boussinesq model, are sensitive to the type of motion unlike the numerical model of Misthyc. However, globally the generated wave is well reproduced and its propagation too. The case of the propagation of a solitary wave enlightens the sensitivity of the NS model of Telemac3D in representing the propagation of a highly nonlinear wave over a long distance. A strong dependence on the time step and a numerical diffusion are shown, which require additional investigations and further studies. It should be emphasized that real tsunami waves do not present such strong nonlinearities. As we will see in the next chapter, such numerical limitation will not affect the reproduction of the Tohoku-Oki event. Finally, three run-up cases are considered. For these phenomena, the models from Telemac2D (NLSWE, Boussinesq) easily represent the transition between wet and dry areas, matching theoretical solutions or measurements.

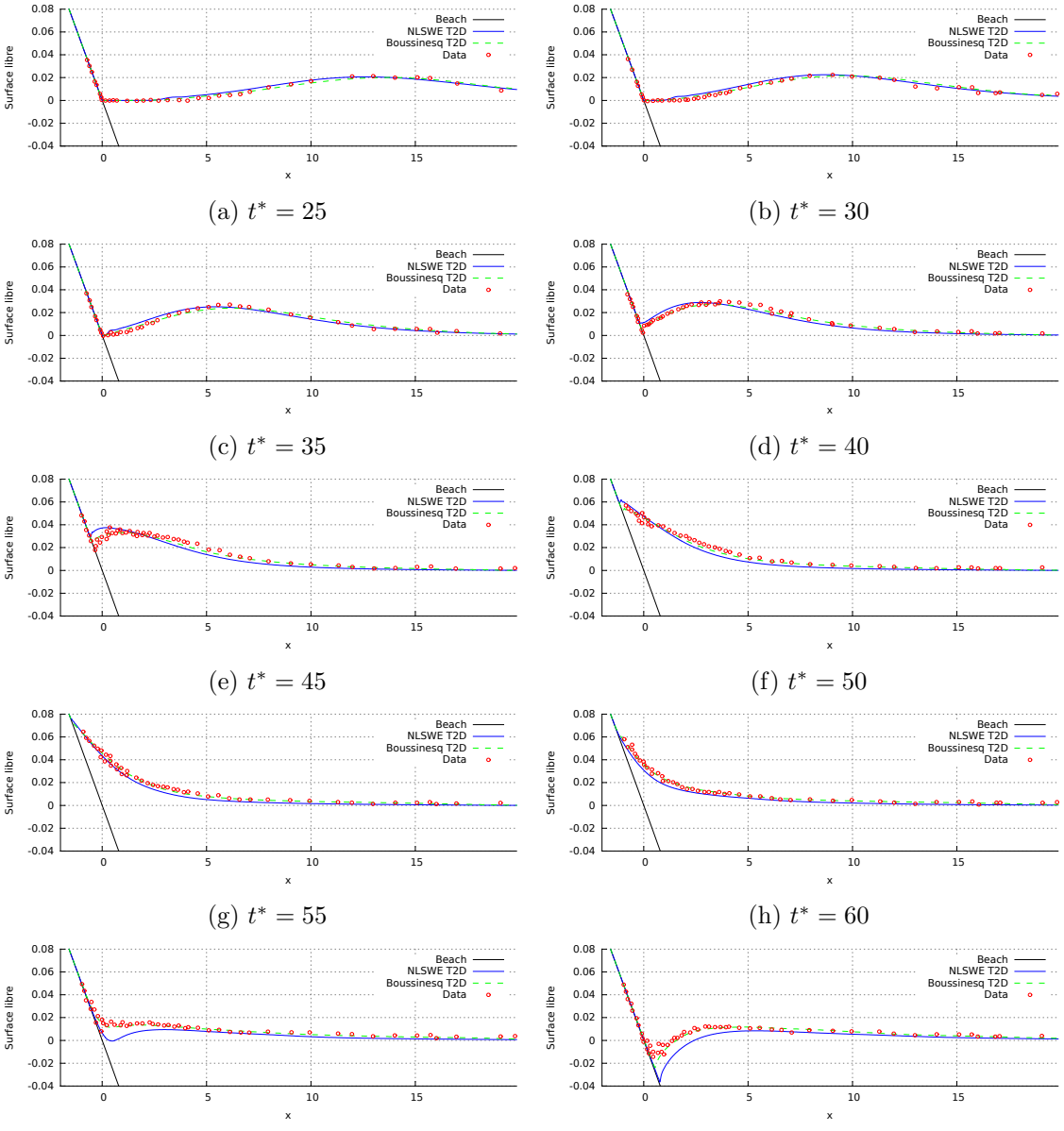

(a) $t^* = 25$ (b) $t^* = 30$

(c) $t^* = 35$ (d) $t^* = 40$

(e) $t^* = 45$ (f) $t^* = 50$

(g) $t^* = 55$ (h) $t^* = 60$

(i) $t^* = 65$ (j) $t^* = 70$

Figure 4.19: Run-up of a solitary wave on a uniform beach – Spatial free surface deformation profiles at different instants. Same nomenclature as Figure 4.18.

Chapter 5

Numerical model of the March 11, 2011 Tohoku event

Pour parfaire l'évaluation des codes numériques, ces derniers sont testés sur un évènement réel. Le contexte du projet TANDEM ainsi que sa vaste banque de donnée ont mené à choisir le tsunami Tohoku-Oki de 2011. Ainsi, ce chapitre décrit le modèle numérique construit pour le système Telemac. Quatre grilles de résolutions sont utilisées pour définir la bathymétrie. La densité du maillage s'adapte à cette dernière : plus le gradient de bathymétrie est important, plus petite est la taille des éléments de maillage. Une attention particulière est apportée à la baie d'Iwate, pour laquelle l'inondation sera regardée. Deux sources co-sismiques sont considérées : celle de Satake et al. [2013] et celle de Shao et al. [2011]. Les générations sont intégrées au modèle numérique des équations de Saint-Venant de Telemac2D. Quatre éléments de comparaisons sont disponibles: des mesures de bouées GPS proches des côtes japonaises, des relevés de bouées DART en océan, les hauteurs d'inondation et les étendues de zones inondées le long de la baie d'Iwate issues de la campagne de mesures de Mori et al. [2011]. Les deux types de générations donnent globalement des résultats satisfaisants tout en étant différents. Le modèle issue de la source de Shao et al. [2011] surestime un peu l'évènement, contrairement au modèle issu de la source de Satake et al. [2013] qui, correspond mieux aux données. Cependant, le frottement du fond n'est pas intégré dans les modèles numériques alors que son effet peut être important à proximité des côtes et lors de l'inondation. Ainsi, sa prise en compte pourrait inverser la précédente conclusion. Pour aller plus loin, un modèle de Boussinesq est construit. Ces résultats ne montrent que peu de différences avec le modèle de Saint-Venant, rejoignant l'analyse théorique préalablement établie.

5.1 State of art

The Tohoku-Oki event that occurred the 11^{th} March 2011 at $14:46:18$, made a lasting impression due to both nuclear disaster and the devastating tsunami. The tsunami was observable all over the Pacific and combining with the earthquake, it killed 15890 people, injured more than 6000 people and cost $220 billion of damage only in Japan (https://www.ngdc.noaa.gov/hazard/data/publications/2011_0311.pdf). The positive part of this catastrophe is the exceptional number of records: this event is well documented and thus is the subject of numerous studies. For these reasons among others, the members of the French project TANDEM (Tsunamis in the Atlantic and the English ChaNnel: Definition of the Effects through numerical Modelling) decided to model this event; the present study comes within its scope.
For this event a multitude of data are available: teleseismic body and long period surface waves, static Global Positioning System (GPS) sensors, offshore GPS buoys, Deep-ocean Assessment and Reporting Tsunami (DART) tsunamigrams and tide gauges records. They permit with an inversion of data to build models for the generation source (Ji et al. [2002]). Toda et al. [2011] described five possible seismic rupture models given by Wei and Sladen [2011] and Simons et al. [2011], Fujii et al. [2011], Shao et al. [2011], Pollitz et al. [2011], Yagi and Fukahata [2011b]. The origin data of these five models are summarised Table 5.1.

Models	teleseismic		static GPS sensors	DART tsunamigrams	tide gauges records
	Body waves	Surface waves			
Wei and Sladen and Simons et al.	X	X	X		
Shao et al.	X	X			
Fujii et al.				X	X
Pollitz et al.			X		
Yagi and Fukahata	X				

Table 5.1: 2011 Tohoku-Oki event – Data set used for the different source models.

Chen et al. [2014] built hydrodynamic models with ocean conditions for these five source models. Depending on the data, the pattern of the ground deformations differs a lot (not shown here). Indeed each data set has an influence on the generated source model. If separated inversions are performed for each single data set as did by Koketsu et al. [2011], different patterns of the slip are obtained, as shown in Figure 5.1.
Chen et al. measures the influence of the source by comparing numerical results (performed by FVCOM system) with observed sea-level displacements at tide gauge locations. The inundation of the coast is also studied at four locations, especially at the Fukushima

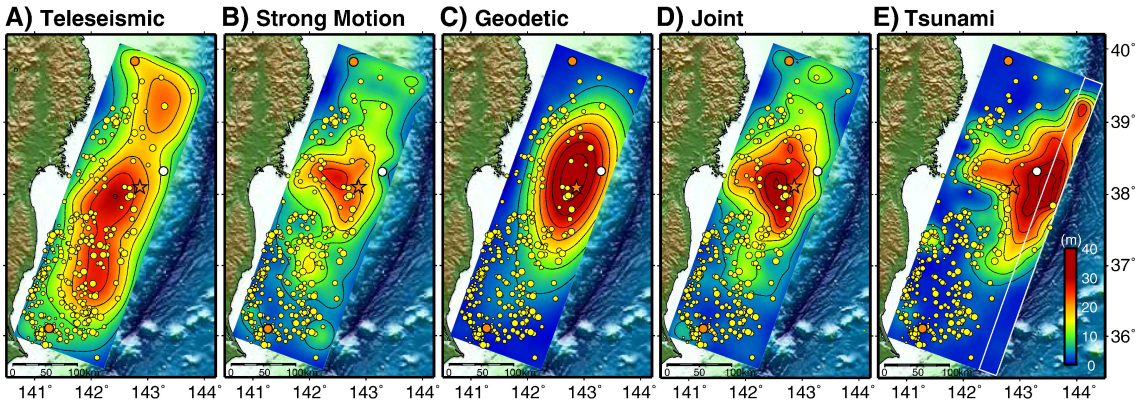

Figure 5.1: 2011 Tohoku-Oki event – Figure issued from the work of Koketsu et al. [2011]. Slip distribution pattern obtained from the single inversion of: A. teleseismic data, B. ground acceleration from seismometers, C. geodetic data, D. teleseismic + ground acceleration+ geodetic data, E. tsunamigram records. The yellow circles are aftershocks and the orange star is the epicenter of the main shock.

Dai-ichi Nuclear Power Plant (FDNPP). The authors concluded that these source models succeed to represent the main features of the tsunami, even if the performance depends on the kind of results and the location. Finally, the model from Shao et al. [2011] provided a better overall result, proving that giving more data set does not improve the source model, compared to the model of Wei and Sladen [2011] and Simons et al. [2011]. However, Chen et al. suggested that using a dynamic seismic model (Romano et al. [2014], Ide and Aochi [2014], Grilli et al. [2013]) coupled with the hydraulic model would permit a better evaluation of these source models. Grilli et al. [2013] developed a 3D Finite Element Modeling of the original subduction zone for which the elastic dislocations along the fault are simulated. This model of the source generation took into account the temporal dependence of the ground deformation and is coupled with a nonlinear and dispersive Boussinesq wave model (FUNWAVE-TVD). The authors compared the numerical result from the coupled model with a numerical model initiated by the Shao et al. model. They found out that globally the developed coupled model gave better results at GPS gauges and DART buoys than the model from Shao et al.. However, the simulated inundations along the Sanriku coast (between 39.2° and 40.2°) are under-predicted, the authors suggested that can be explained by a mesh not fine enough or by a missing Submarine Mass Failures (SMFs) during the generation. The latter suggestion is in agreement with the observed high frequency waves and far field dispersive wave trains, more typical for submarine slides than earthquake source (Trifunac and Todorovska [2002]). Tappin et al. [2014] proposed a model with the combination of a co-seismic source and a SMF. This model provided better result for the run-ups and waveforms than for an alone co-seismic source.

However, in this study only co-seismic sources are considered: numerical models are built from the source generation of Shao et al. [2011] and the kinematic model of Satake et al.

[2013]. the lattest is built with only data obtained from tsunami records. Both source models are presented in Section 5.3.
An other aspect, also studied by Chen et al. [2014] and Grilli et al. [2013], is the non-dispersive/dispersive, hydrostatic/non-hydrostatic importance of this event. While Chen et al. watched the impact of a non-hydrostatic model on the FDNPP, concluding that its effect became important for water depth around $10m$ and shallower but did not change the inundation result, Grilli et al. [2013] compared a Boussinesq-type model with a nonlinear shallow water model (same code but without the dispersion terms). They concluded that the dispersion phenomenon is small near-field and takes importance only far-field.
This chapter follows the construction of the numerical model of the 2011 Tohoku-Oki event with the system Telemac. First, in Section 5.2 the bathymetry and the mesh are described. Secondly, as said in the previous paragraph, the source models of Shao et al. [2011] and Satake et al. [2013] are detailed. Then, the numerical results for a Nonlinear Shallow Water Equation model (NLSWE of T2D) are compared to observed data in Section 5.4. These results concern the propagation of the tsunami near-field and far-field (see Section 5.4.1), and the inundation (see Section 5.4.2). Finally, the issue of the dispersion effects is addressed Section 5.5 with the analytical analysis developed in chapter 2, and completed with a numerical Boussinesq model (T2D).

5.2 Construction of the mesh and bathymetry

Four grids of bathymetric data were used to build the final mesh, the resolution is given in the Mercator projection:

1. a general grid, covering a large part of the Pacific Ocean with a bathymetry from Pr. Sasaki (Sasaki et al. [2012]),
2. a medium grid embracing the East Japan with a resolution of $\sim 2km$,
3. a small grid including the East coast of the Japan with a resolution around $\sim 500m$,
4. a grid focusing on the South Iwate prefecture coast, so called here after the bay of Iwate, with a resolution of $\sim 120m$.

The last three grids are DTM built from data given by the MRI (Meteorological Research Institute) within the scope of the project TANDEM. Figure 5.2 represents the boundary of each grid, respectively grid 1 to 4. The boundary of the grid 1 is the boundary of the domain, and thus the boundary of the mesh. In this case, it is considered as wall type. Except the bay of Iwate, the coastlines are considered as wall. The bathymetry and the mesh are represented in Figure 5.3. The mesh is adapted to the variation of bathymetry with smaller elements close to the fault and the coast. The minimum element length is

$\sim 10m$ close to the coast and the maximum length of the element is $\sim 15km$ far-field. This mesh counts around $680,000$ nodes.

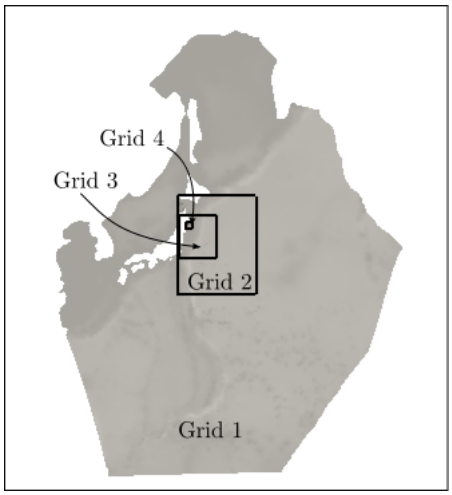

Figure 5.2: 2011 Tohoku-Oki event – Limit of the four grids (black lines) used to create the mesh. The blue line represent the boundary of the Japan islands.

The choice of a unique static numerical mesh is questionable because it is expensive in memory and computational time. A model with nested grids (Chen et al. [2014], Grilli et al. [2013]) or an adaptive model (Popinet [2012], Pons et al. [2016], Arpaia and Ricchiuto [2016]) may be preferable. However, these two methods are not yet available with the Telemac system, which justifies the present choice.

5.3 Initial condition and seismic sources

5.3.1 Shao *et al.*'s Source

As described in the paragraph 5.1, the source issued of the work of Shao et al. [2011] considered only teleseismic body and surface waves. The authors used 27 teleseismic P and 18 SH waveform records (body waves) and 53 surface wave records, and follow the procedure of Ji et al. [2004]. The model is composed of 190 $25km \times 20km$ subfaults. The strike is supposed constant (198°) and the dip angle is fixed at 10°. The length fault is $300km$ and the width fault is estimated at $90km$. The characteristics of each subfault are available on their website (`http://www.geol.ucsb.edu/faculty/ji/big_earthquakes/2011/03/0311_v3/Honshu.html`). Figure 5.4 shows the slip pattern obtain with this inversion.
The initial free surface deformation is calculated using the traditional way to generate

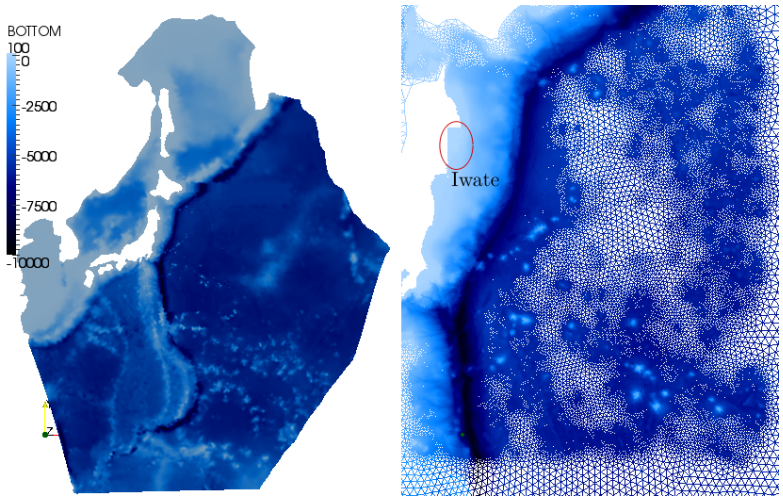

(a) Global view.

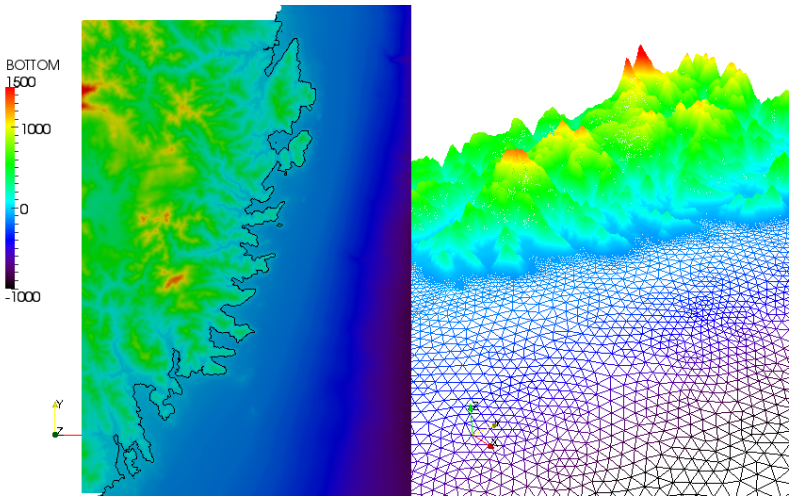

(b) View of the Iwate bay.

Figure 5.3: 2011 Tohoku-Oki event – Bathymetry (left) and mesh (right) of the domain considered in the projection of Mercator. Figure 5.3a gives a glimpse of the total domain and a closest East part of Japan while figure 5.3b shows more precisely the bathymetry and the mesh of the Iwate bay, the thin black line is the isoline for a ground elevation $z = 0$, considered as the coastline.

seismic tsunami and the method of Okada [1992]: its corresponds to the final vertical seafloor deformation. The result with Telemac is compared to the one computed by Chen et al. [2014] in Figure 5.5.

A qualitative comparison permits us to validate this initial state.

However, Shao et al. [2011] estimated a propagation rupture velocity around $1.5km/s$ with rupture starting times proper to each subfault. A second model for the generation is proposed using this kinematics. The duration of the generation is estimated here at $180s$. Figure 5.6 shows a comparison at $t = 180s$ between the kinematic and static generation. The initial deformation amplitude of the static model is larger than the one with the

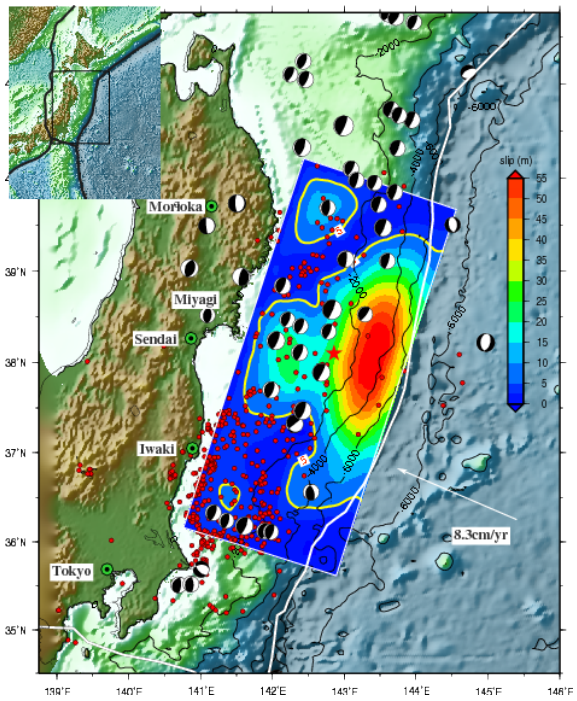

Figure 5.4: 2011 Tohoku-Oki event – Graph issued from the work of Shao et al. [2011]. Snapshot of the slip distribution obtained from teleseismic data. The red star represents the epicenter location, red dots the aftershocks. The white line is the $5m$ slip contour. The white arrow shows the relative motion of tectonic plate.

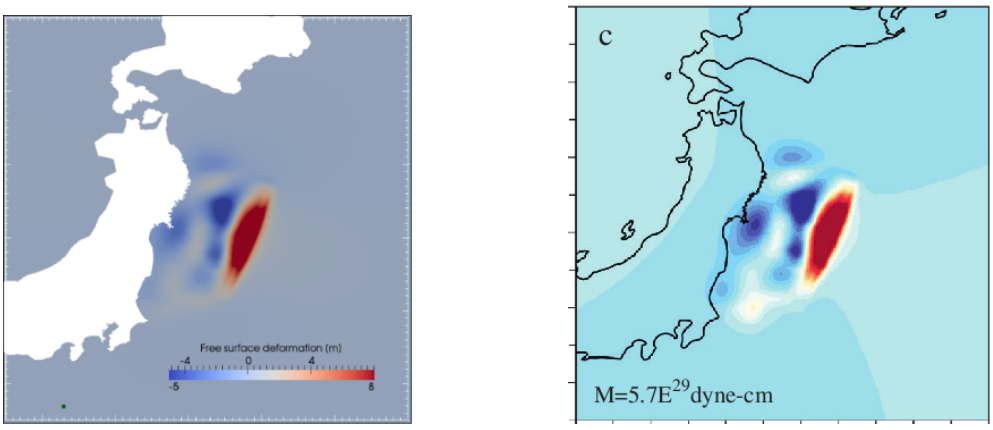

(a) (b)

Figure 5.5: 2011 Tohoku-Oki event – Comparison of the initial free surface deformation (using the traditional way to generate tsunami) with the NLSWE model of Telemac2D (5.5a) and the seafloor deformation calculated by Chen et al. [2014] (5.5b). The scale is identical for both graphs.

kinematic generation. On the contrary at $t = 180s$, the kinematic model give more important waves. Also the static model seems to have an advanced propagation compare to the kinematic one.

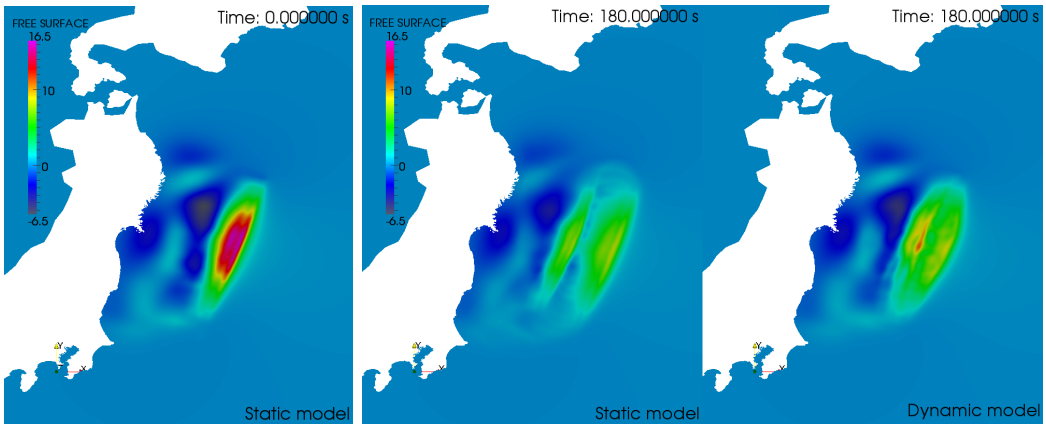

(a) $t = 0s$ (b) $t = 180s$

Figure 5.6: 2011 Tohoku-Oki event – Snapshot of the free surface deformation from NLSWE model of Telemac2D with source models of Shao et al. [2011]. The Figure 5.6a is the initial deformation for the static model. The Figure 5.6b is the free surface deformation at $t = 180s$ from the static initialisation (left) and the kinematic generation (right). The scale is the same for both models.

5.3.2 Satake *et al.*(2013) Source

Satake et al. [2013] expended the preliminary results of Fujii et al. [2011] by integrating more records. They created source model from waveform and tsunami data. At the end, the data set is composed of 11 Ocean Bottom Pressure (OBP) gauges, 10 GPS waves gauges and 32 coastal and tide gauges. The authors considered a grid of 55 subfaults with a constant strike (193°) and slip angle (81°). The subfault sizes are $50km \times 50km$ and $50km \times 25km$ near the main fault. The inversion of data was performed with a resolution by finite difference method for linear Shallow Water Equation. They considered a temporal and spatial distribution of slip. The result slip pattern evolves during $5min$, with updates every $30s$. Figure 5.7 represents the temporal evolution of the slip. The information of the source model are available on the authors website (`http://iisee.kenken.go.jp/staff/fujii/OffTohokuPacific2011/tsunami_inv.html`).
The vertical deformation of the seafloor is estimated at each update with the Okada calculations (Okada [1992]). Snapshots in Figure 5.8 show the temporal evolution of the seafloor, and Figure 5.9 represents the free surface deformation calculated with NLSWE model of Telemac2D at the end of the ground deformation at $t = 5min$ and $t = 4min$ in comparison with the free surface deformation obtained by Satake et al. [2013]. Some small differences appear in the North of the deformation, but globally, the numerical free surface elevation obtain with Telemac2D matches well the one of Satake et al..

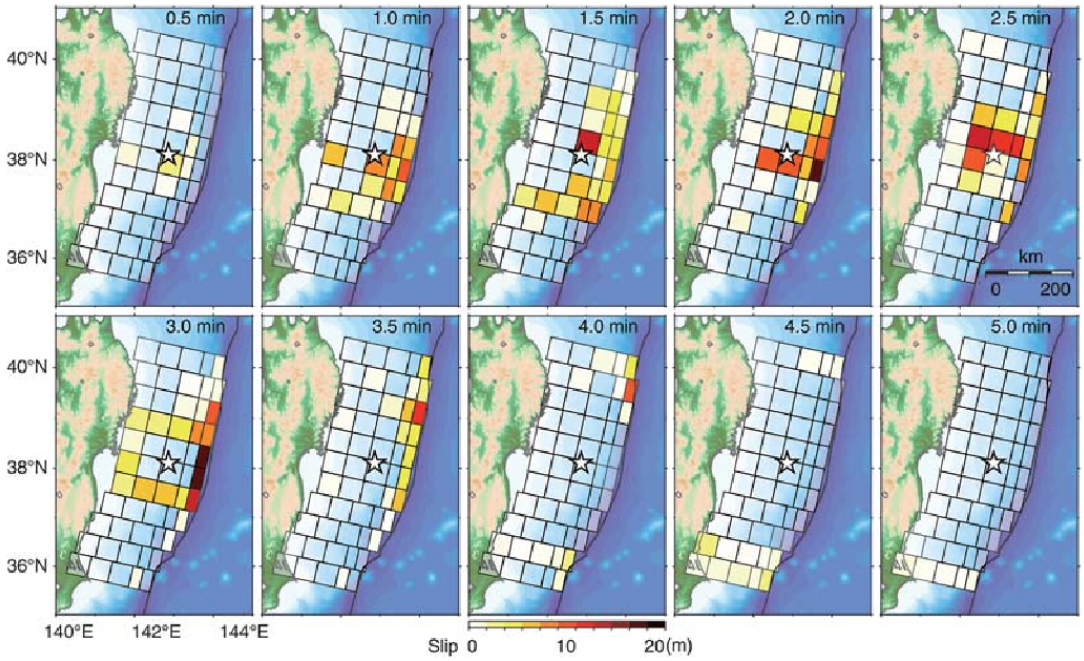

Figure 5.7: 2011 Tohoku-Oki event – Evolution of the slip pattern during $5min$. The interval if each update is $30s$. The white star is the epicenter. Figure issued from the work of Satake et al. [2013].

5.4 Numerical results

5.4.1 Propagation and comparisons with data

The simulations are performed with NLSWE model of T2D. Some snapshots of the numerical propagation of the wave generated are shown in Figure 5.10.

During the event, as said in Section 5.1, many data were recorded. Among them, six GPS buoys situated along the Japan East coast measured the variation of the free surface. Their location are plotted on a simplified map in Figure 5.11.

The comparisons between numerical results of free surface deformation and data are plotted in Figure 5.12.

The measures and numerical results are temporally adjusted by considering the 10^{th} March 2011 at $00:00:00$ as the origin time. Thus, the numerical time of the earthquake is $38.7h$. The simulations concern only the first four hours of the event. The kinematic and static source models from Shao et al. [2011] give similar results. The amplitude of the free surface deformation of the kinematic model is slightly more important than the one from the static model. Also, there is a small phase difference between the models, this delay

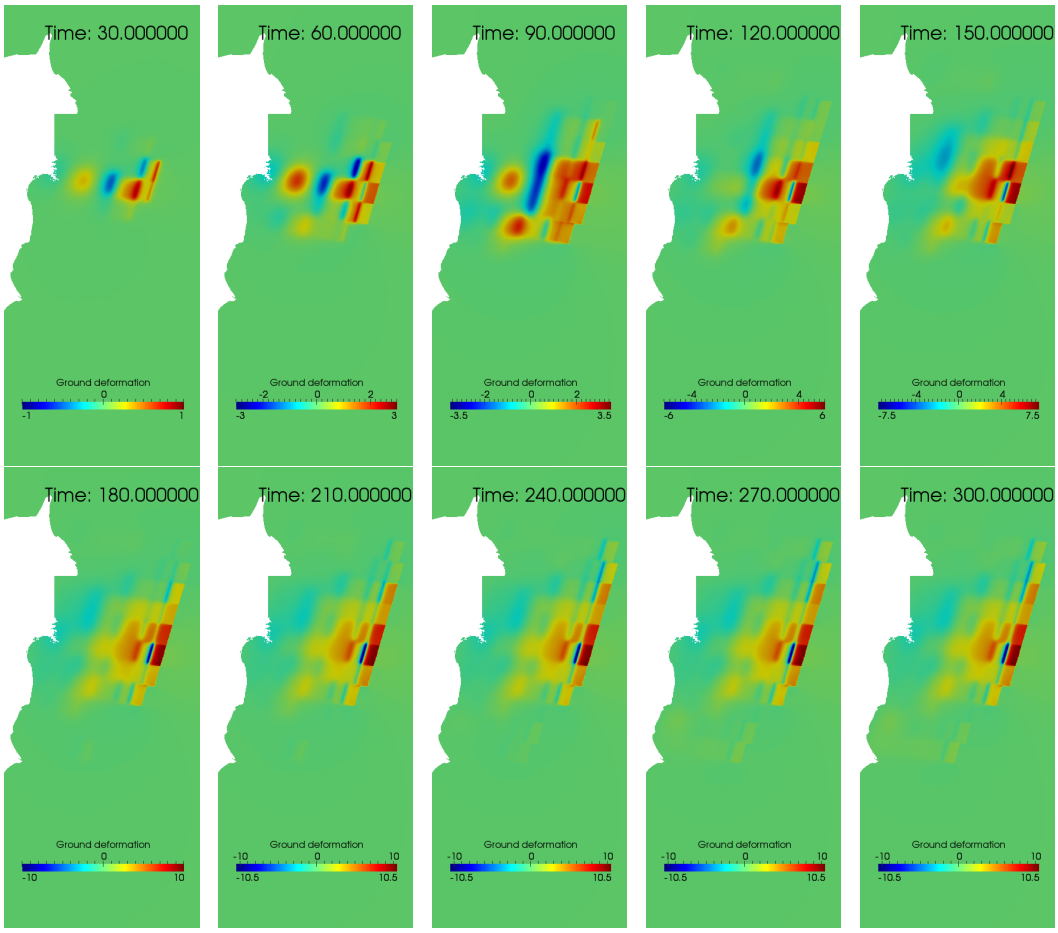

Figure 5.8: 2011 Tohoku-Oki event – Seafloor deformations issued of the model source of Satake et al. [2013] at $30s$ time intervals.

could correspond to the duration of generation, *i.e.* $180s$. As the numerical results are quite not sensitive to the nature of generation (static or kinematic) for the model of Shao et al., only the static generation is considered hereafter.

The numerical results from the models of Shao et al. [2011] and Satake et al. [2013] are quite different. Globally, the leading wave of the model of Shao et al. is larger than the one from the Satake et al. At buoys 807, 804, 802 and 806, the amplitude of the first wave predicted by Shao et al.'s model is closer to the one measured. However, at buoys 803 and 801 the amplitude is over-predicted, more than twice the record at the buoy 801. With Satake et al.'s model, the first wave is under-predicted, while the global temporal evolutions of the free surface are in better agreement with the data than the result from Shao et al.'s model, except for the buoy 806, the farthest from the source, where both models have difficulty to reproduce the waveform: Shao et al.'s model only succeeds to capture the first and second waves.

In addition to the GPS gauges, fours DARTs recorded the event that are localised on the map in Figure 5.13. The free surface elevations associated are plotted in Figure 5.14. For

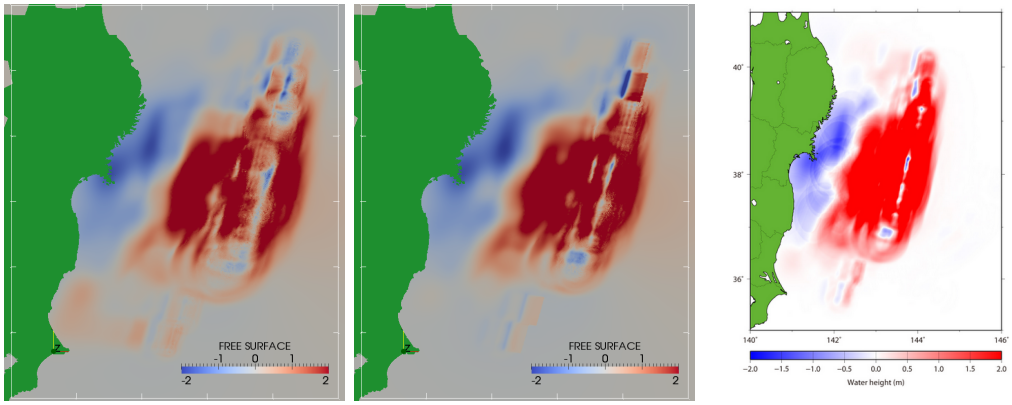

(a) $t = 5min$ (b) $t = 4min$ (c) $t = 4min$

Figure 5.9: 2011 Tohoku-Oki event – Snapshots of the free surface deformation calculated from the source model of Satake et al. [2013] with Telemac2D at the end of the ground motion (5.9a) and at $t = 4min$ (5.9b) in comparison with the free surface deformation obtained by Satake et al. at the same time (5.9c).

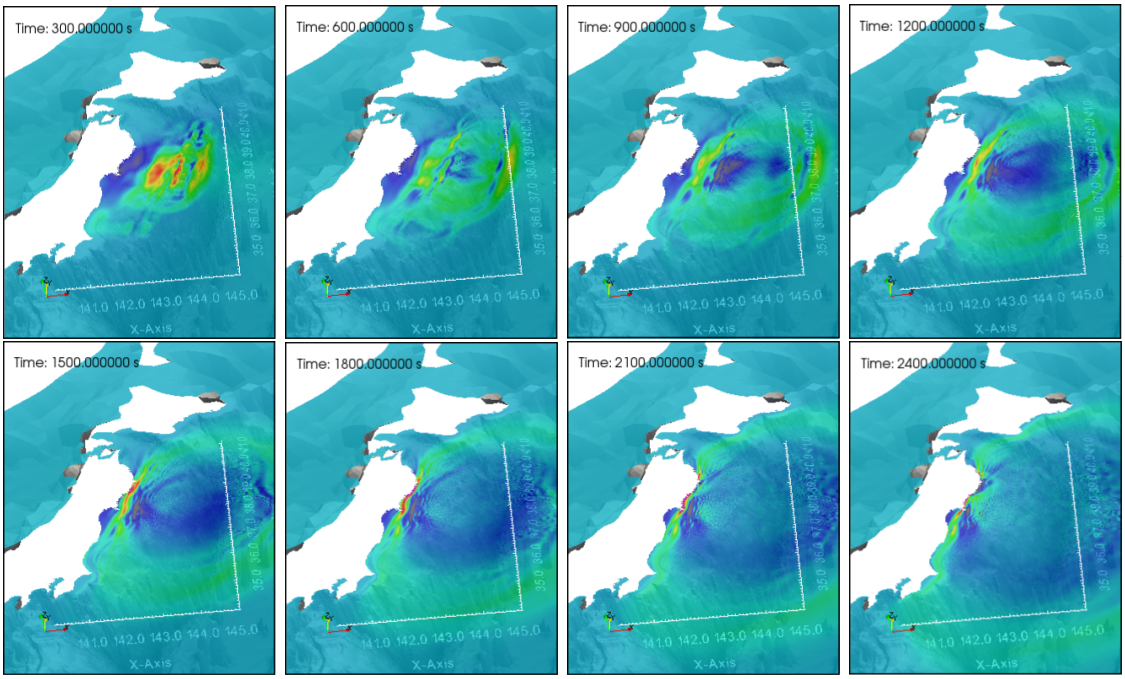

Figure 5.10: 2011 Tohoku-Oki event – Snapshots of the free surface elevation calculated with the NLSWE model of Telemac2D simulation and using the generation issued of Satake et al. [2013]. The snapshots are taken every $5min$ for the first $35min$ of the propagation.

the closest buoys to the coast, *i.e.* 21418 and 21413, the behaviours of the models are similar than for the GPS gauges: the leading wave from Shao et al.'s generation is larger than the one from Satake et al.'s model. However, Shao et al.'s model results match the data while Satake et al.'s model under-predicts the wave amplitude. For the furthest buoys, *i.e.* 52405 and 52402, both numerical results do not really match the data. For the buoy

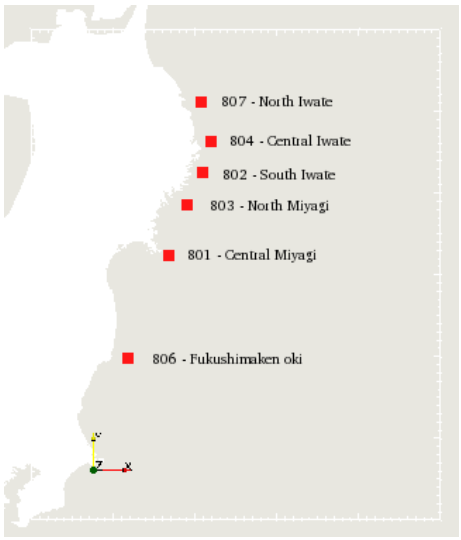

Figure 5.11: 2011 Tohoku-Oki event – Localisations of the GPS buoys along the East Japanese coast.

52405, the numerical models globally catch the waveform and have an approximately good amplitude, while for the buoy 52402, the numerical signal does not correspond anymore to the measures. The buoy 52402 being the furthest to the source ($\sim$ $3500km$), at this stage we can suppose that the propagation model is not good enough for such a distance, and dispersive effects may develop.

5.4.2 Run-ups and inundations

In this section, we come back to local results with flooded and run-up measurements.

5.4.2.1 Run-ups

In their work Mori and Takahashi [2012] lead a survey on the inundations and run-ups. They provide inundation distances, and run-up heights with their locations and dates. These two measurements correspond to the same definitions given for the 1947 New Zealand event (Chapter 3, Figure 3.14). With numerical models, only the inundation height at the shoreline is calculated, as the maximal water depth obtained during four hours. Only inland of the Iwate bay was integrated in the numerical domain, thus, these results concern this part of the coast. In Figure 5.15, numerical results from Telemac2D with the generation of Shao et al. [2011] and Satake et al. [2013] are compared to the inundation height measurements.

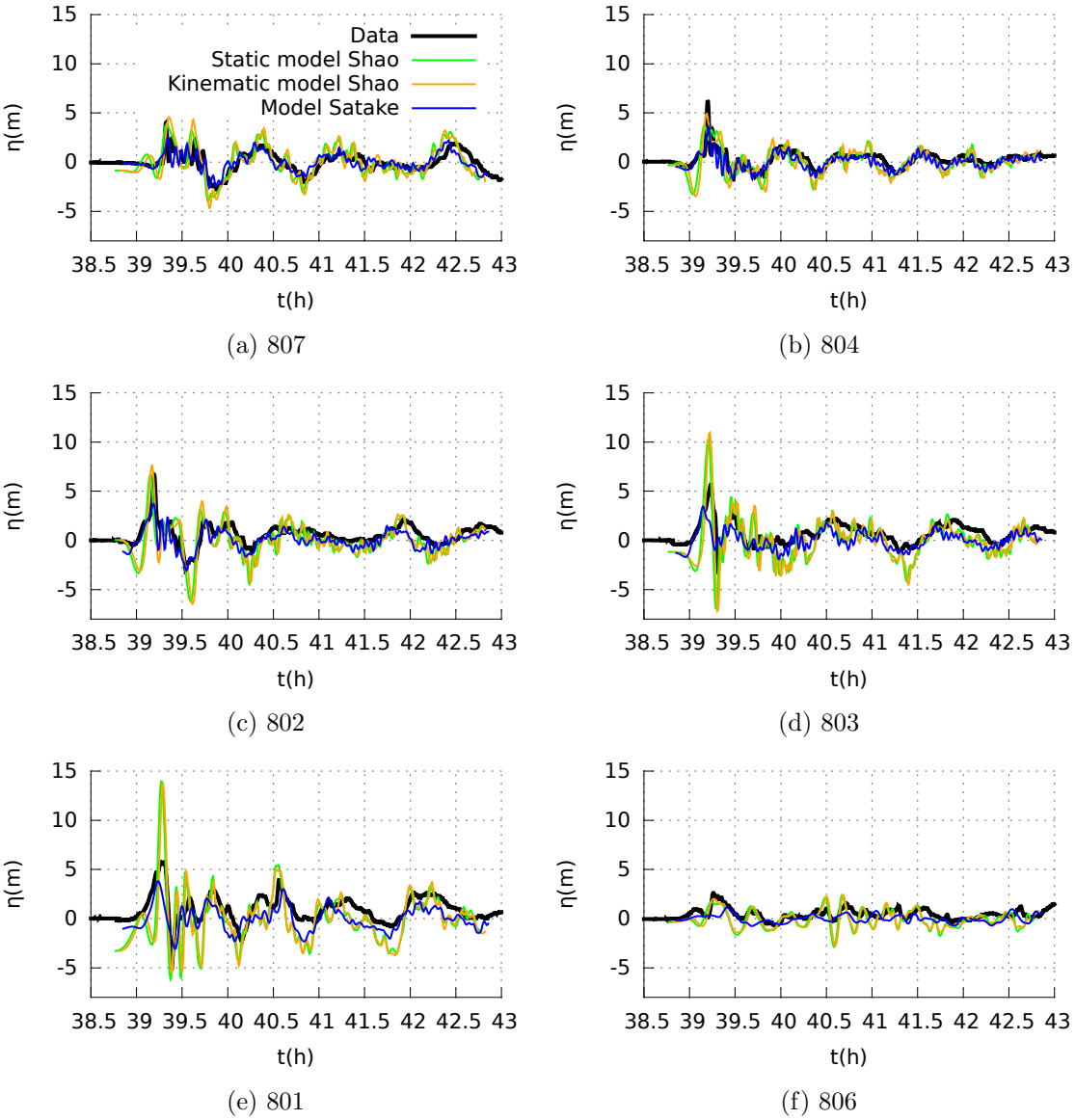

(a) 807 (b) 804

(c) 802 (d) 803

(e) 801 (f) 806

Figure 5.12: 2011 Tohoku-Oki event – Comparisons between measurements from GPS gauges and numerical results of the free surface deformation. The black thick line is the data. The blue line is Telemac2D result from Satake et al. [2013] source. The orange and the green lines are respectively the Telemac2D results from the kinematic and static Shao et al. [2011] sources.

The model issued from the generation of Shao et al. [2011] gives larger inundations than the model with the Satake et al. [2013]'s generation. It is consistent with the larger leading wave. However, globally the numerical results from the model with the generation of Satake et al. are closer to the data.

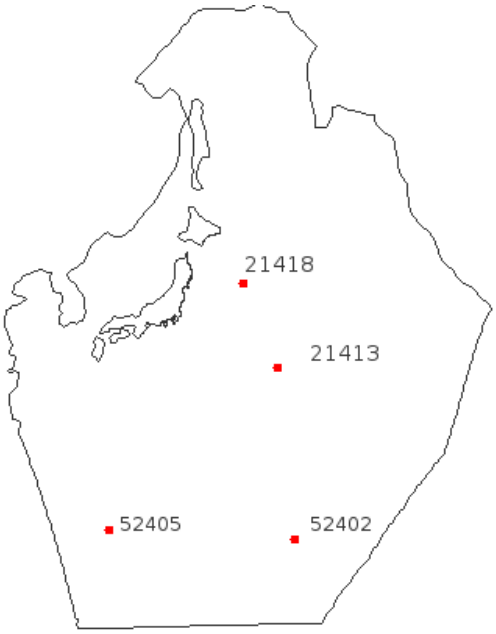

Figure 5.13: 2011 Tohoku-Oki event – Location of the DART buoys. Their measurement are available at https://www.ngdc.noaa.gov/hazard/dart/2011honshu_dart.html.

5.4.2.2 Inundation

As in the previous section, the results of inundation only focus on the Iwate Bay. From the work of Chen et al. [2014], two areas in the Bay of Iwate figure among field survey measurements (Mori et al. [2011]). The areas are referred as the North and the South of Iwate. Comparisons between the numerical flooded areas and the survey are shown in Figures 5.16 and 5.18, respectively North and South of Iwate. In the present results, the minimum water depth considered to have a flooded area is $0.5m$.

At the North Iwate Bay, both models (from Satake et al. [2013] and static Shao et al. [2011] generations) globally well represent the main flooded area. They slightly overestimate the inundation except at the Miyako bay (latitude around 39.64°) where the survey shows inundation along the Hei River that simulations do not succeed to model. It may be a consequence of a too coarse bathymetric grid or mesh. A zoom on this zone is done and shows in Figure 5.17. The mesh is also represented showing the spatial resolution at this location, the element size is at the order of $100m$.. The model from Shao et al. give larger flooded area than the model from Satake et al., the latter being closer to the survey. However, numerical models do not consider a bottom friction, thus this over-prediction was expected.
At the South Iwate bay, the numerical results are close to the survey. The model from Shao et al. [2011] again overestimates the flooded area while the model from Satake et al.

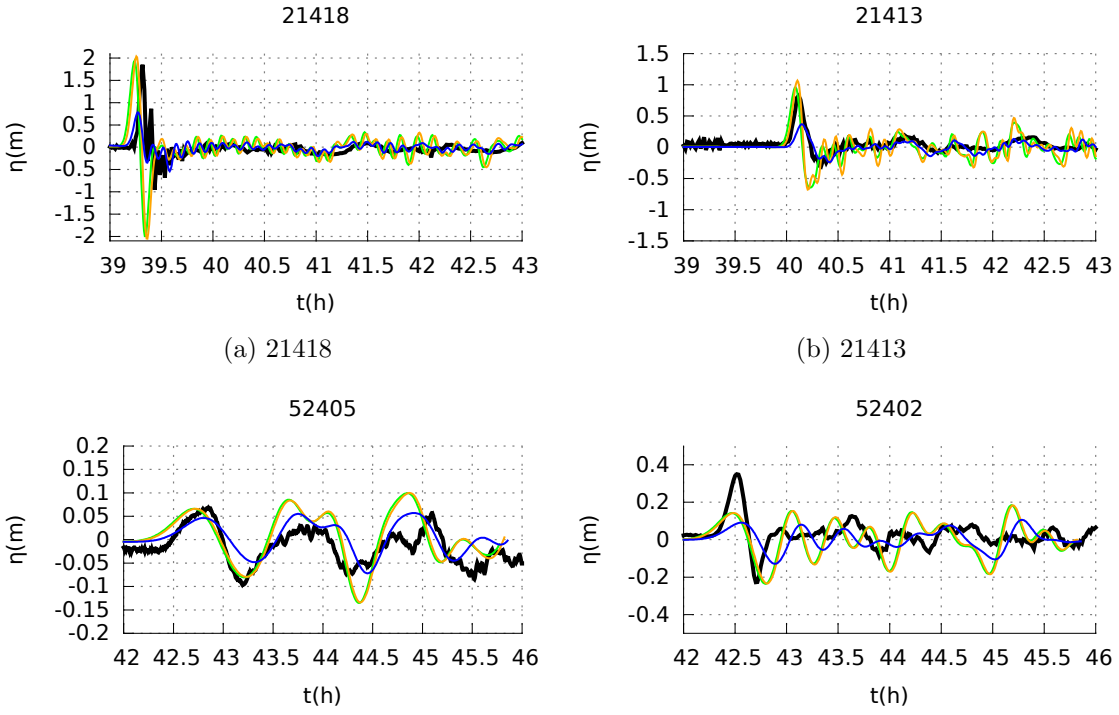

(a) 21418 (b) 21413

(c) 52402 (d) 52402

Figure 5.14: 2011 Tohoku-Oki event – Comparisons between measurements from DART buoys and numerical results of the free surface deformation. The black thick line is the data. The blue line is Telemac2D result from Satake et al. [2013] source. The orange and the green lines are respectively the Telemac2D results from the kinematic and static Shao et al. [2011] source.

[2013] better matches the data, especially at the bottom of the Hirota Bay where the numerical result is in really good agreement with the survey inundation. However, this model unpredicted the inundation behind the Oshima Island.

Results of a NLSWE model of Telemac with Shao et al.'s source and with a law of bottom friction are shown in Figure 5.19. For this model, we used a law of Strickler with a coefficient of $30m^{1/3}/s$, corresponding to areas with vegetations. With this first attempt, we can see that the bottom friction strongly influences the extension flooded areas. However, an uniform friction coefficient seems to be a rough approximation, in this case the model under-predicts the reality. A heterogenous pattern of the friction coefficient may permit a better approach of the phenomenon.

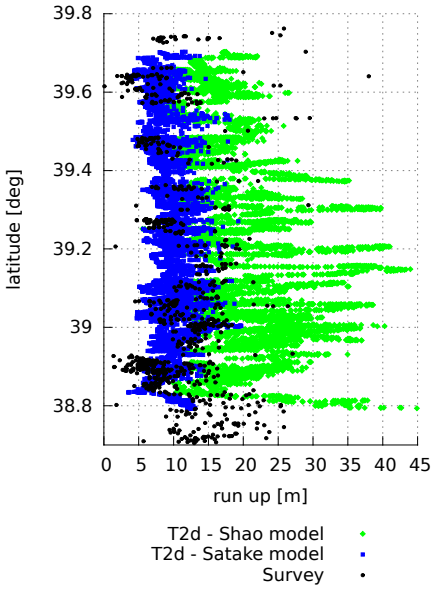

Figure 5.15: 2011 Tohoku-Oki event – Comparison between the inundation heights obtained by the numerical models and the survey measurements at the Iwate Bay. The black dots are data from the 2011 Tohoku Earthquake Tsunami Joint Survey Group, release 20120330, http://www.coastal.jp/ttjt/, the blue dots are numerical result from Telemac2D with the generation from Satake et al. [2013] and the green dots numerical results with the generation from Shao et al. [2011].

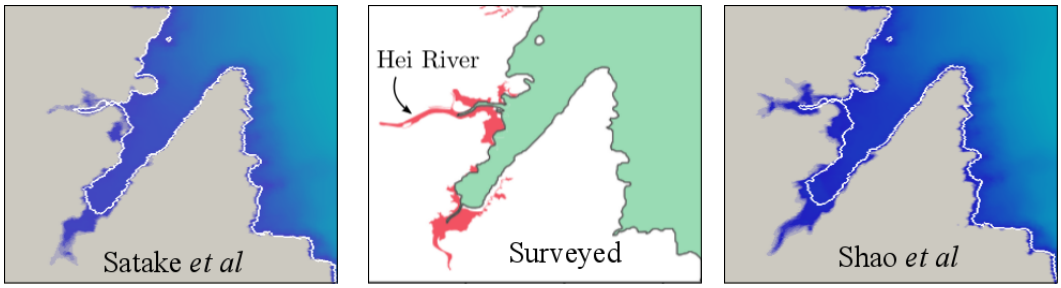

(a) (b) (c)

Figure 5.16: 2011 Tohoku-Oki event – Snapshots of the flooded area obtained by the numerical models in the North area of the bay of Iwate. Results in Figures 5.16a and 5.16c are obtained respectively from the model of Satake et al. [2013] and Shao et al. [2011]. Figure 5.16b is adapted of the work of Chen et al. [2014].

5.5 Dispersion

In this section, the issue of the dispersion phenomena is addressed. Usually, the NLSWE are used to model tsunami event. Nevertheless, recent works pointed out that dispersion may appear, including during the case of the Tohoku-Oki event, see Paragraph 5.1. First an analytical study is performed using the linear solution developed in Chapter 2. Then, numerical simulation is done using the Boussinesq Equation available with Telemac2D. Its

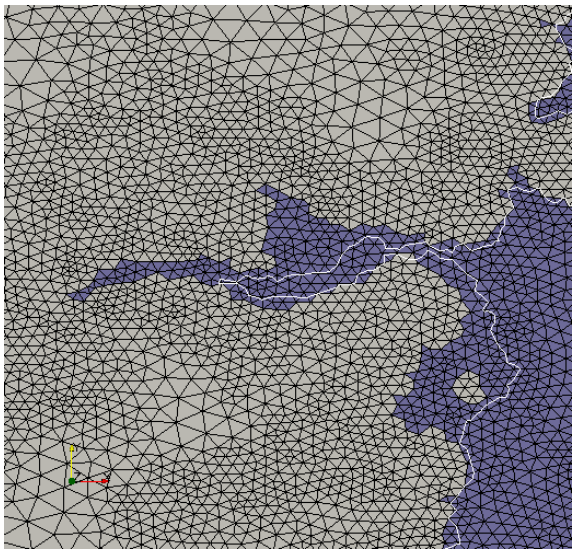

Figure 5.17: 2011 Tohoku-Oki event – Zoom on the Hei River. The grey zone is the land and the blue elements correspond to the flooded area with a minimum water depth of $0.5m$. The elements of the mesh are in black, they are of the order of $100m$. The white line is the initial coastline.

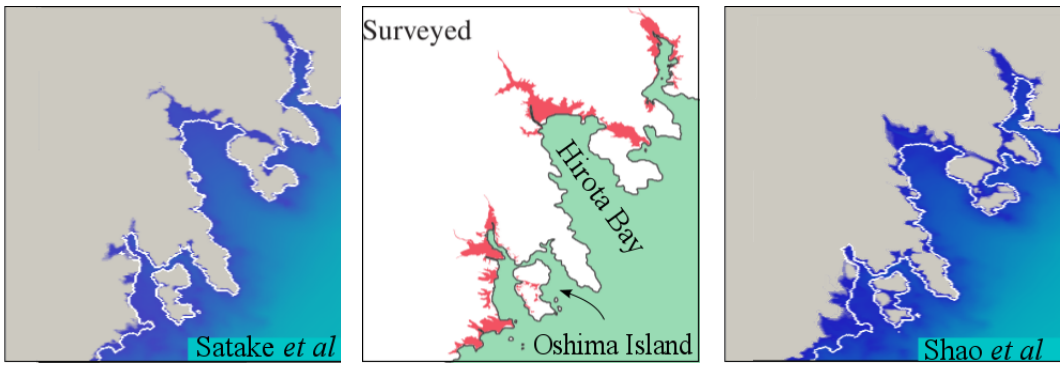

(a) (b) (c)

Figure 5.18: 2011 Tohoku-Oki event – Snapshots of the flooded area obtained by the numerical models in the South area of the bay of Iwate. Results in Figures 5.18a and 5.18c are obtained respectively from the model of Satake et al. [2013] and Shao et al. [2011]. Figure 5.18b is adapted of the work of Chen et al. [2014].

results are compared to data and NLSWE results.

5.5.1 Theoretical analysis

The Japan Meteorological Agency provided the epicenter location: at $38°06,2'$ N and $142°51,6'$ E. The average depth h at this location is around $1500m$. The maximum vertical deformation measured is about $5m$ (Ito et al. [2011]). The length fault is estimated at $L = 400km$. Three rupture velocities are defined in the work of Satake et al. [2013]

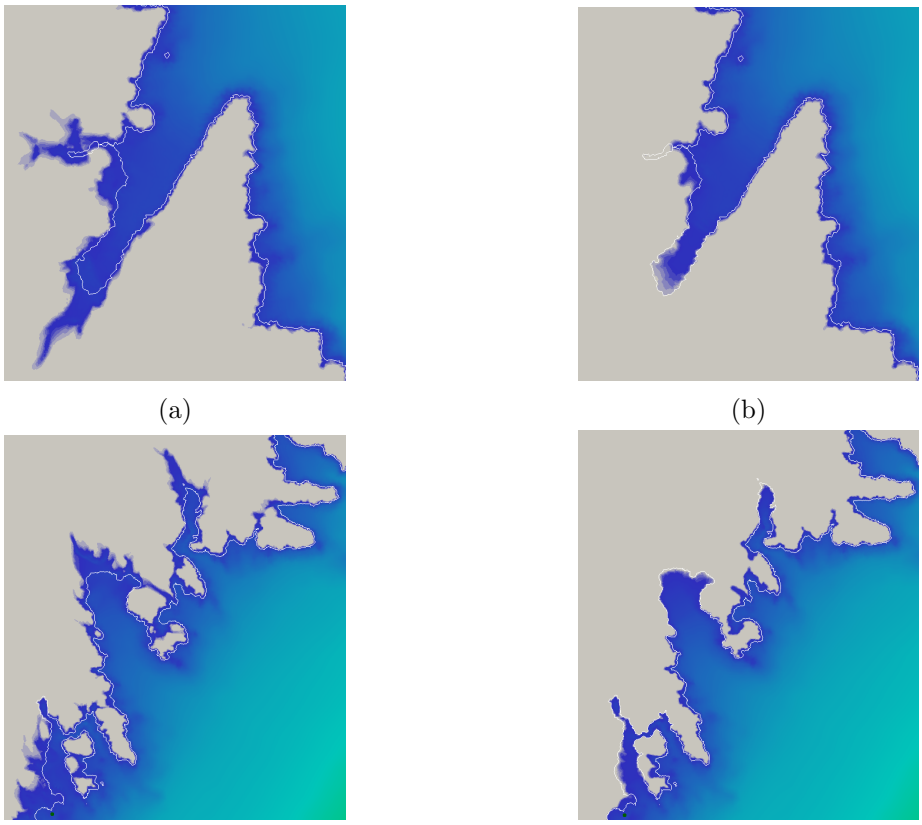

(a) (b)

(c) (d)

Figure 5.19: 2011 Tohoku-Oki event – Snapshots of the flooded area obtained in the North and South areas of the Iwate bay by the NLSWE model of Telemac2D without and with friction bottom, Figures 5.19a, 5.19c and Figures 5.19b, 5.19d, respectively. The friction law is the Strickler law with a coefficient of $30m^{1/3}/s$. The white line is the initial coastline.

and Koketsu et al. [2011]: $v_{p1} = 1.8km.s^{-1}$, $v_{p2} = 1.5km.s^{-1}$, $v_{p3} = 2.5km.s^{-1}$. The instruments of measurement did not catch the vertical deformation of the floor, thus it is supposed instantaneous and t_r small. With these parameters we can define the quantities of interest as described in Chapter 2, being: $\zeta_0^* = 3.10^{-3}$, $L^* = 267$, $v_p^* \in [12.36, 20.60]$ and $\tau^* \ll 1$. These values are summed up in Table 5.2. The energetic ratio ε is defined as in Chapter 2 for an idealized deformation of the sea floor, Equation 2.26. The spectrum of ε is calculated for $L^* = 267$, it is represented in Figure 5.20. The striped grey zone shows the possible temporal parameter values for the Tohoku-Oki event. In this zone, ε has a maximal value around 1% for $\tau^* = 0$, and when τ^* slightly increases, ε value quickly drops to 10^{-6}. Thus for this event we can say that the NLSWE could be locally used. This conclusion can be verified by modeling this event with the Boussinesq model of T2D.

Real values	Non-dimensional
$\zeta_0 = 5m$	$\zeta_0^* = 3.10^{-3}$
$L = 400km$	$L^* = 267$
$v_{p1} = 1.8km.s^{-1}$ $v_{p2} = 1.5km.s^{-1}$ $v_{p3} = 2.5km.s^{-1}$	$v_p^* \in [12.36, 20.60]$
t_r almost null	$\tau^* \ll 1$

Table 5.2: 2011 Tohoku event – non-dimensional temporal and geometric parameters of the Tohoku event. The values are issued of Ito et al. [2011], Satake et al. [2013] and Koketsu et al. [2011].

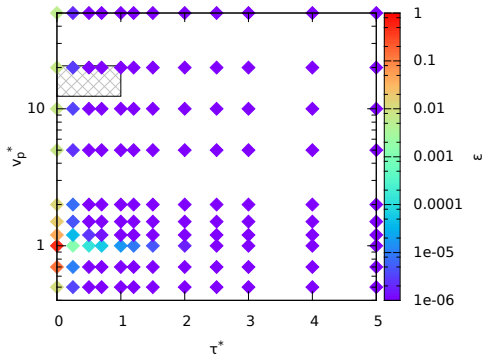

Figure 5.20: 2011 Tohoku-Oki event – Potential energy ratio ε at $t^* = T^*$ for $L^* = 267$. The striped grey zone shows the possible parameter values for the Tohoku, 2011 event.

5.5.2 Boussinesq model of the 2011 Tohoku-Oki event

In this section, a new numerical model is built to evaluate the dispersive effects of the 2011 Tohoku-Oki tsunami event. As said in the previous paragraph, there should no be important differences between the Boussinesq model and the NLSWE model of Telemac2D close to the source. The selected source for this simulation is the kinematic Shao et al. [2011] model. This choice is justified by the fact that the source model from Satake et al. [2013] was built only on water waveform data and the inversion of data is done using a Shallow Water model. Thus, it seemed more honest to keep the Shao et al. [2011] model for this propagation model. A second mesh is constructed with a finer approach to the Japanese coasts (900, 000 nodes at the end). Indeed, the Boussinesq model is more sensitive to the mesh than the NLSWE model, see Hervouet [2007]. However, how far the mesh's refinement is pushed in the material capacity, only one hour of propagation with the Boussinesq model could be calculated before a numerical divergence of the code occured. Thus in this section only a comparison to the GPS gauges is possible as shown

in Figure 5.21.

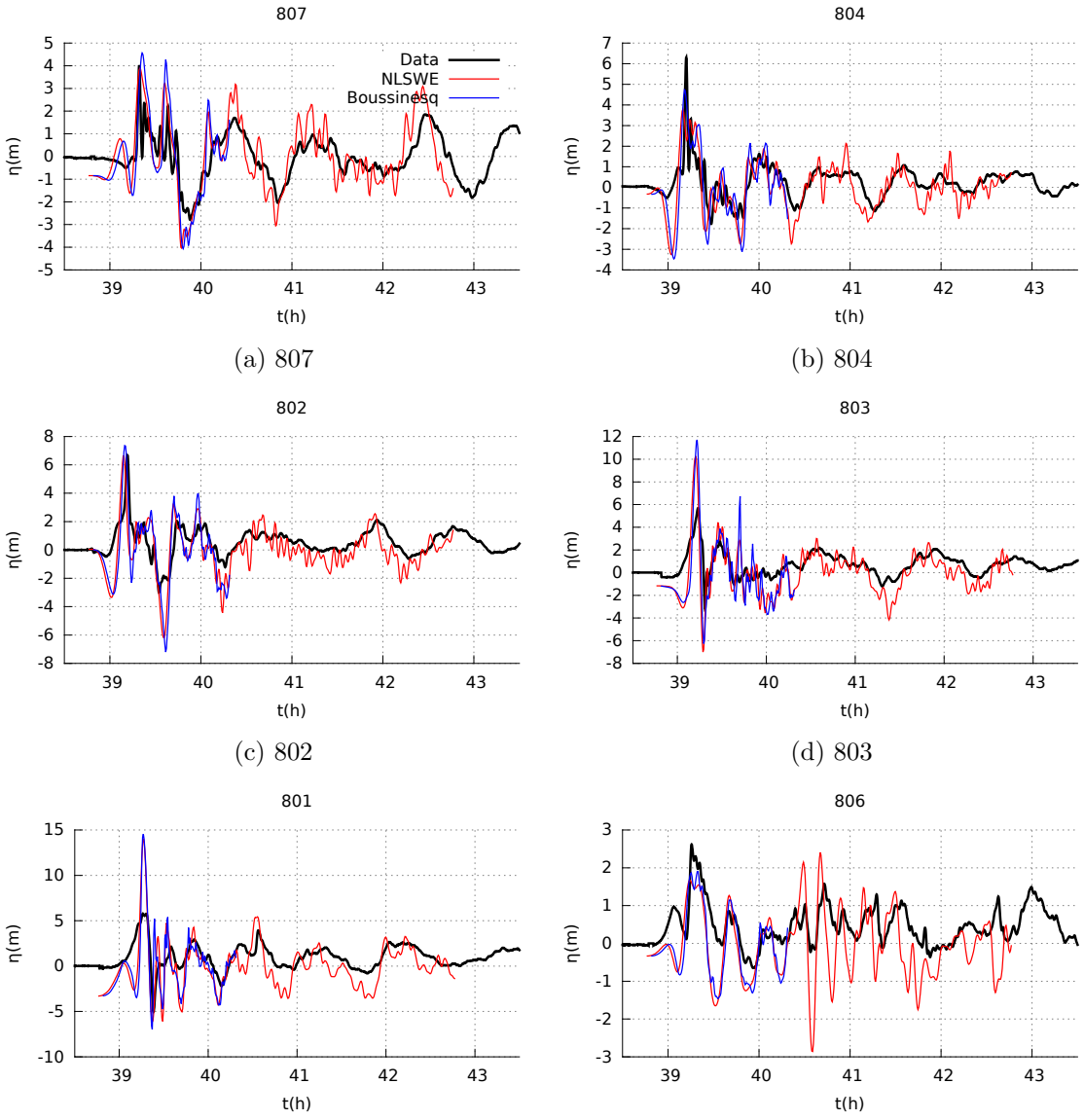

(a) 807 (b) 804

(c) 802 (d) 803

(e) 801 (f) 806

Figure 5.21: 2011 Tohoku-Oki event – Comparisons between measurements and numerical results of the free surface deformation. The black thick line is the data. The red and blue lines are the result from the NLSWE and Boussinesq models of Telemac2D, respectively. The source is the one from the model of Shao et al. [2011].

The results issued from the NLSWE and Boussinesq models are very close. The Boussinesq model does not considerably improve the previous result, and the leading wave is slightly over-estimated. From this lonely result, the numerical results are in agreement with the theoretical conclusion. However, a more sophisticated model would permit to better judge the relevance of this model with comparisons far field, when the propagation distance is

long enough to let the development of dispersive effects (Kirby et al. [2013]), or in local bays as done by Chen et al. [2014], and Baba et al. [2015]. A simulation with the NS model of Telemac3D was also performed on this case for near field propagation, showing no visible difference with the present NLSWE model.

5.6 Conclusions about the Tohoku-Oki model

In this chapter, we constructed and evaluated numerical models of Telemac2D on a real case: the Tohoku-Oki tsunami that occurred in 2011 in Japan. Two co-seismic sources were considered: the source issued of the work of Shao et al. [2011] and the one from Satake et al. [2013]. The numerical results were compared to four types of data: near field and offshore free surface elevation measurements from GPS gauges and DART buoys, respectively, inundation heights and flooded area from the survey of Mori et al. [2011]. The NLSWE model of Telemac2D was used to simulate this case. Both sources give correct results. The model with the source of Shao et al. [2011] over-predicts the event compared to the one with the Satake et al. [2013] generation. A logical scheme between the propagation, the inundation height and the flooded area results is respected: for higher wave during the propagation, the model from Shao et al. [2011] gives higher inundation heights and bigger flooded areas than the model from the geenration by Satake et al. [2013].
In comparison with measurements, excepted for far field (DART buoys), the model issued from Satake et al. is in better agreement with the records and survey than the model of Shao et al., that over-predicts the event. At contrary, as regards far fields, Shao et al.'s model matches the DART records unlike Satake et al., that under-predicts the leading wave.
It is also important to note that these numerical models do not integrate the bottom friction. Thus, an over-prediction of the phenomena at the coast, where the friction may become important, is expected. From now, the Satake et al. generation model gives the best result, however, taking into account the bottom friction may reverse the current trend and finally the Shao et al. generation model may give better results.
To go further, Telemac2D's Boussinesq model was also tested. However, due to numerical issues, only one hour of physical propagation was obtained, that only permited a comparison to the GPS gauges. For this model, the source of Shao et al. [2011] was preferred because built independently of the water wave signal. Matching with the theoretical analysis, the Boussinesq model does not really improve the results. However, some dispersive effects are expected further off shore or at some local bays, that only can be verified with a more sophisticated numerical model, as a nested grids.

Conclusions

Cette thèse a permis de mettre en avant l'influence notable des échelles temporelles lors de la génération sismique des tsunamis dans certaines conditions. Pour cela, deux paramètres ont été définis : la vitesse de propagation de rupture v_p et le temps d'élévation t_r. La nouveauté ici est de travailler avec les deux paramètres simultanément et d'étendre l'étude linéaire théorique au non-linéaire numérique. Cela a permis l'identification d'une zone de résonance, t_r petit et v_p proche de la vitesse des ondes longues, pour laquelle les vagues sont amplifiées et dans laquelle des phénomènes dispersifs se développent. Cette étude théorique est illustrée par un évènement réel, celui du tsunami qui frappa la Nouvelle Zélande en 1947. Le modèle numérique construit à cet effet montre d'importantes différences lorsqu'une génération cinématique est utilisée à la place de la traditionnelle génération statique : les vagues générées sont plus grandes. Cependant, le modèle numérique de Boussinesq n'a pas détecté de phénomènes dispersifs, ce qui peut être dû à une surestimation de ces effets par la théorie ou à un maillage pas assez précis près des côtes. Pour conclure, ce travail permet de montrer la nécessité d'utiliser une source cinématique lors des évènements très lents, tel que les "tsunami earthquakes". Parallèlement, la capacité du système Telemac a été testée pour la modélisation de tsunamis. Que ce soit pour la génération ou le run-up, les modèles numériques donnent de bons résultats. Cependant, certains cas, comme la propagation de l'onde solitaire, ont montré une certaine dépendance aux paramètres numériques. La validation du système Telemac pour les tsunamis est finalisée par la modélisation de l'évènement réel de Tohoku-Oki (2011) pour lequel de nombreuses données sont disponibles. Deux modèles de source ont été testés, les deux donnant des résultats très corrects avec le modèle Saint-Venant. Un modèle de Boussinesq a été mis en place mais une limitation numérique a seulement permis la confrontation des résultats numériques à des données proches de la source. A ces endroits, comme attendu par la théorie, le modèle de Boussinesq reste très

proche de celui de Saint-Venant pour les conditions de ce cas. Les problèmes rencontrés avec l'utilisation des codes Telemac encouragent à une analyse précise des schémas de discrétisation utilisés, ce qui pourrait expliquer certains comportements. De plus, pour un évènement réel, un modèle global couvrant à la fois la génération, la propagation en haute mer et l'inondation n'est peut être pas le plus pertinent pour utiliser le modèle de Boussinesq. Dans cette optique, un modèle emboîté semble être une bonne alternative. De plus, dans cette thèse le frottement du fond n'est pas pris en compte, or son impact peut être non négligeable lors de la phase d'inondation. Insérer un frottement caractéristique à chaque zone inondée serait une belle amélioration pour l'inondation, mais pour cela un modèle des côtes plus précis que celui utilisé dans cette thèse serait nécessaire.

5.7 First concluding remarks

This thesis was shared between the theoretical approach of an idealised generation and concrete applications with codes issued from the Telemac system.
First, the dynamics of the source was identified as the least known part of the tsunami life, leading the research on the kinematic deformation induced by seismic activity. In this aim, a linear potential solution was developed for an idealised deformation of the sea floor as a moving step. This deformation, and thus the solution of the free surface, depends on two temporal parameters, the rise time t_r and the rupture velocity v_p. The novelty of this approach was the study of both t_r and v_p simultaneously. Moreover, the linear theoretical study was extended to non linear numerical studies. These different works permit to highlight a resonance zone, independent of the model of equations, as function of the temporal timescales: v_p close to the long wave celerity $\sqrt{gh}$, and t_r small. Two phenomena appeared in this resonance zone. First, a wave focusing leads to the amplification of the amplitude of the wave generated beside the amplitude of deformation. For the particular values of $v_p = \sqrt{gh}$ and $t_r = 0$, an empirical relation was found between the maximal free surface amplitude and the deformation length at the end of the ground motion. The second phenomenon is the development of dispersive effects. An energetic ratio ε, between the potential energy poorly represented by the Shallow Water Equations and the total potential energy, is defined. According to the temporal parameter values and the geometrical aspect, this ratio can reach important values, questioning the use of the Shallow Water Equations to model such events. Moreover, for substantial enough amplitude of the deformation, the non linear effects lead to the formation of what seemed to be solitary waves.
This theoretical work was illustrated by the real event of March 1947 that occurred in New Zealand. This event is associated to a *tsunami earthquake*, meaning with slow ruptures. Indeed, if the sea floor is idealised, its temporal parameters are included in the theoretical resonance zone. This event was modeled with the NLSWE model of Telemac2D using four generation models varying by the value of v_p and t_r. In concordance with the theory, the rupture velocity v_p has an important impact on the tsunami heights while the rise time t_r has little effect. To go further, this case was also modeled with the Boussinesq model of Telemac2D to test the dispersive effect theory. However, at this point, no dispersive effect was detected. Three assumptions were drawn to explain this behaviour: the energetic ratio ε over-predicted this phenomenon, the distance of propagation considered was too small to allow the development of dispersive effects, and the most probable, the mesh was not adapted to represent the evolution of dispersive waves.
The second aspect of this thesis is the validation of the numerical models issued from Telemac system to simulate test cases about tsunami phenomena. Whether about generations (landslide or seismic types) or run-ups, the models give satisfactory results. However,

the test case about the propagation along a long distance of a solitary wave was more difficult to handle. It reveals a strong dependence of the result to the numerical parameters (CFL). The behaviour of the model would be explained by an analytical study of the numerical schemes, taking as example the work of Burwell et al. [2007].
The real event of Tohoku-Oki 2011 was successfully simulated by the NLSWE model of Telemac2D. Two source models were tested given different results. The numerical free surface elevation from the Satake et al. [2013] source is in good agreement with local buoys and inundation data. However, this model looses its precision on far field prediction. On the contrary, the model with the Shao et al. [2011] source over-predicts the local leading wave and the flooded areas, but better matches the far field measurements. The bottom friction is not included in the numerical models, which should influence the inundation modelling in favour of the Shao et al. [2011] source model. An attempt with the Boussinesq model of Telemac2D was done for this event. Locally, according to the theoretical value of ε, the Shallow Water Equations should be sufficient, and thus weak differences should appear between the Boussinesq and the NLSWE models close to the source. Beside, it was shown in few studies that dispersive effects developed in local areas, as close to the Fukushima Nuclear Power Plant (Chen et al. [2014]) or off shore (Kirby et al. [2013]). However, a numerical limitation did not permit us to have more than one hour of propagation of this event. During this short duration, only the comparisons with local GPS buoys are possible for which the Boussinesq model gives similar result to the NLSWE model, matching the theory.

5.8 Perspectives

The theoretical study and the real application of the 1947 New Zealand event show us the possible strong influence of timescales during seismic generation. This conclusion raises the issue of the limit of the traditional static generation model. Moreover, the Shallow Water Equations are usually used for tsunami modelling, but dispersive effects were locally detected by the theory in certain cases. For this aspect, the numerical model failed to illustrate it, but it can be due to numerical limitation here and a more sophisticate model may improve this result. These conclusions concern a small part of the seismic event, the slow ones that are associated to *tsunami earthquakes*. Even if they stay rare events, they happen. Also, in the numerical model, the choice of the kinematic finite fault method, that is a discrete method, to represent the source is still an approximation of the reality, to better model it a continuous model may be more appropriate.
As far as I am concerned, until now, no advanced studies have been done about tsunamis with the models from the Telemac system. This thesis shows the capacity of the code to model well this kind of events from source to inundation, but also its limitations. An advanced analytical study of the numerical schemes of the models would permit to explain

its behaviour for the delicate cases (propagation of a solitary along a long distance with Telemac3D, theoretical resonance generation with NLSWE model of Telemac2D).
Moreover, for the real event cases, I met some numerical difficulties with the Boussinesq model of Telemac2D. More sophisticate numerical models (finer meshes) may overcome this difficulty. However, this solution is heavy, and using embedded models, as done by other codes within the dedicated scientific community, seems to be a better idea in my opinion.
Finally, during this thesis, the bottom friction is not included in numerical models while some piecewise homogeneous laws are available in the Telemac system, a preliminary model was done but not conclusive. The bottom friction slightly influences the tsunami propagation but can modify the flood prediction. Using heterogeneous friction pattern will be a good improvement, needing a more precise resolution of the coast than done in the present numerical models.

5.9 Main contributions

To conclude this manuscript, this paragraph summarizes the main contributions I performed during these three years. First, theoretically:

- A new formulation was defined for an idealized sea floor deformation depending on two temporal parameters, t_r and v_p.
- Then, a linear solution was developed from the Euler equations with an analytical Fourier transform of the free surface elevation that was numerically transformed in the real space. The numerical inverse Fourier transform was computed with a short program in Fortran using a Simpson integration method.
- The behaviour of wave generation was studied as function of v_p an t_r, numerically extended to nonlinear wave and finally applied to real events.

Secondly, using the Telemac system:

- The six test cases presented in Chapter 4 were performed and one was personally handled in the frame of the TANDEM project.
- For the first time, the real cases of the New Zealand 1947 and Tohoku-Oki 2011 tsunamis were deeply studied at the Saint-Venant Hydraulics Laboratory:
  - until now, the codes of the Telemac system were not adapted to generate real seismically generated tsunamis, even if the Okada's calculations were already computed. Thus, for these events, a kinematic finite fault model was implemented,

– the meshes of the above mentioned models were especially built for this work, from scratch for the New Zealand case and from an existing rough mesh for the Tohoku-Oki event.

Appendix A

Fourier transform of the free surface

In this appendix, the calculations from the Equation 2.20 to the Equation 2.21 are detailed. An inverse Laplace transform is applied. The latter satisfies:

$$\mathscr{L}\{f * g\} = \mathscr{L}\{f\}\,\mathscr{L}\{g\} \tag{A.1}$$

$$\mathscr{L}^{-1}\{f\} * \mathscr{L}^{-1}\{g\} = \mathscr{L}^{-1}\{fg\} \tag{A.2}$$

Where:

$$f * g = \int_0^t f(\tau)g(t-\tau)d\tau \tag{A.3}$$

and

$$\mathscr{L}^{-1}\left\{\frac{s}{s^2+\omega^2}\right\} = \cos(\omega t)H(t) \tag{A.4}$$

$$\mathscr{L}^{-1}\left\{1+e^{-st_r}\right\} = \delta(t) + \delta(t-t_r) \tag{A.5}$$

$$\mathscr{L}^{-1}\left\{\frac{\omega_r}{s^2+\omega_r^2}\right\} = \sin(\omega_r t)\,H(t) \tag{A.6}$$

$$\mathscr{L}^{-1}\left\{\frac{1-e^{-\frac{L}{v_p}(ikv_p+s)}}{ikv_p+s}\right\} = e^{-ikv_p t}(1-H(t-\tfrac{L}{v_p})) \tag{A.7}$$

Thus:

$$\begin{aligned}\tilde{\eta}(k,t) &= \frac{\zeta_0}{2}\frac{\omega_r}{\cosh(kh)}cos(\omega t)H(t) * (\delta(t) + \delta(t-t_r)) \\ &\quad * \sin(\omega_r t)\,H(t) * e^{-ikv_p t}(1-H(t-\frac{L}{v_p}))\end{aligned} \tag{A.8}$$

We then define A as:

$$A = \cos(\omega t)H(t) * \sin(\omega_r t)\, H(t) = \frac{\omega_r}{\omega_r^2 - \omega^2}\left(\cos(\omega t) - \cos(\omega_r t)\right) \tag{A.9}$$

$$A * e^{-ikv_p t}(1 - H(t - \frac{L}{v_p})) = \frac{\omega_r}{\omega_r^2 - \omega^2}\begin{pmatrix} \cos(\omega t) * e^{-ikv_p t} \\ -\cos(\omega t) * e^{-ikv_p t} H(t - \frac{L}{v_p}) \\ -\cos(\omega_r t) * e^{-ikv_p t} \\ +\cos(\omega_r t) * e^{-ikv_p t} H(t - \frac{L}{v_p}) \end{pmatrix} \tag{A.10}$$

also:

$$\cos(\omega t) * e^{-ikv_p t} = \frac{1}{\omega^2 - k^2 v_p^2}\left[ikv_p \cos(\omega t) + \omega \sin(\omega t) - ikv_p e^{-ikv_p t}\right] \tag{A.11}$$

and:

$$\begin{aligned} \cos(\omega t) * e^{-ikv_p t} H(t - \frac{L}{v_p}) &= \frac{H(t - \frac{L}{v_p})}{\omega^2 - k^2 v_p^2} \\ &\times \begin{bmatrix} e^{-iLk}\left(ikv_p \cos(\omega(t - \frac{L}{v_p})) + \omega \sin(\omega(t - \frac{L}{v_p}))\right) \\ -ikv_p e^{-ikv_p t} \end{bmatrix} \end{aligned} \tag{A.12}$$

Thus:
if $B = A * e^{-ikv_p t}(1 - H(t - \frac{L}{v_p}))$

$$\begin{aligned} B = \frac{\omega_r}{\omega_r^2 - \omega^2}\Big(& \frac{1}{\omega^2 - k^2 v_p^2}[ikv_p \cos(\omega t) + \omega \sin(\omega t) - ikv_p e^{-ikv_p t}] \\ & -\frac{1}{\omega_r^2 - k^2 v_p^2}[ikv_p \cos(\omega_r t) + \omega_r \sin(\omega_r t) - ikv_p e^{-ikv_p t}] \\ & -\frac{H(t - \frac{L}{v_p})}{\omega^2 - k^2 v_p^2}[e^{-iLk}(ikv_p \cos(\omega(t - \frac{L}{v_p})) + \omega \sin(\omega(t - \frac{L}{v_p}))) - ikv_p e^{-ikv_p t}] \\ & +\frac{H(t - \frac{L}{v_p})}{\omega_r^2 - k^2 v_p^2}\begin{bmatrix} e^{-iLk}(ikv_p \cos(\omega_r(t - \frac{L}{v_p})) + \omega_r \sin(\omega_r(t - \frac{L}{v_p}))) \\ -ikv_p e^{-ikv_p t} \end{bmatrix}\Big) \end{aligned} \tag{A.13}$$

In order to calculate $C = B * (\delta(t) + \delta(t - t_r))$, we use: $f * \delta(t - a) = f(t - a)H(t - a)$:

$$
\begin{aligned}
C = \frac{\omega_r}{\omega_r^2-\omega^2}\Bigg(& \frac{1}{\omega^2-k^2v_p^2}\left[ikv_p\cos(\omega t)+\omega\sin(\omega t)-ikv_pe^{-ikv_pt}\right] \\
& -\frac{1}{\omega_r^2-k^2v_p^2}\left[ikv_p\cos(\omega_r t)+\omega_r\sin(\omega_r t)-ikv_pe^{-ikv_pt}\right] \\
& +H(t-t_r)\begin{bmatrix} -\frac{1}{\omega_r^2-k^2v_p^2}\left[-ikv_p\cos(\omega_r t)-\omega_r\sin(\omega_r t)-ikv_pe^{-ikv_p(t-t_r)}\right] \\ +\frac{1}{\omega^2-k^2v_p^2}\left[ikv_p\cos(\omega(t-t_r))+\omega\sin(\omega(t-t_r))-ikv_pe^{-ikv_p(t-t_r)}\right]\end{bmatrix} \\
& +H(t-\frac{L}{v_p})\begin{bmatrix} \frac{1}{\omega_r^2-k^2v_p^2}\begin{bmatrix} e^{-iLk}\big(ikv_p\cos(\omega_r(t-\frac{L}{v_p})) \\ +\omega_r\sin(\omega_r(t-\frac{L}{v_p}))\big)-ikv_pe^{-ikv_pt}\end{bmatrix} \\ -\frac{1}{\omega^2-k^2v_p^2}\begin{bmatrix} e^{-iLk}\big(ikv_p\cos(\omega(t-\frac{L}{v_p})) \\ +\omega\sin(\omega(t-\frac{L}{v_p}))\big)-ikv_pe^{-ikv_pt}\end{bmatrix}\end{bmatrix} \\
& +H(t-t_r-\frac{L}{v_p})\begin{bmatrix} \frac{1}{\omega_r^2-k^2v_p^2}\begin{bmatrix} e^{-iLk}\big(-ikv_p\cos(\omega_r(t-\frac{L}{v_p})) \\ -\omega_r\sin(\omega_r(t-\frac{L}{v_p}))-ikv_pe^{-ikv_p(t-t_r)}\end{bmatrix} \\ -\frac{1}{\omega^2-k^2v_p^2}\begin{bmatrix} e^{-iLk}\big(ikv_p\cos(\omega(t-t_r-\frac{L}{v_p})) \\ +\omega\sin(\omega(t-t_r-\frac{L}{v_p}))\big) \\ -ikv_pe^{-ikv_p(t-t_r)}\end{bmatrix}\end{bmatrix}\Bigg)
\end{aligned}
\tag{A.14}
$$

Combining A.8 and A.14 gives the dimension fourier transform of the solution. Applying the non-dimensionalized transformation 2.1, Equation 2.21 is obtained.

Appendix B

Treatment of the singularities

In this appendix, we treat the singularities of $\tilde{\eta}$ appearing in Equation 2.21. We can identify three critical cases where $\tilde{\eta}$ is discontinuous:

1. $k^2 v_p^2 \to \omega_r^2$,

2. $k^2 v_p^2 \to \omega^2$,

3. $\omega \to \omega_r^2$.

As said in pragraph 2.2.3, to keep a continuous function, the limit of $\tilde{\eta}$ is taken when $|k - k_{critical}| < 10^{-6}h$. For case (i), D is defined as:

$$D = ikv_p \cos(\omega_r t) + \omega_r \sin(\omega_r t) - ikv_p e^{-ikv_p t}$$

We have:

$$\frac{D}{\omega_r^2 - k^2 v_p^2} \quad \to \quad \frac{1}{2\omega_r}(\omega_r t e(-i\omega_r t) + \sin(\omega_r t))$$

Thus, when $k^2v_p^2 \to \omega_r^2$:

$$\begin{aligned}
\tilde{\eta}\,(k,t) \;\to\; & \frac{\zeta_{\max}}{2}\frac{v_p}{\cosh kh}\frac{\omega_r^2}{\omega_r^2-\omega^2}\Bigg(\frac{1}{\omega^2-k^2v_p^2}\left(ikv_p\cos(\omega t)+\omega\sin(\omega t)-ikv_pe^{-ikv_pt}\right) \\
& -\frac{1}{2\omega_r}(\omega_r te(-i\omega_r t)+\sin(\omega_r t)) \\
& +H(t-t_r)\begin{bmatrix} \frac{1}{\omega^2-k^2v_p^2}\left(ikv_p\cos(\omega(t-t_r))+\omega\sin(\omega(t-t_r))-ikv_pe^{-ikv_p(t-t_r)}\right) \\ -\frac{1}{2\omega_r}(\omega_r(t-t_r)e(-i\omega_r(t-t_r))+\sin(\omega_r(t-t_r))) \end{bmatrix} \\
& +H(t-\frac{L}{v_p})\begin{bmatrix} -\frac{1}{\omega^2-k^2v_p^2}\begin{pmatrix} e^{-iLk}\big(ikv_p\cos(\omega(t-\frac{L}{v_p})) \\ +\omega\sin(\omega(t-\frac{L}{v_p}))\big)-ikv_pe^{-ikv_pt}\end{pmatrix} \\ -\frac{e(-i\frac{L}{v_p}\omega_r)}{2\omega_r}(\omega_r(t-\frac{L}{v_p})e(-i\omega_r(t-\frac{L}{v_p}))+\sin(\omega_r(t-\frac{L}{v_p}))) \end{bmatrix} \\
& +H(t-t_r-\frac{L}{v_p})\begin{bmatrix} -\frac{1}{\omega^2-k^2v_p^2}\begin{pmatrix} e^{-iLk}\big(ikv_p\cos(\omega(t-t_r-\frac{L}{v_p})) \\ +\omega\sin(\omega(t-t_r-\frac{L}{v_p}))\big)-ikv_pe^{-ikv_p(t-t_r)}\end{pmatrix} \\ -\frac{e(-i\frac{L}{v_p}\omega_r)}{2\omega_r}\begin{pmatrix}\omega_r(t-t_r-\frac{L}{v_p})e(-i\omega_r(t-t_r-\frac{L}{v_p})) \\ +\sin(\omega_r(t-t_r-\frac{L}{v_p}))\end{pmatrix}\end{bmatrix}\Bigg)
\end{aligned} \tag{B.1}$$

For case (ii), the same process is used to get:

$$\begin{aligned}
\tilde{\eta}\,(k,t) \;\to\; & \frac{\zeta_{\max}}{2}\frac{v_p}{\cosh kh}\frac{\omega_r^2}{\omega_r^2-\omega^2}\Bigg(\frac{1}{2\omega}(\omega te(-i\omega t)+\sin(\omega t)) \\
& -\frac{1}{\omega_r^2-k^2v_p^2}\left[ikv_p\cos(\omega_r t)+\omega_r\sin(\omega_r t)-ikv_pe^{-ikv_pt}\right] \\
& +H(t-t_r)\begin{bmatrix} \frac{1}{2\omega}(\omega(t-tr)e(-i\omega(t-tr))+\sin(\omega(t-tr))) \\ +\frac{1}{\omega_r^2-k^2v_p^2}\left(ikv_p\cos(\omega_r t)+\omega_r\sin(\omega_r t)+ikv_pe^{-ikv_p(t-t_r)}\right)\end{bmatrix} \\
& +H(t-\frac{L}{v_p})\begin{bmatrix} -\frac{e(-i\frac{L}{v_p}\omega)}{2\omega}(\omega(t-\frac{L}{v_p})e(-i\omega(t-\frac{L}{v_p}))+\sin(\omega(t-\frac{L}{v_p}))) \\ +\frac{1}{\omega_r^2-k^2v_p^2}\begin{pmatrix} e^{-iLk}\big(ikv_p\cos(\omega_r(t-\frac{L}{v_p})) \\ +\omega_r\sin(\omega_r(t-\frac{L}{v_p}))\big)-ikv_pe^{-ikv_pt}\end{pmatrix}\end{bmatrix} \\
& +H(t-t_r-\frac{L}{v_p})\begin{bmatrix} -\frac{e(-i\frac{L}{v_p}\omega)}{2\omega}\begin{pmatrix}\omega(t-t_r-\frac{L}{v_p})e(-i\omega(t-t_r-\frac{L}{v_p})) \\ +\sin(\omega(t-t_r-\frac{L}{v_p}))\end{pmatrix} \\ +\frac{1}{\omega_r^2-k^2v_p^2}\begin{pmatrix} e^{-iLk}\big(-ikv_p\cos(\omega_r(t-\frac{L}{v_p})) \\ -\omega_r\sin(\omega_r(t-\frac{L}{v_p}))\big)-ikv_pe^{-ikv_p(t-t_r)}\end{pmatrix}\end{bmatrix}\Bigg)
\end{aligned} \tag{B.2}$$

Moreover, if $k \to 0$ and $\omega \to 0$:

$$\begin{aligned}\tilde{\eta}\,(k,t) \;\rightarrow\; & \frac{\zeta_{\max}}{2}\frac{v_p}{\cosh kh}\frac{\omega_r^2}{\omega_r^2-\omega^2}\Bigg(t-\frac{1}{\omega_r^2-k^2v_p^2}\left(ikv_p\cos(\omega_r t)+\omega_r\sin(\omega_r t)-ikv_p e^{-ikv_p t}\right)\\ & +H(t-t_r)\left[\begin{array}{l} t-tr+\frac{1}{\omega_r^2-k^2v_p^2}\left(ikv_p\cos(\omega_r t)\right.\\ \left.+\omega_r\sin(\omega_r t)+ikv_p e^{-ikv_p(t-t_r)}\right)\end{array}\right] \qquad \text{(B.3)}\\ & +H(t-\frac{L}{v_p})\left[\begin{array}{l} -(t-\frac{L}{v_p})+\frac{1}{\omega_r^2-k^2v_p^2}\Big(e^{-iLk}\big(ikv_p\cos(\omega_r(t-\frac{L}{v_p}))\right.\\ \left.+\omega_r\sin(\omega_r(t-\frac{L}{v_p}))\big)-ikv_p e^{-ikv_p t}\Big)\end{array}\right]\\ & +H(t-t_r-\frac{L}{v_p})\left[\begin{array}{l} -(t-t_r-\frac{L}{v_p})+\frac{1}{\omega_r^2-k^2v_p^2}\Big(e^{-iLk}\big(-ikv_p\cos(\omega_r(t-\frac{L}{v_p}))\right.\\ \left.-\omega_r\sin(\omega_r(t-\frac{L}{v_p}))\big)-ikv_p e^{-ikv_p(t-t_r)}\Big)\end{array}\right]\Bigg)\end{aligned}$$

For case (iii), we define:

$$F \;=\; \frac{\omega_r^2}{\omega_r^2-\omega^2}\frac{1}{\omega^2-k^2v_p^2}\frac{1}{\omega_r^2-k^2v_p^2}\left[\begin{array}{c} ikv_p e(-ikv_p t)(\omega^2-\omega_r^2)\\ +ikv_p\left(\omega_r^2\cos(\omega t)-\omega^2\cos(\omega_r t)+k^2v_p^2(\cos(\omega_r t)-\cos(\omega t))\right)\\ +\omega\omega_r^2\sin(\omega t)-\omega_r\omega^2\sin(\omega_r t)\\ +k^2v_p^2(\omega_r\sin(\omega_r t)-\omega\sin(\omega t))\end{array}\right]$$

When $\omega\rightarrow\omega_r$, we get:

$$F \;\rightarrow\; \frac{\omega_r^2}{(\omega_r^2-k^2v_p^2)^2}\left[\begin{array}{c} -ikv_p e(-ikv_p t)\\ +ikv_p\left(\cos(\omega_r t)-\frac{(k^2v_p^2-\omega_r^2)t}{2\omega_r}\sin(\omega_r t)\right)\\ +\omega_r^2\left(\frac{\sin(\omega_r t)}{2\omega_r}-\frac{t}{2}\cos(\omega_r t)\right)\\ +k^2v_p^2\left(\frac{\sin(\omega_r t)}{2\omega_r}+\frac{t}{2}\cos(\omega_r t)\right)\end{array}\right]$$

Thus:

$$
\begin{aligned}
\tilde{\eta}\,(k,t) \;\rightarrow\; & \frac{\zeta_{\max}}{2}\,\frac{v_p}{\cosh kh}\,\frac{\omega_r^2}{(\omega_r^2-k^2v_p^2)^2}\Bigg(-ikv_p e(-ikv_p t) \\
& +ikv_p\left[\cos(\omega_r t)-\frac{(k^2v_p^2-\omega_r^2)t}{2\omega_r}\sin(\omega_r t)\right] \\
& +\omega_r^2\left[\frac{\sin(\omega_r t)}{2\omega_r}-\frac{t}{2}\cos(\omega_r t)\right]+k^2v_p^2\left[\frac{\sin(\omega_r t)}{2\omega_r}+\frac{t}{2}\cos(\omega_r t)\right] \\
& +H(t-t_r)\begin{bmatrix} -ikv_p e(-ikv_p(t-t_r)) \\ +ikv_p\left(\cos(\omega_r(t-t_r))-\frac{(k^2v_p^2-\omega_r^2)(t-t_r)}{2\omega_r}\sin(\omega_r(t-t_r))\right) \\ +\omega_r^2\left(\frac{\sin(\omega_r(t-t_r))}{2\omega_r}-\frac{(t-t_r)}{2}\cos(\omega_r(t-t_r))\right) \\ +k^2v_p^2\left(\frac{\sin(\omega_r(t-t_r))}{2\omega_r}+\frac{(t-t_r)}{2}\cos(\omega_r(t-t_r))\right)\end{bmatrix} \\
& -H(t-\frac{L}{v_p})\begin{bmatrix} -ikv_p e(-ikv_p(t-\frac{L}{v_p})) \\ +ikv_p\left(\cos(\omega_r(t-\frac{L}{v_p}))-\frac{(k^2v_p^2-\omega_r^2)(t-\frac{L}{v_p})}{2\omega_r}\sin(\omega_r(t-\frac{L}{v_p}))\right) \\ +\omega_r^2\left(\frac{\sin(\omega_r(t-\frac{L}{v_p}))}{2\omega_r}-\frac{(t-\frac{L}{v_p})}{2}\cos(\omega_r(t-\frac{L}{v_p}))\right] \\ +k^2v_p^2\left[\frac{\sin(\omega_r(t-\frac{L}{v_p}))}{2\omega_r}+\frac{(t-\frac{L}{v_p})}{2}\cos(\omega_r(t-\frac{L}{v_p}))\right)\end{bmatrix} \\
& -H(t-t_r-\frac{L}{v_p})\begin{bmatrix} -ikv_p\exp(-ikv_p(t-t_r-\frac{L}{v_p})) \\ +ikv_p\begin{pmatrix}\cos(\omega_r(t-t_r-\frac{L}{v_p})) \\ -\frac{(k^2v_p^2-\omega_r^2)(t-t_r-\frac{L}{v_p})}{2\omega_r}\sin(\omega_r(t-t_r-\frac{L}{v_p}))\end{pmatrix} \\ +\omega_r^2\left(\frac{\sin(\omega_r(t-t_r-\frac{L}{v_p}))}{2\omega_r}-\frac{(t-t_r-\frac{L}{v_p})}{2}\cos(\omega_r(t-t_r-\frac{L}{v_p}))\right) \\ +k^2v_p^2\left(\frac{\sin(\omega_r(t-t_r-\frac{L}{v_p}))}{2\omega_r}+\frac{(t-t_r-\frac{L}{v_p})}{2}\cos(\omega_r(t-t_r-\frac{L}{v_p}))\right)\end{bmatrix}\Bigg)
\end{aligned}
\tag{B.4}
$$

Appendix C

Description of the Telemac system

The Telemac system is an open-source code that models the hydrodynamics of free surface flows. This code, initiated by J.-M. Hervout at EDF, is continuously developed and upgraded. The aim of the present Appendix is to briefly describe the modeled equations and the numerical processes. A complete description is available in the book of Hervouet [2007] and in the reference manuals online (http://opentelemac.org/). During this thesis, only two modules have been used: Telemac2D and Telemac3D.

C.1 Telemac2D

Telemac2D can solve the Non-Linear Shallow Water Equations (NLSWE) and the Boussinesq equations. For the NLSWE, the code solves the following equations:

$$\begin{cases} h_t + u.\bigtriangledown(h) + hdiv(\boldsymbol{u}) = S_h \\ u_t + \boldsymbol{u}.\bigtriangledown(u) = -gZ_x + S_x + \frac{1}{h}div(h\nu\bigtriangledown u) \\ v_t + \boldsymbol{v}.\bigtriangledown(u) = -gZ_y + S_y + \frac{1}{h}div(h\nu\bigtriangledown v) \end{cases} \tag{C.1}$$

With:

- h (m) water depth (unknown)
- $\boldsymbol{u} = (u, v)$ (m/s) depth-averaged velocity (unknown)
- t (s) time
- g (m/s^2) gravity acceleration
- ν (m^2/s) momentum diffusion coefficient
- S_h (m/s) source or sink of fluid
- S_x, S_y (m/s^2) source terms in momentum equations

- Z (m) free surface elevation

For real case events, it is possible to add the Coriolis force and the bottom friction in the definition of S_x and S_y. The Coriolis force is calculated such as:

$$\boldsymbol{F_{cor}} = 2\omega \sin\lambda \boldsymbol{u},$$

with ω the angular velocity of the Earth and λ the latitude of the point. For the bottom friction, several laws are proposed but we choose to use the Strickler law:

$$F_{fx} = -\frac{u}{\cos\alpha}\frac{g}{h^{4/3}K^2}\sqrt{u^2+v^2},$$
$$F_{fy} = -\frac{v}{\cos\alpha}\frac{g}{h^{4/3}K^2}\sqrt{u^2+v^2},$$

with α the steepness of the slope and K $(m^{1/3}/s)$ is the coefficient of Strickler. Another important point to take in consideration for real case events as tsunami is the spherical coordinantes. For this case, the differential operator are adapted (see Hervouet [2007]).
If the model needs a non-hydrostatic configuration, it is also possible to solve the Boussinesq equation. Switching from Equations C.1 to the Boussinesq equation is done by adding an extra term, representing the impact of the vertical acceleration, in the momentum equation. The extra term is the following:

$$-\frac{H_0^2}{6} \bigtriangledown [div(\boldsymbol{u}_t)] + \frac{H_0}{2} \bigtriangledown [div(H_0\boldsymbol{u}_t))],$$

where H_0 is an average depth. This new equation corresponds to the weakly dispersive and weakly non linear Boussinesq – Peregrine equations developped by Peregrine [1967].
Numerically, to solve the previous equations, Telemac2D uses a finite element (most used in this thesis) or finite volumes methods on unstructured triangular meshes. By default, to solve the convection, the characteristic method is used with a fractional steps method, meaning that the equations are solved by some distinct steps. The characterisic method is a low diffusion method of order 1. If the system C.1 is rewritted in term of effect, it comes:

$$f_t + \text{advection term} = \text{diffusion term} + \text{source term},$$

where f is the unkonwn scalar. Its discretisation in time is defined such as:

$$f_t = \frac{f^{n+1} - \tilde{f} + \tilde{f} - f^n}{\delta t}.$$

The numerical resolution steps are:

1. the advection of the physical quantities using the characteristics method $\frac{\tilde{f}-f^n}{\delta t} +$ advection term $= 0$,

2. the diffusion and source term with a Finite Element technique $\frac{f^{n+1}-\tilde{f}}{\delta t}$ = diffusion term+ source term.

If the characteristics method is not choosen for the advection, only one step is performed using a Finite Element technique. Thus, the choice of the numerical scheme is let to the convenience of the user. The main numerical schemes used in this thesis, besides the characteristic method, are a mass-conservative PSI distributive scheme and an edge by edge implementation mass conservative scheme of order 2 (adapted for dry zone). (see Pavan [2016]). The time discretization is based on a θ-scheme. It is a semi-implicit formulation, for sake of stability $\theta \in]0.5, 1]$, and if θ is close to 0.5 a nearly second order of discretization. However, with the use of a fractional steps method, the order of the time discritization does not cout.

C.2 Telemac3D

Telemac3D solve the 3D free surface incompressible Navier-Stokes Equations, with hydrostatic hypothesis it gives:

$$\begin{cases} u_x + v_y + w_z = 0 \\ u_t + uu_x + vu_y + wu_z = -gZ_{sx} + \nu \triangle (u) + S_x \\ v_t + uv_x + vv_y + wv_z = -gZ_{sy} + \nu \triangle (v) + S_y \\ p = p_{atm} + \rho_0 g(Z - z) + \rho_0 g \int_z^{Z_s} \frac{\triangle \rho}{\rho_0} dz. \end{cases} \tag{C.2}$$

For non-hydrostatic hypothesis, the previous system is completed by a third momentum equation and a dynamic term is added at the equation of the pressure:

$$\begin{cases} w_t + uw_x + vw_y + ww_z = -gZ_{sz} + \nu \triangle (w) + S_z, \\ p = p_{atm} + \rho_0 g(Z - z) + \rho_0 g \int_z^{Z_s} \frac{\triangle \rho}{\rho_0} dz + P_d. \end{cases} \tag{C.3}$$

w is the third velocity component and P_d the dynamic pressure term. Similarly than Telemac2D, Telemac3D uses Finite Element method with a fractional step algorithm:

$$f_t = \frac{f^{n+1} - f_D + f_D - f_C + f_C - f_n}{\delta t},$$

with f the unknown considered scalar. Thus, the numerical resolution is perfomed in three steps:

- the advection step: $\frac{f_C - f_n}{\delta t}$ + advection terms = 0,
- the diffusion step: $\frac{f_D - f_C}{\delta t}$ + diffusion term = source term,
- the pressure term: $\frac{f^{n+1} - f_D}{\delta t}$ + pressure terms = 0

Again, the choice of the advection scheme for each variable is let to the user, however during this thesis only the characteristic method and a so-called MURD PSI scheme are used. The 3D mesh is composed of prisms, Telemac3D builds the 3D domain from a 2D mesh that is extruded.

Bibliography

S. Abadie, D. Morichon, S. T. Grilli, and S. Glockner. Numerical simulation of waves generated by landslides using a multiple-fluid navier–stokes model. *Coastal Engineering*, 57(9):779–794, 2010.

C. J. Ammon, H. Kanamori, T. Lay, and A. A. Velasco. The 17 july 2006 java tsunami earthquake. *Geophysical Research Letters*, 33(24), 2006.

E. Antoshchenkova, D. Imbert, Y. Richet, L. Bardet, C.-M. Duluc, V. Rebour, A. Gailler, and H. Hébert. Propagation of uncertainties for an evaluation of the Azores-Gibraltar Fracture Zone tsunamigenic potential. In *EGU General Assembly Conference Abstracts*, volume 18 of *EGU General Assembly Conference Abstracts*, page 14477, April 2016.

L. Arpaia and M. Ricchiuto. r-adaptation for shallow water flows: conservation, well balancedness, efficiency. Research Report RR-8956, Inria Bordeaux Sud-Ouest, 2016. URL https://hal.inria.fr/hal-01372496.

T. Baba, N. Takahashi, Y. Kaneda, K. Ando, D. Matsuoka, and T. Kato. Parallel Implementation of Dispersive Tsunami Wave Modeling with a Nesting Algorithm for the 2011 Tohoku Tsunami. *Pure and Applied Geophysics*, 172:3455–3472, December 2015. doi: 10.1007/s00024-015-1049-2.

J.-P. Bardet, C. E. Synolakis, H. L. Davies, F. Imamura, and E. A. Okal. Landslide tsunamis: Recent findings and research directions. *Pure and Applied Geophysics*, 160 (10):1793–1809, 2003. ISSN 1420-9136. doi: 10.1007/s00024-003-2406-0. URL http://dx.doi.org/10.1007/s00024-003-2406-0.

J. A. Battjes. Surf-zone dynamics. *Annual Review of Fluid Mechanics*, 20(1):257–291, 1988.

R. Bell, C. Holden, W. Power, X. Wang, and G. Downes. Hikurangi margin tsunami earthquake generated by slow seismic rupture over a subducted seamount. *Earth and Planetary Science Letters*, 397:1–9, 2014. ISSN 0012-821X. doi: http://dx.doi.org/10.1016/j.epsl.2014.04.005. URL http://www.sciencedirect.com/science/article/pii/S0012821X14002313.

M. Benoit, C. Raoult, and M. Yates. Fully nonlinear and dispersive modeling of surf zone waves: Non-breaking tests. *Coastal Engineering Proceedings*, 1(34):15, 2014. ISSN 2156-1028. URL https://journals.tdl.org/icce/index.php/icce/article/view/7475.

J. C. Borrero, J. F. Dolan, and C. E. Synolakis. Tsunamis within the eastern santa barbara channel. *Geophysical Research Letters*, 28(4):643–646, 2001. ISSN 1944-8007. doi: 10.1029/2000GL011980. URL http://dx.doi.org/10.1029/2000GL011980.

J. C. Borrero, M. R. Legg, and C. E. Synolakis. Tsunami sources in the southern california bight. *Geophysical Research Letters*, 31(13):n/a–n/a, 2004. ISSN 1944-8007. doi: 10.1029/2004GL020078. URL http://dx.doi.org/10.1029/2004GL020078. L13211.

E. Buckingham. On Physically Similar Systems; Illustrations of the Use of Dimensional Equations. *Physical Review*, 4:345–376, 1914. doi: 10.1103/PhysRev.4.345.

D. Burwell, E. Tolkova, and A. Chawla. Diffusion and dispersion characterization of a numerical tsunami model. *Ocean Modelling*, 19(1):10–30, 2007.

G. F. Carrier and H. P. Greenspan. Water waves of finite amplitude on a slopping beach. *Journal of Fluid Mechanics*, 4:97–109, 1958.

G. F. Carrier, T. T. Wu, and H. Yeh. Tsunami run-up and draw-down on a plane beach. *Journal of Fluid Mechanics*, 475:79–99, 2003.

C. Chen, Z. Lai, R. C. Beardsley, J. Sasaki, J. Lin, H. Lin, R. Ji, and Y. Sun. The march 11, 2011 tohoku m9.0 earthquake-induced tsunami and coastal inundation along the japanese coast: A model assessment. *Progress in Oceanography*, 123:84–104, 2014. ISSN 0079-6611. doi: http://dx.doi.org/10.1016/j.pocean.2014.01.002. URL http://www.sciencedirect.com/science/article/pii/S0079661114000111.

B. H. Choi, E. N. Pelinovsky, K. O. Kim, and J. S. Lee. Simulation of the trans-oceanic tsunami propagation due to the 1883 krakatau volcanic eruption. *Natural Hazards and Earth System Science*, 3(5):321–332, 2003.

D. A. Crawford and C. L. Mader. Modeling asteriod impact and tsunami. *Science of Tsunami Hazards*, 16(1):21–30, 1998.

S. F. Dotsenko and S. L. Soloviev. On the role of residual displacements of ocean bottom in tsunami generation by underwater earthquakes. *Bulletin of the Seismological Society of America*, 35:177–199, 1995.

G. Downes and M. W. Stirling. Groundwork for development of a probabilistic tsunami hazard model for New Zealand. In *International Tsunami Symposium 2001*, pages 293–301, 2001.

D. Dutykh. *Mathematical modelling of tsunami waves*. Phd thesis, École normale supérieure de Cachan - ENS Cachan (France), 2007. URL https://tel.archives-ouvertes.fr/tel-00194763.

D. Dutykh and D. Clamond. Efficient computation of steady solitary gravity waves. *Wave Motion*, 51(1):86–99, 2014. ISSN 0165-2125. doi: http://dx.doi.org/10.1016/j.wavemoti.2013.06.007. URL http://www.sciencedirect.com/science/article/pii/S0165212513001169.

D. Dutykh, D. Mitsotakis, X. Gardeil, and F. Dias. On the use of the finite fault solution for tsunami generation problems. *Theoretical and Computational Fluid Dynamics*, 27:177–199, 2013.

F. Enet and S. T. Grilli. Experimental study of tsunami generation by three-dimensional rigid underwater landslides. *Journal of Waterway, Port, Coastal, and Ocean Engineering*, 133(6):442–454, 2007.

H. M. Fritz, W. H. Hager, and H.-E. Minor. Near field characteristics of landslide generated impulse waves. *Journal of Waterway, Port, Coastal, and Ocean Engineering*, 130(6):287–302, 2004.

D. R. Fuhrman and Per A. Madsen. Tsunami generation, propagation, and run-up with a high-order boussinesq model. *Coastal Engineering*, 56:747–758, 2009.

Y. Fujii and K. Satake. Tsunami source of the 2004 sumatra–andaman earthquake inferred from tide gauge and satellite data. *Bulletin of the Seismological Society of America*, 97 (1A):S192–S207, 2007.

Y. Fujii, K. Satake, S. Sakai, M. Shinohara, and T. Kanazawa. Tsunami source of the 2011 off the pacific coast of tohoku earthquake. *Earth, Planets and Space*, 63(7):815–820, 2011. ISSN 1343-8832. doi: 10.5047/eps.2011.06.010. URL http://dx.doi.org/10.5047/eps.2011.06.010.

N. Gedik, E. Irtem, and S. Kabdasli. Laboratory investigation on tsunami run-up. *Ocean Engineering*, 32(5–6):513–528, 2005. ISSN 0029-8018. doi: http://dx.doi.org/10.1016/j.oceaneng.2004.10.013. URL http://www.sciencedirect.com/science/article/pii/S0029801804002276.

G. Gelfenbaum and B. Jaffe. *Erosion and Sedimentation from the 17 July, 1998 Papua New Guinea Tsunami*, pages 1969–1999. Birkhäuser Basel, Basel, 2003. ISBN 978-3-0348-7995-8. doi: 10.1007/978-3-0348-7995-8_10. URL http://dx.doi.org/10.1007/978-3-0348-7995-8_10.

S. Glimsdal, G. K. Pedersen, C. B. Harbitz, and F. Løvholt. Dispersion of tsunamis: does it really matter? *Natural Hazards and Earth System Science*, 13(6):1507–1526, 2013. doi: 10.5194/nhess-13-1507-2013. URL http://www.nat-hazards-earth-syst-sci.net/13/1507/2013/.

S. T. Grilli and P. Watts. Tsunami generation by submarine mass failure. i: Modeling, experimental validation, and sensitivity analyses. *Journal of Waterway, Port, Coastal, and Ocean Engineering*, 131(6):283–297, 2005. doi: 10.1061/(ASCE)0733-950X(2005)131:6(283). URL http://dx.doi.org/10.1061/(ASCE)0733-950X(2005)131:6(283).

S. T. Grilli, J. C. Harris, T. S. Tajalli Bakhsh, T. L. Masterlark, C. Kyriakopoulos, J. T. Kirby, and F. Shi. Numerical simulation of the 2011 tohoku tsunami based on a new transient fem co-seismic source: Comparison to far- and near-field observations. *Pure and Applied Geophysics*, 170(6):1333–1359, 2013. ISSN 1420-9136. doi: 10.1007/s00024-012-0528-y. URL http://dx.doi.org/10.1007/s00024-012-0528-y.

J. Hammack. *Tsunami-A model of their generation and propagation*. PhD thesis, California Institute of Technology, 1972.

J. Hammack. A note on tsunamis: their generation and propagation in an ocean of uniform depth. *Journal of Fluid Mechanics*, 60:769–799, 1973.

C. B. Harbitz, F. Lovholt, G. Pedersen, and D. G. Masson. Mechanisms of tsunami generation by submarine landslides: a short review. *Norsk Geologisk Tidsskrift*, 86(3):255, 2006.

J.-M. Hervouet. *Hydrodynamics of free surface flows: modelling with the finite element method*. John Wiley & Sons, 2007.

T. Hibiya and K. Kajiura. Origin of the abiki phenomenon (a kind of seiche) in nagasaki bay. *Journal of the Oceanographical Society of Japan*, 38(3):172–182, 1982.

S. Ide and H. Aochi. Modeling earthquakes using fractal circular patch models with lessons from the 2011 tohoku-oki earthquake. *J. Disaster Res*, 9:264–271, 2014.

F. Imamura and K. Hashi. Re-examination of the source mechanism of the 1998 papua new guinea earthquake and tsunami. *Pure and Applied Geophysics*, 160(10):2071–2086, 2003. ISSN 1420-9136. doi: 10.1007/s00024-003-2420-2. URL http://dx.doi.org/10.1007/s00024-003-2420-2.

Y. Ito, T. Tsuji, Y. Osada, M. Kido, D. Inazu, Y. Hayashi, H. Tsushima, R. Hino, and H. Fujimoto. Frontal wedge deformation near the source region of the 2011 tohoku-oki earthquake. *Geophysical Research Letters*, 38(7):n/a–n/a, 2011. ISSN 1944-8007. doi: 10.1029/2011GL048355. URL http://dx.doi.org/10.1029/2011GL048355. L00G05.

T. Jamin, L. Gordillo, G. Ruiz-Chavarría, M. Berhanu, and E. Falcon. Experiments on generation of surface waves by an underwater moving bottom. *Proceedings of the Royal Society of London A: Mathematical, Physical and Engineering Sciences*, 471 (2178), 2015. ISSN 1364-5021. doi: 10.1098/rspa.2015.0069. URL http://rspa.royalsocietypublishing.org/content/471/2178/20150069.

A. Jansa, S. Monserrat, and D. Gomis. The rissaga of 15 june 2006 in ciutadella (menorca), a meteorological tsunami. *Advances in Geosciences*, 12:1–4, 2007. doi: 10.5194/adgeo-12-1-2007. URL http://www.adv-geosci.net/12/1/2007/.

A. Jensen, G. K. Pedersen, and D. J. Wood. An experimental study of wave run-up at a steep beach. *Journal of Fluid Mechanics*, 486:161–188, 2003.

C. Ji, D. J. Wald, and D. V. Helmberger. Source description of the 1999 Hector Mine, California, earthquake, part I: Wavelet domain inversion theory and resolution analysis. *Bulletin of the Seismological Society of America*, 92(4):1192–1207, 2002. doi: 10.1785/0120000916. URL http://www.bssaonline.org/content/92/4/1192.abstract.

C. Ji, D. V. Helmberger, and D. J. Wald. A teleseismic study of the 2002 denali fault, alaska, earthquake and implications for rapid strong-motion estimation. *Earthquake Spectra*, 20(3):617–637, 2004.

L. Jiang and P. H. LeBlond. The coupling of a submarine slide and the surface waves which it generates. *Journal of Geophysical Research: Oceans*, 97(C8):12731–12744, 1992.

L. Jiang and P. H. Leblond. Three-dimensional modeling of tsunami generation due to a submarine mudslide. *Journal of physical oceanography*, 24(3):559–572, 1994.

J. M. Johnson and K. Satake. Estimation of seismic moment and slip distribution of the April 1, 1946, Aleutian tsunami earthquake. *Journal of Geophysical Research*, 102(11): 765–11, 1997.

R. S. Johnson. *A modern introduction to the mathematical theory of water waves*, volume 19. Cambridge university press, 1997.

H. Kanamori. Mechanism of tsunami earthquakes. *Physics of the Earth and Planetary Interiors*, 6:346–359, 1972.

U. Kânoğlu. Nonlinear evolution and runup-rundown of long waves over a sloping beach. *Journal of Fluid Mechanics*, 513:363–372, 2004.

U. Kânoğlu, V. Titov, E. Bernard, and C. E. Synolakis. Tsunamis: bridging science, engineering and society. *Philosophical Transactions of the Royal Society of London A*, 373(2053):20140369, 2015.

M. Kikuchi and H. Kanamori. Source characteristics of the 1992 nicaragua tsunami earthquake inferred from teleseismic body waves. *pure and applied geophysics*, 144(3-4): 441–453, 1995.

J. T. Kirby, F. Shi, B. Tehranirad, J. C. Harris, and S. T. Grilli. Dispersive tsunami waves in the ocean: Model equations and sensitivity to dispersion and coriolis effects. *Ocean Modelling*, 62:39–55, 2013. ISSN 1463-5003. doi: http://dx.doi.org/10.1016/j.ocemod.2012.11.009. URL http://www.sciencedirect.com/science/article/pii/S1463500312001692.

K. Koketsu, Y. Yokota, N. Nishimura, Y. Yagi, S. Miyazaki, K. Satake, Y. Fujii, H. Miyake, S. Sakai, Y. Yamanaka, and T. Okada. A unified source model for the 2011 tohoku earthquake. *Earth and Planetary Science Letters*, 310(34):480–487, 2011. ISSN 0012-821X. doi: http://dx.doi.org/10.1016/j.epsl.2011.09.009. URL http://www.sciencedirect.com/science/article/pii/S0012821X11005206.

A. A. Kurkin and E. N. Pelinovsky. Freak waves: facts, theory and modelling. *Nizhegorodski State Univ*, 2004.

T. Lay, C. J. Ammon, H. Kanamori, Y. Yamazaki, K. F. Cheung, and A. R. Hutko. The 25 october 2010 mentawai tsunami earthquake (mw 7.8) and the tsunami hazard presented by shallow megathrust ruptures. *Geophysical Research Letters*, 38(6), 2011.

B. Le Méhauté and S. Wang. *Water waves generated by underwater explosion*, volume 10. World Scientific, 1996.

S.-J. Lee, G. T. Yates, and T. Y. Wu. Experiments and analyses of upstream-advancing solitary waves generated by moving disturbances. *Journal of Fluid Mechanics*, 199: 569–593, February 1989. doi: 10.1017/S0022112089000492.

B. Levin and M. Nosov. *Physics of tsunamis*. Springer Science, 2009.

Y. Li and F. Raichlen. Breaking criterion and characteristics for solitary waves on slopes-discussion, 1998.

Y. Li and F. Raichlen. Energy balance model for breaking solitary wave runup. *Journal of Waterway, Port, Coastal, and Ocean Engineering*, 129(2):47–59, 2003.

P. Lin, K.-A. Chang, and P. L.-F. Liu. Runup and rundown of solitary waves on sloping beaches. *Journal of Waterway, Port, Coastal, and Ocean Engineering*, 125(5):247–255, 1999.

P. L.-F. Liu, Y.-S. Cho, M. J. Briggs, U. Kânoğlu, and C. E. Synolakis. Runup of solitary waves on a circular island. *Journal of Fluid Mechanics*, 302:259–285, 1995.

P. L.-F. Liu, P. Lynett, and C. E. Synolakis. Analytical solutions for forced long waves on a sloping beach. *Journal of Fluid Mechanics*, 478:101–109, 2003.

P. L.-F. Liu, H. Yeh, and C. E. Synolakis. Advanced numerical models for simulating tsunami waves and runup. *Advances in Coastal and Ocean Engineering*, 10:250, 2008.

A. M. López and E. A. Okal. A seismological reassessment of the source of the 1946 aleutian 'tsunami'earthquake. *Geophysical Journal International*, 165(3):835–849, 2006.

P. J. Lynett, D. Swigler, S. Son, D. Bryant, and S. Socolofsky. Experimental study of solitary wave evolution over a 3d shallow shelf. *Coastal Engineering Proceedings*, 1(32): 1, 2011.

C. L. Mader and M. L. Gittings. Modeling the 1958 lituya bay mega-tsunami, ii. *Science of Tsunami Hazards*, 20(5):241–250, 2002.

C. L. Mader and M. L. Gittings. Numerical model for the krakatoa hydrovolcanic explosion and tsunami. *Science of Tsunami Hazards*, 24(3):174, 2006.

Per A. Madsen and H. A. Schaeffer. Analytical solutions for tsunami runup on a plane beach: single waves, n-waves and transient waves. *Journal of Fluid Mechanics*, 645: 27–57, 2010.

Per A. Madsen, D. R. Fuhrman, and H. A. Schäffer. On the solitary wave paradigm for tsunamis. *Journal of Geophysical Research: Oceans*, 113(C12), 2008.

W. Malfliet. Solitary wave solutions of nonlinear wave equations. *American Journal of Physics*, 60(7):650–654, 1992. doi: http://dx.doi.org/10.1119/1.17120. URL http://scitation.aip.org/content/aapt/journal/ajp/60/7/10.1119/1.17120.

S. R. Massel. Tsunami in coastal zone due to meteorite impact. *Coastal Engineering*, 66: 40–49, 2012.

D. G. Masson, C. B. Harbitz, R. B. Wynn, G. Pedersen, and F. Løvholt. Submarine landslides: processes, triggers and hazard prediction. *Philosophical Transactions of the Royal Society of London A: Mathematical, Physical and Engineering Sciences*, 364 (1845):2009–2039, 2006.

T. Masterlark and K. L. H. Hughes. Next generation of deformation models for the 2004 m9 sumatra-andaman earthquake. *Geophysical Research Letters*, 35(19):n/a–n/a, 2008. ISSN 1944-8007. doi: 10.1029/2008GL035198. URL http://dx.doi.org/10.1029/2008GL035198. L19310.

C. C. Mei, M. Stiassnie, and Dick K.-P. Yue. Theory and applications of ocean surface waves. *Advanced Series on Ocean Engineering*, 23, 2005. World Scientific Publishing.

Don J. Miller. *Giant waves in lituya bay, alaska.* US Government Printing Office Washington, DC, 1960.

J. S. Mitchell, K. A. Mackay, H. L. Neil, E. J. Mackay, A. Pallentin, and P. Notman. Undersea new zealand, 1:5,000,000. 2012, 2016. URL https://www.niwa.co.nz/our-science/oceans/bathymetry. NIWA Chart, Miscellaneous Series No. 92.

S. Monserrat, I. Vilibic, and A. B. Rabinovich. Meteotsunamis: atmospherically induced destructive ocean waves in the tsunami frequency band. *Natural Hazards and Earth System Science*, 6(6):1035–1051, December 2006. URL https://hal.archives-ouvertes.fr/hal-00299394.

N. Mori and T. Takahashi. Nationwide post event survey and analysis of the 2011 tohoku earthquake tsunami. *Coastal Engineering Journal*, 54(01):1250001, 2012.

N. Mori, T. Takahashi, T. Yasuda, and H. Yanagisawa. Survey of 2011 tohoku earthquake tsunami inundation and run-up. *Geophysical Research Letters*, 38(7):n/a–n/a, 2011. ISSN 1944-8007. doi: 10.1029/2011GL049210. URL http://dx.doi.org/10.1029/2011GL049210. L00G14.

T. S. Murty. Tsunami wave height dependence on landslide volume. *Pure and Applied Geophysics*, 160(10):2147–2153, 2003. ISSN 1420-9136. doi: 10.1007/s00024-003-2423-z. URL http://dx.doi.org/10.1007/s00024-003-2423-z.

T. Nomitsu. A theory of tsunamis and seiches produced by wind and barometric gradient. *Mem. Coll. Sci. Imp. Univ. Kyoto A*, 18(4):201–214, 1935.

M. Nosov. Tsunami waves of seismic origin: The modern state of knowledge. *Izvestiya, Atmospheric and Oceanic Physics*, 50(5):474–484, 2014. ISSN 0001-4338. doi: 10.1134/S0001433814030098. URL http://dx.doi.org/10.1134/S0001433814030098.

Y. Okada. Internal deformation due to shear and tensile faults in a half-space. *Bulletin of the Seismological Society of America*, 82, No 2:1018–1040, 1992.

H. Park, D. T. Cox, P. J. Lynett, D. M. Wiebe, and S. Shin. Tsunami inundation modeling in constructed environments: a physical and numerical comparison of free-surface elevation, velocity, and momentum flux. *Coastal Engineering*, 79:9–21, 2013.

S. Pavan. *New advection schemes for free surface Wows.* PhD thesis, Ecole Doctorale SIE, 2016.

E. N. Pelinovsky. Tsunami wave hydrodynamics. *Institute Applied Physics Press, Nizhny Novgorod*, 1996. In russian.

D. H. Peregrine. Long waves on a beach. *Journal of Fluid Mechanics*, 27(04):815–827, 1967.

F. F. Pollitz, R. Bürgmann, and P. Banerjee. Geodetic slip model of the 2011 m9.0 tohoku earthquake. *Geophysical Research Letters*, 38(7):n/a–n/a, 2011. ISSN 1944-8007. doi: 10.1029/2011GL048632. URL http://dx.doi.org/10.1029/2011GL048632. L00G08.

K. Pons, M. Ersoy, F. Golay, and R. Marcer. Adaptive mesh refinement method. part 2: Application to tsunamis propagation. working paper or preprint, July 2016. URL https://hal.archives-ouvertes.fr/hal-01330680.

S. Popinet. Adaptive modelling of long-distance wave propagation and fine-scale flooding during the tohoku tsunami. *Natural Hazards and Earth System Science*, 12(4):1213–1227, 2012.

C. Raoult. *Nonlinear and dispersive numerical modeling of nearshore waves.* PhD thesis, Ecole Doctorale SIE, université de Paris-Est, 2016.

C. Raoult, M. Benoit, and M. L. Yates. Validation of a fully nonlinear and dispersive wave model with laboratory non-breaking experiments. *Coastal Engineering*, 114:194–207, 2016.

F. Romano, E. Trasatti, S. Lorito, C. Piromallo, A. Piatanesi, Y. Ito, D. Zhao, K. Hirata, P. Lanucara, and M. Cocco. Structural control on the tohoku earthquake rupture process investigated by 3d fem, tsunami and geodetic data. *Scientific reports*, 4, 2014.

J. S. Russell. Report on water waves. *British Assoc. Report*, 1844.

J. Sasaki, K. Ito, T. Suzuki, R. U. A. Wiyono, Y. Oda, Y. Takayama, K. Yokota, A. Furuta, and H. Takagi. Behavior of the 2011 tohoku earthquake tsunami and resultant damage in tokyo bay. *Coastal Engineering Journal*, 54(01):1250012, 2012. doi: 10.1142/S057856341250012X. URL http://www.worldscientific.com/doi/abs/10.1142/S057856341250012X.

K. Satake. Mechanism of the 1992 Nicaragua Tsunami Earthquake. *Geophysical Research Letters*, 21(23):2519–2522, 1994. ISSN 1944-8007. doi: 10.1029/94GL02338. URL http://dx.doi.org/10.1029/94GL02338.

K. Satake, Y. Fujii, T. Harada, and Y. Namegaya. Time and space distribution of coseismic slip of the 2011 tohoku earthquake as inferred from tsunami waveform data. *Bulletin of the Seismological Society of America*, 103(2B):1473–1492, May 2013.

G. Shao, X. Li, C. Ji, and T. Maeda. Focal mechanism and slip history of the 2011 mw 9.1 off the pacific coast of tohoku earthquake, constrained with teleseismic body and surface waves. *Earth, Planets and Space*, 63(7):559–564, 2011. ISSN 1343-8832. doi: 10.5047/eps.2011.06.028. URL http://dx.doi.org/10.5047/eps.2011.06.028.

M. Simons, S. E. Minson, A. Sladen, F. Ortega, J. Jiang, S. E. Owen, L. Meng, J.-P. Ampuero, S. Wei, R. Chu, D. V. Helmberger, H. Kanamori, E. Hetland, A. W. Moore, and F. H. Webb. The 2011 magnitude 9.0 tohoku-oki earthquake: Mosaicking the megathrust from seconds to centuries. *Science*, 332(6036):1421–1425, 2011. doi: 10.1126/science.1206731. URL http://www.sciencemag.org/content/332/6036/1421.abstract.

T. S. Stefanakis, F. Dias, and C. E. Synolakis. Tsunami generation above a sill. *Pure and Applied Geophysics*, 172(3):985–1002, 2015. ISSN 1420-9136. doi: 10.1007/s00024-014-1021-6. URL http://dx.doi.org/10.1007/s00024-014-1021-6.

C. E. Synolakis. The runup of solitay waves. *Journal of Fluid Mechanics*, 185:523–545, 1987.

C. E. Synolakis, J.-P. Bardet, J. C. Borrero, H. L. Davies, E. A. Okal, E. A. Silver, S. Sweet, and D. R. Tappin. The slump origin of the 1998 papua new guinea tsunami. *Proceedings of the Royal Society of London A: Mathematical, Physical and Engineering Sciences*, 458(2020):763–789, 2002. ISSN 1364-5021. doi: 10.1098/rspa.2001.0915. URL http://rspa.royalsocietypublishing.org/content/458/2020/763.

C. E. Synolakis, E. N. Bernard, V. V. Titov, U. Kânoğlu, and F. I. González. Standards, criteria, and procedures for noaa evaluation of tsunami numerical models. 2007.

D. Tappin, P. Watts, and S. Grilli. The papua new guinea tsunami of 17 july 1998: anatomy of a catastrophic event. *Natural Hazards and Earth System Science*, 8(2):243–266, 2008.

D. R. Tappin, S. T. Grilli, J. C. Harris, R. J. Geller, T. Masterlark, J. T. Kirby, F. Shi, G. Ma, K.K.S. Thingbaijam, and P. Martin Mai. Did a submarine landslide contribute to the 2011 tohoku tsunami? *Marine Geology*, 357:344–361, 2014. ISSN 0025-3227. doi: http://dx.doi.org/10.1016/j.margeo.2014.09.043. URL http://www.sciencedirect.com/science/article/pii/S0025322714002898.

W. C. Thacker. Some exact solutions to the nonlinear shallow-water wave equations. *Journal of Fluid Mechanics*, 107:499–508, 6 1981. ISSN 1469-7645. doi: 10.1017/S0022112081001882. URL http://journals.cambridge.org/article_S0022112081001882.

S. Tinti, G. Pagnoni, and A. Piatanesi. Simulation of tsunamis induced by volcanic activity in the gulf of naples (italy). *Natural Hazards and Earth System Science*, 3(5):311–320, 2003.

S. Toda, J. Lin, and R. S. Stein. Using the 2011 mw 9.0 off the pacific coast of tohoku earthquake to test the coulomb stress triggering hypothesis and to calculate faults brought closer to failure. *Earth, Planets and Space*, 63(7):725–730, 2011.

M. Todesco, A. Neri, T. E. Ongaro, P. Papale, G. Macedonio, R. Santacroce, and A. Longo. Pyroclastic flow hazard assessment at vesuvius (italy) by using numerical modeling. i. large-scale dynamics. *Bulletin of Volcanology*, 64(3-4):155–177, 2002.

M. I. Todorovska and M. D. Trifunac. Generation of tsunamis by a slowly spreading uplift of the sea floor. *Soil Dynamics and Earthquake Engineering*, 21:151–167, 2001.

M. D. Trifunac and M. I. Todorovska. A note on differences in tsunami source parameters for submarine slides and earthquakes. *Soil Dynamics and Earthquake Engineering*, 22(2):143–155, 2002. ISSN 0267-7261. doi: http://dx.doi.org/10.1016/S0267-7261(01)00057-4. URL http://www.sciencedirect.com/science/article/pii/S0267726101000574.

A. Vaschy. Sur les lois de similitude en physique. *Annales Télégraphiques*, 19:25–28, 1892. In French.

I. Vilibić, S. Monserrat, and A. B. Rabinovich. *Meteorological Tsunamis: The US East Coast and Other Coastal Regions*. Springer, 2014.

D. Violeau. Wp1: Qualifying numerical tools for tsunami studies contribution of wp1 to the project's 1st year. Technical report, TANDEM, January 2015.

D. Violeau, S. Abadie, R. Ata, M. Benoit, J. Chicheportiche, L. Clous, A. Gailler, H. Hébert, D. Imbert, A. Joly, et al. A database of validation cases for tsunami numerical modelling. In *Proc. 4th IAHR Europe Congress, Liège (Belgium)*, pages 27–29, 2016.

S. N. Ward and E. Asphaug. Asteroid impact tsunami: a probabilistic hazard assessment. *Icarus*, 145(1):64–78, 2000.

S. N. Ward and E. Asphaug. Impact tsunami–eltanin. *Deep Sea Research Part II: Topical Studies in Oceanography*, 49(6):1073–1079, 2002.

S. N. Ward and E. Asphaug. Asteroid impact tsunami of 2880 march 16. *Geophysical Journal International*, 153(3):F6–F10, 2003.

S. Wei and A. Sladen. Tohoku source model v.1. Technical report, Caltech, 2011. URL http://www.tectonics.caltech.edu/slip_history/2011_taiheiyo-oki/.

T. Y. Wu. Long waves in ocean and coastal waters. *Journal of Engineering Mechanics*, 107(EM3):501–522, 1981.

T. Y. Wu. Generation of upstream advancing solitons by moving disturbances. *Journal of Fluid Mechanics*, 184(75-99):3–4, 1987.

Y. Yagi. Source rupture process of the 2003 tokachi-oki earthquake determined by joint inversion of teleseismic body wave and strong ground motion data. *Earth, Planets and Space*, 56(3):311–316, 2004.

Y. Yagi and Y. Fukahata. Introduction of uncertainty of green's function into waveform inversion for seismic source processes. *Geophysical Journal International*, 186(2):711–720, 2011a. doi: 10.1111/j.1365-246X.2011.05043.x. URL http://gji.oxfordjournals.org/content/186/2/711.abstract.

Y. Yagi and Y. Fukahata. Rupture process of the 2011 tohoku-oki earthquake and absolute elastic strain release. *Geophysical Research Letters*, 38(19):n/a–n/a, 2011b. ISSN 1944-8007. doi: 10.1029/2011GL048701. URL http://dx.doi.org/10.1029/2011GL048701. L19307.

M. L. Yates and M. Benoit. Accuracy and efficiency of two numerical methods of solving the potential flow problem for highly nonlinear and dispersive water waves. *International Journal for Numerical Methods in Fluids*, 77(10):616–640, 2015. ISSN 1097-0363. doi: 10.1002/fld.3992. URL http://dx.doi.org/10.1002/fld.3992.

V.-E. Zakharov. Stability of periodic waves of finite amplitude on the surface of a deep fluid. *Journal of Applied Mechanics and Technical Physics*, 9:190–194, 1968. doi: 10.1007/BF00913182.